Investigation and characterisation of material degradation mechanisms across extremely hot interfaces in molten salts

Harry Edward Bullock

Submitted in accordance with the requirements for the degree of

Doctor of Philosophy

University of Leeds

Institute of Functional Surfaces

School of Mechanical Engineering

Publication Statement

The candidate confirms that the work submitted is his/her own and that appropriate credit has been given where reference has been made to the work of others.

This copy has been supplied on the understanding that it is copyright material and that no quotation from the thesis may be published without proper acknowledgement.

© 2024 The University of Leeds and Harry Edward Bullock

Acknowledgements

I would firstly like to thank my primary supervisor Dr Frederick Pessu for his supervision, enthusiasm, and advice throughout the course of my PhD. I am also grateful for the supervision provided by Professor Richard Barker during my PhD. I have learned a great deal from both of you and without you both, this research would not have been possible. I would also like to thank the IFS technicians for all of their assistance throughout this PhD. Their advice and assistance in the labs have been invaluable.

To all the friends I have made in IFS, I'd also like to express my thanks. In particular to Dan Jones, Raeesa Bhamji and Rob Jacklin for always being up for a pint and a game of pool after work, as well as Beth, Mike, Josh Owen, Josh Armitage, Amber, and Joseph for always making sure I was fuelled up on biscuits and coffee.

I would also like to thank my friends at Burley RUFC for giving me an amazing support network outside of university and providing a fantastic outlet from university life. In particular, I'd like to thank Lloyd Roberts, Sam Heaton, Harry Francis, and Ali Trace for their support as well as Sam Parry and Jamie Manson for constantly reminding me that they're already Doctors and questioning when I'm going to be finished.

To my family (Mum, Dad, and Annabel) who have supported me since day one of my 9-year adventure in Leeds, I express my greatest thanks. You have always believed in me and supported me in everything I have done and for that I will always be grateful! To my Grandparents, especially my grandpa and my Pappy, I thank you both for inspiring me so long ago to pursue a career in engineering. Pappy, although you are not here to see my completed thesis, I know you would be proud.

Finally, a massive thank you to my girlfriend Charlotte for her constant support and positive can-do attitude towards everything she does. You inspire me daily to get up and do my best, especially on the days where I feel like I cannot see the light at the end of the tunnel.

Abstract

The molten salt reactor (MSR) is a Generation – IV nuclear reactor, designed to use molten salts as a carrier fuel for nuclear material and as a heat transfer fluid. However, many the molten salt combination proposed for use in the MSR are highly corrosive to many of the proposed materials, including Ni-based alloys. There is still a limited understanding of the corrosion behaviour of Ni-based alloys in molten salt environment, particularly in those containing oxygen as a contaminant. Therefore, the synergy of oxidation and corrosion in molten salt environments was the focus of this research.

A high temperature furnace was used to conduct isothermal high temperature oxidation and molten salt corrosion experiments on coupons of Hastelloy C276 under conditions similar to those of a molten salt reactor environment. These included exposing coupons to temperatures of 700 °C, in dry air environments with and without molten FLiNaK salt. Results from the experimental research of high temperature oxidation were used to validate empirical and mechanistic predictive models for high temperature oxidation of Ni-based alloys before the mechanistic model was developed further to provide predictions for molten salt corrosion of Ni-based alloys in FLiNaK salt.

For the high temperature oxidation of Hastelloy C276, parabolic oxidation kinetics were observed experimentally, with a parabolic rate constant of 2.57×10^{-7} $mg^2/cm^4/s$ being calculated to reflect the high temperature oxidation behaviour of Hastelloy C276 in the time period of 0 to 200 hours. In the same time period and in a molten salt environment, Hastelloy C276 was observed to exhibit high corrosion rates, in excess of 0.3 mmpy. Material loss from Hastelloy C276 was observed to follow a linear relationship, indicating that any corrosion product layers were offering no protection to the underlying substrate from the corrosive medium.

Table of Contents

Publication Statement ..... **ii**
Acknowledgements ..... **iii**
Abstract ..... **iv**
Table of Contents ..... **v**
Table of Figures ..... **x**
Table of Tables ..... **xxvi**
List of Abbreviations ..... **xxx**
Chapter 1 – Introduction **1**
1.1 Project Background 1
1.2 Contribution to Literature 5
1.3 Project Objectives 5
1.4 Thesis Structure 6
Chapter 2 – Literature Review I **8**
2.1 Introduction 8
2.2 Generation – IV nuclear reactors – A summary 8
2.3 Development of the MSR 13
2.3.1 Historical development of the MSR 14
2.4 Current Generation – IV MSR Configurations 17
2.5 Potential mechanisms of material degradation 23
2.5.1 Uniform Corrosion 23
2.5.2 Crevice Corrosion 25
2.5.3 Stress Corrosion Cracking (SCC) 25
2.5.4 Pitting Corrosion 27
2.5.5 Galvanic Corrosion 28
2.5.6 Intergranular Corrosion 29
2.5.7 Material Dealloying 30
2.6 Summary of literature review: The Generation – IV nuclear reactors and MSR development 31
Chapter 3 – Literature Review II **33**
3.1 Introduction 33
3.2 Fundamentals of alloy oxidation 34
3.2.1 Definition of oxidation 34
3.2.2 Thermodynamics of metal oxidation 34

3.2.3 Thermodynamics of alloy oxidation 36
3.2.4 Diffusion of alloying elements 39
3.2.5 Rates of oxide growth and their governance 42
3.3 Thermodynamic concepts used in predictive modelling 46
3.3.1 Predictive modelling using neural networks 53
3.4 Oxidation of Ni – based alloys in high temperature environments . 55
3.4.1 Impact of environmental conditions on the oxidation of Ni-based alloys 55
3.4.2 Effect of alloy composition on its oxidation behaviour 61
3.4.3 Effect of microstructure on alloy oxidation 66
3.5 Alloy corrosion in molten salt environments 69
3.5.1 Thermodynamics of molten salt corrosion 70
3.5.2 Kinetics of material corrosion in molten salts 73
3.5.3 Numerical modelling of molten salt corrosion: A mechanistic approach 75
3.6 Corrosion of Ni-based alloys in molten fluoride salt environments. 78
3.6.1 Influential factors on corrosion in molten fluoride salts 79
3.7 Corrosion of irradiated materials in molten salt environments 108
3.7.1 Irradiation emulation Methods 109
3.7.2 Combined irradiation and molten salt corrosion studies 111
3.8 Summary of literature review 112
Chapter 4 – Materials, Experimental and Numerical Methods 114
4.1 Introduction 114
4.2 Introduction to High Temperature Oxidation and Molten Salt Corrosion 115
4.2.1 Basic Experimental Methodology Description 116
4.2.2 Material Selection 117
4.2.3 Coupon preparation for corrosion and oxidation testing 120
4.2.4 Experimental Conditions and Protocols 121
4.2.5 Post – experimental Analysis Techniques 123
4.2.6 Use of experimental results as validation evidence 128
4.3 Use of empirical model for oxide growth prediction 128
4.3.1 Development of empirical model – Application of underpinning theory 129
4.3.2 Development of empirical model – Calculation of Gibbs free energy change of Cr_2O_3 132

4.3.3 Development of empirical model – Relationship between U and K_P 134
4.3.4 Development of empirical model – Predicting oxide layer thickness 138
4.4 Use of MATLAB functions in predicting corrosion and oxidation behaviour 140
4.4.1 Overview of MATLAB partial differential equation solver 140
4.4.2 Development of a mechanistic model in MATLAB – Predicting element distribution 141
4.4.3 Development of a mechanistic model in MATLAB – Predicting mass changes due to oxide growth 148
4.4.4 Development of a mechanistic model in MATLAB – Predicting elemental depletion depths and depletion depth due to corrosion. 150
4.5 Summary of research methods 154
Chapter 5 – Results I 155
5.1 Introduction 155
5.2 Prediction of oxide growth – Empirical Model 156
5.2.1 Empirical Model – Model Description 156
5.2.2 Empirical Model – Oxide growth prediction 156
5.2.3 Empirical Model – Oxide Layer Prediction 157
5.3 Predictions of oxide growth and element depletion – Diffusion Based Model 158
5.3.1 Diffusion Based Model – Model Description 158
5.3.2 Diffusion Based Model – Sensitivity Study 159
5.3.3 Diffusion Based Model – Validation of Mass Change Prediction against Literature 165
5.3.4 Diffusion Based Model – Oxide growth prediction 170
5.3.5 Diffusion Based Model – Elemental Distributions 174
5.4 Experimental Results and Oxide Layer Characterisation 179
5.4.1 Experimental Methodology 179
5.4.2 Experimental Results – Mass Change Measurements 179
5.4.3 Characterisation of Oxide Layer – SEM analysis 181
5.4.4 Characterisation of Oxide Layer – EDX analysis 185
5.4.5 Characterisation of Oxide Layer – XRD analysis 191
5.5 Experimental Results versus Numerical Predictions 192
5.6 Summary of Results 194

Chapter 6 - Results II..... 196
6.1 Introduction..... 196
6.2 Prediction of corrosion – Mechanistic Model 197
6.2.1 Diffusion Based Model - Model Description..... 197
6.2.2 Diffusion Based Model - Sensitivity Study 197
6.2.3 Diffusion Based Model - Corrosion Predictions 202
6.3 Experimental Results and Corrosion product characterisation 205
6.3.1 Experimental Results - Mass change measurements..... 206
6.3.2 Characterisation of corrosion products – SEM analysis 211
6.3.3 Characterisation of corrosion products – EDX analysis..... 216
6.3.4 Characterisation of corrosion products – XRD analysis..... 223
6.4 Experimental Results versus Numerical Predictions..... 224
6.5 Summary of Results 227
Chapter 7 – Discussion..... 228
7.1 Introduction..... 228
7.2 High temperature oxidation mechanism of Hastelloy C276 229
7.2.1 Effect of oxide layer formation on oxidation kinetics..... 230
7.2.2 Effect of diffusion behaviour on oxide layer growth 234
7.2.3 Considering reaction kinetics for oxide formation 243
7.2.4 Short circuit diffusion of O_2 in NiO layers..... 244
7.3 Use of modelling techniques for the prediction of high temperature oxidation kinetics 245
7.3.1 Impact of modelling assumptions on high temperature oxidation predictions 246
7.3.2 Empirical and mechanistic model validation 247
7.4 Corrosion behaviour of Hastelloy C276 in FLiNaK molten salt 248
7.4.1 Proposed mechanism of Hastelloy C276 in molten FLiNaK salt 249
7.4.2 Correlation of corrosion product formation and corrosive attack 253
7.4.3 Assessment of corrosion product formation and corrosive attack correlation..... 257
7.5 Molten salt corrosion modelling using a mechanistic approach ... 262
7.5.1 Impact of modelling assumptions on corrosion depth predictions 264

Chapter 8 – Conclusions and Future Work 266
8.1 Conclusions of Research.....266
8.2 Future Work.....270
References 273
Appendix A.....285
A.1 Introduction.....285
A.2 Empirical model sensitivity to input parameters.....286
A.3 Mechanistic model sensitivity to input parameters 288

Table of Figures

Figure 1.1 – Timeline proposed by the GIF for the research and development of the six Generation – IV nuclear reactors, adapted from [5]..... 2

Figure 1.2 – Schematic showing MSR operation cycles with salt cycles labelled. Figure adapted from [5] 3

Figure 1.3 - Project framework highlighting the aims and objectives of the research project to understand the degradation of materials in molten salt environments. 6

Figure 2.1 – Key areas and the associated goals for the Generation – IV nuclear reactors [5]..... 9

Figure 2.2 – Updated research and development timeline for Generation - IV nuclear reactors, introduced in 2014, adapted from [5, 19] 13

Figure 2.3 – Illustration of the Th fuel cycle where U-233 is produced from Th-232 [24]. The depicted process shows the interaction of Th-232 with a neutron followed by two subsequent radioactive decays to become U-233..... 14

Figure 2.4 – Image illustrating the structure of solid nuclear fuel design for MSR applications, including a solid UO_2 core surround by layers of graphite, pyrolytic carbon, and SiC. Figure adapted from [7]..... 18

Figure 2.5 – Analysis from work by Olson et al. [53] showing a) micrograph of cross section showing corrosion damage to Hastelloy N after immersion in molten FLiNaK salt at 850 °C for 500 hours and b) showing EDX analysis of cross-section presented in a) showing uniform depletion of Cr to depths of approximately 45 µm. Image adapted from [53]. 24

Figure 2.6 – Illustration of structural defects that may form during irradiation, such as vacancies and dislocation loops. The formation of dislocation loops is shown by a) the presence of vacancies, b) the movement of vacancies and c) the formed dislocation loop. 26

Figure 2.7 – Changes in percentage elongation observed for Alloy 617 before and after irradiation processes. Results show significant reductions in percentage elongation with increasing irradiation damage, which is indicative of material embrittlement. Figure created with data from [62]. 27

Figure 2.8 – Specific mass changes results for Incoloy 800H coupons immersed in FLiNaK molten salt at 850 °C for 500 hours in crucibles constructed from Ni-201, graphite, PyBN and Incoloy 800H showing increases in the specific mass loss of factors of 142, 165 and 4 for the Ni-201, Graphite and PyBN crucibles respectively [69]. 29

Figure 2.9 – Intergranular corrosion of stainless steels and Ni-based alloys in molten FLiNaK salt at 850 °C. Coupons of a) Incoloy 800H ,b) Inconel 617, c) Haynes-230 and d) Hastelloy X were immersed for a duration of 500 hours. Images taken from [70]. 30

Figure 2.10 – Ligaments and pores formed at the substrate – molten salt interface of Ni62Fe38 alloy after exposure to NaCl – KCl – $MgCl_2$ molten salt at 350 °C. Figure adapted from [45]. 31

Figure 3.1 – Ternary phase diagram for Fe-Ni-O system showing phases formed at different partial pressures of O_2 and molar fractions of Ni [79]. Result shows regions where oxide formation is possible, and the oxides formed. 38

Figure 3.2 – Phase diagrams for a) A-B-O, b) A-C-O and c) B-C-O ternary systems for an alloy A-B-C in contact with a single oxidant, adapted from [80]. 39

Figure 3.3 – Image showing diffusion and transport processes involved in the oxidation of alloys which include the diffusion of ions to the substrate – air interface and their subsequent reactions to form a metallic oxide layer [77, 83]. At later time intervals, species are shown to diffuse across the oxide layer to the oxide – air interface to continue oxide layer formation.....42

Figure 3.4 – Figure detailing the types of oxidation kinetics discussed in this section, showing linear, parabolic, sub-parabolic and linear-parabolic types of oxidation kinetics. 45

Figure 3.5 – Comparison of the oxidation kinetics of Ni at 800 °C and 1300 °C, illustrating a linear relationship between the specific mass change and the square root of time at 1300 °C, from which, parabolic oxidation kinetics can be concluded. Image taken from [85]. 46

Figure 3.6 – Graph of U for Al_2O_3 formation against K_p values, obtained for alloys of Rene N5, SCA425+0.25Si, CMSX-4 and PWA-1484 alloys at 900 °C. Mathematical analysis indicates an R^2 of 0.58, indicating very little correlation between data points used to develop empirical relationship [87, 88, 91]. 51

Figure 3.7 - Illustration of a nodal structure applied to the geometry over which the concentration of alloying elements in a metallic alloy is being solved. 52

Figure 3.8 – Plot of natural logarithm of K_P against the reciprocal of temperature in K for data collected for the oxidation of RR1000 between 700 °C and 900 °C by Taylor et al. [101], showing linear relationship between the two parameters. 57

Figure 3.9 – Results for the specific mass change of Inconel 600 alloy, exposed to a dry air environment at 700 °C, 800 °C and 900 °C for durations up to 100 hours showing increasing specific mass change with increasing temperature [104].....58

Figure 3.10 – Micrographs of Inconel 600 coupons, exposed to a) dry air environment, b) dry air environment containing 5% humidity and c) dry air environment containing 19% humidity, all at 800 °C. Results show increasing oxide layer coverage of the exposed surface within increasing humidity. Figure adapted from [105]. 59

Figure 3.11 – Comparison of oxidation results for Haynes 230 in a dry air environment at 850 °C and steam containing environment at 700 °C and 800 °C, showing that moisture content increases the oxidation rate of Haynes 230 to a similar level of that observed at 850 °C in a dry air environment. Data collected from [106, 108, 110]. 60

Figure 3.12 – Comparison of oxide scales formed on the exposed surfaces of Inconel 617 in a) dry air environment and b) steam environment at 750 °C after 500 hours, showing oxide scales are more densely packed after exposure to dry air environment, resulting in a greater diffusion barrier for ions, resulting in a slower oxidation rate in air. Figure adapted from [111]. 61

Figure 3.13 – Micrographs showing formation of discontinuous (a – b) and continuous (c – d) Al_2O_3 layers with varying concentrations of Ti, with lower concentrations of Ti showing improved oxidation resistance. Figure adapted from [95]. 62

Figure 3.14 – Plot of oxide layer thicknesses as a function of temperature for pure Ni, Ni20Cr and Ni15Al alloys, tested at temperatures between 700 °C and 1200 °C for 576 hours [112]. 63

Figure 3.15 – Comparison of oxide layers of (a and b) Ni and (c and d) Ni20Cr at 700 °C and 900 °C respectively highlighting the presence of voids and cracks at 900 °C, resulting in a discontinuous diffusion barrier and hence decreased oxidation resistance. Figure adapted from [112]. 64

Figure 3.16 – Comparison of the oxidation behaviour of (a – d) Ni20Cr and (e – h) Ni15Al alloys highlighting the differences between the oxide layers at increasing temperatures that result in the improved oxidation resistance of the Ni15Al alloy. Figure adapted from [112]. 65

Figure 3.17 – Oxidation kinetics of Hastelloy N with both coarse- and fine-grain microstructures with mass changes for coarse – grained Hastelloy N being much greater initially before spallation whilst fine – grained Hastelloy N showed a much lower and consistent rate of oxidation. Figure adapted from [113]. 67

Figure 3.18 - Oxidation kinetics of Haynes 230 alloy after heat treatments to achieved coarse – and fine – grain microstructures. Both alloys are observed to have very similar oxidation kinetics, although the fine – grained Haynes 230 does have a higher final mass gain. Figure taken from [113]. 68

Figure 3.19 – Cracking and subsequent spallation of the oxide layer of coarse grained Hastelloy N after exposure to air at 800 °C after a) 300 hours and b) 500 hours of exposure. Figure adapted from [113]. .69

Figure 3.20 – Figure showing Gibbs free energy of formation of molten salt constituents and metallic fluoride compounds at a temperature of 1000 K [29, 53, 117]. 72

Figure 3.21 – Mass loss per unit area of Incoloy 800H coupons immersed in FLiNaK molten salt containing metallic fluoride impurities of a) CrF_3, b) FeF_2, c) FeF_3 and d) NiF_2 in quantities between 0 and 10 mol.% at 650 °C [123]. 80

Figure 3.22 - Graph showing percentage change in Cr concentration after corrosion in FLiNaK containing different additives showing Cr dissolution is greatest after exposure to FLiNaK containing 3.4 mol.% CrF_3. 81

Figure 3.23 – Graph of corrosion depth with respect to time of Hastelloy N in pure FLiNaK salt and FLiNaK salt containing 0.4 wt.% CrF_3 at 700 °C at time intervals of 100, 300 and 1000 hours [124]. 82

Figure 3.24 – EDX mapping analysis showing depletion of Cr, Mn and Fe from the grain boundaries of 316L after immersion in a) – d) molten FLiNaK salt at 700 °C and e) – h) molten FLiNaK containing 0.4 wt.% CrF_3 for durations of 1000 hours. Image taken from Yin et al. [124].83

Figure 3.25 – Specific mass loss of a) Hastelloy N and b) Hastelloy B3 Ni-based alloys after immersion in a molten FLiNaK salt environment containing 1.91 and 3.19 wt.% H_2O at 700 °C for 100 and 200 hours. Results, adapted from Ouyang et al. [127], show a drastic increase in the alloy mass loss when H_2O content is increased.....85

Figure 3.26 – Micrographs of coupons of a) – d) Hastelloy B3 and e) – h) Hastelloy N, immersed in FLiNaK molten salt at 700 °C containing 1.91 wt.% and 3.19 wt.% H_2O for 100 and 200 hours showing both intergranular and intragranular corrosive attack as labelled. Figures taken from experimental study by Ouyang et al. [127]. 86

Figure 3.27 – Micrographs of a) MONICR, b) HN80M-VI and c) HN80MTY alloys after immersion in LiF – NaF – BeF_2 molten salt at 700 °C after 240 hours showing that HN80MTY was much less susceptible to IGC than HN80M-VI and MONICR alloys. Figure adapted from [43].....91

Figure 3.28 – Graphs of a) depth of Cr corrosion attack against time for 316L, corroded in FLiBe molten salt at 700 °C in a 316L crucible and a graphite crucible, with greater corrosion depth being observed after immersion in FLiBe salt in a graphite crucible [74]. 93

Figure 3.29 – Schematic of the experimental flow loop combined with micrographs taken of Hastelloy N samples taken from each region. Micrographs show the wide range of corrosion behaviour observed at the different operating temperatures [27] 96

Figure 3.30 – Graph showing corrosion rate against temperature for stainless steels 304 and 316L as well as Ni-based alloys Hsatelloy C276, Inconel 600 and Inconel 625 showing better corrosion resistance of Ni-based alloys in FLiBe molten salt [71, 141]..... 99

Figure 3.31 – Plots of material loss against the square root of time for the corrosion of stainless steels (a) 316 and (b) 321 in Solar Salt at 565 °C under dynamic molten salt conditions. Results show increasing mass losses when velocity of the melt is increased from 1 m/s to 3 m/s. Since linear trends are observed on these plots, corrosion kinetics were concluded to be parabolic in nature..... 101

Figure 3.32 – Specific mass change measurements for coarse – and fine – grained Ni-Cr alloys showing an increase in the specific mass changes for fine – grained Ni-Cr alloys when immersed in molten FLiNaK salt at 700 °C. 104

Figure 3.33 – Graph showing material mass loss of Hastelloy N, GH3535 and MONICR alloys in molten FLiNaK salt at 650 °C after 200, 500 and 750 hours of immersion. Results show that MONICR has the best corrosion performance of the three alloys, attributed to its larger grain size and a smaller number of high angle grain boundaries [42]. 105

Figure 3.34 – Results presented from study of Ouyang et al. [127], showing specific mass change results obtained at 600 °C and 700 °C for the corrosion of (a) Hastelloy N and (b) Hastelloy B3 in FLiNaK molten salt containing 1.91 wt.% and 3.19 wt.% moisture. Results show that both increasing temperature and moisture concentration increase the extent of material degradation. 107

Figure 3.35 – Illustration of atom occupying an interstitial site in a crystalline material structure leaving a vacancy in the material structure. Image adapted from [77]. 109

Figure 3.36 – Bubble formation in GH3535 Ni-based alloy after undergoing He-ion irradiation. Bubbles were identified using an over-focused and under-focused technique which identifies bubbles by their change in colour [149, 150]. 110

Figure 3.37 – Exposure of increased surface area to molten salt by the intersection of the corrosion interface and bubble layer, aggravating the corrosion mechanism. 111

Figure 4.1 - Flow chart of the experimental and subsequent analysis undertaken during this thesis using as-received samples. 116

Figure 4.2 – Diagram showing basic test set up used for high temperature corrosion and oxidation testing of Hastelloy C276 with key components of the test set-up labelled..... 117

Figure 4.3 – Graph of corrosion depth of Hastelloy C276, Hastelloy X and Inconel 600 after immersion in FLiNaK molten salt at 750 °C for time intervals of 50, 100, 200 and 300 hours. Results indicate that Hastelloy C276 has better corrosion resistance to FLiNaK molten salt over both Hastelloy X and Inconel 600.....118

Figure 4.4 – Micrograph of Hastelloy C276 showing equiaxed grain structures with sizes ranging from 30 µm to 60 µm. Examples of annealing twins were observed within the microstructure, and are arrowed red. Micrograph of Hastelloy C276 taken from research by Zhang et al. [100]. 119

Figure 4.5 – Flowchart of processes undertaken to prepare coupons of Hastelloy C276, ready for studies relating to their high temperature molten salt corrosion and oxidation. 120

Figure 4.6 – Heating approaches deployed for high temperature isothermal oxidation and corrosion testing of metallic materials as per ISO 21608 and ISO 17245 experimental testing standards [156, 157]. 122

Figure 4.7 – Flowchart illustrating the process undertaken to obtain specific mass changes and corrosion rates of Hastelloy C276 coupons, corroded in molten FLiNaK salt at 700 °C after 200 hours of immersion.....124

Figure 4.8 – Image showing Carl Zeiss EVO MA15 SEM utilised for imaging corroded and oxidised coupons throughout this study [159]. 125

Figure 4.9 – Image of Siemens Bruker D8 Advance XRD machine, used to identify corrosion and oxidation product structures on coupons of Hastelloy C276 after immersion in a dry air environment or in FLiNaK molten salt. Adapted from [65]. 127

Figure 4.10 – Plot of the natural logarithm of K_P against U for alloy data presented in Table 4.8. A calculated R^2 value of 0.390 indicates that no correlation exists between the K_P and U data for the selected alloys. 137

Figure 4.11 – Plot of LN(K_P) against U for alloys of GH586, GH202, Hastelloy C276, Udimet 720, Waspaloy and Astroloy [99, 164, 166, 168] . Plot shows improved relationship between LN(K_P) against U for these alloys, with a calculated R^2 of 0.8126. 138

Figure 4.12 – Stages involves in developing a diffusion-based model using the MATLAB partial differential equation solver. 141

Figure 4.13 – Diagram of simplified modelling geometry, allowing for the modelling of elemental changes in a coupon of Hastelloy C276 in 1-D Cartesian coordinates. 143

Figure 4.14 – Depiction of symmetry conditions in x and y directions through the centre of the Hastelloy C276 coupon. 147

Figure 5.1 – Prediction of specific mass change of Hastelloy C276 over a 200-hour test duration at a constant temperature of 700 °C using the empirical modelling methodology. Specific mass change of 0.4555 mg/cm^2 for Hastelloy C276 was predicted at the specified temperature and duration. 157

Figure 5.2 – Prediction of oxide layer thickness, calculated from specific mass change results obtained from the developed empirical modelling methodology. Oxide layer thickness is predicted to be 7.66 µm after 200 hours of exposure of Hastelloy C276 to dry air at 700 °C. 158

Figure 5.3 - Specific mass change prediction against the number of modelling nodes for Hastelloy C276 exposed to a dry air environment at 700 °C for durations up to 200 hours. Result shows specific mass change result converges around 25001 modelling nodes using a time interval of 1 hour. 160

Figure 5.4 – Specific mass change prediction when using time intervals of 0.25, 0.50, 1.00, 2.00 and 5.00 hours when using 125001 modelling nodes. Results indicate a difference of 0.05% between the minimum and maximum specific mass change predictions, suggesting that the number of modelling nodes has a bigger influence on the result than the time interval..... 161

Figure 5.5 – Cr depletion depth prediction when using time intervals of 0.25, 0.50, 1.00, 2.00 and 5.00 hours and 125001 modelling nodes. Results show a maximum difference of 0.82% between the minimum and maximum Cr depletion depth predictions at the different time intervals, indicating that the number of modelling nodes influences the result more heavily. 161

Figure 5.6 – Computation time of mechanistic model when using time intervals of 0.25, 0.50, 1.00, 2.00 and 5.00 hours and 125001 modelling nodes. Result show decreasing computation time with increasing time intervals. 162

Figure 5.7 – Graph of computation time against the number of modelling nodes shows a roughly squared relationship in the range of 1001 to 250001 nodes with a drastic increase in computation time being observed when in excess of 125001 modelling nodes are used. 164

Figure 5.8 – Graph of the computation time and the percentage deviation in the average specific mass change and the Cr depletion depth showing decreasing deviation of both monitored parameters with increasing computation time. Graph shows very little change in the two monitored parameters past 0.2 hours of computation time (100001 nodes). 165

Figure 5.9 – Plot of LN(K_P) against 1/T showing developed relationship for the oxidation of Hastelloy C276 using experimental results of Li et al. [99] and Park et al. [161]. The developed relationships indicate activation energies, Q, for the oxidation of Hastelloy C276 of 207995.53 J/mol and 274777.60 J/mol in the temperature regions of 450 °C to 550 °C and 600 °C to 800 °C, respectively. 168

Figure 5.10 – Combined prediction of the fully temperature range showing that the predicted data bisects the two sets of data from literature. This prediction yields an activation energy of 268192.51 J/mol..170

Figure 5.11 - Diffusion based prediction of specific mass change of Hastelloy C276 at 700 °C, over the time interval of 0 to 200 hours. Result shows parabolic oxidation behaviour of Hastelloy C276, characterised by a specific mass change of 0.3948 mg/cm^2 and K_P value of 2.17x10^{-7} mg^2/cm^4/s. 171

Figure 5.12 – Comparison of specific mass change predictions for the oxidation of Hastelloy C276, oxidised in dry air at 700 °C for 200 hours, using empirical modelling and mechanistic modelling methodologies. The empirical modelling methodology predicted a specific mass change of 0.4555 mg/cm^2. This prediction is 14.3% greater than the prediction of 0.3948 mg/cm^2 made by the diffusion-based model. 172

Figure 5.13 – Prediction from the mechanistic model of oxide layer thickness formation over 200 hours of Hastelloy C276, exposed to a dry air environment at 700 °C. An oxide layer thickness of 7.13 µm was obtained. 173

Figure 5.14 – Comparison of predictions of oxide layer thickness formation over 200 hours of Hastelloy C276, exposed to a dry air environment at 700 °C from empirical modelling and mechanistic modelling methodologies. The empirical and mechanistic modelling methodologies predicted oxide layer thicknesses of 7.66 µm and 7.13 µm, respectively. 174

Figure 5.15 - Calculated depletion depths of Ni, Cr, Mo and Fe based on concentration changes presented in Figure 5.16 to Figure 5.19 showing depletion depths of 3.05 µm, 1.68 µm, 6.15 µm and 1.57 µm for alloying elements of Ni, Mo, Cr and Fe respectively after 200 hours of exposure to a dry air environment at 700 °C.....175

Figure 5.16 – Elemental distribution profile of Ni in the near surface region next to the substrate – air interface showing predicted depletion behaviour at time intervals of 50, 100 and 200 hours after exposure to dry air at 700 °C.....176

Figure 5.17 - Elemental distribution profile of Cr in the near surface region next to the substrate – air interface showing predicted depletion behaviour at time intervals of 50, 100 and 200 hours after exposure to dry air at 700 °C.....177

Figure 5.18 - Elemental distribution profile of Mo in the near surface region next to the substrate – air interface showing predicted depletion behaviour at time intervals of 50, 100 and 200 hours after exposure to dry air at 700 °C. 178

Figure 5.19 - Elemental distribution profile of Fe in the near surface region next to the substrate – air interface showing predicted depletion behaviour at time intervals of 50, 100 and 200 hours after exposure to dry air at 700 °C. 178

Figure 5.20 - Experimentally determined specific mass change results of Hastelloy C276 coupons, oxidised in a dry air environment at 700 °C for a duration of 200 hours. A final mass change of 0.4300 mg/cm^2 was measured after 200 hours of exposure..... 180

Figure 5.21 – Plot of square of specific mass change of Hastelloy C276 coupons, oxidised in dry air at 700 °C for a duration of 200 hours using an experimental methodology, against time. Result shows linear trend with an R^2 value of 0.9646. 181

Figure 5.22 - Micrographs of oxidised surfaces of Hastelloy C276 coupons, taken at a magnification of X5000, after a) 50 hours, b) 100 hours and c) 200 hours of exposure to a dry air environment at 700 °C with average oxide crystal size labelled..... 182

Figure 5.23 – Micrographs of cross-sections of Hastelloy C276 coupons, exposed to a dry air environment at 700 °C for durations of a) 50 hours, b) 100 hours and c) 200 hours. The substrate – oxide interface in each case is shown in red, with internal and external oxide layers labelled. Average total oxide layer thicknesses are also labelled.183

Figure 5.24 – Average oxide crystal size and oxide layer thickness, measured on Hastelloy C276 coupons after exposure to a dry air environment, held at 700 °C for durations of 50, 100 and 200 hours. 184

Figure 5.25 – Plot of the square of oxide crystal size and oxide layer thickness measurements against time, showing a linear relationship for both sets of measurements, confirming parabolic growth law of both oxide crystal size and oxide layer thickness. 184

Figure 5.26 – EDX maps of micrographs of oxidised surfaces of Hastelloy C276 coupons, presented in Figure 5.22, after a) 50 hours, b) 100 hours and c) 200 hours of oxidation in a dry air environment at 700 °C. 186

Figure 5.27 – Point and ID analysis of individual oxide crystals, formed on Hastelloy C276 coupons after 50 hours of exposure to dry air at 700 °C, showing high concentrations of Ni and trace amount of Cr and Fe. 187

Figure 5.28 – Point and ID analysis of individual oxide crystals, formed on Hastelloy C276 coupons after 100 hours of exposure to dry air at 700 °C, showing high concentrations of Ni and reduced amounts of Cr and Fe. Regions of Mo enrichment was also observed. 188

Figure 5.29 – Point and ID analysis of oxide crystals, formed on Hastelloy C276 coupons after 200 hours of exposure to dry air at 700 °C, showing similar concentration of both Cr and Fe as well as Ni and O. 189

Figure 5.30 – EDX line scans conducted on cross-sections of Hastelloy C276 coupons after exposure to dry air at 700 °C for durations of a) 50 hours, b) 100 hours and c) 200 hours. Results show increasing depletion of Cr from the substrate material as well as continuous growth of the oxide layer. 190

Figure 5.31 – XRD analysis conducted on coupons of Hastelloy C276 after exposure to dry air at 700 °C for durations of 50, 100 and 200 hours. Peaks were identified using Xpert Highscore software and have been labelled as per their designated structure. 191

Figure 5.32 – Comparison of experimentally determined specific mass changes of Hastelloy C276 coupons, exposed to dry air environment at 700 °C for durations of 50, 100 and 200 hours and numerical predictions of specific mass change for the same conditions. Numerical predictions were made by empirical modelling and mechanistic modelling methodologies developed in this thesis.193

Figure 5.33 – Comparison of oxide layer thicknesses determined by exposure of Hastelloy C276 coupons to a dry air environment at 700 °C for durations of 50, 100 and 200 hours to numerical predictions from empirical and mechanistic models developed in this research. 194

Figure 6.1 – Illustration of corrosion system, in which the diffusion of corrosive species HF, CrF_2 and O_2 was predicted. 198

Figure 6.2 – Changes in concentrations of HF, CrF_2 and O_2 at the molten salt – substrate interface with varying number of modelling nodes showing that increasing the number of modelling nodes has no impact on the predicted concentrations of the investigated species. 199

Figure 6.3 – Concentration predictions of CrF_2, HF and O_2 at the substrate – molten salt interface at 700 °C in the time period of 0 to 200 hours. Due to the faster diffusion kinetics of these species, rapid changes are initially observed before reaching a constant value. 200

Figure 6.4 – Graph showing the computation time with varying number of modelling nodes used for the prediction of concentration changes of CrF_2, HF and O_2 within the corrosion model. 201

Figure 6.5 – Intrinsic corrosion depths with respect to the number of modelling nodes used in the corrosion model. This result shows convergence of the intrinsic corrosion depth when increasing the number of modelling nodes from 1001 to 250001 within the corrosion model whilst using 125001 modelling nodes within the oxidation mechanistic model. Convergence is observed when in excess of 25001 modelling nodes are used in the corrosion model. 202

Figure 6.6 - Graph of predicted corrosion depth due of Hastelloy C276 after immersion in FLiNaK molten salt at 700 °C for time periods up to 200 hours, with a maximum corrosion depth of 33.34 µm being predicted up to 200 hours of immersion. 203

Figure 6.7 - Graph of mass change per unit area prediction of Hastelloy C276 coupons after immersion in molten FLiNaK salt at 700 °C for time periods up to 200 hours showing a specific mass loss of approximately 4.77 mg/cm^2. 204

Figure 6.8 – Predicted corrosion rate of Hastelloy C276 coupons immersed in a molten FLiNaK salt environment, containing oxygen at a temperature of 700 °C for a duration of 200 hours. Result shows an initial spike in the corrosion rate to approximately 3.50 mmpy before rapidly dropping below 0.5 mmpy within 50 hours of immersion.205

Figure 6.9 – Specific mass change of Hastelloy C276 coupons, corroded in FLiNaK molten salt at 700 °C for up to 200 hours showing overall mass gain due to corrosion product growth. 207

Figure 6.10 - Mass change per unit area measurements made on Hastelloy C276 coupons after immersion in molten FLiNaK salt at 700 °C, with measurements being taken after 50, 100 and 200 hours of static immersion. 208

Figure 6.11 - Corrosion rate of Hastelloy C276, calculated from mass change measurements at time intervals of 50, 100 and 200 hours. Results show a consistent corrosion rate over time, with a maximum difference of 23.4% between corrosion rates measured after 100 and 200 hours of immersion. 209

Figure 6.12 – Comparison of measured specific mass changes before and after corrosion product removal, showing synergy of corrosion product formation and corrosion, indicating change in kinetics of corrosion product layer as a function of time. 210

Figure 6.13 – Comparison of specific mass changes for Hastelloy C276 in molten FLiNaK salt, including overall specific mass change, specific mass change due to material loss and specific mass change due to corrosion product formation. 211

Figure 6.14 – Micrographs of the exposed surfaces of Hastelloy C276 coupons, immersed in molten FLiNaK salt for a) 50 hours, b) 100 hours and c) 200 hours at 700 °C in an air environment. Regions of corrosion product and exposed substrate are labelled. 212

Figure 6.15 – SEM images of regions of corrosion product on the exposed surfaces of Hastelloy C276 coupons, identified after a) 50 hours, b) 100 hours, c) and d) 200 hours of immersion in molten FLiNaK salt at 700 °C in an air environment. 213

Figure 6.16 – SEM images of regions of corroded substrate, exposed by the loss of corrosion products, of Hastelloy C276 coupons, identified after a) 50 hours, b) 100 hours and c) 200 hours of immersion in molten FLiNaK salt at 700 °C 214

Figure 6.17 – SEM images of cross-sections of corroded Hastelloy C276 coupons after a) 50 hours, b) 100 hours and c) and d) 200 hours of immersion in molten FLiNaK salt at 700 °C at 500 and 1000X magnifications respectively. In each case, the substrate – molten salt interface is presented by a dashed red line. Corrosion product layers are labelled, with their defects circled in blue. Corrosions depths, measured from the substrate – molten salt interface is labelled, with any element depletion zones being arrowed blue. 215

Figure 6.18 – Depth of corrosive attack with respect to time, measured from the thickness of the corrosion interfaces presented in Figure 6.17, showing a linear trend similar to that observed for the specific mass change of Hastelloy C276 coupons presented in Figure 6.10. 216

Figure 6.19 – EDX analysis of corrosion product layer after a) 50 hours, b) 100 hours and c) 200 hours of exposure of Hastelloy C276 coupons to FLiNaK molten salt at 700 °C.....217

Figure 6.20 – EDX analysis of corroded substrate material after a) 50 hours, b) 100 hours and c) 200 hours of exposure of Hastelloy C276 coupons to FLiNaK molten salt at 700 °C showing consistent concentrations of Ni and Fe with depleted concentrations of Cr and O.....218

Figure 6.21 – EDX point and ID analysis showing large reduction in the Cr concentration present when the test duration increases from a) 50 hours to b) 100 hours. At the substrate – molten salt interface, the average Cr concentration was observed to drop from 10.94 wt.% to 2.19 wt.% with the increase in exposure time. The region corresponding to high Cr concentration in Figure 6.20b was shown to have much larger concentrations of Cr and O. 219

Figure 6.22 - EDX line scan analysis showing evolution of element distribution throughout the formed corrosion product layer and substrate of Hastelloy C276 exposed to FLiNaK salt for a) 50 hours, b) 100 hours and c) 200 hours at 700 °C. 221

Figure 6.23 – EDX line scans of cross – section of Hastelloy C276 after 100 hours of immersion showing both internal and external oxidation of Cr. However, the result shows that the external oxidation of Cr is greater than that that occurs internally. 222

Figure 6.24 – XRD analysis conducted on coupons of Hastelloy C276 after exposure to molten FLiNaK salt at 700 °C for experimental durations up to 200 hours. 223

Figure 6.25 – Comparison between experimentally determined and numerically predicted mass changes for the Ni-based alloy Hastelloy C276 in molten FLiNaK salt at 700 °C for exposure times up to 200 hours.....224

Figure 6.26 - Comparison between experimentally determined and numerically predicted corrosion rates of Hastelloy C276, exposed to a molten FLiNaK molten salt environment at 700 °C for a duration of 200 hours. 225

Figure 6.27 – Comparison between experimentally determined and numerically predicted corrosion depth of Hastelloy C276 coupons using the mechanistic model, exposed to a molten FLiNaK molten salt environment at 700 °C for a duration of 200 hours, showing good agreement between predicted and experimentally determined corrosion depths at 50 and 100 hours, with a large discrepancy being observed after 200 hours of immersion. 226

Figure 7.1 – Schematic showing process of alloy oxidation in high temperature environment, illustrating changes in the oxidation rate with increasing oxide layer thickness using an arbitrary K_P value of $1x10^{-5}$ $mg^2/cm^4/s$. 231

Figure 7.2 – SEM analysis of cross-sections of Hastelloy C276 exposed to a dry air environment at 700 °C for durations of 50, 100 and 200 hours, highlighting the different oxides present within the oxide layer showing a NiO outer layer and Cr_2O_3 inner layer with a $NiCr_2O_4$ layer being observed at longer time intervals. 233

Figure 7.3 – Schematic showing concentration changes of an arbitrary alloying element within an alloy, with defined concentrations relating to the concentration deviation calculation defined in equation 7.1, with C_{BS} and C_i representing the bulk and interfacial concentrations of an arbitrary alloying element. 234

Figure 7.4 – Bar chart showing concentration deviation from initial concentration, highlighting the concentration changes of Cr and Ni are greater than those of Fe and Mo. 235

Figure 7.5 – Comparison of concentration changes of Ni, Cr, Fe and Mo as a function of distance from the substrate – air interface, showing Ni and Cr are more greatly depleted from the substrate when compared with Fe and Mo at time intervals of a) 50 hours, b) 100 hours and c) 200 hours. 236

Figure 7.6 – EDX maps of cross-section of Hastelloy C276 exposed to a dry air environment for duration of 100 hours with key interfaces labelled showing internal oxidation of Cr to Cr_2O_3 and external oxidation of Ni to NiO. 238

Figure 7.7 – EDX line scans of cross-section of Hastelloy C276 exposed to a dry air environment after 100 hours of exposure showing diffusion of O into the substrate, enrichment of Cr at the substrate – air interface and enrichment of Ni within the external oxide layer... 239

Figure 7.8 – Graph showing growth of Cr_2O_3 and NiO layers as a function of time, with Cr_2O_3 thickness increasing by 107.8% from 1.31 µm to 2.72 µm and NiO by 101.4% from 1.31 µm to 2.64 µm. 240

Figure 7.9 – Plot of square of oxide layer thicknesses for NiO and Cr_2O_3 against time, showing strong linear relationships, confirming parabolic oxidation kinetics of both oxide layers. Growth of oxides can be characterised by K_P values of $7.20x10^{-5}$ and $7.61x10^{-5}$ $\mu m^2/s$ for NiO and Cr_2O_3, respectively. 241

Figure 7.10 – Comparison of experimentally measured Cr_2O_3 and NiO layer thicknesses and those predicted by the mechanistic model showing similar oxidation kinetics of both oxides. Mechanistic model predictions are observed to fall within experimental errors. 242

Figure 7.11 – Schematic showing the diffusion coefficients of Ni, Cr and O_2 within a NiO layer at 700 °C showing that diffusion coefficients of O_2 and Cr are smaller than that of Ni by several orders of magnitude. 243

Figure 7.12 – Images highlighting regions of exposed substrate material to the molten salt environment as well as defects within the corrosion product layer which may lead to its removal. 249

Figure 7.13 – Micrographs of cross-sections of Hastelloy C276 coupons immersed in molten FLiNaK salt at 700 °C for a) 100 and b) 200 hours, showing voids present within the substrate material. 250

Figure 7.14 – Cross-sectional image of Hastelloy C276 coupon, exposed to FLiNaK molten salt at 700 °C for a) 100 hours and b) 200 hours illustrating Cr depletion from the substrate material in the near surface region, with depletion zones labelled.....252

Figure 7.15 - Schematic highlighting regions of alloying element enrichment and depletion on Hastelloy C276 cross-sections after 200 hours of exposure to molten FLiNaK salt.....253

Figure 7.16 – Comparison of corrosion and oxidation rates of Hastelloy C276 in a molten FLiNaK salt at 700 °C for durations up to 200 hours, showing that the corrosion product formation outweighs corrosion mechanism. 254

Figure 7.17 – Comparison of specific mass changes due to corrosion product formation in a molten salt environment and high temperature in a dry air environment. Corrosion product formation in a molten salt environment is much greater than the dry oxidation behaviour of Hastelloy C276 in a dry air environment, indicating that substrate oxidation and hence corrosion product formation is enhanced by Cr dissolution from the substrate by a corrosive medium. 255

Figure 7.18 – Comparison between measured and predicted specific mass changes due to corrosion product formation, showing a large discrepancy between data points at 50 and 200 hours. Good agreement is observed between data points generated at 100 hours. 256

Figure 7.19 – Schematic showing a) initial Cr dissolution from the substrate material, followed by b) indicating the presence of O_2 at the substrate – molten salt interface resulting in corrosion product formation. The mass change result is shown in c) which shows much greater mass loss due to corrosion than mass gain due to corrosion product formation. 257

Figure 7.20 – Measured corrosion product layer thickness with respect to time, with measurements taken on Hastelloy C276 coupons immersed in molten FLiNaK salt for 50, 100 and 200 hour at 700 °C. Results shows corrosion product layer formation occurs linearly, matching the specific mass loss kinetics. 258

Figure 7.21 – Comparison of experimentally measured corrosion product specific mass change, predicted specific mass change from corrosion damage specific mass change and specific mass change predicted by conversion of corrosion product layer thickness after immersion periods of 50, 100 and 200 hours in FLiNaK molten salt. 259

Figure 7.22 – Numerical study investigating the impact of reducing corrosion product formation specific mass change on the corrosion damage, with results showing that decreasing the corrosion product specific mass change decreases the corrosion damage which is as expected. 261

Figure 7.23 – Illustration of cleaning and mass measurement protocol, showing convergence of corroded coupon mass with increasing cleaning time [158]. 262

Figure 7.24 – Bar chart illustrating percentage differences between experimental and predicted specific mass changes, corrosion rates and corrosion depths at time intervals of 50, 100 and 200 hours of exposure of Hastelloy C276 coupons in molten FLiNaK salt at 700 °C, with the largest discrepancy being observed between experimentally observed corrosion depths, and those predicted mechanistically for durations of 200 hours. 263

Figure 7.25 – Schematic showing the proposed corrosion mechanism with initial corrosion being shown in (a) where substrate is fully exposed to the molten salt. At time (b) the corrosion product has begun to form, with Cr and O_2 cations and anions needing to diffuse to the corrosion product – molten salt interface to continue corrosion product formation. Finally, in (c), the corrosion product thickness increases, increasing the diffusion barrier and hence reducing the rate of corrosion product formation. 265

Figure 8.1 – Future work suggestions to compliment understanding of corrosion behaviour of Ni-based alloys in molten salt environments for MSR applications. 270

Figure 8.2 – Correlation coefficients for specific mass changes and parabolic rate constants of Hastelloy C276 in dry air at 700 °C up to 200 hours showing values are less than unity. Hence, the mechanistic model is not very sensitive to changes in the input diffusion coefficients of each alloying element. 289

Figure 8.3 – CC values for the concentration changes each alloying element present in Hastelloy C276 when diffusion coefficients were varied by 1%, 5% and 10% in both the positive and negative directions. Results show very little change in the element concentrations; hence, concentration values are insensitive to the input diffusion coefficients. 290

Figure 8.4 – Repeat image of diffusion based prediction for the high temperature oxidation of Hastelloy C276 in a dry air environment at 700 °C, with error bars showing the minimum and maximum specific mass change predictions based on the different diffusion coefficients. 292

Figure 8.5 – CC values comparing differences in the diffusion coefficients presented in Table A.3 to the predicted minimum and maximum concentration changes for each element, showing CC values less than unity, confirming that the mechanistic model is insensitive to significantly large changes in the input parameters. 293

Table of Tables

Table 2.1 - Summary of design features of Generation - IV nuclear reactors in meeting GIF goals [4]. 10

Table 2.2 – Summary of key reactor characteristics of the Generation – IV nuclear reactors [4]. 11

Table 2.3 - Industrial applications that may be fulfilled by adapted versions of the Generation - IV nuclear reactors. Table adapted from work of John Kelly [4]..... 12

Table 2.4 – Comparison of properties of coolant salts used in MSRE and MSBR [29, 30]. 16

Table 2.5 – Comparison of properties of molten chloride salt properties with FLiBe molten salt showing comparable thermal and physical properties [29, 33, 34] 17

Table 2.6 – Summary of thermal spectrum, liquid fuel MSR project and developments outlined by the GIF [10]. 19

Table 2.7 - Summary of fast spectrum, liquid fuel MSR projects and developments outlined by the GIF [10]. 20

Table 2.8 - Summary of thermal spectrum, solid fuel MSR projects and developments outlined by the GIF [10]. 21

Table 2.9 – Comparison of properties of FLiBe and FLiNaK molten salts [29, 31]..... 22

Table 3.1 – Compositions of Ni-based alloys used in the published artificial neural network study by Kim et al. [94] (wt.%). 54

Table 3.2 – Summary of parabolic rate constants of RR1000, gathered over the temperature range of 700 °C to 900 °C, from the study conducted by Taylor et al. [101]..... 56

Table 3.3 – Summary of composition ranges of elements, alloyed with Ni, in the study conducted by Park et al. [95]. 61

Table 3.4 – Summary of manufacturing methods and heat treatments undergone by Haynes 230 and Hastelloy N Ni-based alloys to achieve coarse and fine grain structures [113]. Average grain sizes also provided. 66

Table 3.5 – Comparison of predictive modelling and experimentally determined mass losses for Inconel MA754, GH3535 and Hastelloy N Ni-based alloys from study by Lee et al. [118]..... 76

Table 3.6 – Summary of Te intergranular cracking experimental conditions utilised in the studies of Ignatiev et al. [43, 135] showing the introduction of Te into the salt in the form of Cr_3Te_4. 90

Table 3.7 – Composition of HN80M-VI, HN80MTY and MONICR alloys used in Te intergranular cracking studies by Ignatiev et al. [43, 135] highlighting the difference in Al concentration as a contributing factor to the improved cracking resistance of HN80MTY. 92

Table 3.8 - Summary of alloy compositions used in molten chloride salt corrosion studies by Ghaznavi et al. [73] (at.%). 103

Table 3.9 – Comparison of concentrations of less noble elements present in Hastelloy N, GH3535 and MONICR showing the reduced concentrations of these elements in MONICR when compared with the other alloys. Concentrations provided in wt.% [42]. 106

Table 4.1 – Composition of commercial specification for Hastelloy C276 material as received from Goodfellows Cambridge (wt.%). 119

Table 4.2 - Calculation of effective valence, performed by Bensch et al. using microsegragation method [88]. 130

Table 4.3 – Calculation of effective valence for SCA425+ using nominal alloy composition and calculation method described by Bensch et al. [88] using theory introduced by Sato et al. [87]. 131

Table 4.4 – Element concentration limits for Cr, Mo, Fe and W present in Hastelloy C276 as defined in material specification. 131

Table 4.5 – Modelling cases for variations in the composition of Hastelloy C276 covering minimum, nominal and maximum concentrations of Cr and Mo. 132

Table 4.6 – Coefficients used when calculating the Gibbs free energy change of Cr_2O_3, defined in equation 4.12 [162]. 133

Table 4.7 – Summary of alloy compositions considered for use in the empirical model study [99, 101, 163-168] [169-171]. 135

Table 4.8 – Summary of Ni-based alloy K_p data at 700 °C used to generation plots of LN(K_P) against U. 136

Table 4.9 – Constant values for standard form required by MATLAB's partial differential equation solver. 144

Table 4.10 – Summary of all diffusion coefficient data used from literature for each alloying element. 145

Table 4.11 - Initial concentration values for each element modelled in MATLAB. 146

Table 4.12 - Summary of oxide forming reactions taking place between metallic species and oxygen to form metallic oxides. 149

Table 4.13 – Diffusion coefficients for CrF_2 and HF in molten salt environments, obtained from literature sources [180-182]. 153

Table 5.1 – Percentage reduction in time interval versus percentage reduction in modelling elements used to obtain oxidation prediction, showing very small reductions in time interval compared with reduction in modelling elements. 163

Table 5.2 – Summary of time intervals and maximum number of modelling nodes when modelling test durations of 240 and 1000 hours, as per the tests of Li et al. [99]. 166

Table 5.3 - Composition of Hastelloy C276 used in the study by Li et al. [99] when investigating the oxidation behaviour of Hastelloy C276 at temperatures of 450, 500 and 550 °C. 167

Table 5.4 – Summary of temperature and K_P data obtained for Hastelloy C276 in a dry air environment by Li et al. [99]. 167

Table 5.5 – Summary of data collected from study by Park et al. [161] into the oxidation of Hastelloy C276 foils at temperatures of 600, 700 and 800 °C using O_2 concentrations of 100%. 167

Table 5.6 – Comparison between values, predicted by the developed mechanistic model and experimental results obtained from literature, of oxidation reaction activation energy, Q, in temperature ranges of 450 °C to 550 °C and 600 °C to 800 °C and their corresponding data sets from literature [99, 161]. Predictions made using 125001 modelling nodes and a time interval of 1.00 hours. 169

Table 6.1 – Gibbs free energy changes of metallic fluorides that may form during the reactions between Ni-based alloy and FLiNaK molten salt at 727 °C, showing that CrF_2 is more thermodynamically stable than other metallic fluorides [29]. 220

Table 7.1 – Summary of experimentally determined and numerically predicted values of specific mass change, K_P and oxide layer thickness for Hastelloy C276 in a dry air environment at 700 °C after 200 hours of exposure. 230

Table 7.2 – Diffusion coefficients for Ni and Cr in a NiO layer at 700 °C, showing the faster diffusion kinetics of Ni [188, 189]. 232

Table 7.3 – Summary of percentage differences between experimental and predicted values of specific mass change, K_P and oxide layer thickness over the 200-hour time duration, showing good agreement between the data sets. 245

Table 7.4 – Summary of experimentally determined mass losses and their corresponding calculated corrosion rates of Hastelloy C276 coupons immersed in molten FLiNaK salt at 700 °C for experiment durations of 50, 100 and 200 hours. 248

Table 7.5 – Summary of discrepancies between experimental and predicted specific mass changes after 50 and 200 hours of immersion of Hastelloy C276 coupons in FLiNaK molten salt at 700 °C..... 259

Table A.1 - Summary of input parameters to empirical and mechanistic models for predicting the high temperature oxidation and molten salt corrosion behaviour of Hastelloy C276. 285

Table A.2 – Summary of input parameters to empirical and mechanistic models for predicting the high temperature oxidation and molten salt corrosion behaviour of Hastelloy C276. 287

Table A.3 – Summary of diffusion coefficients utilised in this research, as originally defined in Table 4.10, with the difference between the diffusion coefficients for each element expressed as a percentage difference.....291

List of Abbreviations

a	Thermodynamic activity
A	Area (cm^2)
Al	Aluminium
ANN	Artificial Neural Network
ARE	Aircraft Reactor Experiment
B	Boron
BeF_2	Beryllium Fluoride
BeO	Beryllium Oxide
C	Carbon
C_A	Element Concentration (mol)
CC	Correlation Coefficient
Cl^-	Chloride Ion
Cl_2	Chlorine
Co	Cobalt
CoF_2	Cobalt (II) Fluoride
CoO	Cobalt (II) Oxide
CO_3^{2-}	Carbonate Ion
C_P	Heat Capacity (J/K)
Cr	Chromium
CrF_2	Chromium (II) Fluoride
CrF_3	Chromium (III) Fluoride
Cr_2O_3	Chromium (III) Oxide
CR	Corrosion Rate
CSP	Concentrating Solar Power
dpa	Displacements Per Atom
D	Diffusion Coefficient (cm^2/s)

e^-	Electron
E_a	Anodic Potential
E_c	Cathodic Potential
EDX	Energy Dispersive X-Ray Spectroscopy
EuF_3	Europium (III) Fluoride
F	Faradays Constant (96485 C/mol)
F^-	Fluoride Ion
F_2	Fluorine
Fe	Iron
$FeCl_2$	Iron (II) Chloride
FeF_2	Iron (II) Fluoride
FeF_3	Iron (III) Fluoride
FeO	Iron (II) Oxide
FLiBe	$LiF – BeF_2$
FLiNaK	LiF – NaF – KF
GFR	Gas-cooled Fast Reactor
GIF	Generation IV International Forum
h	Coupon Height (cm)
h_{ac}	Active Corrosion Depth
h_{ic}	Intrinsic Corrosion Depth
h_{tot}	Total Corrosion Depth
H	Enthalpy (J/kg)
H_2	Hydrogen
Hf	Hafnium
HF	Hydrogen Fluoride
HTF	Heat Transfer Fluid
IGC	Intergranular Cracking
J	Diffusive Flux (mol/cm^2)
K	Reaction Rate Constant

KCl	Potassium Chloride
KF	Potassium Fluoride
K_L	Linear Rate Constant (mg/cm^2/s)
K_P	Parabolic Rate Constant (mg^2/cm^4/s)
Li_2O	Lithium Oxide
LiCl	Lithium Chloride
LFR	Lead-cooled Fast Reactor
LiF	Lithium Fluoride
m	Mass (g)
M	Metallic Alloying Element
M^{n+}	Metallic Ion
$MgCl_2$	Magnesium Chloride
MR	Relative molecular mass (g/mol)
MSR	Molten Salt Reactor
Mn	Manganese
$MnCr_2O_4$	Manganese-Chromium Oxide
MnF_2	Manganese (II) Fluoride
MnO_2	Manganese (IV) Oxide
Mo	Molybdenum
MoF_3	Molybdenum (III) Fluoride
MoF_6	Molybdenum (VI) Fluoride
MoO_3	Molybdenum (VI) Oxide
MSBR	Molten Salt Breeder Reactor
MSRE	Molten Salt Reactor Experiment
$NaBF_4$	Sodium Tetrafluoroborate
NaCl	Sodium Chloride
NaF	Sodium Fluoride
Nb	Niobium
Ni	Nickel

$NiCr_2O_4$	Nickel-Chromium Oxide
NiF_2	Nickel (II) Fluoride
NiO	Nickel (II) Oxide
NO_3^{2-}	Nitrate Ion
O_2	Oxygen
O^{2-}	Oxide Ion
OH^-	Hydroxide Ion
ORNL	Oak Ridge National Laboratory
ppm	Parts Per Million
P	Phosphorus
Pa	Protactinium
Q	Activation Energy (kJ/mol)
r	Coupon Radius (cm)
R	Universal Gas Constant (8.314J/mol/K)
S	Entropy (J/K)
S	Sulphur
SCC	Stress Corrosion Cracking
SEM	Scanning Electron Microscopy
SWCR	Supercritical Water-Cooled Reactor
SFR	Sodium-cooled Fast Reactor
Si	Silicon
SiC	Silicon Carbide
SiO_2	Silicon (IV) Oxide
SO_4^{2-}	Sulphate Ion
SWCR	Supercritical Water-Cooled Reactor
t	Time (s, hrs)
T	Temperature (K)
Ta	Tantalum
Te	Tellurium

Ti	Titanium
Th	Thorium
ThF_4	Thorium (IV) Fluoride
U	Kinetic Parameter (kJ/mol)
UF_4	Uranium (IV) Fluoride
UO_2	Uranium (IV) Oxide
V	Vanadium
V_2O_5	Vanadium (V) Oxide
VHTR	Very-High Temperature Reactor
W	Tungsten
WF_6	Tungsten (VI) Fluoride
WO_3	Tungsten (VI) Oxide
x	Diffusion distance in x – direction (cm)
X	Oxide Layer Thickness (μm)
XRD	X-Ray Diffraction
y	Diffusion distance in y – direction (cm)
ZrF_2	Zirconium (II) Fluoride
ZrF_4	Zirconium (IV) Fluoride
β^-	Beta – minus particle
ΔE	Potential Difference (V)
ΔG	Gibbs Free Energy Change (J)
ΔG^0	Standard Gibbs Free Energy Change (J)
Δm	Mass Change (g)
ΔW	Specific Mass Change (mg/cm^2)
ρ	Density (g/cm^3)
$\overline{\nu_e}$	Anti-electron neutrino
π	Mathematical Constant Pi (3.14159265)

Chapter 1 – Introduction

1.1 Project Background

Recent predictions show that the world population is set to grow to 10 billion people by the year 2050 [1], which is expected to lead to a drastic increase in global energy demand. To meet the unavoidable increases in energy demand, current energy production technologies need to be expanded. However, the expansion of non-renewable energy production methods may come to the detriment of our environment, contributing to global climate change. Therefore, additional clean energy production alternatives to meeting the world's energy demand are required [2].

One technology with the potential to play a key role in contributing to the world's energy demand is nuclear energy. Nuclear energy has been researched since the 1950's when the Generation – I reactors were developed. Since then, several generations of nuclear reactors have been introduced [3]. However, in order to keep up with growing energy demand, new nuclear systems are required which may not only be capable of producing electricity for domestic utilisation but could also be expanded to support a wider range of functions including hydrogen (H_2) production, petroleum refining, cogeneration of steam and electricity and district heating [4]. As a result of this requirement, the Generation – IV nuclear reactors were proposed.

At the inception of the Generation – IV International Forum (GIF) in 2002, six nuclear reactors with the potential to contribute towards global energy production were identified. The six chosen reactors were also identified as having the potential to support a wide range of functions. These reactors include the Gas-cooled Fast Reactor (GFR), Lead-cooled Fast Reactor (LFR), Molten Salt Reactor (MSR), Sodium-cooled Fast Reactor (SFR), Supercritical Water-Cooled Reactor (SWCR) and the Very High Temperature Reactor (VHTR) [5].

Each of the introduced reactor designs vary from one another in terms of their operating conditions, heat transfer method and energy outputs, meaning they may be adapted to support additional functions alongside the production of electricity. When introduced, the technology for the new reactors was not readily available and hence a long-term research and development plan was introduced. This test plan was divided into three sections. Reactor viability, where the basic concepts and technologies were evaluated, reactor performance, where engineering processes and material capabilities are tested and verified under reactor conditions

and reactor demonstration which involves the construction and operation of prototype Generation – IV reactors.

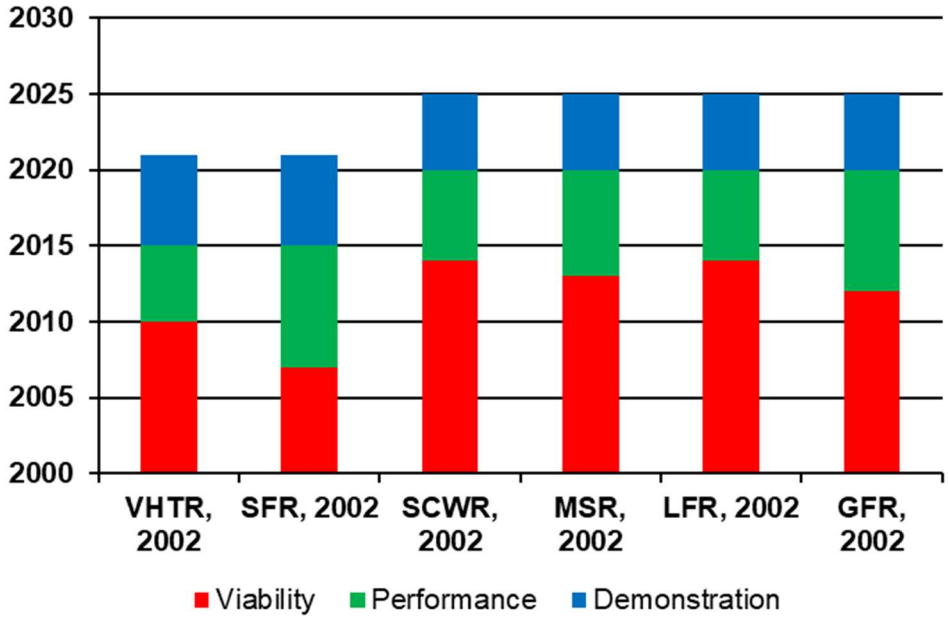


Figure 1.1 – Timeline proposed by the GIF for the research and development of the six Generation – IV nuclear reactors, adapted from [5].

Referring to Figure 1.1, one of the reactors requiring the most research to understand its viability and work in the performance phase of development is the MSR. The MSR differs from a conventional nuclear reactor as no solid source of nuclear fuel is used. Instead, nuclear fuel is circulated through the reactor core in a carrier salt, typically at temperatures that can range from 600°C to 800 °C [4, 6, 7]. To remove heat from the carrier salt, a secondary salt is used as a heat transfer fluid (HTF). The removed heat can then be transported to a power generation circuit and used in the production of electricity as shown in Figure 1.2.

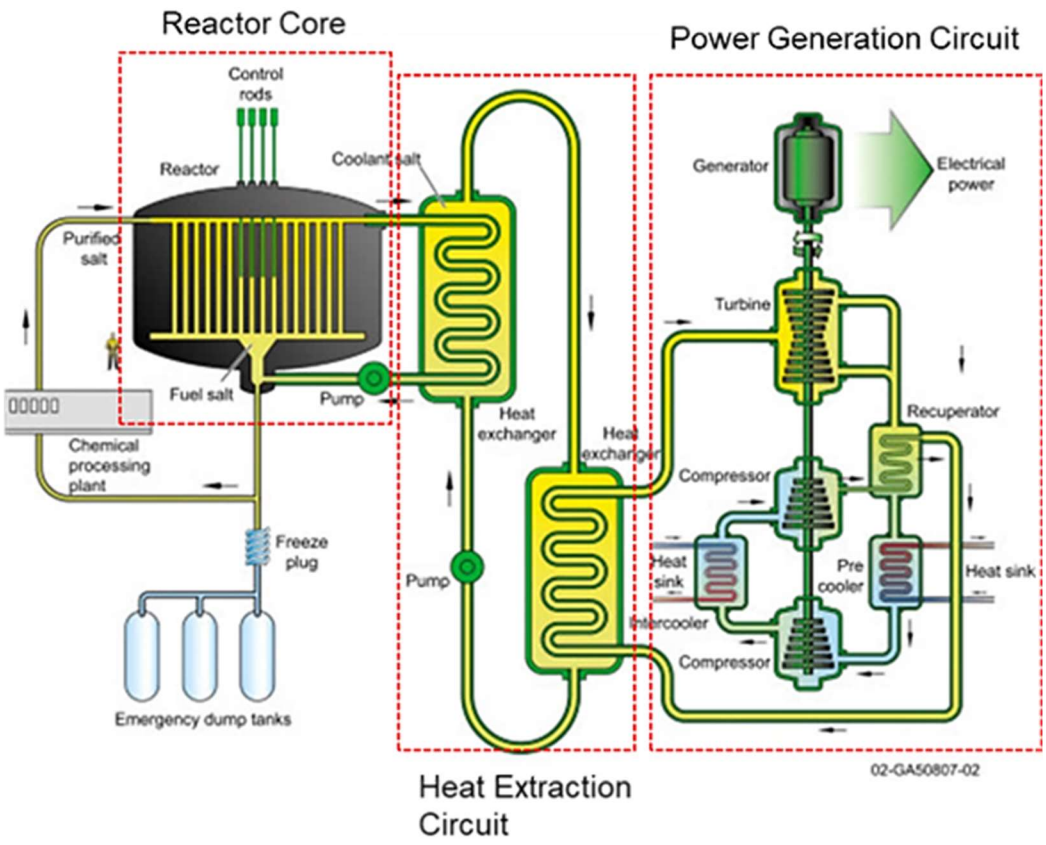


Figure 1.2 – Schematic showing MSR operation cycles with salt cycles labelled. Figure adapted from [5] .

Currently, a wide selection of molten salt combinations exist due to their potential use, not only in MSRs but in concentrating solar power (CSP) technologies also [8]. Due to their potential use in nuclear application, the selection criteria for these combinations of molten salts are meticulous and highlights the importance of salt selection on the successful operation of the MSR. Molten salt used in the MSR must have a small neutron cross-section, be thermally stable at extremely high temperatures, have a low vapour pressure, and have adequate heat transfer and hydrodynamic properties, as well as being compatible with container and reactor materials [9]. Currently, two salt combinations are used to fulfil the role of a HTF in the MSR, these being FLiBe and FLiNaK [10]. FLiBe molten salt is a combination of lithium fluoride (LiF) and beryllium fluoride (BeF_2) in a mixture of 34 mol% - 66 mol% and is the HTF that has been used historically [11]. FLiNaK molten salt is a eutectic mixture of LiF, sodium fluoride (NaF) and potassium fluoride (KF), in a mixture of 46.5 mol% - 11.5 mol% - 42.0 mol%. Although FLiBe is currently the most commonly used, due to its use as the carrier salt for nuclear fuel as well as the HTF, FLiNaK has the potential to also be an effective HTF in MSR environments [12].

Due to the high operating temperatures of the MSR, efficient electricity generation is possible as well as other applications [13]. However, due to the extreme operating environment, a number of materials challenges need to be understood and overcome. The first materials challenge to understand is corrosion, which costs the nuclear industry in the US $4.2 billion per year [14]. Corrosion typically occurs in MSR environments due to the interactions of the salt's constituents with alloying elements present in the materials used within the reactor. This process is commonly driven by impurities within the salt and can be expressed as a system of electrochemical reactions. The anodic and cathodic are expressed as equations 1.1 and 1.2 [15]:

$$M \rightarrow M^{n+} + ne^- \quad \textbf{1.1}$$

$$Ox + ne^- \rightarrow Red \quad \textbf{1.2}$$

where M is a metallic alloying element, Ox is the oxidant and Red the reduced species. In the case of fluoride molten salt, the cathodic reaction can be expressed as [16]:

$$\frac{n}{2}F_2 + ne^- \rightarrow nF^- \quad \textbf{1.3}$$

The overall resulting equation can be expressed as:

$$M + \frac{n}{2}F_2 \rightarrow MF_n \quad \textbf{1.4}$$

Therefore, a comprehensive understanding of the corrosive nature of molten salts and their interactions with materials is of imperative importance to the industry. To achieve this, experiments replicating the conditions of an MSR should be conducted in a laboratory environment as closely as is practicable.

Another problem specific to nuclear system is irradiation of material, which left unchecked could result in failure of components by stress corrosion cracking (SCC) when in synergy with a corrosive environment [17].

Similarly, the introduction of oxygen (O_2) during salt processing may also play a part in material degradation by the formation of non-protective or soluble oxide layers within molten salt environments. It is therefore critical to fully comprehend the impact of material oxidation, molten salt corrosion and nuclear irradiation on material performance in MSR environments.

1.2 Contribution to Literature

This thesis will deploy a combination of numerical and experimental methods to characterise the oxidation of nickel (Ni)-based alloys at high temperatures as well as characterise and investigate the corrosion behaviour of Ni-based alloys in molten salt environments. Within the literature there remains a need for an effective tool for predicting the oxidation and corrosion kinetics of Ni-based alloys. Therefore, this work will develop numerical models for predicting the oxidation and molten salt corrosion of Ni-based alloys.

Numerical modelling will be supported by static experimental techniques to aid in understanding the corrosion mechanism of materials in molten salt environments in isolation of any additional corrosion degradation mechanisms. Experiments will aim to replicate the operating temperatures, materials and salt combinations typically utilised within an MSR environment.

As previously discussed, the irradiation of Ni-based alloys in molten salt environments may also have a detrimental impact on material performance in the harsh environments associated with the MSR. Hence, an understanding of the damage induced by nuclear irradiation and the impact it has on a materials corrosion behaviour in molten salt environments is also explored.

1.3 Project Objectives

In previous work it has been highlighted that the corrosion of Ni-based alloys by molten fluoride salts is a major issue to the development of the MSR. The overall aim of this work is therefore to investigate and characterise the material degradation of Ni-based alloys at the molten salt-metal interface at extremely high temperatures. This will be achieved using both experimental methods and numerical modelling. The objectives of this work are as follows:

1. To develop an understanding of the chemical, electrochemical, diffusion and heat transfer reactions and processes.
2. To develop semi-empirical and mechanistic models for predicting the molten salt corrosion and high – temperature oxidation behaviour of Ni-based alloys in molten fluoride salts.
3. To characterise and quantify the oxidation and corrosion behaviour of Ni-based alloys in molten fluoride salts using a thermogravimetric method.

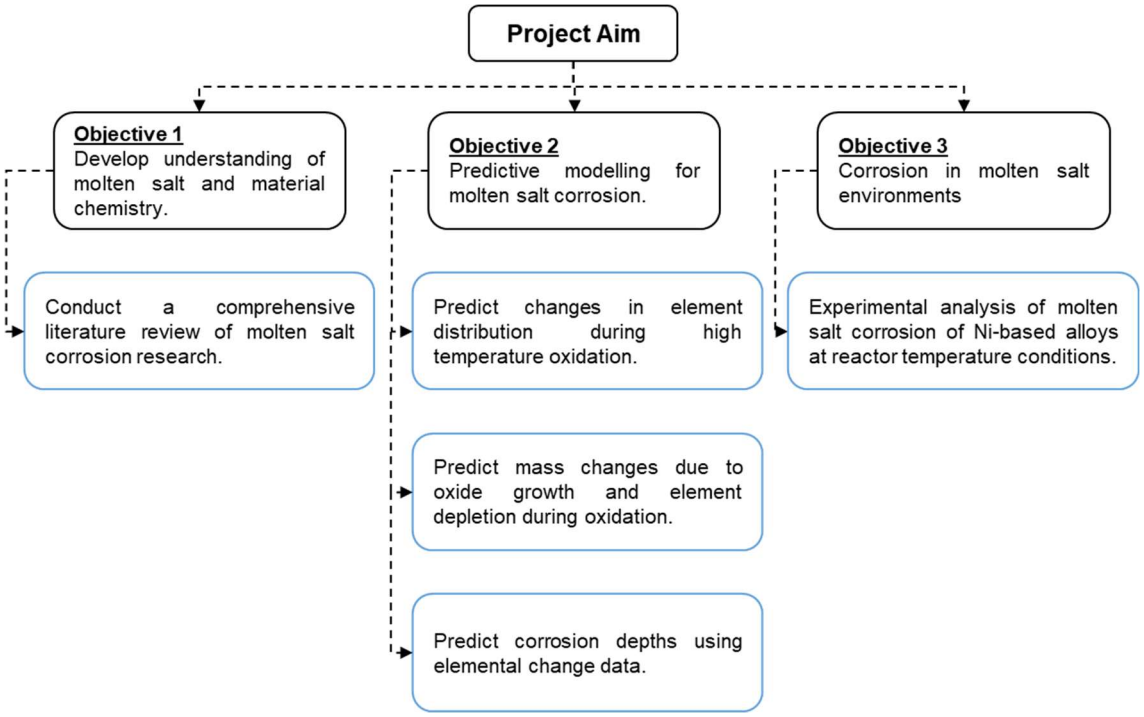


Figure 1.3 - Project framework highlighting the aims and objectives of the research project to understand the degradation of materials in molten salt environments.

1.4 Thesis Structure

This thesis is presented in 8 chapters. The first chapters of the thesis outline the necessary background information and underpinning theory in the fields of high temperature alloy oxidation and molten salt corrosion, including any literature that may pertain to studies within these fields. The section of chapters following this outline the experimental and numerical methods deployed and the results obtained from the deployment of these methods. The final chapters of this thesis discuss the experimental and numerical results presented in the previous results chapters, presenting the key findings and the conclusions from the research.

The current chapter, Chapter 1, has provided a summary of the background information for the project, including the project aims and objectives. This chapter has also provided an overview into the research that will be conducted throughout this thesis.

Chapter 2 is the first literature review chapter, which provides an overview and introduction of the GIF and Generation – IV nuclear reactors, including discussion on how the Generation – IV reactors meet the four goals of the GIF, and how their

specific designs may influence their future applications. This Chapter then provides specific insight into the development of the MSR and current MSR configurations in development globally.

The second literature review chapter, Chapter 3, provides a comprehensive review of the literature relevant to the high temperature oxidation and molten salt corrosion of Ni-based alloys under conditions relevant to the MSR, as presented in Chapter 2. This includes providing a detailed discussion of the underpinning physics of high temperature oxidation and molten salt corrosion and factors that may influence these methods of material degradation.

Chapter 4 describes the main experimental methodologies to complete static high temperature oxidation and molten salt corrosion testing of Ni-based alloys as well as the numerical modelling methods that will be deployed to predict the high temperature oxidation and corrosion behaviour.

The results obtained from the oxidation studies of Ni-based alloys using experimental and numerical modelling methodologies will be presented in Chapter 5, whilst the results of the molten salt corrosion study will be presented in Chapter 6. In both cases, results of surface analysis of oxidised and corroded samples were used to develop a more detailed understanding of the oxidation and corrosion behaviour of Ni-based alloys.

The results presented in Chapter 5 and Chapter 6 will be thoroughly discussed throughout Chapter 7 with reference to the underpinning science of molten salt corrosion and high temperature oxidation. A comparison between experimental and numerical modelling methodologies will be provided. Any reasons for discrepancies will also be discussed.

The key conclusions that can be drawn from the research conducted throughout this thesis will be presented in Chapter 8 along with any suggestions for future work that would relate to this study.

Chapter 2 – Literature Review I

Generation – IV nuclear reactors and MSR development

2.1 Introduction

In order to meet the energy demands of an ever-growing population, cleaner methods of energy generation need to be implemented to prevent the adverse environmental impact associated with expanding today's non-renewable energy generation methods. This includes adopting nuclear energy as part of a robust energy program to meet future energy needs. The use of nuclear energy is not limited to energy production but can also be expanded to other useful areas such as H_2 generation, natural gas refinement and water desalination [4]. For nuclear energy to be used in this way, new nuclear energy systems are needed, along with significant research and development into such systems. The need for research and development in the field of nuclear energy has resulted in the introduction of the Generation – IV nuclear reactors.

The Generation – IV nuclear reactors consist of six nuclear reactors that have the potential to become useful components in a sustainable, economic, safe, and clean energy production program. This chapter aims to:

- Detail the main aims and objectives associated with the development of the Generation – IV nuclear reactors.
- Illustrate the differences between all of the Generation – IV nuclear reactors and how the reactors may be used for different applications to fulfil future energy demands.
- Discuss the historical development of the MSR alongside current challenges to MSR development and current MSR configurations.
- Introduce the potential corrosion mechanisms by which materials may degrade in molten salt environments.

2.2 Generation – IV nuclear reactors – A summary

Reviews of the six nuclear reactors have covered the differences in operating conditions between the reactors, their specific design considerations when trying to achieve the GIF aims and objectives and their potential to be used for applications other than electricity generation. The first aspect to consider is the GIF aims and objectives and how each reactor has been designed to meet these.

In 2002, the GIF stated that the aims of the Generation – IV nuclear reactors would be focused on four key areas: sustainability, economics, safety, and reliability and, proliferation resistance and physical protection. Within each of these four areas, clear goals were defined by the GIF. These goals are summarised in Figure 2.1.

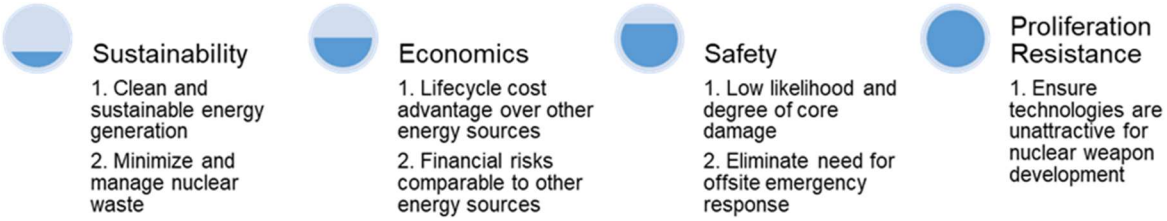


Figure 2.1 – Key areas and the associated goals for the Generation – IV nuclear reactors [5].

The six Generation – IV nuclear reactors have been analysed to assess the likelihood of each reactor meeting the goals outlined in Figure 2.1. In their work, John Kelly [4] highlighted some of the key design features of each of the nuclear reactors and how these design features may aid each reactor in meeting the GIF goals. A summary of their findings is presented in Table 2.1.

Table 2.1 - Summary of design features of Generation - IV nuclear reactors in meeting GIF goals [4].

Reactor Type	Goal	Design Considerations
VHTR	Safety	Restricted energy output; graphite structure hence very stable; no fuel damage below 1600 °C; able to use a single inert coolant
	Sustainability	Not currently a focus during development
	Economics	Very high thermal efficiency due to high temperature operation; potential applications beyond electricity generation
SFR	Safety	Natural circulation cooling in place; single inert coolant used; coolant stable at high temperatures
	Sustainability	Potential for greater uranium utilisation; potential for transmutation of long-lived waste, resulting in significant reductions in radioactivity
	Economics	Good thermodynamic efficiency.
SCWR	Safety	Passive safety systems can be implemented; single inert coolant can be used
	Sustainability	Can be designed for higher conversion ratios; potential transmutation of waste material resulting in significant reductions in radioactivity
	Economics	Has pedigree in previous nuclear reactor generations; high thermodynamic efficiency
GFR	Safety	Complex engineered safety system implemented
	Sustainability	Comparable sustainability characteristics to SFR
	Economics	High thermodynamic efficiencies; potential beyond power generation
LFR	Safety	Single inert coolant; natural circulation cooling in place
	Sustainability	Comparable sustainability characteristics to SFR and GFR
	Economics	Good thermodynamic efficiency
MSR	Safety	No possibility of fuel meltdown; low fissile inventory; low fission product inventory
	Sustainability	Chemical recycling plant is main design feature
	Economics	High thermodynamic efficiency; application beyond electricity generation

Due to the different design features described in Table 2.1, there are key differences between each of the nuclear reactors, specifically in the neutron spectrum, which describes the energy distribution of neutrons within the reactor core. System temperatures, pressures, cooling methods and power outputs are also observed to differ between reactors. A summary of these differences is presented in Table 2.2.

Table 2.2 – Summary of key reactor characteristics of the Generation – IV nuclear reactors [4].

Generation – IV Reactor	Neutron Spectrum	System Pressure (MPa)	Cooling Method	Outlet Temperature (ºC)	Size (MWe)
VHTR	Thermal	8	Helium	900-1000	100-300
SFR	Fast	0.3	Sodium	550	50-1500
SCWR	Thermal	25	Water	510-625	1000-1600
GFR	Fast	7	Helium	850	1000
LFR	Fast	0.3	Lead, Lead/Bismuth	480-800	20-1200
MSR	Epithermal	0.6	Molten Salts	700-800	1000

The highlighted differences in the operation of each of the six nuclear reactors, aids in highlighting how each reactor may be used for applications other than electricity generation. For example, for any of the Generation – IV nuclear reactor designs to be used in H_2 production, an outlet temperature between 800 and 1000 °C would be required [18], hence the VHTR and the GFR are potential options when adapting nuclear reactor technology to this industrial application. Similarly, to perform the function of desalinating water, an outlet temperature between 80 and 200 °C would be required [4]. Each Generation – IV nuclear reactor could potentially be adapted to fulfil this function. The following table highlights several industrial applications that the Generation – IV nuclear reactors could be adapted to perform.

Table 2.3 - Industrial applications that may be fulfilled by adapted versions of the Generation - IV nuclear reactors. Table adapted from work of John Kelly [4].

Application	Temperature Range (ºC)	LFR	SCWR	SFR	MSR	GFR	VHTR
District heating and desalinisation	80-200	✓	✓	✓	✓	✓	✓
Petroleum refining	250-550	✓	✓	✓	✓	✓	✓
Oil shale and oil sand processing	300-600				✓	✓	✓
Cogenerate steam and electricity	350-800				✓	✓	✓
Steam reforming of natural gas	500-900				✓	✓	✓
H_2 production and coal gasification	800-1000					✓	✓

Despite their clear potential in being used to fulfil a number of different functions alongside their primary function of energy production, a great deal of research and development still remains to be performed on each of the Generation – IV nuclear reactors. In many cases, the areas requiring additional research and development are centred on the materials, what materials to use for such harsh environments and understanding how the materials will behave during operation [10]. Due to the unique challenges presented by the reactors, a new development timeline was introduced in 2013, extending the research timeline of many of the reactors [19].

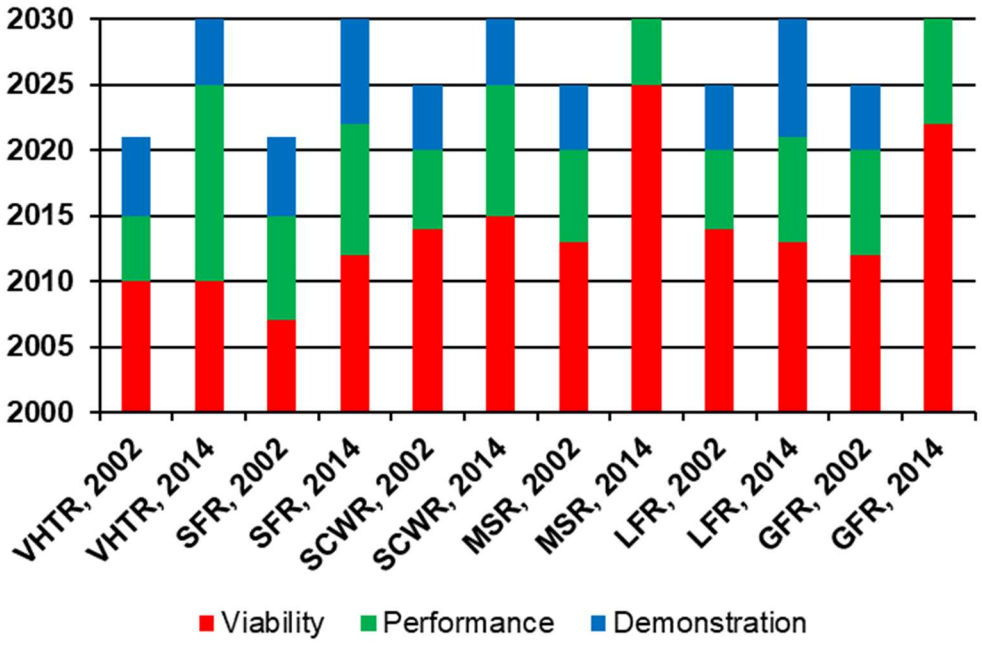


Figure 2.2 – Updated research and development timeline for Generation - IV nuclear reactors, introduced in 2014, adapted from [5, 19] .

In many cases, additional time has been added to both the viability and performance phases, with reactors such as the MSR and GFR now not completing the viability phase until the early 2020's, highlighting how complex these reactor designs are that they require an additional decade of research compared to the original timeline.

In 2021, an update was provided by the GIF highlighting the progress and remaining research and development areas for each of the six reactors. The case for many of the discussed reactors is that corrosion control remained a key area for research and development [20].

2.3 Development of the MSR

As shown in Section 2.2, the MSR has great potential in being utilised for a variety of functions and meeting the goals outlined by the GIF. However, due to the challenging environment on which the MSR technology is based, its development has been delayed, as shown in Figure 2.2. This may be due to its unique operation characteristics, such as the utilisation of molten salts to carry nuclear fuel to the reactor core and using a secondary molten salt as an HTF. However, a great deal of research and development has already been conducted on the MSR, starting in the 1950's.

This section aims to outline the historical development work that has been conducted on the MSR, as well as discuss current reactor designs and current research and development needs of the MSR.

2.3.1 Historical development of the MSR

Research into the MSR has been conducted over several decades, starting with the Aerospace Propulsion Program at Oak Ridge National Laboratory (ORNL). The original MSR concept was to use an MSR as a method of aerospace propulsion [21, 22]. The initial MSR was designed to assess the nuclear stability of circulating molten salts through a reactor core. The first Aircraft Reactor Experiment (ARE) used a fuel salt containing sodium, zirconium (IV) and uranium (IV) fluorides (NaF, ZrF_4 and UF_4 respectively) which was circulated through a reactor core with a beryllium oxide (BeO) moderator. In this original work fluoride salts were chosen due to their low vapour pressures and stability at high temperatures [22].

It was quickly deemed that the MSR would not be suitable for aerospace propulsion, however, this work led to the proposition of a molten salt breeder reactor (MSBR). The preliminary breeder reactor designs were predicated on the thorium (Th) fuel cycle, in which Th-232 is used to produce U-233 [23]. This is achieved through a series of radioactive decays as shown in Figure 2.3.

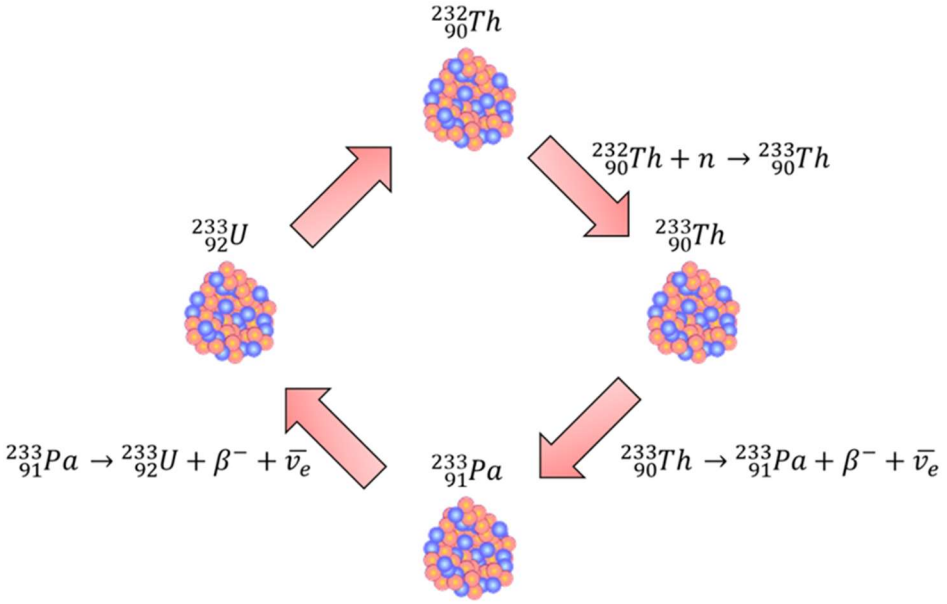


Figure 2.3 – Illustration of the Th fuel cycle where U-233 is produced from Th-232 [24]. The depicted process shows the interaction of Th-232 with a neutron followed by two subsequent radioactive decays to become U-233.

Although it was decided that the MSBR would operate on the Th fuel cycle, two main designs for the MSBR were conceptualised. These were the one and two fluid breeder reactors. In both cases, the fuel salt would contain U-233, however,

the two fluid breeder reactor would contain a salt blanket which surrounded the core. The salt blanket would contain Th-232, the aim of the blanket being to catch any stray neutrons. By absorbing neutrons, Th-232 would also be converted to U-233 which could then be added to the fuel salt to circulate through the reactor core.

The first MSBR was built in the 1960's and was a single fluid breeder reactor. Although the reactor was defined as a 'breeder' reactor, this function was not fulfilled to aid in the simplicity of the reactor operation [25]. This first reactor was known as the Molten Salt Reactor Experiment (MSRE). The MSRE used a fuel salt composition that differed from that used by the ARE, with the fuel salt being composed of lithium fluoride (LiF), beryllium fluoride (BeF_2), ZrF_4 and UF_4. In order to cool the system, a secondary coolant salt was used which was composed of LiF and BeF_2 [26].

The MSRE went critical in 1965 and was operated until 1969, during which time a number of experiments were conducted to benchmark the reactors performance and define key characteristics of the system. During its operation, materials compatibility was raised as an issue within the MSR, with analysis of fuel salt showing elevated concentrations of Cr [25]. Although a speciality Ni-based alloy Hastelloy–N, developed for specifically for the MSRE [6], was used due to its reduced Cr content, an increase in the Cr concentration within the fuel salt was observed, which is indicative of a dealloying corrosion mechanism of Hastelloy–N [27].

Further analysis of the Hastelloy – N material upon conclusion of the MSRE revealed two key material degradation issues. The first being the embrittlement of Hastelloy – N when subjected to high temperatures and neutron irradiation. As a result, the strain that Hastelloy – N could be subjected to before failure was reduced, making component failure more likely. Secondly, embrittlement of the grain boundaries due to intergranular corrosion was observed. Exposure of the Hastelloy – N to fuel salt resulted in recession, and embrittlement, of the grain boundaries by between 5 mm and 10 mm, ultimately resulting in crack formation in the heat exchangers.

Based on the lessons learned from the MSRE, the MSBR was proposed. This reactor was due to be a 1000 MW_e breeder reactor, operating on a thorium fuel cycle and with a thermal neutron spectrum due to the success achieved using these parameters during the MSRE. However, altered coolant salt chemistry was proposed, with a combination of NaF and sodium tetrafluoroborate ($NaBF_4$) being preferred to the combination of LiF and BeF_2. This salt combination was chosen due to its potential improved materials compatibility compared to those used during

the MSRE. The salt combination of NaF and $NaBF_4$ was believed to show good heat transfer and fluid flow properties and was considered for use in the MSBR as a HTF in the secondary molten salt circuit [28]. A comparison of the coolant salts used in the MSRE and MSBR is presented in Table 2.4.

Table 2.4 – Comparison of properties of coolant salts used in MSRE and MSBR [29, 30].

Coolant Salt	Composition (mol%)	Density (kg/m^3)	Viscosity (Pa.s)	Specific Heat Capacity (J/kg/K)	Thermal Conductivity (W/m.K)
$LiF – BeF_2$	66 – 34	1940	0.0056	2414.17	1.00
$NaF – NaBF_4$	8 – 92	1750	0.0009	1506.24	0.40

Despite its good material compatibility and fluid flow properties, the thermal properties of the $LiF - BeF_2$ molten salt combination far outweigh those shown by the $NaF – NaBF_4$ molten salt combination, with $LiF – BeF_2$ showing far greater specific heat capacities and thermal conductivity.

In these early works, fluoride molten salt combinations were favourable over other options such as chloride molten salts. Some considerations that may have resulted in fluoride salts being favourable over chloride alternatives were outlined by Williams et al. [9]. These considerations include the salt components and how these may interact with materials, the salt stability under neutron irradiation doses, salt stability at high temperature, solubility of fissile material within the salt as well as the salts thermal and hydrodynamic properties.

Studies performed by Williams et al. [9, 30] and Forsberg et al. [31] led to the elimination of chloride salts from consideration as both fuel and coolant salts in MSRs. Both studies eliminated chloride salts due to three key reasons, the first being the larger neutron cross-section of chlorine compared to fluorine. This may lead to neutron absorption by the salt constituents, preventing its absorption by the fuel salt and reducing reactor efficiency [31].

Secondly, a long-term activation study performed by Williams et al. [9] showed that a chlorine-36 (Cl-36) radioactive isotope still had a very high activity when formed during reactor operation. Due to the high mobility and long half-life of Cl-36, issues may arise when processing used fuel and coolant salts and managing nuclear waste [9]. The final reason is due to the corrosive nature of the chloride system and their aggressiveness compared with a fluoride containing environment [9].

However, despite the studies of Williams et al. [9, 30] and Forsberg et al. [31], some fast spectrum nuclear reactors that are under-development by TerraPower and Elysium Industries use chloride molten salts as the coolant [10, 32]. Some of these molten chloride salts include combination of lithium chloride (LiCl), sodium chloride (NaCl), potassium chloride (KCl) and magnesium chloride ($MgCl_2$). Some of the most common combinations of chloride salts include NaCl – KCl – $MgCl_2$, NaCl – $MgCl_2$ and KCl – $MgCl_2$. The properties of these molten chloride salt combinations have been shown to be comparable to their molten fluoride counterparts. A comparison of common chloride based molten salt to the LiF – BeF_2 salt combination is provided in Table 2.5.

Table 2.5 – Comparison of properties of molten chloride salt properties with FLiBe molten salt showing comparable thermal and physical properties [29, 33, 34]

Coolant Salt	Composition (mol%)	Density (kg/m^3)	Viscosity (Pa.s)	Specific Heat Capacity (J/kg/K)	Thermal Conductivity (W/m.K)
LiF – BeF_2	67 – 33	1940	0.0056	2414.17	1.00
NaCl – KCl – $MgCl_2$	33.0 – 21.6 – 45.4	1565.5	0.00129	1180	0.69
NaCl – $MgCl_2$	45.8 – 54.2	1804	0.00136	1284	1.00
KCl – $MgCl_2$	68 – 32	1611	0.00140	1193	1.02

The comparison presented in Table 2.5 shows that chloride salt combinations have comparable thermal properties to the molten FLiBe salt, with the NaCl – $MgCl_2$ salt combination having the most similarities to the FLiBe salt. The chloride salt properties presented in Table 2.5 are also consistent with the general requirements for molten salt coolants and would be viable from a heat transfer standpoint [35].

2.4 Current Generation – IV MSR Configurations

Current MSR configurations can be broken down into three categories, thermal spectrum MSRs which utilise both molten salts as a carrier salt for nuclear fuel and as a coolant, with fast neutron spectrum MSRs utilising molten salts for the same purpose [36]. The third category utilises a thermal neutron spectrum, but, a molten salt is used as a coolant only, with a solid fuel being used instead of molten salt [37]. This solid fuel source is typically uranium (IV) oxide (UO_2) which is coated

with layers of graphite, pyrolytic carbon and silicon carbide (SiC) [38] as shown in Figure 2.4.

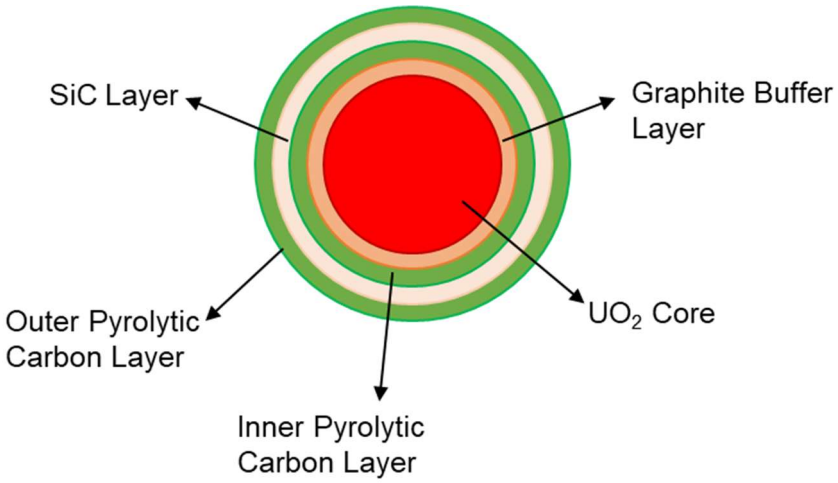


Figure 2.4 – Image illustrating the structure of solid nuclear fuel design for MSR applications, including a solid UO_2 core surround by layers of graphite, pyrolytic carbon, and SiC. Figure adapted from [7].

The graphite layer aids in the absorption of radiation and is porous to allow for the release of fission gases produced during the nuclear irradiation process [7]. Surrounding this layer is an inner pyrolytic carbon layer, followed by the SiC layer and an outer pyrolytic carbon layer. The purpose of the pyrolytic carbon layers is to shrink under irradiation and provide support and protect the inner layers of the nuclear fuel.

The use of a solid fuel source may be favourable due to simplification of the reactor core design, as well as removing the need to optimise the composition of the fuel salt to ensure efficient reactor operation [39]. The following tables outline the current MSR configurations being developed in each of the three categories defined above.

Table 2.6 – Summary of thermal spectrum, liquid fuel MSR project and developments outlined by the GIF [10].

Name	Institute	Power Output (MW_{th})	Fuel	Coolant	Moderator
Thorium Molten Salt Reactor, Liquid Fuel (TMSF-LF)	Shanghai Institute of Applied Physics, China	395	ThF_4-$^{233}UF_4$	LiF-BeF_2 (FLiBe)	Graphite
Integral Molten Salt Reactor (IMSR)	Terrestrial Energy, Canada, and the United States	400	UF_4	NaF-BeF_2 (and or LiF)	Graphite
ThorCon Reactor	ThorCon International, Singapore	557	UF_4	NaF-BeF_2	Graphite
Liquid-Fluoride Thorium Reactor (LFTR)	FLiBe Energy, United States	600	ThF_4-$^{233}UF_4$	LiF-BeF_2 (FLiBe)	Graphite
FUJI-U3	Japan	450	ThF_4-$^{233}UF_4$	LiF-BeF_2 (FLiBe)	Graphite
Advanced Molten-salt Break-even Inherently safe Dual-mission Experimental and Test Reactor (AMBIDEXTER)	Ajou University, Korea	250	ThF_4-$^{233}UF_4$	LiF-BeF_2 (FLiBe)	None
Transatomic Power MSR (TAP)	Transatomic Power, United States	1250	UF_4	LiF-NaF-KF (FLiNaK)	SiC Cladding
Compact Used Fuel BurnEr (CUBE)	Seaborg Technologies, Denmark	250	SNF	Fluorides	Graphite
Process Heat Reactor	Thorenco, United States	50	UF_4	NaF-BeF_2	Be Rods
Stable Salt Thermal Reactor	Moltex Energy, UK	300-2500	UF_4	ZrF_4 – ZrF_2 – NaF	Graphite

Table 2.7 - Summary of fast spectrum, liquid fuel MSR projects and developments outlined by the GIF [10].

Name	Institute	Power Output (MW_{th})	Fuel	Coolant	Moderator
Molten Salt Fast Reactor	SAMOFAR, France-EU-Switzerland	3000	ThF_4-UF_4	LiF-ThF_4-UF_4	None
Molten Salt Actinide Recycler and Transformer (MOSART)	Kurchatov Institute, Russia	2400	$TRUF_3$ or ThF_4-UF_4	LiF-BeF_2 (FLiBe)or NaF-LiF-BeF_2	None
U-Pu Fast Molten Salt Reactor (U-Pu FMSR)	VNIINM, Russia	3200	UF_4-PuF_3	LiF-NaF-KF (FLiNaK)	None
Indian Molten Salt Breeder Reactor (IMSBR)	BARC, India	1900	ThF_4-UF_4	LiF-ThF_4-UF_4	None
Stable Salt Fast Reactor (SSR-W)	Moltex Energy, UK	750-2500	PuF_3	ZrF_4 – ZrF_2 – NaF	None
Molten Chloride Fast Spectrum Reactor (MCFR)	TerraPower, United States	Data Unavailable	U-Pu	Chlorides	None
Molten Chloride Salt Fast Reactor (MCSFR)	Elysium Industries, United States and Canada	100-5000	U-Pu	Chlorides	None
Dual Fluid Reactor (DFR)	Dual Fluid Reactor, Germany	3000	Actinide chlorides (U-Pu)	Lead	None

Table 2.8 - Summary of thermal spectrum, solid fuel MSR projects and developments outlined by the GIF [10].

Name	Institute	Power Output (MW_{th})	Fuel	Coolant	Moderator
Molten Salt Reactor with nano-particle fuel	Kurchatov Institute, Russia	16	TRISO-coated LEU	LiF-BeF_2 (FLiBe)	Graphite Pebble Bed
Advanced High Temperature Reactor (AHTR)	ORNL, United States	3400	Coated U particles in blocks or plates	LiF-BeF_2 (FLiBe)	Graphite
Small Advanced High Temperature Reactors (SmAHTR)	ORNL, United States	125	Coated U particles in blocks or plates	LiF-BeF_2 (FLiBe)	Graphite
Pebble Bed – Fluoride Salt Cooled High Temperature Reactors (PB-FHR)	UC Berkeley, MIT and UW, United States	242	TRISO-coated LEU	LiF-BeF_2 (FLiBe)	Graphite Pebble Bed
Thorium Molten Salt Reactor, Solid Fuel (TMSR-SF)	SINAP, China	395	TRISO-coated U-Th	LiF-BeF_2 (FLiBe)	Graphite Pebble Bed
Indian High Temperature Reactor (IHTR)	BARC, India	600	TRISO-coated U-Th	LiF-BeF_2 (FLiBe)	Graphite Pebble Bed

Comparison of the MSRs presented in Table 2.6, Table 2.7 and Table 2.8 highlight the differences between each of the three categories of reactor, with fast spectrum MSRs utilising a fuel salt having a higher power output than the thermal spectrum reactors, regardless of whether a fuel salt or solid fuel is used. This may be due to the increased quantity of fissile material used within the fuel source of a fast reactor when compared with that of a thermal reactor [24].

Despite the difference in power output between the reactors, there remain many similarities, particularly in the coolant salts used in each case. Although many MSRs presented in each table are leaning towards the use of the LiF – BeF_2 salt (FLiBe) combination discussed previously, some reactors have been designed to use a combination of lithium, sodium, and potassium fluoride salts (LiF, NaF and

KF respectively). The LiF – NaF – KF salt combination, known as FLiNaK, has been shown to be a very promising coolant salt due to its thermal and physical properties when compared to FLiBe molten salt. A comparison between these properties is presented in Table 2.9.

Table 2.9 – Comparison of properties of FLiBe and FLiNaK molten salts [29, 31].

Coolant Salt	T_{melt} (°C)	Density (kg/m^3)	Viscosity (Pa.s)	Specific Heat Capacity (J/kg/K)	Thermal Conductivity (W/m.K)
LiF – BeF_2	459	1940	0.0056	2414.17	1.00
LiF – NaF – KF	454	2020	0.0029	1882.8	0.92

As can be seen in Table 2.9, the thermal and physical properties of FLiBe and FLiNaK are very similar, although FLiBe boasts slightly improved thermal properties. However, the lower melting point of FLiNaK and slightly improved fluid flow properties may improve reactor performance and component longevity over longer operation times. The lower toxicity of the FLiNaK components when compared with those of FLiBe also decreases the need for extensive handling protocols [40].

Despite the similar properties of the two salt combinations, presented in Table 2.9, the use of FLiNaK would be limited to a secondary coolant and not a component of the fuel salt. This is due to the FLiNaK molten salt combinations poor nuclear properties when compared with those of FLiBe [9]. Despite its comparable properties to FLiBe, further study into the corrosion of materials in FLiNaK salt has been recommended as preliminary studies have shown higher rates of material degradation in FLiNaK molten salt when compared with FLiBe [41].

Although they have been shown to corrode in both FLiBe and FLiNaK salt, many research institutes continue to favour the use of Ni-based alloys as the primary structural materials in their designs, with alloys such as the GH3535, Hastelloy N and MONICR Ni-based alloys being favoured due to their lower Cr content than other high temperature alloys [42]. Russian institutes have also contributed specially designed Ni-based alloys for MSR application, these being the HN80M series of alloys, which also contains less Cr than other high temperature alloys [43]. The reduction in the Cr content has a favourable impact on the corrosion

behaviour of Ni-based alloys which will be discussed more extensively in Chapter 3.

2.5 Potential mechanisms of material degradation

Within MSRs, materials may be affected by different mechanisms of material degradation depending on a number of environmental and chemical factors [16]. Some of these factors include salt contaminants, interactions between dissimilar materials in the presence of an electrolyte within the MSR environment, temperature gradients, the flow velocity of fuel and coolant salt and nuclear irradiation of materials during operation [16]. All of these factors can impact the corrosion behaviour of materials in different ways and induce different corrosion mechanisms.

Due to the critical nature of corrosion in an MSR, understanding the potential mechanisms by which corrosion can occur is of critical importance. In literature, the most commonly observed corrosion mechanisms are uniform corrosion, pitting corrosion, intergranular corrosion, galvanic corrosion and dealloying [44, 45]. However, in other molten salt systems, such as concentrating solar power plants, mechanisms such as crevice corrosion and stress corrosion cracking (SCC) have also been identified [46]. Therefore, this section aims to outline the common forms of material degradation mechanisms encountered in molten alt systems.

2.5.1 Uniform Corrosion

Uniform corrosion is classified as corrosive attack that causes the even receding of material over its entire surface [47]. For the corrosive attack to be classified as being uniform, a large portion of the exposed surface area has to have receded at the same rate [48].

However, uniform corrosion is normally relatively easy to protect against through the use of corrosion resistant or passivating materials, for example, Ni-based alloys may be used in combination with surface passivating treatments and surface coatings [49]. However, this may not be the case in MSR systems due to the highly corrosive and aggressive nature of molten salt environments. Hence, the use of passivating materials in such environments may not be sufficient to achieve corrosion resistance. The main reason for this is due to the solubility of normally protective metallic oxides in molten salt environments [16, 50, 51]. The result of the use of such materials may be the catastrophic failure of components due to severe corrosive attack.

This has been investigated by, Olson et al. [52] who experimented with using a Ni-plating on the Ni-based alloy Incoloy 800H and compared its corrosion behaviour to non-plated Incoloy 800H in FLiNaK salt at 850 °C. The result showed that the corrosion rate of Ni-plated Incoloy 800H was much less than that of Incoloy 800H without the Ni-plating. This was due to the marked decrease in the diffusion of alloying elements, particularly Cr, diffusing through the Ni-plating to the substrate – molten salt interface.

In an earlier work by Olson et al. [53], several alloys were immersed in FLiNaK molten salt at 850 °C for 500 hours, with the corrosion behaviour being quantified using a mass change method. The corrosion damage was characterised using scanning electron microscopy (SEM) and energy dispersive X-ray (EDX) analysis, as illustrated in Figure 2.5.

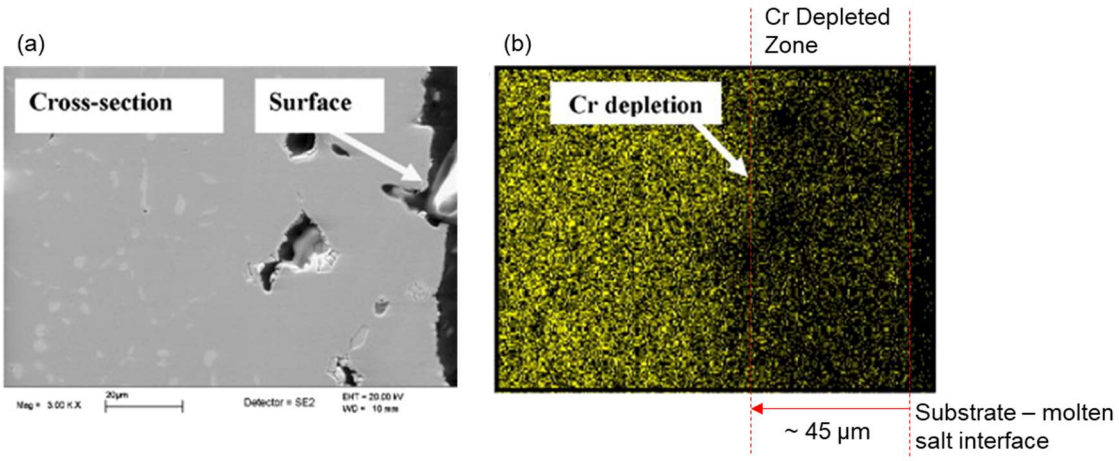


Figure 2.5 – Analysis from work by Olson et al. [53] showing a) micrograph of cross section showing corrosion damage to Hastelloy N after immersion in molten FLiNaK salt at 850 °C for 500 hours and b) showing EDX analysis of cross-section presented in a) showing uniform depletion of Cr to depths of approximately 45 µm. Image adapted from [53].

SEM and EDX analysis of the Ni-based alloy Hastelloy N, presented in Figure 2.5, showed uniform depletion of Cr from the substrate material. The same research also stated that uniform Cr depletion was observed in both Inconel 617 and Hastelloy X. Although, the rate of Cr depletion was observed to be at a much faster rate for Hastelloy X and Inconel 617 than Hastelloy N. By comparison of the Cr concentrations in each alloy, Hastelloy N has a much smaller concentration of Cr when compared with Hastelloy X and Inconel 617, which may account for the reduced rate of Cr dissolution. Hastelloy N also has a higher concentration of Mo than both Hastelloy X and Inconel 617, a key attribute that gives Hastelloy N greater corrosion resistance. A deeper discussion of the impact of an alloys composition on its corrosion behaviour is included as Section 3.6.1.8.

Although material was not removed from the exposed surface at a constant rate, as would be observed by the traditional definition of uniform corrosion, Cr was removed from the substrate material at an approximately constant rate across the entire exposed surface.

2.5.2 Crevice Corrosion

Despite not being commonly observed in molten salt nuclear applications, crevice corrosion has been observed in other high temperature environments, in which highly corrosive salts can be introduced [54]. Crevice corrosion is a form of localised corrosion, in which a corrosive medium stagnates and cannot be removed. The result of this is highly localised corrosion in the region of the corrosive substance which is commonly seen in regions of complex geometry or under oxidation or corrosion deposits [55].

Crevice corrosion has been observed in the aerospace and marine applications, in which salt deposits become trapped in regions of complex component geometry and hence are not able to be removed or replenished [55]. In the case of marine engines, these salts can be combinations of sulphate and chloride salts which can be highly corrosive, causing a high degree of damage, leading to component failure [56].

2.5.3 Stress Corrosion Cracking (SCC)

Similarly to crevice corrosion, SCC is not as commonly observed in MSR applications, but is common in other nuclear applications, as well as the oil and gas and aerospace industries [57]. SCC commonly occurs when a material reacts with a corrosive environment whilst being under load, leading to the formation of cracks. SCC can take many forms, including intergranular SCC where cracks form at grain boundaries or transgranular SCC where cracks form within the grains themselves along crystalline planes [58].

In alloys, SCC tends to occur due to the difference in reactivity's of different alloying elements within the alloy. For example, in Ni-based alloys containing a combination of metallic alloying, elements such as aluminium (Al) or chromium (Cr) would be preferentially removed over elements such as iron (Fe) or Ni.

SCC can also be enhanced by the introduction of damage due to neutron irradiation. In an MSR environment, structural materials are expected to be exposed to irradiation doses of 10 displacements per atom (dpa) per year over the reactors operation [59]. The enhancement of SCC due to irradiation doses has been shown to be caused by the embrittlement of materials after irradiation

exposure [60]. This occurs by the introduction of many different potential structural defects such as single vacancies and interstitial pairs, vacancy and interstitial clusters and dislocation loops which are formed by the migration of vacancies to the same plane, examples of which are illustrated in Figure 2.6.

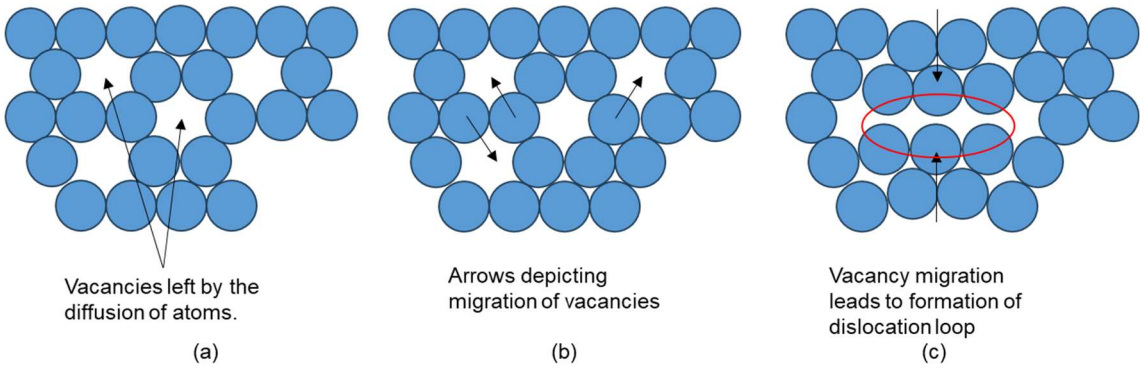


Figure 2.6 – Illustration of structural defects that may form during irradiation, such as vacancies and dislocation loops. The formation of dislocation loops is shown by a) the presence of vacancies, b) the movement of vacancies and c) the formed dislocation loop.

The introduction of such defects leads to increased stresses within the material microstructure due to defect growth. In turn this leads to embrittlement of the irradiated material [61]. This result was observed in the study by Nanstad et al. [62] who investigated the impact of irradiation on the mechanical properties of several Ni-based alloys with potential for use in MSR environments. One measurement taken was the percentage total elongation of the Ni-based alloys after irradiation. The result for Alloy 617 is presented in Figure 2.7.

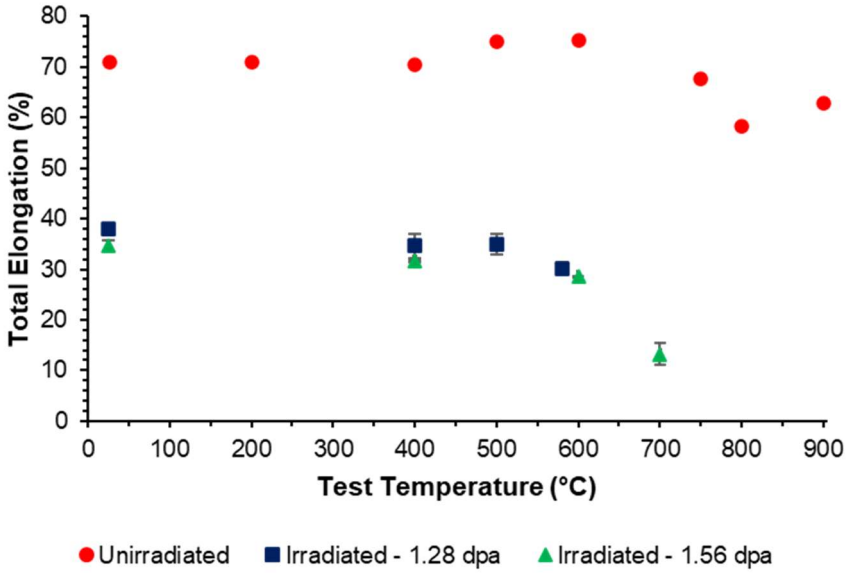


Figure 2.7 – Changes in percentage elongation observed for Alloy 617 before and after irradiation processes. Results show significant reductions in percentage elongation with increasing irradiation damage, which is indicative of material embrittlement. Figure created with data from [62].

Figure 2.7 shows that the percentage total elongation of Alloy 617 decreased when the level of irradiation was increased. The percentage total elongation reduced by as much as 86.2% when irradiated to 1.56 dpa when compared with unirradiated coupons which is indicative of material embrittlement. Embrittlement of the substrate material when undergoing irradiation degradation is likely to increase the probability of crack formation in the irradiated material and hence make the material more susceptible to SCC.

2.5.4 Pitting Corrosion

Pitting corrosion is a highly localised form of corrosion that can form deep holes in a materials surface and is commonly observed in molten salt corrosion studies. Pitting corrosion commonly occurs in regions where a materials oxide layer, or corrosion product layer, breaks down, allowing for attack of the underlying substrate material by the corrosive substance. Pitting corrosion should be quantified and characterised in accordance with ISO 11463 [63], which defines the acceptable methods for evaluating pitting corrosion.

Similarly, to SCC, this form of corrosion is commonly observed in the oil and gas industry, with many researchers carrying out extensive research to understand the formation of protective corrosion product layers in oil and gas environments [64-66]. However, pitting corrosion has also been identified as a potential cause of catastrophic failures in the pressurised water reactor (PWR) due to the presence

of chlorides (Cl^-) and O_2 within the water solution, leading to a build-up of Cl^- in porous regions of a materials oxide layer, leading to the reaction between Cl^- and metallic ions.

In MSR systems the introduction of O_2 can result in the formation of many metallic oxides, if the concentration of oxide ions (O^{2-}) within the salt is high enough. However, many metallic oxides are soluble in molten salt combinations such as FLiNaK and FLiBe [50]. Therefore, the formation and subsequent dissolution of oxide layers may result in the localised exposure of the metallic alloy to molten salt, resulting in highly localised corrosion behaviour [67].

2.5.5 Galvanic Corrosion

Galvanic corrosion is common in molten salt systems and occurs when two dissimilar materials are placed in contact through a molten salt electrolyte [68]. In molten salt corrosion testing, the corrosion rate of alloys under test has been shown to be greatly increased by the introduction of a galvanic couple. In particular, the use of crucible materials dissimilar to the test material have shown to increase the corrosion rate drastically.

A corrosion study by Olson et al. [69] quantified the corrosion behaviour of Incoloy 800H in four types of crucible using a mass loss method, showing that the corrosion behaviour of Incoloy 800H in molten FLiNaK salt increased drastically when corroded in crucibles constructed from Ni-201, graphite and pyrolytic boron nitride (PyBN) when compared with a crucible constructed from Incoloy 800H, in which the smallest specific mass loss was observed. A summary of the results is presented in Figure 2.8.

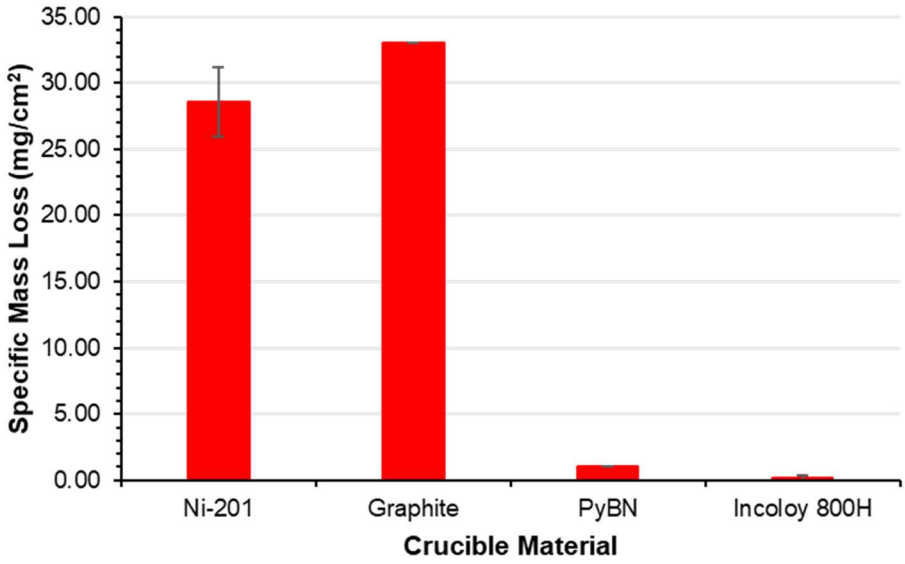


Figure 2.8 – Specific mass changes results for Incoloy 800H coupons immersed in FLiNaK molten salt at 850 °C for 500 hours in crucibles constructed from Ni-201, graphite, PyBN and Incoloy 800H showing increases in the specific mass loss of factors of 142, 165 and 4 for the Ni-201, Graphite and PyBN crucibles respectively [69].

This increase in corrosion damage was attributed to the establishment of a galvanic couple between the corroding coupon of Incoloy 800H and the crucible material whilst in the presence of the molten salt electrolyte. This allowed for the interactions between species which primarily promoted the dissolution of Cr from the alloy, resulting in greater specific mass losses.

2.5.6 Intergranular Corrosion

In this research, one of the main mechanisms of corrosion of interest is intergranular corrosion, which is described as the localised attack of alloying elements along grain boundaries, with minimal attack being observed within the grains themselves. In the case of many alloys, intergranular corrosion is caused by the precipitation of Cr-rich carbides at the grain boundaries, followed by the depletion of Cr from the regions around the carbide phases. The diffusion of Cr from the bulk is then too slow to replenish the Cr that has been depleted, resulting in intergranular corrosion [70]. This has been shown in recent studies that show correlations between mass losses of alloys immersed in molten fluoride salts with the Cr and C content of alloys [70].

Intergranular corrosion has been observed in many molten salt corrosion studies involving different materials, including carbon steels, stainless steels, and Ni-based alloys [41, 70, 71]. These studies have each shown preferential corrosion at the

grain boundaries of materials in molten salt environments, with the preferential dissolution of Cr from the grain boundaries being observed. Examples of intergranular corrosion of stainless steels and Ni-based alloys from the study by Olson et al. [70] are shown in Figure 2.9.

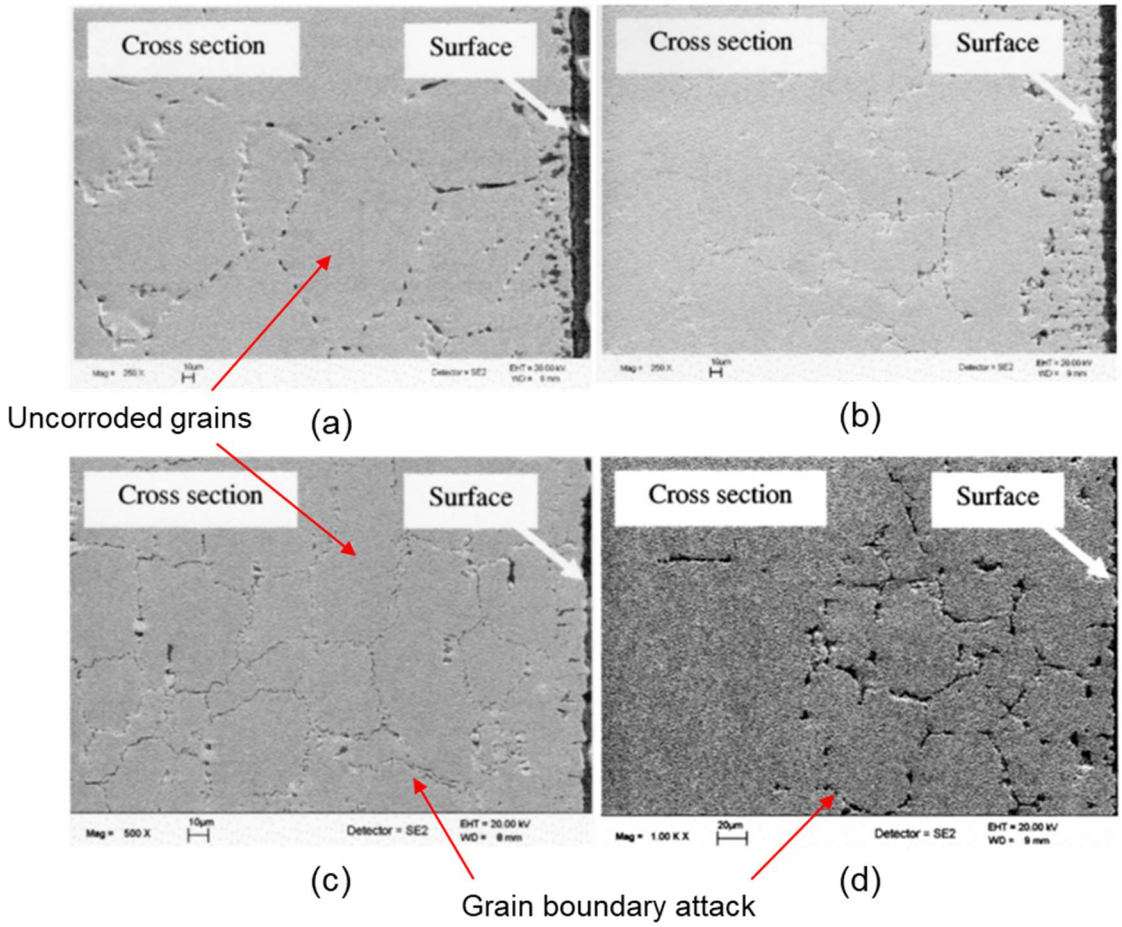


Figure 2.9 – Intergranular corrosion of stainless steels and Ni-based alloys in molten FLiNaK salt at 850 °C. Coupons of a) Incoloy 800H ,b) Inconel 617, c) Haynes-230 and d) Hastelloy X were immersed for a duration of 500 hours. Images taken from [70].

2.5.7 Material Dealloying

Dealloying of a material can be defined as the dissolution of less noble alloying elements from a metallic solid solution [72] resulting in a more porous structure of the more noble alloying elements [73]. Dealloying of more reactive alloying elements such as Cr and Fe has been reported in previous literature, in both chloride and fluoride molten salts, and has been shown to be detrimental to material performance in corrosive environments [74].

More recent studies have focused on developing a deeper understanding of the mechanisms of dealloying in molten salt environments, in particular investigating

the effect of temperature and alloy composition on the corrosion behaviour of alloys in molten salt environments [44, 73].

In such studies, the dealloying corrosion damage presents itself as large pores and ligaments in the dealloyed region [44]. These characteristics can commonly be identified by SEM analysis of the corroded regions. This analysis can be supported by EDX analysis to confirm the depletion of alloying elements. An example of these features, formed on coupons of a Ni – Fe alloy containing 62 wt.% Ni and 38 wt.% Fe after immersion in molten NaCl – KCl – $MgCl_2$ at 350 °C are presented in Figure 2.10.

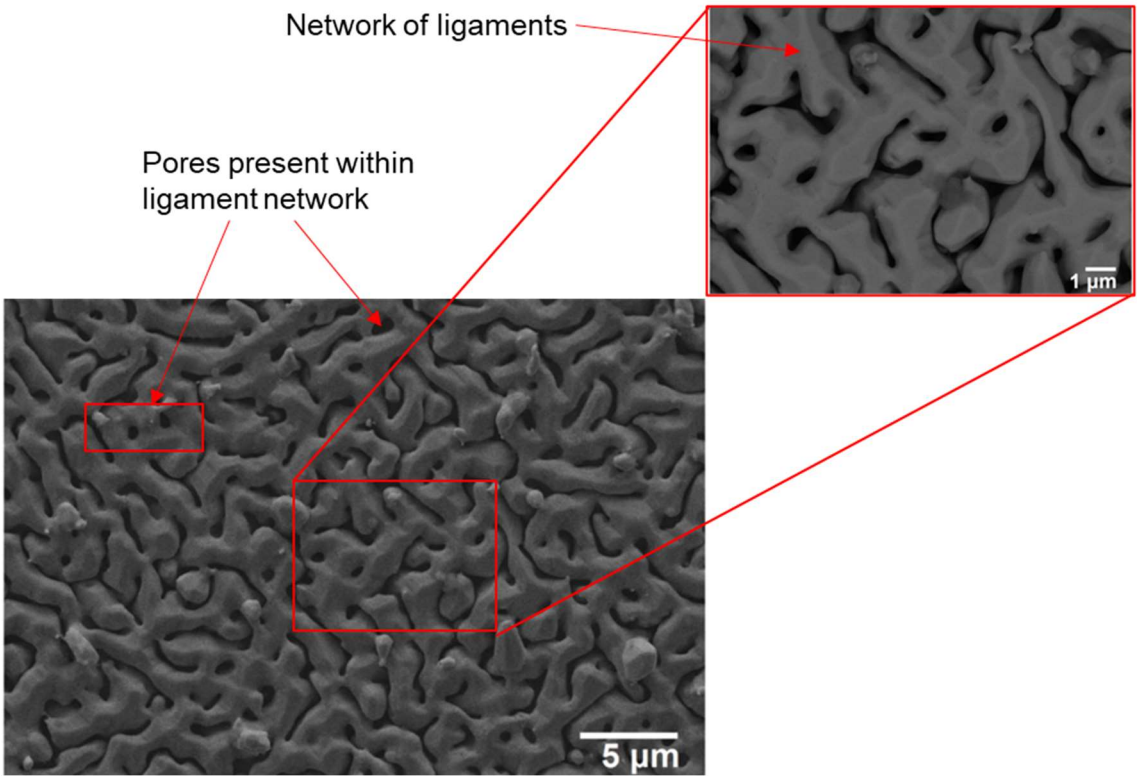


Figure 2.10 – Ligaments and pores formed at the substrate – molten salt interface of Ni62Fe38 alloy after exposure to NaCl – KCl – $MgCl_2$ molten salt at 350 °C. Figure adapted from [45].

2.6 Summary of literature review: The Generation – IV nuclear reactors and MSR development

In this section an overview of the Generation – IV nuclear reactors have been discussed, in particular the aims and objectives of the Generation – IV nuclear reactors. The focus of this section also focused on the MSR, its history and development as well as its future direction. This has included providing an overview of the current MSRs in development as well as material and HTF choices.

Through this literature review the aims of the Generation-IV nuclear reactors have been illustrated with the MSR being shown to be a particularly challenging design. The MSR has been estimated to have a high likelihood of achieving efficient energy generation although it's thought that its current technical feasibility is low due to issues regarding the transportation of corrosive and radioactive salts throughout each of the reactor circuits. This highlights the importance of understanding the corrosion mechanisms at play in a molten salt system so that methods of limiting or mitigating the corrosive and radioactive effect of these salts can be implemented.

The choice of salt will have a great impact on the MSR's technical feasibility. From this section it has been made clear that FLiBe molten salt has been very commonly used in both fuel and coolant salt applications. As discussed, no salt combination has previously been able to compete with its superior combined thermal and nuclear properties However, the emergence of new molten salt combinations such as FLiNaK allow for different salts to be used for coolant and fuel salt applications allowing for more suitable salts to be used to different MSR applications. Researching the corrosion behaviour of different materials, particularly metallic alloys, in FLiNaK molten salt is therefore of great importance in the development and eventual implementation of MSR technology for energy generation.

The role of neutron irradiation is an area of research that requires further investigation. The effect of such irradiation on graphite is known and has been shown to drastically reduce its longevity. However, the effect of irradiation on metallic alloys within MSR environments containing molten salt is not as well documented. Although research into this area has gained some traction in recent years, it remains an area that requires more dedicated research.

Therefore, the understanding of the effects of molten salt corrosion and irradiation are vital in improving the technical feasibility of the MSR. However, this research will primarily focus on using FLiNaK molten salt in corrosion studies and assessing the corrosion of materials within this environment.

Chapter 3 – Literature Review II

Molten Salt Corrosion and High Temperature Oxidation

3.1 Introduction

There are some major challenges associated with materials performance in MSR environments that require further research to develop a full understanding of the interactions between molten salts and materials. Without a comprehensive and robust understanding of material degradation mechanisms in molten salt environments, MSR development will be extremely challenging.

In general, the key areas that require further research and understanding are oxidation and molten salt corrosion of materials, as well as the impact of neutron irradiation on material performance. This section aims to outline the current understanding of oxidation, molten salt corrosion and neutron irradiation as well as their synergy in material degradation.

Due to the high operational temperature of the MSR, particularly within the reactor core and in heat exchanging circuits, and corrosive nature of the MSR environment, materials capable of operating under these conditions are required. Typically, materials used in these environments are high temperature corrosion resistant alloys such as stainless steels and Ni-based alloys. Hence, this study will focus on these material types. To develop a full understanding of the corrosion and oxidation behaviour of Ni-based alloys, this literature review will cover:

- The fundamentals of alloy oxidation including the thermodynamic fundamentals of alloy oxidation, the diffusion of alloying elements and how these factors relate to an alloy's oxidation kinetics.
- How oxidation fundamentals have been utilised in the predictive modelling of alloy oxidation and previous investigations into the oxidation of alloys in different environments.
- A discussion on molten salt corrosion of alloys, including the thermodynamic fundamentals, the factors influencing molten salt corrosion and previous studies investigating the corrosion behaviour of different alloys.
- An introduction to the methods of emulating the irradiation damage that may be introduced in material during MSR operation and the impact of irradiation on the corrosion behaviour of alloys.

3.2 Fundamentals of alloy oxidation

Due to the potential introduction of oxygen contaminants into the molten fluoride salts during plant operation, it is of vital importance to understand how alloys that may be used for molten salt applications oxidise in high temperature environments. This section aims to outline the theory of oxide formation and the driving forces behind oxidation. This will include discussion of current literature pertinent to the oxidation of materials.

3.2.1 Definition of oxidation

The oxidation of a metal or metal alloy is defined as the formation of an oxide layer on the metal surface at the interface between the air and the metal [75, 76]. According to Wagner's theory of oxidation, the high temperature oxidation of metallic alloys differs from the oxidation behaviour of pure metals [75, 76]. The differences in oxidation behaviour were summarised in two statements, the first being that the oxide layer composition formed on an alloy by the reactions of metallic elements with oxygen, will depend on the alloying elements mobility within the alloy and the formed oxide layer as well as each alloying elements affinity for oxygen. Based on the mobility of all alloying elements and their potential to form a metallic oxide, some regions of the formed oxide layer may become enriched with specific metallic oxides when compared with different regions of the same oxide layer.

The second difference is that the developed oxide layer may consist of several layers, composed of different oxide phases. This, again, can be attributed to the mobility of alloying elements within the alloy and the oxide layer. This phenomenon has been observed in literature for Ni-based alloys.

These oxidation processes differ from the oxidation of a pure metal where, typically, a single layer, monophase oxide is formed at the interface between the substrate material and the air. Further growth of this oxide scale is dictated by the diffusion of pure metallic ions to the oxide – air interface where they are able to react with O_2. The growth of such an oxide layer typically follows a parabolic rate law.

3.2.2 Thermodynamics of metal oxidation

For an oxide layer to form, it must be thermodynamically favourable for it to do so. This is achieved by determining the most stable state of the system, which, at a constant temperature and pressure, is done using the Gibbs free energy, which is expressed as:

$$\Delta G = H - TS \tag{3.1}$$

where ΔG is the Gibbs free energy change of the reaction, H the reaction enthalpy in units of J/kg, T the reaction temperature in K, and S the entropy of the reaction in units of J/K. Based on the value of the Gibbs free energy change of the reaction, the reaction may be thermodynamically favourable and occur spontaneously, where $\Delta G < 0$, in a state of equilibrium, where $\Delta G = 0$, or a thermodynamically impossible process, where $\Delta G > 0$ [77]. The thermodynamics of a reaction can also be used to determine key information regarding the kinetics of the chemical reaction [78].

By considering the oxidation of a metal to form a metallic oxide, the standard reaction described by equation 3.2 can be derived.

$$\frac{x}{y}M + \frac{1}{2}O_2 \xrightarrow{K} \frac{1}{y}M_xO_y \tag{3.2}$$

where M represents any metallic element, O represents an oxygen atom, and K represents the rate constant for the reaction. For the reaction described in equation 3.2, the Gibbs free energy change of the reaction can be defined as:

$$\Delta G = \Delta G^0 + RT \ln\left(\frac{a_{M_xO_y}^{1/y}}{a_M^{x/y} p_{O_2}^{1/2}}\right) \tag{3.3}$$

where ΔG^0 is the standard Gibbs free energy change of the reaction. The standard Gibbs free energy change is defined as the Gibbs free energy change of the reaction when all reactants and products are in their standard states. In equation 3.3, $a_{M_xO_y}^{1/y}$ and $a_M^{x/y}$ are the thermodynamic activities of the reactant and product species. In the case of metal oxidation, the activities of the reactants and products are measures of the effective concentrations of the species involved in the reaction. The standard Gibbs free energy change of the reaction presented in equation 3.2 can be expressed by:

$$\Delta G^0 = \frac{1}{y}\Delta G_{M_xO_y}^0 - \frac{x}{y}\Delta G_M^0 - \frac{1}{2}\Delta G_{O_2}^0 \tag{3.4}$$

In the case where ΔG is equal to zero i.e., the system is considered to be in chemical equilibrium, hence, the value of ΔG^0 can be expressed as:

$$\Delta G^0 = -RT \ln\left(\frac{a_{M_xO_y}^{1/y}}{a_M^{x/y} p_{O_2}^{1/2}}\right)_{eq} \tag{3.5}$$

From equation 3.5, the rate of the oxidation reaction, denoted as K in equation 3.2 can be calculated. The rate of a chemical reaction can be given as:

$$K = \frac{a_{M_xO_y}^{1/y}}{a_M^{x/y} p_{O_2}^{1/2}} \quad \textbf{3.6}$$

Therefore, equation 3.5 can be rewritten as:

$$\Delta G^0 = -RT \ln(K) \quad \textbf{3.7}$$

Therefore, the rate of the oxidation reactions for a pure metal can be expressed as:

$$K = \exp\left(-\frac{\Delta G^0}{RT}\right) \quad \textbf{3.8}$$

In the case of a base metal becoming a metallic oxide, it can be assumed that the thermodynamic activity of the metal and oxide are equal to unity. This is based on the assumption that both the metal and oxide are immiscible solids [77]. Therefore equation 3.8 can also be written as:

$$K = \exp\left(-\frac{\Delta G^0}{RT}\right) = \frac{1}{p_{O_2}^{1/2}} \quad \textbf{3.9}$$

where p_{O_2} is the dissociation pressure of the oxide which is defined as the pressure of the gas in equilibrium with the metallic oxide [78]. Consider the reaction of Ni with 1 mol of O_2 to form NiO shown as equation 3.10:

$$2Ni + O_2 \xrightarrow{} 2NiO \quad \textbf{3.10}$$

The standard Gibbs free energy change of this reaction can be given by the equation [77]:

$$\Delta G^0 = -468690 + 168.6T \quad \textbf{3.11}$$

where T is the oxidation temperature in K. At a temperature of 700 °C, the value of ΔG^0 is equal to -304616.91 J/mol which, using equation 3.9, can be used to calculate the equilibrium constant for the reaction. Alongside the equilibrium constant, the dissociation pressure of the oxide can also be calculated. These values are calculated to be 2.24×10^{16} mol/L and 1.99×10^{-33} atm respectively. At 1.99×10^{-33} atm of O_2, Ni and NiO exist in equilibrium. However, when the partial pressure of O_2 is less than this, Ni would not oxidise. The converse can be said at O_2 partial pressures greater than, where NiO would form readily.

3.2.3 Thermodynamics of alloy oxidation

Due to the presence of additional metallic elements within a metal alloy, the oxidation of alloys is much more complex than that of pure metals. Instead of there

being contributions from only one metallic component, alloy oxidation must consider contributions from all metallic alloying elements present within the alloy. This includes considering the equilibrium reactions between the alloy and oxides that have formed during the oxidation process [78].

Thermodynamic analysis of alloys can be broken down further into considering binary alloys and more complex multicomponent alloys. In a binary alloy that reacts with O_2, the formation of one oxide is likely to be more favourable than the other. According to Wallwork [75] the oxidation of an alloy can result in either the formation of an oxygen – solid solution or the formation of simple or multiphase oxides. In this case of a binary alloy, this will depend on the nobility of the alloying elements and the quantities of each alloying elements within the alloy.

However, upon formation of an oxide layer, the binary system becomes a ternary system. The ternary system exists between the two alloy constituents and the oxide layer. In order to understand this ternary system, equilibrium equations between the substrate material and the formed oxides needs to be understood. Such reactions can be expressed as competing oxide reactions, for example, in a Fe – Ni binary alloy may have a reaction as illustrated by equation 3.12:

$$Ni + FeO \rightarrow NiO + Fe \qquad \textbf{3.12}$$

The standard Gibbs free energy change of this reaction can be expressed as the difference between the standard Gibbs free energy changes for the formation of NiO and the dissociation of FeO:

$$\Delta G^0 = \Delta G^0(NiO) - \Delta G^0(FeO) \qquad \textbf{3.13}$$

However, this will not be the only equilibrium reaction taking place as the concentrations of Ni and Fe within the alloy, alongside the partial pressure of O_2 will dictate the metallic oxides formed during oxidation. To characterise the phases formed phase diagrams are commonly used. A phase diagram shows the potential phases formed at a constant temperature based on the concentrations of alloying elements and oxygen present [77]. At a temperature of 1000 ºC, Rhamdhani et al. [79] developed a ternary phase diagram for the Fe-Ni-O system. The result is presented as Figure 3.1.

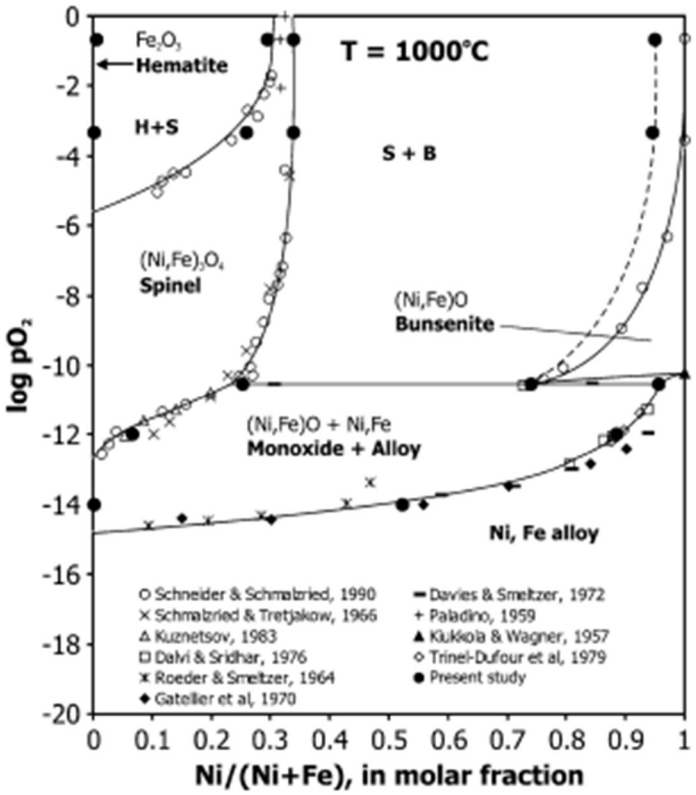


Figure 3.1 – Ternary phase diagram for Fe-Ni-O system showing phases formed at different partial pressures of O_2 and molar fractions of Ni [79]. Result shows regions where oxide formation is possible, and the oxides formed.

When considering more complex alloys, such as a ternary alloy, in contact with an oxidant, a quaternary system is formed, meaning numerous different phase diagrams would have to be used to determine the composition of the oxide layer. This was illustrated by Shen et al. [80] who proposed that for a ternary alloy of arbitrary metallic elements A-B-C, phase diagrams for the A-B-O, A-C-O and B-C-O systems would all need to be considered, as shown in Figure 3.2.

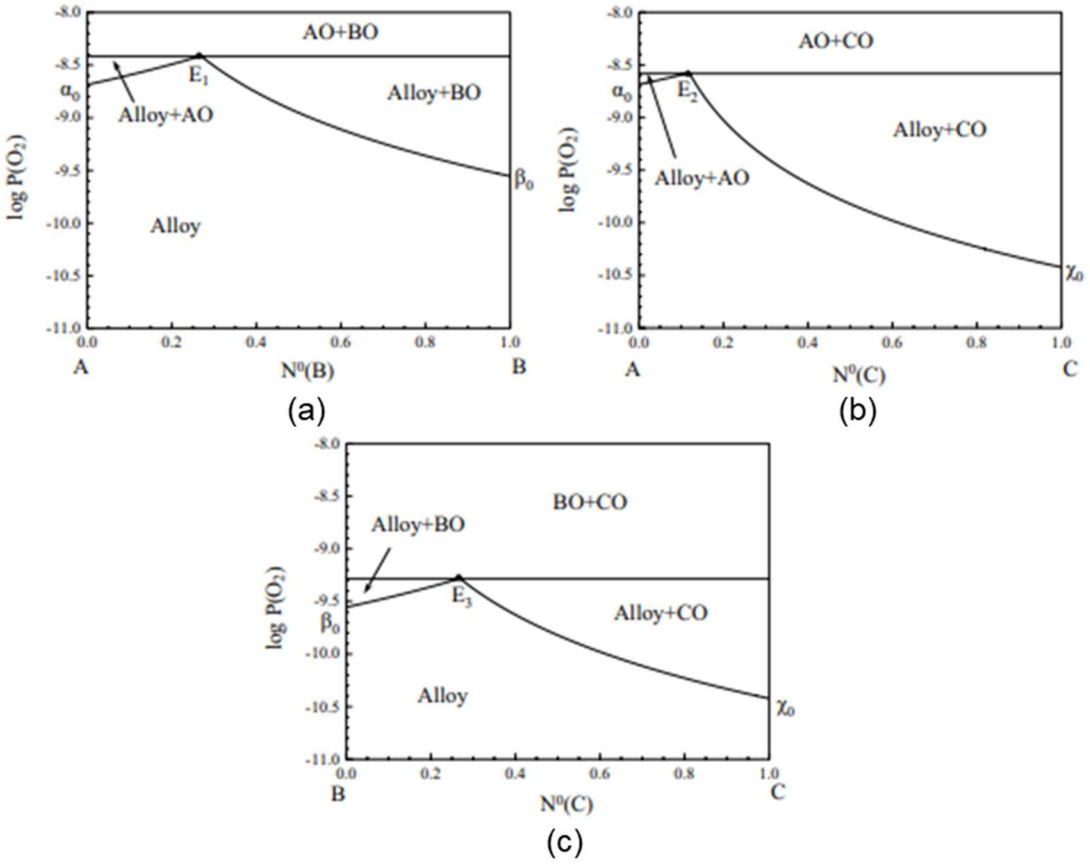


Figure 3.2 – Phase diagrams for a) A-B-O, b) A-C-O and c) B-C-O ternary systems for an alloy A-B-C in contact with a single oxidant, adapted from [80].

By considering each individual system of the arbitrary alloy, with constituents A-B-C, in contact with an oxidant, as shown in Figure 3.2, an overall understanding of the system of metallic oxides present within the oxide layer can be established.

3.2.4 Diffusion of alloying elements

Within an alloy, many alloying elements exist, each of which is able to move within the substrate material. Generally, movement of alloying elements occurs by solid state diffusion from a region of high concentration to an area of low concentration. In the case of a coupon of an alloy material, elements will diffuse from the bulk material to the material – air interface due to the lower concentrations of alloying elements at this interface. Reactions at the material – air interface are then driven by the thermodynamics of each reaction, as well as the diffusion of species to the interface. The diffusion of each alloying element can be characterised by a diffusion coefficient, often denoted as D. The diffusion coefficient for alloying elements may differ based on the element, but also the type of material, for example, Cr diffuses

faster in an Ni-matrix, such as a Ni-based alloy, when compared with its diffusion in a Fe-matrix, such as that of a stainless steel [81, 82].

3.2.4.1 Diffusion within the alloy substrate

Diffusion of alloying elements during alloy oxidation is a complex phenomenon, particularly in multicomponent alloys with many alloying elements able to diffuse to the substrate – air interface, react with O_2 and form metallic oxides. To develop the complexity of the model, Wagner [75, 76] initially considered a binary alloy consisting of metallic elements A and B, in which only element A is able to form a metallic oxide. Within the metal alloy, the transport of element A per unit area and in one dimension can be given by Fick's first law of diffusion:

$$J_A = -D\frac{\partial C_A}{\partial x} \qquad \textbf{3.14}$$

where J is the diffusion flux in units of mol/cm^2/s, D is the interdiffusion coefficient of the alloy in units of cm^2/s, C_A is the concentration of alloying element A in units of mol/cm^3 and x is the diffusion distance in cm. The interdiffusion coefficient can be expressed in the form of the Arrhenius equation, presented as equation 3.15

$$D = D_0 e^{-\frac{Q}{RT}} \qquad \textbf{3.15}$$

where D_0 is the pre-exponential constant with units of cm^2/s, Q is the activation energy of the reaction in units of kJ/mol, R the Universal gas constant with a value of 8.3145 J/mol/K and T the temperature in units of K.

In an ideal metallic solution, the activity of alloying element A, defined as the effective concentration of a species within a mixture, is equal to the molar fraction of the same element in the alloy, denoted by N_A and the concentration of element multiplied by molar volume, denoted as V_A, as shown in equation 3.16:

$$a_A = N_A = C_A V_A \qquad \textbf{3.16}$$

This result means that the transport of element A can also be expressed as a function of the activity of element A by equation 3.17:

$$J_A = -\frac{D}{V}\frac{\partial a_A}{\partial x} \qquad \textbf{3.17}$$

Based on this result, Fick's second law of diffusion can be presented as:

$$\frac{\partial C_A}{dt} = D\frac{\partial^2 C_A}{\partial x^2} = \frac{D}{V}\frac{\partial^2 a_A}{\partial x^2} \qquad \textbf{3.18}$$

For a multicomponent system with many alloying elements, such as Ni-based alloys, all with the potential to form metallic oxides, adaptations need to be made

to the diffusion equations presented as equations 3.14 - 3.18. Firstly, the total element flux needs to be defined as a summation of the flux of each element present within the alloy. This is achieved as shown in equation 3.19:

$$J_i = -\sum_{j=1}^{n-1} D_{ij}^{n} \frac{\partial C_j}{\partial x} \qquad \textbf{3.19}$$

where J_i is the flux of element i, D_{ij}^{n} is the interdiffusion coefficient of diffusion elements i and j in the solute n. In the case of a Ni-based alloy, the interdiffusion coefficient for each element is for each element in a Ni-matrix. Based on equation 3.19, Fick's second law of diffusion can be expressed in a similar form as shown in equation 3.20:

$$\frac{\partial C_i}{\partial t} = \sum_{j=1}^{n-1} D_{ij}^{n} \frac{\partial^2 C_j}{\partial x^2} \qquad \textbf{3.20}$$

3.2.4.2 Diffusion in the oxide layer

In the case of the oxide layer, the diffusion characteristics of alloying elements can be different when compared with their behaviour in the metallic alloy. Within the oxide layer, diffusion is accomplished by metallic cations and electrons as shown in Figure 3.3.

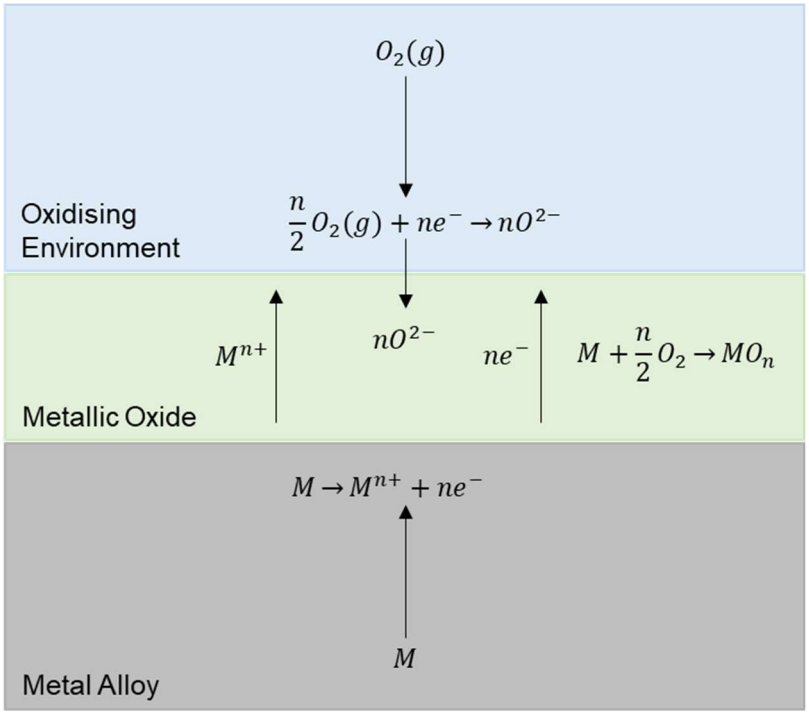


Figure 3.3 – Image showing diffusion and transport processes involved in the oxidation of alloys which include the diffusion of ions to the substrate – air interface and their subsequent reactions to form a metallic oxide layer [77, 83]. At later time intervals, species are shown to diffuse across the oxide layer to the oxide – air interface to continue oxide layer formation.

Considering again a binary alloy containing alloying elements A and B, the transport of element A can be given by the equation:

$$J'_A = -D'C'_A\left(\frac{\partial \ln(a_A)}{\partial x}\right) + u_x C'_A \qquad \textbf{3.21}$$

where D' is the self-diffusion coefficient of element A within the oxide layer, C'_A is the concentration of element A within the oxide layer, a_A is the activity of element A and u_x is the velocity of the oxide toward the bulk alloy due to the recession of the alloy – oxide interface [77]. The change in concentration with respect to time can therefore be expressed as:

$$\frac{\partial C'_A}{\partial t} = -D'C'_A\left(\frac{\partial^2 a'_A}{\partial x^2}\right) \qquad \textbf{3.22}$$

3.2.5 Rates of oxide growth and their governance

Depending on the mechanism by which oxide growth is controlled, different rates of oxide growth can occur. Generally, the oxidation rate of an alloy can be expressed as a function of time as shown in equation 3.23:

$$\frac{dX}{dt} = f(t) \quad \textbf{3.23}$$

where X is the oxide thickness, and t the oxidation time. When considering the rate of oxide growth, two types of reactions occur, those within the oxide layer, and those outside the oxide layer.

When considering the reactions and transport processes, shown previously in Figure 3.3, the redox reactions occur at the interface, dominating the oxidation process and forming an oxide layer. This is typically the case at extremely elevated temperatures, in excess of 1000 °C, where volatilisation of any formed oxides may occur, and no diffusion barrier exists between the species in the substrate material and air [84]. When this is the case, linear oxidation kinetics are observed, which can be expressed as:

$$\frac{dX}{dt} = K_L \quad \textbf{3.24}$$

which can be integrated to show that:

$$X = K_L t \quad \textbf{3.25}$$

where K_L is the linear oxidation rate constant, and t is the oxidation time. In the case of linear oxidation kinetics, the electrochemical reactions taking place at the alloy – air interface control the oxidation kinetics, i.e., the oxidation of alloying elements to metal ions and the reduction of oxygen gas to oxide ions which subsequently react to create the metal oxide. To continuously achieve a linear growth law, the source of metallic ions at the substrate – air interface needs to be replenished. This is achieved by diffusion of metallic ions within the substrate material, as described in Section 3.2.4.1, to the substrate – air interface where they are able to react with O_2.

However, the oxidation kinetics can also be controlled by the diffusion of species, through a formed oxide layer to the air – oxide interface. This is typically achieved at temperatures less than 1000 °C where volatilisation of the formed oxides is more unlikely to occur. Under these conditions, parabolic oxidation kinetics are observed, which can be expressed as:

$$\frac{dX}{dt} = \frac{K_P}{X} \quad \textbf{3.26}$$

Which when integrated gives the following:

$$X^2 = 2K_P t \quad \textbf{3.27}$$

where K_P is the parabolic rate constant. In a case such as parabolic oxidation kinetics, the rate of oxide growth is dependent on the thickness of the oxide layer. Metallic ions must initially diffuse from the substrate to the substrate – oxide interface and then through the oxide layer to the oxide – air interface. Due to the increasing thickness of the oxide layer, the size of the diffusion barrier is increased, resulting in more time taken for alloying elements to travel to the oxide – air interface, resulting in a gradual reduction in the oxidation rate over time. Parabolic oxidation kinetics can also be classified as being sub-parabolic oxidation which follows the relationship shown in equation 3.28 where n is the oxidation exponent that takes a value less than 0.5.

$$X = K.t^n \quad \textbf{3.28}$$

In many cases, it is possible for the early stages of oxidation to be controlled by linear type oxidation kinetics, and later stages to be controlled by parabolic oxidation kinetics. This occurs when the reactions occurring at the substrate – air interface initially dominate the reaction before a non-porous oxide layer is formed. Following the formation of a non-porous oxide layer, the process of oxidation must now be controlled by the diffusion of elements to the oxide – air interface, ultimately resulting in parabolic oxidation kinetics. This type of oxidation kinetics is therefore expressed using square and linear terms for the oxide thickness. The general expression is presented as equation 3.29:

$$X^2 + LX = Kt + c \quad \textbf{3.29}$$

where L and c are constants. The oxidation kinetics described throughout this section are depicted in Figure 3.4.

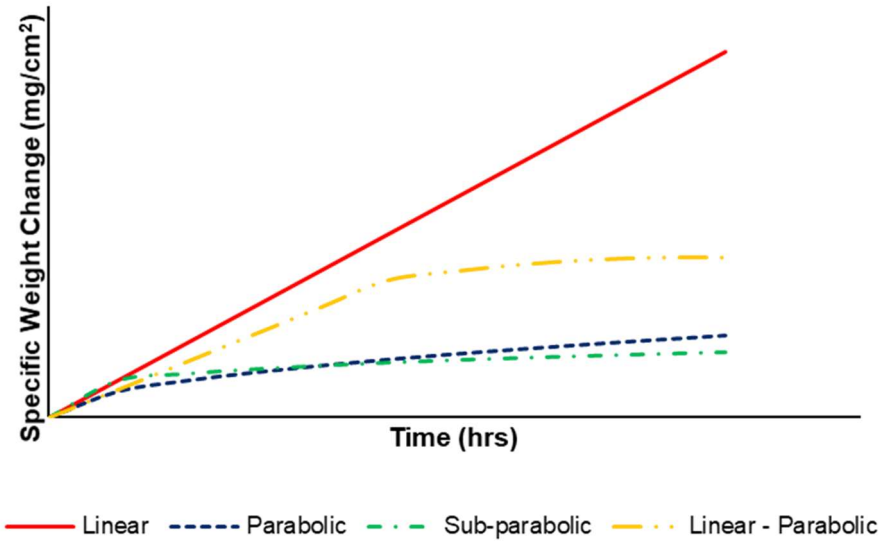


Figure 3.4 – Figure detailing the types of oxidation kinetics discussed in this section, showing linear, parabolic, sub-parabolic and linear-parabolic types of oxidation kinetics.

Pure Ni is an example of a metal which follows sub – parabolic and parabolic oxidation kinetics, depending on the temperature at which oxidation is taking place. A study by Haugsrud [85] investigated the effect of temperature on the oxidation kinetics of high – purity Ni by taking thermogravimetric measurements of Ni coupons at temperatures ranging from 500 to 1300 °C. At temperatures of 500 °C, 600 °C and in excess of 1100 °C, parabolic oxidation kinetics were observed. However, in the range of 700 – 1000 °C, sub – parabolic oxidation kinetics were observed for high – purity Ni. A comparison between the oxidation kinetics at 800 °C and 1300 °C is presented in Figure 3.5 which illustrates a linear relationship between the specific mass change and the square root of time at 1300 °C which is indicative of parabolic oxidation kinetics. At 800 °C a non-linear relationship was observed; hence the oxidation kinetics cannot be classified as parabolic.

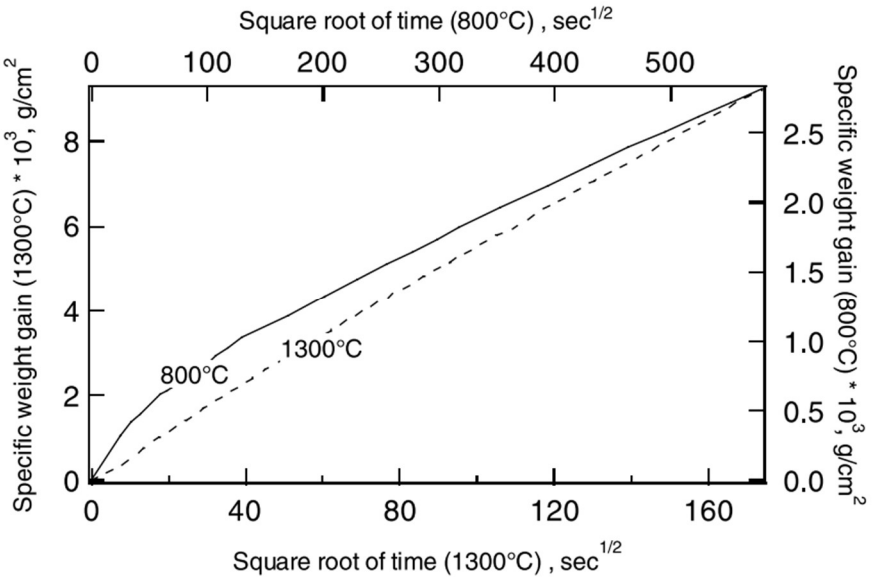


Figure 3.5 – Comparison of the oxidation kinetics of Ni at 800 °C and 1300 °C, illustrating a linear relationship between the specific mass change and the square root of time at 1300 °C, from which, parabolic oxidation kinetics can be concluded. Image taken from [85].

The difference in the oxidation kinetics at different temperatures was discussed, with the diffusion behaviour of O_2 in the NiO layer being cited as the main reason for the difference in kinetics. Within the temperature range of 700 – 1000 °C, O_2 is assumed to penetrate the oxide scale as a gaseous species, resulting in the internal oxidation of Ni. As a result of this internal oxidation, Ni was not diffusing to the oxide – air interface and hence parabolic oxidation kinetics were not observed.

High temperature isothermal oxidation studies have also been conducted on high purity Cr, which showed that Cr exhibited parabolic oxidation kinetics. In the research of Mortimer and Post [86], high purity Cr was oxidised at temperatures between 650 °C and 950 °C, with thermogravimetric results showing that Cr followed parabolic oxidation kinetics within this temperature range. Mortimer and Post [86] discussed that the process of Cr oxidation was controlled by the diffusion of Cr across a Cr_2O_3 layer to the oxide – air interface, which is consistent with the mechanism associated with parabolic oxidation kinetics.

3.3 Thermodynamic concepts used in predictive modelling

It has been discussed throughout this section that the oxidation behaviour of alloys is highly dependent on the favourability of the reactions taking place and the diffusion of alloying elements to the oxidation interface, whether this be at the alloy – air or oxide – air interfaces. When developing predictive models, it is important to combine oxidation chemical reactions with thermodynamic theory discussed

throughout this chapter, to establish an accurate modelling methodology for oxidation prediction.

One such model is that developed by Sato et al. [87], who developed an empirical model to predict the oxidation behaviour of the Ni-based alloy SCA425+ and Rene N5 at temperatures in excess of 900 °C [87, 88]. In predictive modelling, empirical models can be very useful tools, utilising experimental data to infer relationships between key parameters. However, due to the use of experimental data, empirical models can often be volatile, with results varying depending on the data used to determine relationships [89]. It's therefore critically important to use a robust data set with a strong correlation.

The empirical model developed by Sato et al. [87] was also deployed by Bensch et al. [88] to predict the oxidation behaviour of alumina forming Ni-based alloys. The underlying theory of the empirical model was based on the oxidation of an alloying element, M, within an alloy, forming a metal oxide of the form M_xO_y by the reaction defined by equation 3.30:

$$\left(\frac{2x}{y}\right)M + O_2 \overset{K_p}{\Rightarrow} \left(\frac{2}{y}\right)M_xO_y \qquad \textbf{3.30}$$

where K_P is the parabolic rate constant for the reactions and can be expressed according to Wagner's theory of oxidation as:

$$K_p = -\frac{\sigma_t t_{ion} t_{el}}{{z_c}^2 {z_a}^2 e^2}\Delta G_f \qquad \textbf{3.31}$$

where σ_t represents the conductivity of the oxide, t represents the transport numbers of ionic species and electrons respectively, z represents the metal and oxygen valences, e is the elementary charge and ΔG_f the Gibbs free energy of formation of the metal oxide. Based on the oxidation theory discussed previously, the Gibbs free energy of formation of the oxide can be expressed in terms of the activity of the metallic oxide and the metallic ions.

In the original study by Sato et al. [87], the growth of alumina (Al_2O_3) was investigated. As such, it was assumed that Al_2O_3 acted as an n-type semiconductor i.e. an oxide with an excess of electrons that can be donated. The assumption of Al_2O_3 as a n-type semiconductor was made due to the oxidation kinetics of Al_2O_3 scales at temperatures in excess of 900 °C of interest to Sato et al. [87]. A study by Pint et al. [90] showed that at 900 °C, θ – Al_2O_3 formed as opposed to the more stable α – Al_2O_3 by the outward diffusion of cations to the substrate – air interface. θ – Al_2O_3 is considered to be a conductor of electrons, hence, the assumption of Al_2O_3 as an n-type semiconductor. This assumption allows for t_{el} to take a value equal to unity. Hence equation 3.31 can be written as:

$$K_p = -\frac{\sigma_t t_{ion}}{{z_c}^2 {z_a}^2 e^2} \Delta G_f \quad \textbf{3.32}$$

By expressing the value of t_{ion} as the summation of the transport numbers of anions and cations, equation 3.32 can be written as:

$$K_p = -\frac{\sigma_t (t_a + t_c)}{{z_c}^2 {z_a}^2 e^2} \Delta G_f \quad \textbf{3.33}$$

where t_a and t_c are the transport numbers of the anions and cations, respectively. In the case of an n-type semiconductor, the transport number of the anions is much greater than that of the cations, hence the conductivity of the anions dominates the oxidation process. This means that K_P can be written only in terms of the anion conductivity, as shown in equation 3.34:

$$K_p = -\frac{\sigma_a}{{z_c}^2 {z_a}^2 e^2} \Delta G_f \quad \textbf{3.34}$$

where σ_a is the conductivity of anions through the oxide layer. According to the Nernst – Einstein relation, the conductivity of the anions can be expressed as:

$$\sigma_o = \frac{D_o {z_a}^2 F^2 c_o}{RT} \quad \textbf{3.35}$$

where D_0 is the diffusion coefficient of the anion through the oxide layer. In the case of the oxidation of a metallic ion to a metallic oxide, the anion is the oxide ion (O^{2-}). In equation 3.35, c_0 represents the concentration of oxygen in the oxide layer and F represents Faraday's constant (96485.33 C/mol). Combining and simplifying equations 3.34 and 3.35 gives the following equation:

$$K_p = -\frac{D_o F^2 c_o}{RT {z_c}^2 e^2} \Delta G_f \quad \textbf{3.36}$$

which can be simplified further to equation 3.37:

$$K_p = -\frac{D_o c_o}{{z_c}^2 kT} \Delta G_f \quad \textbf{3.37}$$

where k is the Boltzmann constant (1.380649 x10^{-23} $m^2 kgs^{-2} K^{-1}$). It can be assumed that the dominant defect within the oxide scale is a double charged oxide ion (O^{2-}), it follows that:

$$K_p = -\frac{D_{V_{\ddot{O}}} V_{\ddot{O}}}{{z_c}^2 kT} \Delta G_f \quad \textbf{3.38}$$

Where $D_{V_{\ddot{O}}}$ represented the diffusion coefficient of a doubly charged oxygen ion and $V_{\ddot{O}}$ represents the concentration of doubly charged oxygen ions in the oxide. Therefore, it can be inferred that K_P is proportional to the oxygen concentration and the Gibbs free energy of formation of the oxide.

$$K_p \ \alpha \ V_{\ddot{O}} \Delta G_f \quad \textbf{3.39}$$

If we consider an impurity in the oxide scale, a chemical equation can be written to define the presence of this impurity within the oxide. For example, consider that Ni is the main impurity in a Al_2O_3 scale. It can be said that:

$$se' + sNiO + \frac{1}{2}O_2 \overset{\square}{\leftrightarrow} sNi_{Al'} + 3O_o \quad \textbf{3.40}$$

So that s mol of electrons are reduced. To maintain charge neutrality, the following reaction must occur:

$$sNiO + \frac{1}{2}O_2 \overset{\square}{\leftrightarrow} sNi_{Al'} + 3O_o + \frac{s}{2}V_{\ddot{O}} \quad \textbf{3.41}$$

Based on this, it can be said that the reduction of s mol of Ni^{2+} can be related to production of $s/2$ mol of $V_{\ddot{O}}$ i.e. that the change in electron concentration is proportional to the concentration of doubly charged oxygen vacancies, or:

$$\Delta e' \ \alpha \ V_{\ddot{O}} \quad \textbf{3.42}$$

where $\Delta e'$ is the net electron concentration change within the oxide scale. This can be extended to include other oxide impurities. Consider s mol of NiO, t/2 mol of Cr_2O_3 and u/2 mol of Ta_2O_5 impurities in an Al_2O_3 scale, applying the same charge neutrality equation as before, it can be written that:

$$sNiO + \frac{t}{2}Cr_2O_3 + \frac{u}{2}Ta_2O_5 \overset{\square}{\leftrightarrow} sNi_{Al'} + tCr_{Al} + uTa_{\ddot{A}l} + (-s + 2u)e' + \frac{3(s+t+u)}{2}O_o + \left(-\frac{s}{4} + \frac{u}{2}\right)O_2 \quad \textbf{3.43}$$

In equation 3.43, the net electron concentration change can be given by:

$$\Delta e' = -s + 2u \quad \textbf{3.44}$$

Where –s and 2u were determined by subtracting the valence of Al from the valence of Ni and Ta respectively. Hence, the total effective valence, Val^{eff}, can be written as:

$$Val^{eff} = \sum_{i=1}^{n} [(z_i - z_{Al}).x_i] \quad \textbf{3.45}$$

Where x_i is the atomic fraction of element i in the oxide scale. Based on equations 3.39, 3.42 and 3.45, the following relationship for K_P can be determined:

$$K_P \ \alpha \sum_{i=1}^{n} [(z_i - z_{Al}).x_i] \, . \, \Delta G_{f,Al_2O_3} \quad \textbf{3.46}$$

By defining this calculation as its own parameter, a relationship between K_P and the parameter can later be determined. This parameter will be denoted as the kinetic factor, U in units of kJ/mol, and will be expressed as:

$$U = \sum_{i=1}^{n} [(z_i - z_{Al}).x_i] \, \Delta G_{f,Al_2O_3} \quad \textbf{3.47}$$

To complete the empirical model, a relationship between U and K_P was defined. Similarly, to the diffusion coefficient equation presented as equation 3.15, the parabolic rate constant is dependent on the temperature and therefore can be presented in the form of the Arrhenius equation, which takes the form of:

$$K_P = K_0 e^{-\frac{Q}{RT}} \quad \textbf{3.48}$$

where K_0 is the pre-exponential constant in units of kJ/mol, Q the activation energy of the reaction taking place in units of kJ/mol, R the Universal gas constant with a value of 8.3145 J/K/mol and T the test temperature in units of K. Based on this general form, the relationship between K_P and U was defined by:

$$K_P = Ae^{bU} \quad \textbf{3.49}$$

where A and b are constants that can be determined from experimentally derived data. This was achieved by writing equation 3.49 in the form of a linear equation and plotting the natural logarithm of K_P against U, with the resulting equation being used to predict the oxide layer thickness.

When Bensch et al. [88] utilised this model in the prediction of the oxidation behaviour of Rene N5 and SCA425+ Ni-based alloys, results showed an overprediction of the Al_2O_3 layer thickness formed on the Rene N5 alloy. When examining the result for SCA425+, the prediction was validated against a single data point, taken after 100 hours of exposure, therefore, this result is hard to validate without additional data points over the full time period. The overprediction of the oxidation of Rene N5 may partly be due to the data used to develop the empirical relationship defined in equation 3.49. In this case, four data points are used to develop the relationship between K_P and U at 900 °C. A summary of the data used to develop the relationship between K_P and U at 900 °C is shown in Figure 3.6.

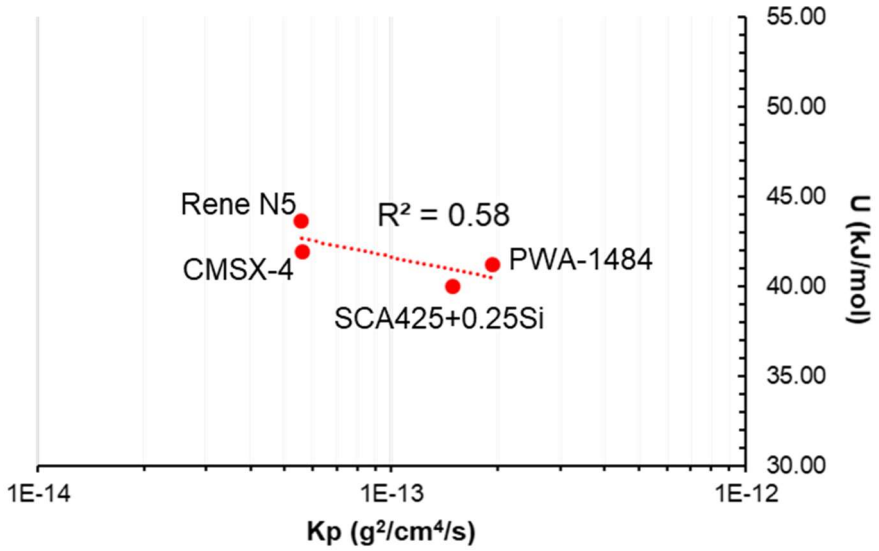


Figure 3.6 – Graph of U for Al_2O_3 formation against K_p values, obtained for alloys of Rene N5, SCA425+0.25Si, CMSX-4 and PWA-1484 alloys at 900 °C. Mathematical analysis indicates an R^2 of 0.58, indicating very little correlation between data points used to develop empirical relationship [87, 88, 91].

Mathematical analysis conducted on the data set utilised by Bensch et al. [88], presented in Figure 3.6, shows very little correlation within the data set, with a regression value of 0.58 being calculated. This suggests that the use of this data to build a robust predictive model may be inappropriate. Within the same research by Bensch et al. [88], a similar number of data points were utilised to develop a relationship between U and K_P and predict the oxidation behaviour of alloys at 1000 ºC. However, the data points used to develop a prediction at 1000 °C were observed to show a greater correlation when compared with the data presented in Figure 3.6 for predictions at 900 °C.

To capture the full extent of the oxidation behaviour of Ni-based alloys in high temperature environments the diffusion characteristics of alloying elements can also be considered. In the case of the oxidation of alloys, the diffusion of alloying elements to the substrate – air interface and the diffusion of elements to the oxide – air interface are also important factors in developing a compete and robust understanding.

In an expansion to the original model by Sato et al. [87], Bensch et al. [88] developed a substrate response model that was designed to predict the microstructural changes of the Ni-based alloy substrate during their oxidation [88]. The substrate response model was designed to predict the fractions of each microstructural phase present in the substrate material after oxidation. This was

achieved by considering the diffusion of elements within the substrate material, the oxidation of the material occurring at the substrate – air interface and the thermodynamics of oxidation of the Ni-based alloys being tested. The results of the substrate response model showed good agreement with experimental measurements of the phases presented, measured using a quadrant back scattering detector (QBSD) in a scanning electron microscope. The QBSD allows for the generation of a diffraction pattern which can then be used to identify the phases present within the microstructure of the material [92].

Modelling studies considering the microstructural evolution of Ni-based alloys during oxidation have also been undertaken by Karunaratne et al. [93]. A finite difference method was deployed by Karunaratne et al. [93] to predict the elemental distribution of the CMSX-4 Ni-based alloy in air between temperatures of 850 and 1050 ºC. The finite difference method involved the discretisation of Fick's first and second laws of diffusion, presented as equations 3.14 and 3.18. The discretised finite element approximations of Fick's first and second laws were developed from a Taylor's series expansion. For the finite element approximations to be used, a nodal structure needs to be applied to the geometry over which the equations are being solved. An example of the applied nodal structure is presented as Figure 3.7.

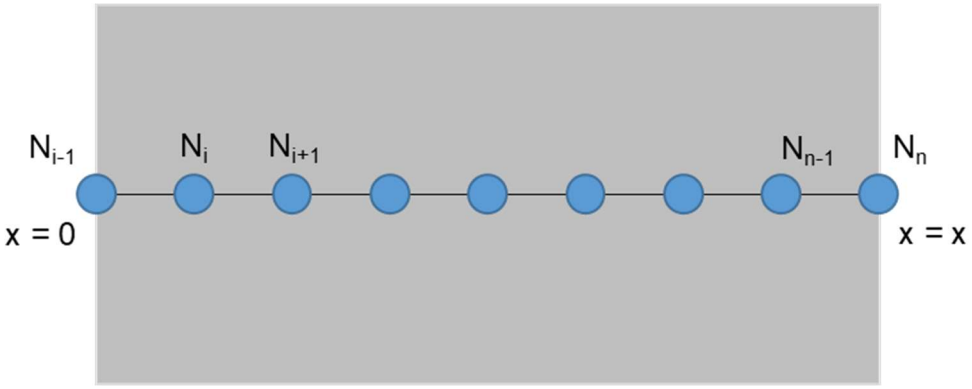


Figure 3.7 - Illustration of a nodal structure applied to the geometry over which the concentration of alloying elements in a metallic alloy is being solved.

Based on the nodal structure applied to the geometry being solved, the first and second derivatives of the element concentration with respect to the diffusion distance can be presented as shown in equations 3.50 and 3.51.

$$\frac{\partial C_i}{dx} = \frac{C^i_{J,N+1} - C^i_{J,N-1}}{2\Delta X} \qquad \textbf{3.50}$$

$$\frac{\partial^2 C_i}{dx^2} = \frac{C^i_{J,N+1} - 2C^i_{J,N} + C^i_{J,N-1}}{\Delta X^2} \qquad \textbf{3.51}$$

where i refers to the diffusing element, N refers to the node number and the subscript j represents the current iteration at a given time interval t. In order to formulate Fick's second law of diffusion, the concentration change with respect to time also needs to be expressed with regards to the nodal structure presented in Figure 3.7. This equation is presented as:

$$\frac{\partial C_i}{dt} = \frac{C^i_{J+1,N} - C^i_{J,N}}{\Delta t} \quad \textbf{3.52}$$

Based on these finite difference equations the elemental concentration profiles of alloying elements can be predicted based on the interdiffusion coefficients of each alloying element in a Ni solute. To calculate the diffusion coefficient of each alloying element, present in the CSMX-4 alloy, a linear form of equation 3.15 was developed, as shown in equation 3.53:

$$\ln(D) = \ln(D_0) - \frac{Q}{RT} \quad \textbf{3.53}$$

Karunaratne et al. [93] then developed empirical relationships between the natural logarithm of D_0 and alloying element concentration, as well as Q and the alloying element concentration, with the relationships taking the form of a third order polynomial expression. Based on the literature data and the expressions devised by Karunaratne et al. [93], the diffusion coefficients for each alloying element were calculated. Based on this model, the elemental profiles for each alloying element were predicted at a temperature of 850 °C for time intervals of 0, 190, 1000, 2000 and 10000 hours. The predicted results were compared to EDX analysis conducted on oxidised samples after 190 hours of exposure to a dry air environment at temperatures of 850 and 950 °C and 10000 hours of exposure at 1050 °C. A comparison of the experimental and predicted concentration profiles show good agreement between experimental and predicted results at temperature of 850 and 950 °C, however, larger discrepancies were observed at 1050 °C. This may be due to the data collected when developing empirical relationships for the diffusion coefficients. Many of the studies used to develop the empirical models use temperatures outside of the range of this model, and hence the diffusion coefficients were calculated using linear extrapolation. Although not an ideal method for calculating diffusion coefficients, it has been a commonly used method when diffusion coefficient data is not available at the desired test temperature.

3.3.1 Predictive modelling using neural networks

Due to the abundance of published data that has been generated from oxidation studies, the use of neural networks to predict the oxidation behaviour of alloys has become a new area of modelling research, with a recent example of this being the

work by Kim et al. [94], who used an artificial neural network (ANN) to predict the oxidation behaviour of 62 alloys with varying concentrations of alloying elements such as Co, Cr, Mo, W, Al, Ti, Ta, C and B. Based on experimental data published by Park et al. [95], the alloy compositions and mass changes due to oxidation at a single temperature were inputted into the learning model for the artificial neural network. The mass change predictions for five Ni-based alloys were then made, with the alloy compositions varying greatly as shown in Table 3.1.

Table 3.1 – Compositions of Ni-based alloys used in the published artificial neural network study by Kim et al. [94] (wt.%).

Elements	GTD-111	IN738LC	CM247LC	Aa1	B1
Ni	Bal.	Bal.	Bal.	Bal.	Bal.
Co	9.5	8.5	9.3	12.95	4.74
Cr	14	16	8	9.64	16.09
Mo	1.5	1.8	0.5	< 0.01	0.63
W	4	2.5	9.5	8.79	5.3
Al	3	3.5	5.5	5.14	4.87
Ti	5	3.5	0.7	0.98	1.53
Ta	3	1.5	3.2	2.93	5.98
C	0.1	0.1	0.07	0.097	0.07
B	0.01	0.01	0.15	0.016	0.017
Nb	0	1	0	0	0
Hf	0	0	1.4	< 0.01	< 0.01
Zr	0	0.06	0.01	0.007	0.007
Fe	0	0	0	0.022	0.06
Si	0	0	0	0.03	0.03

The predicted result for the mass change of each of the alloys shown in Table 3.1 showed good agreement with experimental data, suggesting that artificial neural networks may be useful prediction tools when studying the oxidation behaviour of alloys. However, an artificial neural network such as the one used by Kim et al. [94] does not allow for a deeper understanding of the oxidation behaviour of the alloy, with only the mass change being predicted. To fully characterise the oxidation behaviour of an alloy, an understanding of microstructural changes to the alloy

throughout the oxidation process and the oxide layer formation as a function of time need to be had.

3.4 Oxidation of Ni – based alloys in high temperature environments

The oxidation behaviour of Ni-based alloys is an area of research that has received much interest due to the use of Ni-based alloys in extreme environments, such as those in aerospace, concentrating solar power and nuclear industries [96]. There are a wide variety of parameters that may influence the oxidation behaviour of an alloy. These may include the oxidation temperature, the type of environment in which the alloy is used, the composition of the alloy itself or the microstructure of the alloy. This section therefore aims to address these factors that can heavily impact an alloys oxidation behaviour and hence an alloys useful lifetime.

3.4.1 Impact of environmental conditions on the oxidation of Ni-based alloys

In each industrial application, Ni-based alloys may be subjected to different environments, whether these by in dry air environments or oxidising environments containing steam, all of which can be maintained at different temperatures. Of the two types of environment mentioned previously, dry air environments are more applicable to MSR applications due to the purification processes molten fluoride salts undergo to remove impurities such as moisture [97]. However, both cases (dry and moisture containing) need to be fully understood as an alloys oxidation resistance in these environments will dictate their useful lifetime in their chosen application [98]. Therefore, this section of the literature review aims to discuss the oxidation behaviour of Ni-based alloys in both dry and moisture containing oxidising environments.

3.4.1.1 Effect of Temperature

A study that investigated the corrosion characteristics of Hastelloy C276 in both air and moisture containing oxidising environments was performed by Li et al. [99], who subjected Hastelloy C276 coupons to dry air environments of 450, 500 and 550 °C, as well as a supercritical water environment at 500 °C under a pressure of 25 MPa. In both sets of experiments the oxidation behaviour was quantified using a weight change method, with the result expressed as the weight gain per unit area. Results of the dry air experiments showed that Hastelloy C276 followed

parabolic oxidation kinetics, with the parabolic rate constant, K_P, being observed to increase from 2.47 x10^{-8} $mg^2/cm^4/hr$ at 450 °C to 2.56 x10^{-6} $mg^2/cm^4/hr$ at 550 °C. In a supercritical water environment, sub-parabolic oxidation kinetics were observed, with an initially fast rate of reaction followed by the gradual slowing of the oxidation rate. The mass change per unit area results of Hastelloy C276 in supercritical water conditions were approximately double those in dry air conditions. Characterisation of the oxidation products was performed of both dry and wet oxidation tests, with results indicating the presence of an inner Cr_2O_3 and $NiCr_2O_4$ layer, with an outer Fe_2O_3 and NiO layer. These findings were corroborated by Zhang et al. [100] who conducted tests at 500, 550 and 600 °C under the same pressure of 25 MPa as Li et al. [99] to simulate a supercritical water environment.

Isothermal oxidation experiments are commonly used to characterise the oxidation behaviour of Ni-based alloys, with several studies conducting experiments over several temperatures to understand the effect of temperature on the oxidation behaviour. Conducting experiments over a range of temperatures allows for the Arrhenius equation which relates the oxidation rate and temperature, presented as equation 3.48, to be used to develop a general equation to characterise an alloys oxidation behaviour. One such study, conducted by Taylor et al. [101], placed coupons of RR1000, a Ni-Co-Cr aerospace alloy, in a furnace at temperatures ranging from 700 °C to 900 ºC. In each case, parabolic oxidation kinetics were observed suggesting oxidation of this alloy was controlled by the diffusion of alloying elements through the oxide layer to the oxide – air interface [102]. A summary of the results is presented as Table 3.2.

Table 3.2 – Summary of parabolic rate constants of RR1000, gathered over the temperature range of 700 °C to 900 °C, from the study conducted by Taylor et al. [101].

Temperature (ºC)	Parabolic Rate Constant ($mg^2/cm^4/s$)
700	3.23x10^{-9}
750	3.15x10^{-8}
800	1.86x10^{-7}
850	9.32x10^{-7}
900	3.13x10^{-6}

Based on the results presented in Table 3.2, the oxidation behaviour of RR1000 can be characterised within the temperature range of 700 °C to 900 °C. This is achieved by plotting the natural logarithm of K_P against the reciprocal of the

temperature in K as per the rearranged version of equation 3.48 presented as equation 3.54:

$$\ln(K_P) = \ln(K_0) - \frac{Q}{RT} \qquad \textbf{3.54}$$

The resultant plot then provides a linear relationship between the natural logarithm of K_P and the reciprocal of temperature, as per the result presented in Figure 3.8

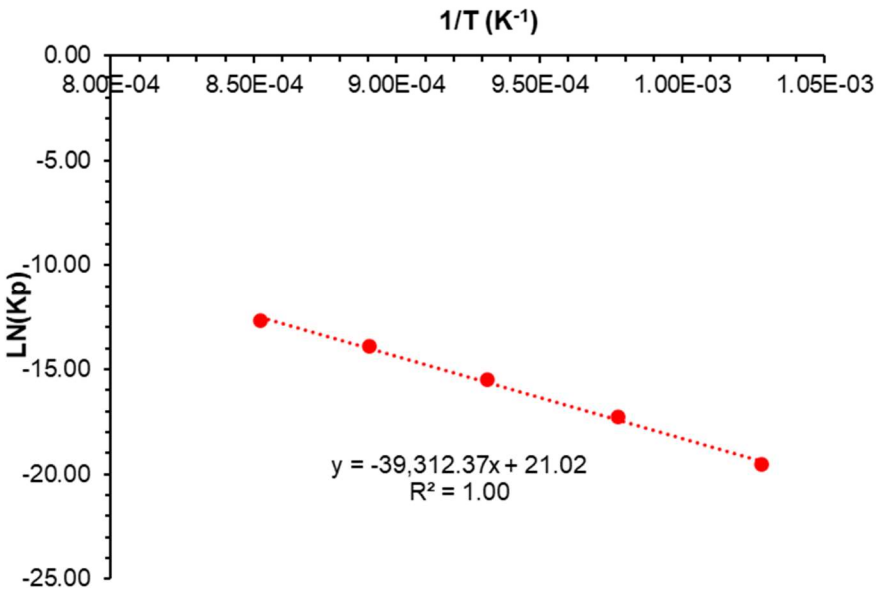


Figure 3.8 – Plot of natural logarithm of K_P against the reciprocal of temperature in K for data collected for the oxidation of RR1000 between 700 °C and 900 °C by Taylor et al. [101], showing linear relationship between the two parameters.

Therefore, the oxidation behaviour of RR1000 in the temperature range of 700 °C to 900 °C can be expressed as:

$$\ln(K_P) = 21.02 - \frac{39312.37}{T} \qquad \textbf{3.55}$$

or, if expanded by taking the exponential of both sides:

$$K_p = 1.39 \times 10^9 e^{-\frac{39312.37}{T}} \qquad \textbf{3.56}$$

Such analysis can be performed for a number of oxidation studies in which Ni-based alloys, relevant to the development of Generation – IV nuclear reactors, are subjected to an isothermal oxidising environment.

A material that has been used historically in the MSR, and has therefore been the subject of many oxidation and molten salt corrosion studies, is Inconel 600 [103]. In a recent study by Li et al. [104], the oxidation behaviour of Inconel 600 was characterised at temperatures of 700 °C, 800 °C and 900 °C after 100 hours using a mass change method. Results of the study indicated that Inconel 600 did not

follow parabolic oxidation kinetics, instead following sub-parabolic kinetics. Li et al. [104] therefore expressed the mass change per unit area of Inconel 600 coupons using the following equation:

$$\Delta m = a.t^b \qquad \textbf{3.57}$$

where Δm is the specific mass change in units of mg/cm^2, t is the oxidation time in units of hours and a and b are constants. Specific mass change results, calculated from the constant values of a and b presented by Li et al. [104] are presented in Figure 3.9.

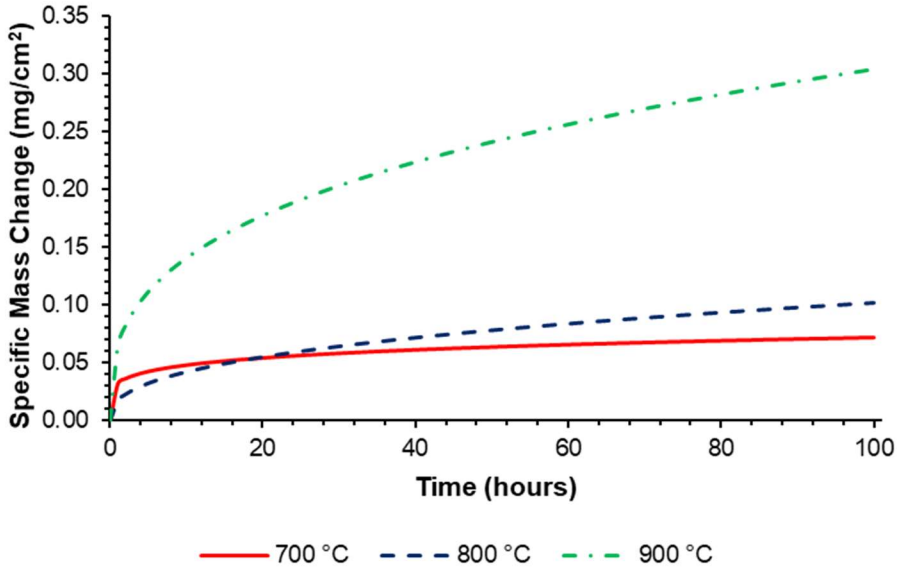


Figure 3.9 – Results for the specific mass change of Inconel 600 alloy, exposed to a dry air environment at 700 °C, 800 °C and 900 °C for durations up to 100 hours showing increasing specific mass change with increasing temperature [104].

Results presented in Figure 3.9 show that increasing the oxidation temperature increased the specific mass gain considerably, with analysis of the formed oxide layers at 700 °C and 800 °C being comprised of the main metallic constituents of Fe, Cr and Ni. In each case, an inner layer consisting of a Ni-Cr spinel oxide in the form $NiCr_2O_4$ was observed, along with an outer layer consisting of Fe, Cr and Ni oxides. However, at 900 °C, the presence of Mn was also observed within the inner layer spinel – oxide layer, replacing Ni. The outer layer was also observed to be a spinel oxide of the form $MnCr_2O_4$. The formation of spinel oxides was believed to be due to the solid-phase reaction between oxide layers. For example, the formation of $NiCr_2O_4$ was formed by the reaction of NiO with Cr_2O_3 defined by equation 3.58:

$$NiO + Cr_2O_3 \xrightarrow{} NiCr_2O_4 \qquad \textbf{3.58}$$

3.4.1.2 Effect of Moisture

The presence of moisture can also drastically impact the oxidation behaviour of stainless steels and Ni-based alloys. In an environment containing moisture, the oxidation of Inconel 600 was studied by Xiao et al. [105] over a temperature range of 600 °C – 900 °C, with the study focusing on the impact of moisture on the oxidation behaviour over time periods of 24 to 150 hours. In their study, Xiao et al. [105] varied the humidity of the test environment between 5% and 19% and showed that introducing moisture increased the extent of oxidation. However, this was observed from micrographs of the exposed surfaces of tested samples, included as Figure 3.10, and not quantified with mass change measurements. Rate constants are therefore not available to compare directly with the dry oxidation study of Li et al. [104].

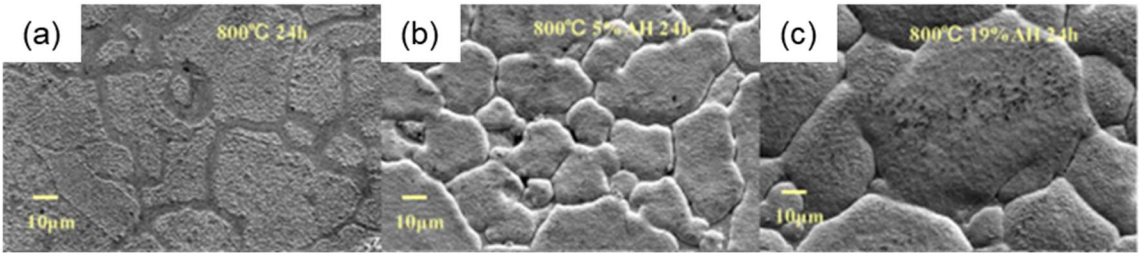


Figure 3.10 – Micrographs of Inconel 600 coupons, exposed to a) dry air environment, b) dry air environment containing 5% humidity and c) dry air environment containing 19% humidity, all at 800 °C. Results show increasing oxide layer coverage of the exposed surface within increasing humidity. Figure adapted from [105].

When assessing the oxidation of stainless steels and Ni-based alloys in moisture containing environments, Dudziak et al. [106-108] have conducted several studies comparing the oxidation performance of different materials in high temperature, steam containing environments. An alloy of interest in the studies of Dudziak et al. [106] is Haynes 230 which is a speciality high temperature Ni – based alloy [109]. In their study, the oxidation behaviour of Haynes 230 was assessed in a steam containing environment at 700 °C and 800 °C, with the oxidation behaviour being quantified by a mass gain. Haynes 230 was also of interest in the isothermal oxidation study of Rashidi et al. [110] in which Haynes 230 was oxidised at 850 °C in a dry air environment for 600 hours. A comparison of the oxidation results for Haynes 230 in dry and moisture containing air is shown in Figure 3.11.

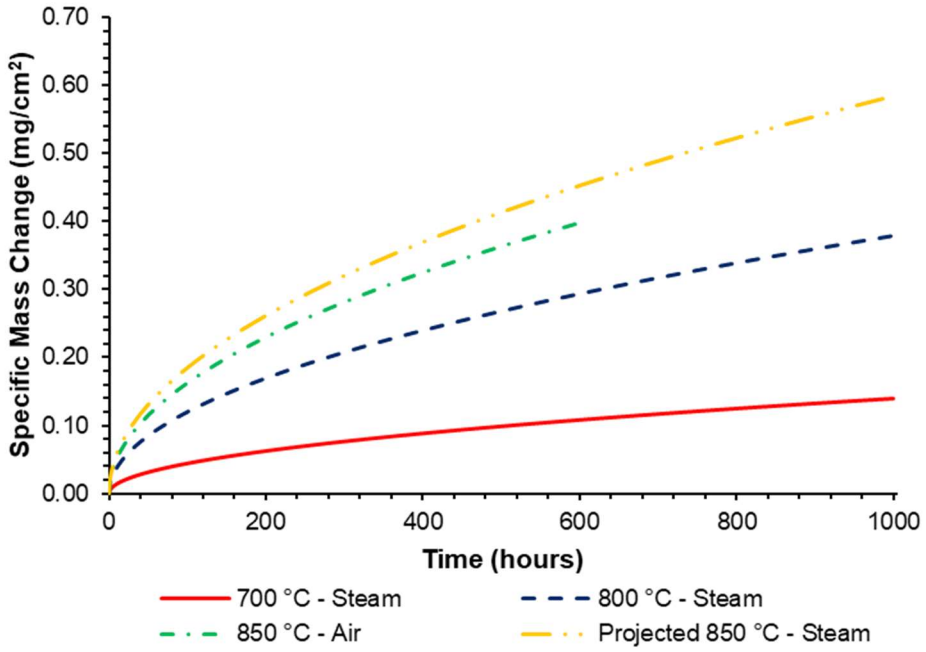


Figure 3.11 – Comparison of oxidation results for Haynes 230 in a dry air environment at 850 °C and steam containing environment at 700 °C and 800 °C, showing that moisture content increases the oxidation rate of Haynes 230 to a similar level of that observed at 850 °C in a dry air environment. Data collected from [106, 108, 110].

Results presented in Figure 3.11 indicate that increasing the moisture content causes an increase in the oxidation rate with the projected K_P values of Haynes 230 after exposure to steam at 850 °C for 1000 hours being 9.52×10^{-8} $mg^2/cm^4/s$. This represents a 29.3% increase in the oxidation rate of Haynes 230 in an air environment due to the presence of moisture during oxidation.

An increase in the rate of oxidation of Inconel 617 was also observed when oxidised in dry and steam environments at 750 °C. The research, conducted by Archana et al. [111], showed that under these conditions, parabolic oxidation kinetics were observed. However, the parabolic rate constant increased from 2.96×10^{-6} $mg^2/cm^4/s$ to 1.83×10^{-5} $mg^2/cm^4/s$ when Inconel 617 was exposed to the steam environment at 750 °C when compared with the dry environment. Analysis of the oxide layers showed that the layer thickness increased in a steam environment when compared to the dry air environment. This observation corroborates the same observation made by Xiao et al. [105] for Inconel 600. However, the oxide scales formed during exposure to air were more densely packed than those formed during exposure to steam, as shown in Figure 3.12.

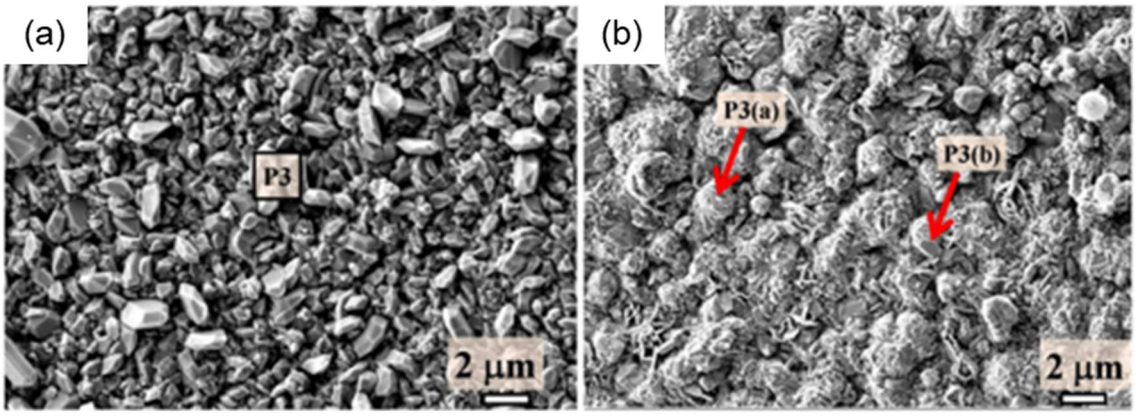


Figure 3.12 – Comparison of oxide scales formed on the exposed surfaces of Inconel 617 in a) dry air environment and b) steam environment at 750 °C after 500 hours, showing oxide scales are more densely packed after exposure to dry air environment, resulting in a greater diffusion barrier for ions, resulting in a slower oxidation rate in air. Figure adapted from [111].

The more densely packed oxide scales formed on Inconel 617 in a steam environment, shown in Figure 3.12 indicates that metal ions and O_2 can diffuse to the substrate – oxide interface more readily in a steam containing environment when compared with a dry air environment, resulting in a greater rate of oxidation.

3.4.2 Effect of alloy composition on its oxidation behaviour

A study, conducted by Park et al. [95], conducted a comprehensive investigation into the impact of an alloys compositions on its oxidation behaviour. In their study, 62 alloys were used to identify the impact of using Co, Cr, Mo, W, Al, Ti, Ta, C and B as alloying elements with Ni. The composition ranges used are presented in Table 3.3.

Table 3.3 – Summary of composition ranges of elements, alloyed with Ni, in the study conducted by Park et al. [95].

Element	Co	Cr	Mo	W	Al	Ti	Ta	C	B
Composition Range (wt.%)	0-15	8-15	0-5	0-10	3-8	0-5	0-10	0.1	0.01

Coupons of the 62 different alloys were placed in a high temperature air environment at a temperature of 850 °C for a duration of 300 hours. Throughout the study the oxidation kinetics were quantified using a mass change technique. The quantification of the oxidation kinetics and the wide compositional ranges of alloys used allowed for the contributions of combinations of alloying elements to be identified. The results showed that the addition of Al improved the oxidation resistance of the alloy. This protective behaviour was observed to be enhanced

when paired with low concentrations of Ti which aided in the promotion of a continuous Al_2O_3 layer as shown in Figure 3.13.

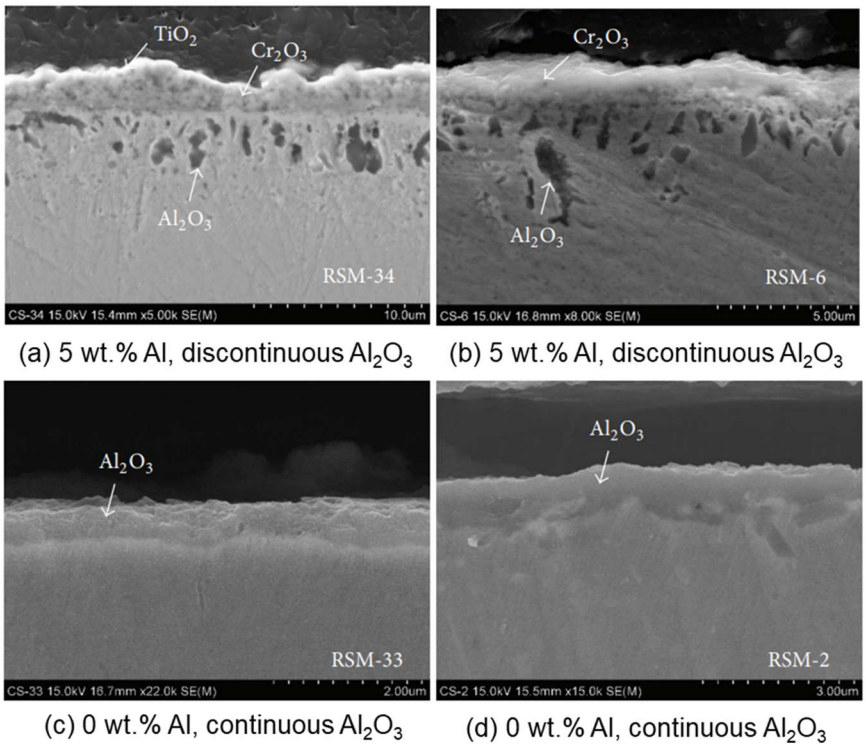
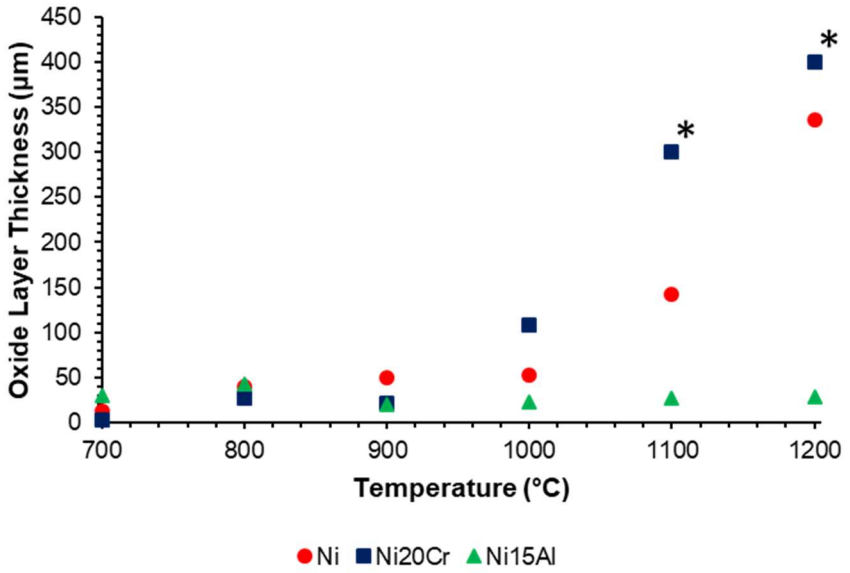


Figure 3.13 – Micrographs showing formation of discontinuous (a – b) and continuous (c – d) Al_2O_3 layers with varying concentrations of Ti, with lower concentrations of Ti showing improved oxidation resistance. Figure adapted from [95].

Similar oxidation behaviour was observed in alloys containing Cr; however, this was only observed when in the absence of W. When W was included, Cr did not impact the oxidation behaviour, with the introduction of W actually reducing the oxidation rate of alloys when Cr was not present. This was observed due to the slower diffusion kinetics of W compared with Cr.

When studying the impact of Al and Cr addition to Ni, Ma et al. [112] found that adding these elements can drastically improve the oxidation resistance of Ni. In the study, Ma et al. [112] used Ni-based alloys containing 20 at.% Cr and 15 at.% Al (Ni20Cr and Ni15Al respectively). In the study, oxidation tests were performed at temperature in the region of 700 °C to 1200 °C for durations up to 576 hours. The quantification of the oxidation behaviour of each tested alloy was done using a mass change method. Oxide layer thickness measurements were determined from cross-sectional images and subsequently used to determine the extent of oxidation of each alloy. A plot of the oxide layer thickness measurements for each of the tested alloys is presented as Figure 3.14:



*Values in paper by Ma et al. [112] were defined as >300 and >400 for Ni20Cr alloy at temperatures of 1100 °C and 1200 °C. Plotted values are at 300 µm and 400 µm at 1100 °C and 1200 °C respectively.

Figure 3.14 – Plot of oxide layer thicknesses as a function of temperature for pure Ni, Ni20Cr and Ni15Al alloys, tested at temperatures between 700 °C and 1200 °C for 576 hours [112].

Results presented in Figure 3.14 show that adding 20 at.% Cr to Ni drastically reduces its oxidation rate between 700 °C and 900 °C. However, between 1000 °C and 1200 °C the oxide layer thickness increases massively. This was believed to be due to the volatilisation of Cr_2O_3 to CrO_3, at these elevated temperatures, caused by the reaction of Cr_2O_3 with O_2 as shown in equation 3.59 [84] :

$$Cr_2O_3 + \frac{3}{2}O_2 \xrightarrow{\square} 2CrO_3 \qquad \textbf{3.59}$$

The result of the volatilisation of Cr_2O_3 is the removal of the oxide layer, resulting in a lack of protection for the underlying substrate [84]. Hence, the increased oxidation rate observed in Figure 3.14 at temperatures in excess of 1000 °C. The addition of 15 at.% Al to Ni was observed to show much better oxidation resistance at the elevated temperatures than the addition of 20 at.% Cr, with the rate of oxidation remaining below that for Ni. However, performance at lower temperatures, 700 and 800 °C, were very similar to both Ni and the Ni20Cr alloy.

As expected, the Ni coupons formed a single NiO layer on the exposed surfaces which increased in thickness from 12.2 µm to 336.9 µm as the temperature was increased from 700 °C to 1200 °C. The NiO layer was observed to contain voids. The presence of voids limited the protection that the oxide layer provided to the underlying Ni substrate. At more elevated temperatures, voids were also observed in the oxide scales of the Ni20Cr. However, the inclusion of Cr lead to the formation

of a more complex oxide scale, with an inner Cr_2O_3 layer and Ni-Cr layer being observed at each temperature. At temperatures in excess of 800 °C an outer NiO layer was also observed. The voids and cracks observed within the oxide scales limit their protective nature as they represent a discontinuous diffusion barrier, hence, species can diffuse across more readily. Examples of the oxide layers formed on Ni and Ni20Cr at 700 °C and 900 °C are compared in Figure 3.15, indicating the presence of cracks and voids within the oxide layers.

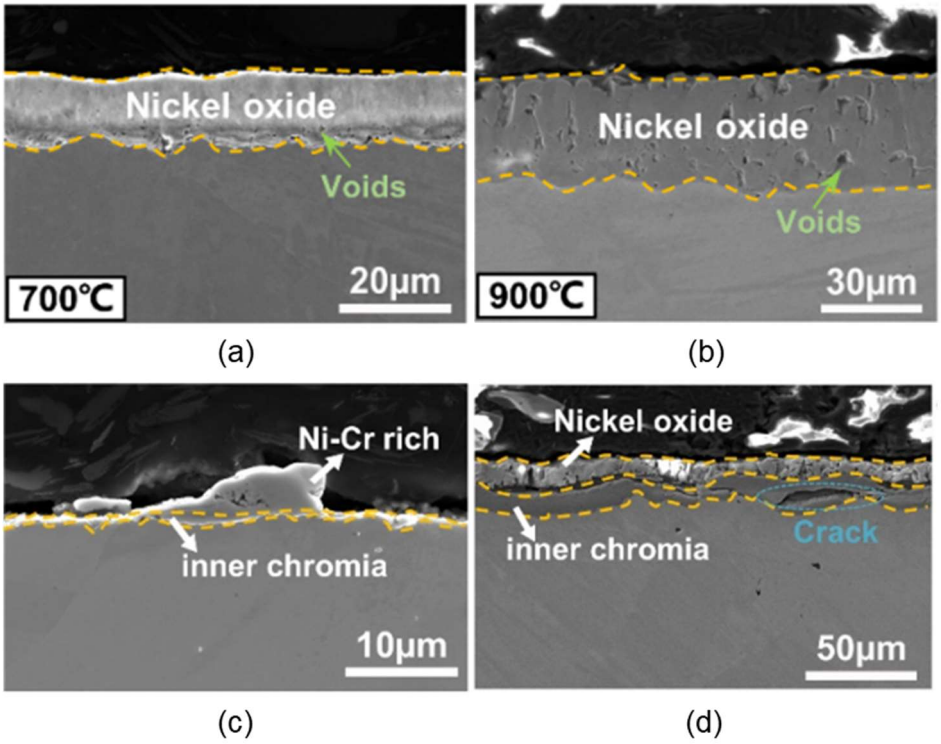


Figure 3.15 – Comparison of oxide layers of (a and b) Ni and (c and d) Ni20Cr at 700 °C and 900 °C respectively highlighting the presence of voids and cracks at 900 °C, resulting in a discontinuous diffusion barrier and hence decreased oxidation resistance. Figure adapted from [112].

These observations differ greatly to those observed for Ni15Al, which shows an external NiO layer but also an internal oxidation zone which consists of many Al-oxides. The internal oxidation zone is separated from the substrate by a thin Al_2O_3 layer which increases in thickness with the temperature. This is highlighted in Figure 3.16, which compares the multi-layer oxide structure of Ni20Cr and Ni15Al at temperatures between 700 °C and 1000 °C, highlighting differences between the layers that result in the improved oxidation behaviour of the Ni15Al alloy.

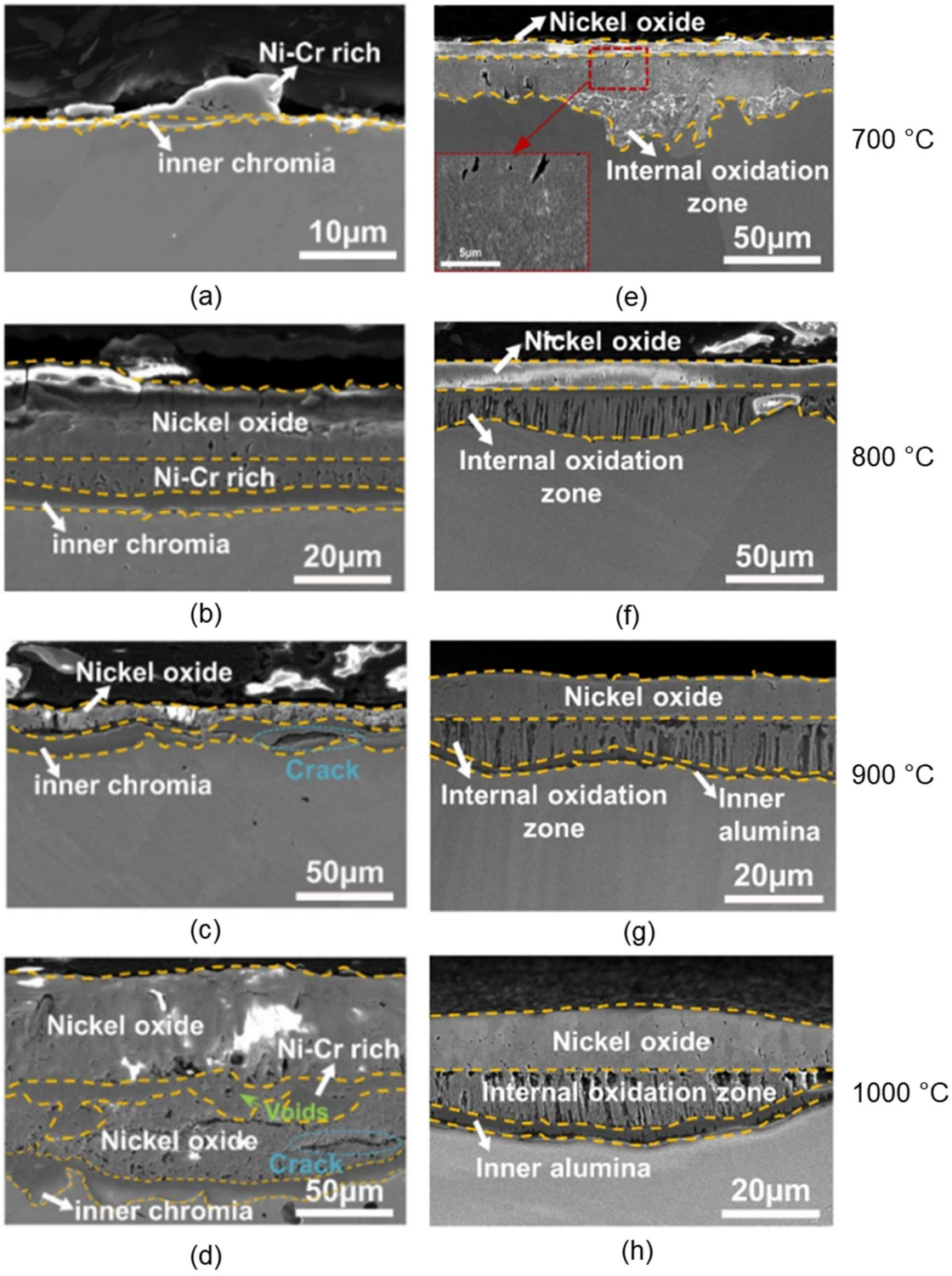


Figure 3.16 – Comparison of the oxidation behaviour of (a – d) Ni20Cr and (e – h) Ni15Al alloys highlighting the differences between the oxide layers at increasing temperatures that result in the improved oxidation resistance of the Ni15Al alloy. Figure adapted from [112].

Since the Al_2O_3 layers do not contain any cracks or voids, the oxidation resistance is greatly improved, as the oxide layers form a continuous diffusion barrier. The

result of which is much lower specific mass changes to the alloy, as illustrated by measurements presented in Figure 3.14.

3.4.3 Effect of microstructure on alloy oxidation

The effects of microstructure on the oxidation of Haynes 230 and Hastelloy N Ni-based alloys were investigated by Wang and Szpunar [113]. In the study, samples of Haynes 230 and Hastelloy N were manufactured using a cold rolling manufacturing method. The method was carried out until the thickness of each material had been reduced by 70%. Test materials were then heat treated to achieve coarse and fine grain structures. A summary of the heat treatment processes and average grain sizes, are presented in Table 3.4.

Table 3.4 – Summary of manufacturing methods and heat treatments undergone by Haynes 230 and Hastelloy N Ni-based alloys to achieve coarse and fine grain structures [113]. Average grain sizes also provided.

Sample Information	Coarse Grain Haynes 230	Fine Grain Haynes 230	Coarse Grain Hastelloy N	Fine Grain Hastelloy N
Heat Treatment	Annealing – 1200 °C, 30 minutes	Annealing – 1000 °C, 40 minutes	Annealing – 1100 °C, 2 hours	Annealing – 1000 °C, 2 minutes
Average Grain Size (μm)	35.4	3.9	51.6	4.7

Samples of each material and grain size were oxidised in air at 800 and 900 °C for durations up to 1000 hours. The oxidation kinetics were quantified using a mass change method and showed little difference in the oxidation kinetics of Haynes 230 in the coarse- and fine- grained states. However, the coarse- and fine- grained Hastelloy N coupons exhibited very different kinetics as shown in Figure 3.17.

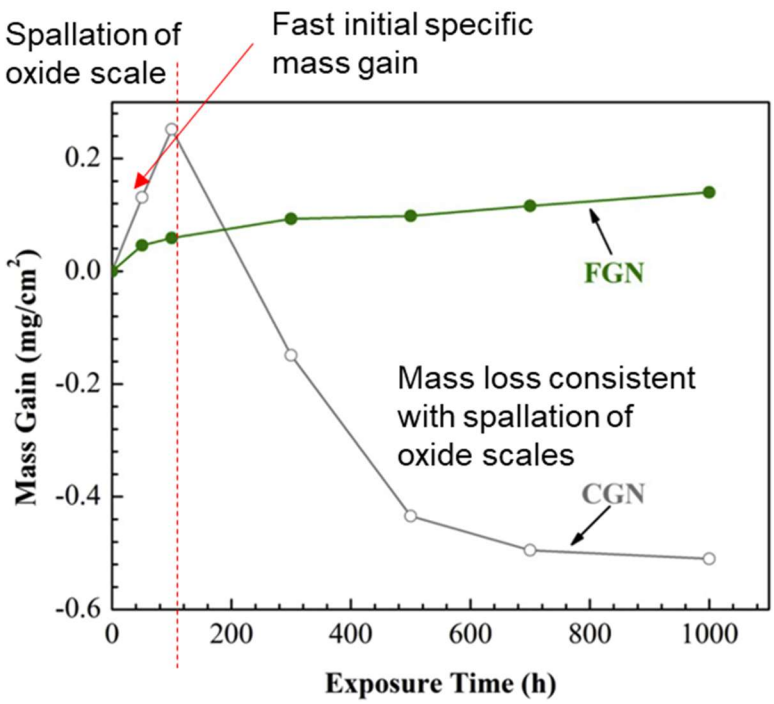


Figure 3.17 – Oxidation kinetics of Hastelloy N with both coarse- and fine-grain microstructures with mass changes for coarse – grained Hastelloy N being much greater initially before spallation whilst fine – grained Hastelloy N showed a much lower and consistent rate of oxidation. Figure adapted from [113].

The results presented in Figure 3.17 show that the oxidation kinetics of coarse–grained Hastelloy N were initially much greater than those for the fine–grained Hastelloy N coupons. After 100 hours of exposure to dry air, the oxide layer on the coarse - grained Hastelloy N began to spall, resulting in significant mass loss. This result highlighted that the heat treatment conducted on Hastelloy N to achieve a fine–grained microstructure, had enhanced its oxidation resistance. This conclusion is only valid for Hastelloy N though as negligible difference was observed between coarse- and fine – grained Haynes 230 as shown in Figure 3.18.

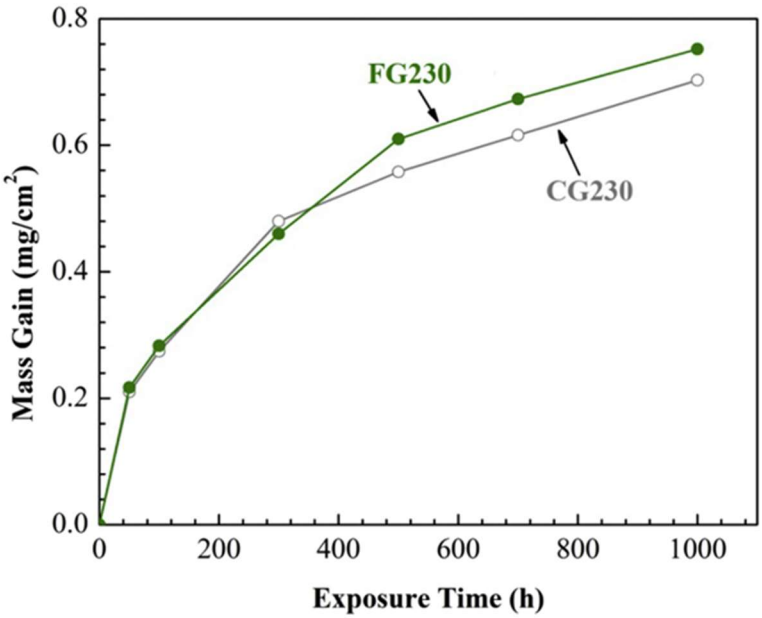


Figure 3.18 - Oxidation kinetics of Haynes 230 alloy after heat treatments to achieved coarse – and fine – grain microstructures. Both alloys are observed to have very similar oxidation kinetics, although the fine – grained Haynes 230 does have a higher final mass gain. Figure taken from [113].

The differences observed in the oxidation behaviour of the two alloys was attributed to their compositions. The Haynes 230 and Hastelloy N alloys have different concentrations of Cr, 22 wt.% and 7 wt.% respectively. The reduced concentration of Cr within Hastelloy N was done to reduce the corrosion characteristics of the alloy whilst maintaining moderate oxidation resistance [114]. However, with a coarse grain structure, 7 wt.% Cr was too little to form a uniform Cr_2O_3 layer [115]. This was shown through SEM and EDX analysis of the coarse grain Hastelloy N which showed the growth of a Cr and Mn rich combined layer, as well as the formation of NiO, with very little uniform Cr_2O_3. The result of this was the formation of a porous oxide layer which was not able to prevent the penetration of O_2 to the substrate – oxide interface, resulting in the continued oxidation of the substrate material. This in turn resulted in the cracking and subsequent spallation of the oxide layers as shown in Figure 3.19.

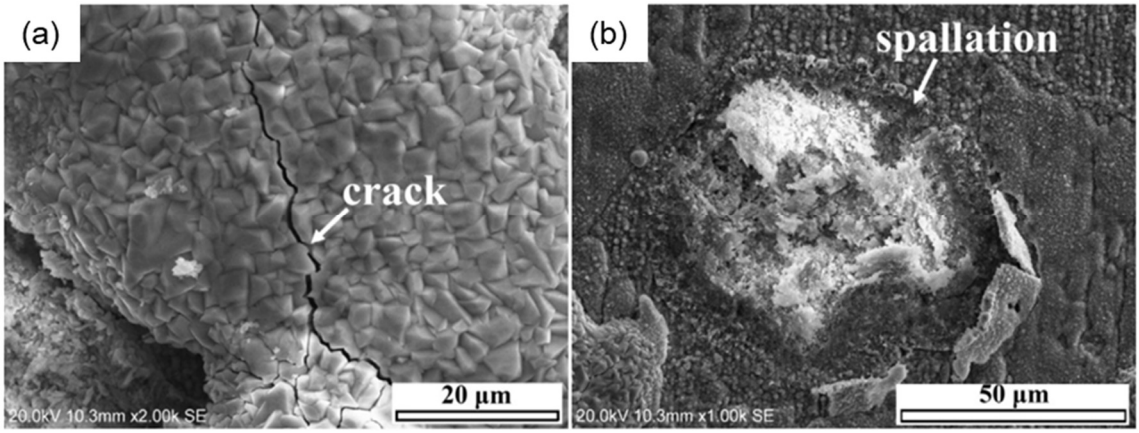


Figure 3.19 – Cracking and subsequent spallation of the oxide layer of coarse grained Hastelloy N after exposure to air at 800 °C after a) 300 hours and b) 500 hours of exposure. Figure adapted from [113].

The reduction in the grain size resulted in the growth of a uniform Cr_2O_3 layer which did cover the surface. This was believed to be due to the increased number of grain boundaries, introduced during grain boundary refinement. The increased number of grain boundaries increased the diffusion of Cr resulting in a more uniform growth of the Cr_2O_3 layer.

3.5 Alloy corrosion in molten salt environments

The second portion of this research will focus on the corrosion of Hastelloy C276 in a FLiNaK molten salt environment. In a typical high-temperature, corrosive environment, corrosion resistance if often achieved by the formation of a protective oxide layer. However, due to the aggressive nature of molten salt systems, the formation of a protective oxide layer cannot be relied upon for protection of materials.

Due to the non-protective nature of many oxide layers in molten salt environments, the corrosion of the underlying substrate material will progress by the selective dissolution of less noble alloying elements such as Cr and Fe. The corrosion that follows is driven by several factors, including, the thermodynamics of the corrosion reactions, inclusion of impurities within the melt, temperature gradients, galvanic interactions, and the electrochemical reactions themselves.

Therefore, this section of the thesis aims to explain each of the considerations stated previously and how they may impact the corrosion of Ni-based alloys in molten salt environments.

3.5.1 Thermodynamics of molten salt corrosion

When understanding the corrosion mechanisms of alloys in molten salt environments, it is important to understand the reactions taking place. When considering corrosion of a material by a corrosive media, Wagner and Traud [116] stated that there must be simultaneous dissolution of metal, the anodic reaction, and the reduction of an oxidant, the cathodic reaction. These processes are described by equations 3.60 and 3.61 [15].

$$M \rightarrow M^{n+} + ne^- \quad \textbf{3.60}$$

$$Ox + ne^- \rightarrow Red \quad \textbf{3.61}$$

where M represents any metallic alloying element, Ox represents the oxidising, R the reduced species and n the number of electrons involved in the reaction. Based on these reactions, the overall reaction can be expressed as:

$$M + Ox \rightarrow M^{n+} + Red \quad \textbf{3.62}$$

In the case of a fluoride molten salt system, equations 3.61 and 3.62 can be rewritten as [16]:

$$\frac{n}{2}F_2 + ne^- \rightarrow nF^- \quad \textbf{3.63}$$

$$M + \frac{n}{2}F_2 \rightarrow MF_n \quad \textbf{3.64}$$

Similarly, if another oxidising agent is introduced into the melt i.e. O_2, then the cathodic and overall reactions presented as equations 3.65 and 3.66 would also be true:

$$\frac{n}{2}O_2 + ne^- \rightarrow nO^{2-} \quad \textbf{3.65}$$

$$M + \frac{n}{2}O_2 \rightarrow MO_{n/2} \quad \textbf{3.66}$$

In either case the thermodynamic considerations of both sets of reactions can predict whether the system will be stable or whether the metal will corrode. This case be determined by the Gibbs free energy change, which, for an electrochemical reaction can be expressed as:

$$\Delta G = -nF\Delta E \quad \textbf{3.67}$$

where F is the Faraday constant (96485 C/mol) and ΔE the potential difference between the anodic and cathodic reactions which can be expressed as E_a and E_c respectively, where ΔE can be expressed as:

$$\Delta E = E_c - E_a \quad \textbf{3.68}$$

For corrosion of the materials immersed in molten salt to occur spontaneously, the Gibbs free energy change must be less than zero. For this to be true, the cathodic potential must be more positive than the anodic potential. The anodic and cathodic potentials can be expressed as a function of the standard electrode potential, E^o, and the activity of the species presented in the anodic and cathodic half cells equations, equations 3.60 and 3.61 respectively. These equations are:

$$E_a = E_a^o + \frac{RT}{nF}\ln\left(\frac{a_{M^{n+}}}{a_M}\right) \quad \textbf{3.69}$$

$$E_c = E_c^o + \frac{RT}{nF}\ln\left(\frac{a_{Ox}}{a_{Red}}\right) \quad \textbf{3.70}$$

For the formation of MX_n shown in equation 3.64, the Gibbs free energy change is equal to the standard Gibbs free energy change and can be related to the electrode potentials as expressed in equation 3.71:

$$\Delta G(MX_n) = \Delta G^0(MX_n) = nFE^0_{M^{n+}/M}(vs.\ X_2/X^-) \quad \textbf{3.71}$$

3.5.1.1 Gibbs free energy comparison – Molten salt constituents and impurities

When considering the corrosion behaviour of metallic alloys in molten salt environments, it is important to consider the Gibbs free energy of formation of the salt constituents themselves, as well as any metallic fluorides that may be formed and any impurities. As discussed previously in Section 3.2.2, these values for Gibbs free energy will give an indication of which reactions are more favourable in a molten salt system. A figure showing a comparison of the Gibbs free energy change of formation of FLiNaK and FLiBe salt constituents against different metallic fluorides and potential impurities is shown in Figure 3.20.

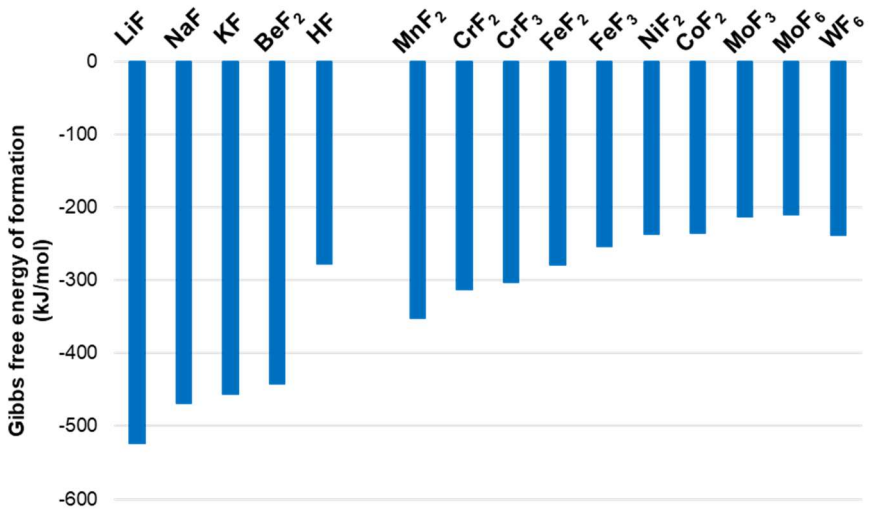


Figure 3.20 – Figure showing Gibbs free energy of formation of molten salt constituents and metallic fluoride compounds at a temperature of 1000 K [29, 53, 117].

As can be seen in Figure 3.20, the four main salt constituents (LiF, NaF, KF and BeF_2) have much more negative than the metallic fluorides that may be formed by the reaction of alloying elements with the molten salt, meaning that the salt constituents are more stable than the fluoride compounds that can form. Therefore, it is more thermodynamically favourable for the salt constituents to remain in their state. However, a contaminant, such as HF, has a more positive Gibbs free energy of formation than the salt constituents, meaning it is less stable within the molten salt system. Therefore, to achieve a more negative Gibbs free energy change, HF can react with alloying elements to form of metallic fluorides. Examples of this process are shown for Cr and Mn, which are shown in Figure 3.20 to have more negative Gibbs free energy of formation than HF, in equations 3.72 and 3.73:

$$Cr + 2HF \rightarrow CrF_2 + H_2 \qquad \textbf{3.72}$$

$$Mn + 2HF \rightarrow MnF_2 + H_2 \qquad \textbf{3.73}$$

In the case of the reaction between Cr and HF, the Gibbs free energy of CrF_2 is more negative than that of HF. Similarly, the Gibbs free energy of formation of MnF_2 is less than HF. In both cases the system has entered a more stable state by the reaction of HF with alloying elements.

Therefore, the introduction of contaminants such as HF and the subsequent corrosion behaviour of alloys can be detrimental to material performance and needs to be understood. As a result, the corrosion of Ni-based alloys by different contaminants will be discussed throughout Section 3.6.

3.5.2 Kinetics of material corrosion in molten salts

The corrosion kinetics in molten salt environments are high dependent on the ionic species present in the melt. In the research documented here, these species are likely to be halides and oxyanions due to the fact a fluoride salt combination is being used in an air atmosphere without a cover gas. The corrosion processes due to both of these types of ions can be described by acid/base models. This section aims to introduce in detail the oxyanionic and halide acid/base models.

3.5.2.1 Oxyanionic acid/base model

Oxyanionic salts are oxide ion (O^{2-}) containing metallic salts, of the form R_xAO_y which can dissociate upon modelling in a reversible chemical reaction. In the form presented, R represents any alkaline metal and AO_y can represent any oxyanion such as carbonate (CO_3^{2-}), nitrate (NO_3^{2-}), sulphate (SO_4^{2-}) or hydroxide (OH^-). The dissociation reaction for oxyanionic salts can take the form described by equation 3.74.

$$R_xAO_y \leftrightarrow xR^{n+} + {AO_y}^{n-} \quad \textbf{3.74}$$

Depending on the environmental factors of the melt, the oxyanion can then dissociate further, which takes the general form of equation 3.75.

$${AO_y}^{n-} \leftrightarrow {AO_{y-1}}^{2-n} + O^{2-} \quad \textbf{3.75}$$

The relationship presented as equation 3.75 is referred to as the Lux-Flood model and defines O^{2-} as the basic species and the gaseous oxide species (AO_{y-1}^{2-n}) as the acidic species. Depending on the activity of O^{2-} in the melt, dissolution of metallic oxides can occur, where the basicity of the melt can be defined as the log of the O^{2-} concentration and denoted by pO^{2-} as shown in equation 3.76.

$$pO^{2-} = -\log([O^{2-}]) \quad \textbf{3.76}$$

If the basicity of the melt is low, then a metal oxide may dissociate into its corresponding metallic ion and O^{2-}. This is deemed to be acidic dissolution of the oxide layer and can be described by equation 3.77.

$$M_xO_y \leftrightarrow xM^{n+} + yO^{2-} \quad \textbf{3.77}$$

The release of O^{2-} back into the molten salt by this mechanism increases the basicity and hence will prevent further dissolution of the oxide layer by this mechanism. Whereas, if the basicity of the melt is high and the activity of O^{2-} is

high, then a reaction can occur between O^{2-} and any metallic oxides to form oxide complexes as per equation 3.78.

$$M_xO_y + zO^{2-} \overset{\square}{\leftrightarrow} {M_xO_{y+z}}^{2-} \quad \textbf{3.78}$$

The formed complexes may also be soluble within the molten salt, hence leading to the dissolution of the oxide layer. Similarly, to the releasing of O^{2-} by the acidic dissolution of the oxide layer, the formation of these metallic oxide complexes aids in reducing the O^{2-} activity in the melt, reducing the basicity of the melt and hence reducing the dissolution of the oxide layer by this mechanism.

3.5.2.2 Halide acid/base model

The halide acid/base model is similar to that for oxyanions described previously. This acid/base model is based on the dissociation reaction of an alkaline metal halide which can take the form RA_y where R represents an alkaline metal ion and A the halide ion. The dissociation reaction of a metal halide salt upon melting is given as:

$$RA_y \overset{\square}{\rightarrow} R^{y+} + yA^- \quad \textbf{3.79}$$

The halide acid/base model, referred to as the Lewis acid/base model, defines the halide ion (A^-) as the basic species and the alkaline metal ion (R^{y+}) as the acidic species. In the case of this research into fluoride molten salt corrosion, a highly basic salt will be produced due to the production of fluoride (F^-) into the melt. Similarly, to the oxyanionic acid/base model, the basicity of the melt can be expressed as:

$$pF^- = -\log([F^-]) \quad \textbf{3.80}$$

However, salt basicity can be reduced by the reaction of fluoride species with cations, forming metallic fluorides, as per the reactions defined in Section 3.5.1, and reducing fluoride activity within the melt. Since studies have shown that corrosion in molten fluoride salt environments is heavily influenced by the fluorination of metal cations, a reduction in fluoride activity will result in a less corrosive salt.

The reduction of fluoride activity is often achieved by the formation of ionic complexes, similar to those described by equation 3.78 for the oxyanionic acid/base model [16]. This was shown by Olson et al. [53] who theorised that Lewis acids such as chromium (II) fluoride (CrF_2) and iron (II) fluoride (FeF_2) could react with fluoride ions to form ionic complexes, as shown in equations 3.81 and 3.82:

$$CrF_2 + 2F^- \rightarrow CrF_4^{2-} \quad \textbf{3.81}$$

$$FeF_2 + 2F^- \rightarrow FeF_4^{2-} \quad \textbf{3.82}$$

The formation of these fluoride complexes would aid in the reduction of the fluoride activity within the melt, reducing basicity and therefore the corrosive nature of the melt and materials that come into contact with it.

3.5.3 Numerical modelling of molten salt corrosion: A mechanistic approach

Due to the complexity of the mechanisms of molten salt corrosion of Ni-based alloys, attempts to predict the corrosion behaviour of alloys have been limited. However, the research by Lee et al. [118] has managed to predict the corrosion behaviour of three Ni-based alloys in the molten fluoride salt FLiNaK at 750 °C using a mechanistic modelling methodology. The three alloys tested were Inconel MA754, GH3535 and Hastelloy N. Both GH3535 and Hastelloy N have been specifically designed for molten salt application, however, the Inconel MA754 was developed to provide high strength and creep resistance at temperatures up to 1000 °C [118]. Experimentally determined mass changes of the three test alloys were then used in the validation of the mechanistic model.

The predictive model was built in the finite element package ABAQUS and was used to predict the depletion of alloying elements present in each of the three alloys under investigation at 750 °C over a test duration of 300 hours. The depletion of alloying elements was predicted using the diffusion coefficients of each alloying element, with diffusion coefficients being taken from literature. The diffusion behaviour of alloying elements was converted into concentration gradients for each alloying element, and subsequently, the mass change of each alloying element. Predicted mass losses were validated using experimental methods from the same study. Coupons of each material were immersed in molten FLiNaK salt at 750 °C for 300 hours under an argon cover gas to prevent contamination of the system by air. The predicted mass loss results for each alloy showed good agreement with the experimentally determined mass losses, a summary of the results are presented in Table 3.5.

Table 3.5 – Comparison of predictive modelling and experimentally determined mass losses for Inconel MA754, GH3535 and Hastelloy N Ni-based alloys from study by Lee et al. [118].

Alloy	Predicted Specific Mass Loss (mg/cm^2)	Experimental Specific Mass Loss (mg/cm^2)	Percentage Differences (%)
Inconel MA754	4.90	4.80	2.04
GH3535	2.50	2.55	2.00
Hastelloy N	2.63	2.81	6.84

Although good agreement can be observed between the results presented in Table 3.5, results of predictive models such as this one can be skewed by the input data. For example, in this model, the diffusion coefficients used for each alloying element modelled were taken from literature. However, more recent literature of the diffusion coefficients for elements such as Cr are different by as much as 10^4 cm^2/s [82, 119]. Similarly, the variance in the diffusion coefficients for Mn range from 10^{-15} cm^2/s up to 10^{-11} cm^2/s which can heavily impact the predicted result [82, 120].

To mitigate against the influence of diffusion data from literature, Li et al. [121] turned to a different approach when considering the impact of chloride (Cl^-) impurities on the corrosion of Ni-based alloys in the nitrate salt combination known as Solar Salt, consisting of 60 wt.% sodium nitrate and 40 wt.% potassium nitrate ($NaNO_3$ and KNO_3 respectively). The model focused on what Li et al. [121] termed, intrinsic and active corrosion, denoted by h_{ac} and h_{ic} respectively, where active corrosion is defined as the corrosion process caused by the Cl^- impurities and the intrinsic corrosion is the corrosion of the material by the pure Solar Salt. Since oxygen is present in Solar Salt, the corrosion process would lead to the formation of an oxide layer, where the total layer thickness, h_{tot}, can be expressed as:

$$h_{tot} = h_{ac} + h_{ic} \quad \textbf{3.83}$$

The model by Li et al. [121] was based on a four step active corrosion process which was based on the movement of iron (II) chloride ($FeCl_2$). This four-step process involves the reaction of Cl^- with an iron oxide layer to form Cl_2 which then penetrates the oxide – substrate interface and reacts with the substrate material to form metallic chlorides such as $FeCl_2$. The $FeCl_2$ is then oxidised, releasing Cl_2 which can then repenetrate the oxide layer. This active corrosion process therefore is assumed to be controlled by the diffusion of $FeCl_2$. This can be characterised by the flux of $FeCl_2$ which can be expressed by Fick's first law, either as a function of $FeCl_2$ diffusion or $FeCl_2$ concentration:

$$J_{FeCl_2} = -D_{FeCl_2}\frac{dC_{FeCl_2}}{dh_{ac}} \quad \textbf{3.84}$$

$$J_{FeCl_2} = -C_{FeCl_2}\frac{dh_{ac}}{dt} \quad \textbf{3.85}$$

which when combined give an equation of the growth rate of the oxide scale thickness due to active corrosion:

$$\frac{dh_{ac}}{dt} = D_{FeCl_2}\frac{1}{C_{FeCl_2}}\frac{dC_{FeCl_2}}{dh_{ac}} \quad \textbf{3.86}$$

where D_{FeCl_2} is the diffusion coefficient of $FeCl_2$ in the oxide layer and C_{FeCl_2} is the concentration of $FeCl_2$ within the oxide layer. When the reaction reaches equilibrium, the rate of oxide layer growth can be expressed as:

$$\frac{dh_{ac}}{dt} = D_{FeCl_2}\frac{1}{C_{FeCl_2}}\frac{\Delta C_{FeCl_2}}{h_{ac}} \quad \textbf{3.87}$$

where ΔC_{FeCl_2} represents the difference in $FeCl_2$ concentration at the molten salt – oxide and the oxide – substrate interfaces. If the concentration of oxidised $FeCl_2$ is assumed to be negligible then the concentration of $FeCl_2$ at the oxide – substrate interface needs to be considered. Similarly, assuming that all Cl_2 is transformed into $FeCl_2$ then the concentration of Cl_2 at the oxide – substrate interface needs to be considered. Therefore:

$$\frac{dh_{ac}}{dt} = D_{FeCl_2}\frac{1}{C_{FeCl_2}}\frac{C_{Cl_2}^{in}}{h_{ac}} \quad \textbf{3.88}$$

where $C_{Cl_2}^{in}$ represents the concentration of Cl_2 at the oxide – substrate interface. Considering the diffusion of Cl_2 across the oxide scale now needs to be considered. In the model by Li et al. [121], the transport of Cl_2 across the oxide layer was assumed to happen instantaneously and hence followed a linear trend. Therefore, the transport of Cl_2 could be represented as follows:

$$C_{Cl_2}^{in} = \gamma\varphi(Cl^-) \quad \textbf{3.89}$$

where γ is a linear constant taking a value between 0 and 1 and $\varphi(Cl^-)$ is the concentration fraction of Cl^- in the molten salt melt. Equation 3.88 can now be expressed as:

$$\frac{dh_{ac}}{dt} = D_{FeCl_2}\frac{1}{C_{FeCl_2}}\frac{\gamma\varphi(Cl^-)}{h_{ac}} \quad \textbf{3.90}$$

which can be integrated to give an expression for h_{ac}:

$$h_{ac} = \sqrt{D_{FeCl_2} \frac{1}{C_{FeCl_2}} \gamma \varphi (Cl^-) t} \quad \textbf{3.91}$$

When considering the value of h_{ic}, Li et al. [121] assumed parabolic oxidation kinetics, assuming that the oxide layer would grow as defined in equation 3.27. The summation of h_{ac} and h_{ic} was then compared to experimental results for the corrosion for stainless steels 304 and 316L in molten nitrate Solar Salt, with results showing good agreements between the results obtained experimentally and from numerical modelling methods. However, in the model by Li et al. [121], the assumption of the linear transport of Cl_2 across the oxide layer may not be correctly capture the diffusion behaviour. To fully characterise the corrosion behaviour of a material within the molten Solar Salt, the diffusion characteristics of the Cl_2 across the oxide layer would need to be fully considered.

3.5.3.1 Impact of modelling assumptions on predictive models

The models discussed within this section both make assumptions to allow for simplification of the numerical models. However, these assumptions can impact the results obtained from each model, calling into question the validity of the results. In both models, the diffusion behaviour of species is considered, with assumptions made regarding the diffusion coefficients of alloying elements or the way in which diffusion behaviour can be characterised.

As mentioned previously when discussing the research of Lee et al. [118], the used diffusion coefficients were obtained from literature. However, great variance is observed between reported diffusion coefficients for alloying elements in a Ni – matrix. Hence, utilising only one diffusion coefficient may be inappropriate given that diffusion coefficients can vary greatly between literature sources. Therefore, in the numerical modelling undertaken within this research, multiple diffusion coefficients will be utilised for alloying elements, with the aim to capture the potential range of concentration changes based on these diffusion coefficients, leading to a more representative result of the oxidation and corrosion behaviour of Hastelloy C276.

3.6 Corrosion of Ni-based alloys in molten fluoride salt environments

In recent years there have been many corrosion studies conducted in molten fluoride salt environments using different combinations of materials and

environmental conditions. Typically, the fluoride salt combinations used in these studies are FLiBe and FLiNaK molten salt, with the materials being used commonly being Ni-based alloys due to their application to the nuclear industry.

This section aims to address current research regarding the high-temperature molten salt corrosion of different Ni-based alloys in both FLiBe and FLiNaK molten salts. Alongside this, this section also aims to discuss some of the major factors that may influence the corrosion of Ni-based alloys in molten fluoride salt environments.

3.6.1 Influential factors on corrosion in molten fluoride salts

A recent review by Guo et al. [16] highlighted several key factors that may influence the corrosion of a metallic material in a molten fluoride salt environment. These factors include the introduction of salt contaminants, galvanic interactions, temperature gradients, flow velocity and material microstructure. This section will focus on discussing studies that address each of these influential factors.

3.6.1.1 Introduction of salt contaminants: Secondary Reaction Products

Within a molten salt system, contaminants can be introduced into the salt by external conditions, such as the dissolution of moisture or oxygen into the melt from the air, or by the reactions between a metal alloy and the molten fluoride salt, forming metallic fluorides [122]. A study of the impact of different metallic fluorides on the corrosion behaviour of Incoloy 800H was conducted by Pavlik et al. [123], who added different concentrations of iron (II) fluoride (FeF_2), iron (III) fluoride (FeF_3), chromium (III) fluoride (CrF_3) and nickel (II) fluoride (NiF_2), ranging from 0 up to 10 mol.%, to a FLiNaK salt melt at 650 °C under an argon (Ar) cover gas in alumina crucibles. The corrosion damage of the Incoloy 800H coupons was quantified using the mass change of the coupons and expressed as a mass loss per unit area. The result obtained by Pavlik et al. [123] is presented as Figure 3.21.

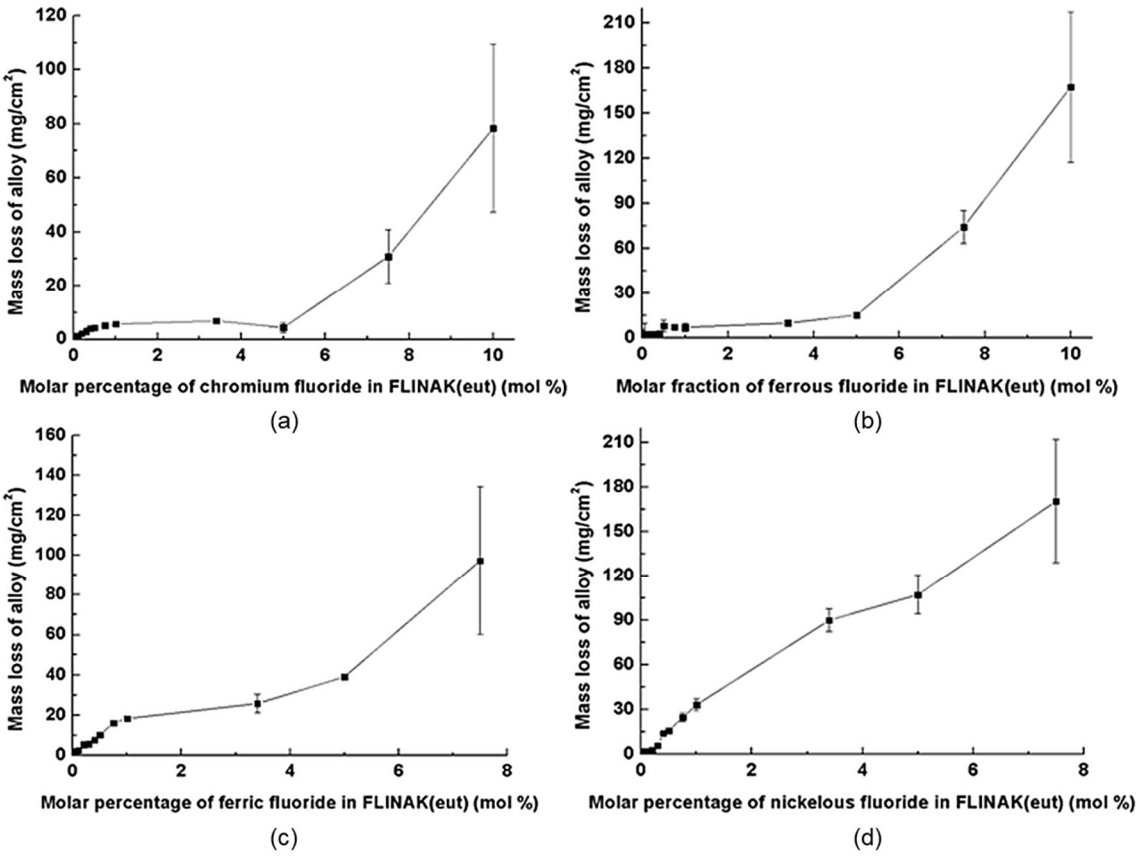


Figure 3.21 – Mass loss per unit area of Incoloy 800H coupons immersed in FLiNaK molten salt containing metallic fluoride impurities of a) CrF_3, b) FeF_2, c) FeF_3 and d) NiF_2 in quantities between 0 and 10 mol.% at 650 °C [123].

The result presented in Figure 3.21 shows that introducing increasing concentrations of metallic fluoride impurities into the melt results in an increase in the corrosion damage observed to the immersed material. The largest mass change was observed when NiF_2 was added to the FLiNaK molten salt. This may be due to NiF_2 being the least thermodynamically stable of the four metallic fluorides tested, as shown in Figure 3.20. The result of the thermodynamic instability of NiF_2 may be its dissociation in the FLiNaK melt and the production of F^- into the melt [123]. This would result in a more basic and corrosive molten salt. The most stable additive added to the melt was CrF_3, with specific mass change results reflecting this by showing the least mass change of all additives tested as shown in Figure 3.21. However, despite being the most stable additive, EDX results obtained for the substrate material indicated that the most Cr was lost from the Incoloy 800H substrate exposed to FLiNaK and CrF_3 as shown in Figure 3.22.

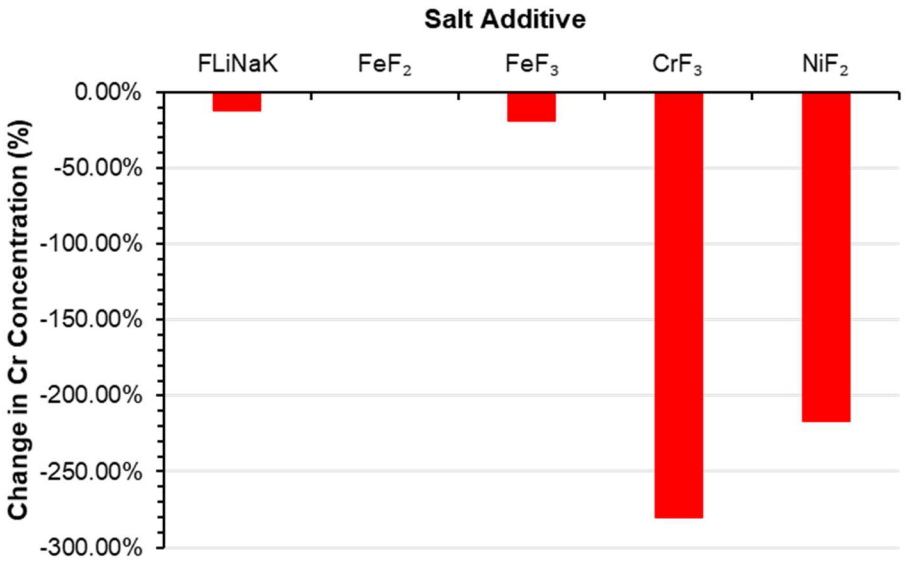


Figure 3.22 - Graph showing percentage change in Cr concentration after corrosion in FLiNaK containing different additives showing Cr dissolution is greatest after exposure to FLiNaK containing 3.4 mol.% CrF_3.

Despite having the smallest specific mass loss, exposure to FLiNaK containing CrF_3 resulted in the greatest dissolution of Cr from the substrate. This aggravation of Cr dissolution from the substrate has been observed in other research studies, with authors proposing that CrF_3 catalyses the dissolution of Cr from the substrate by the reaction defined by equation 3.92:

$$2CrF_3 + Cr \rightarrow 3CrF_2 \qquad \textbf{3.92}$$

Investigating the effect of introducing CrF_3 on the corrosion behaviour of different materials in molten salt environments has been performed by several authors, including Yin et al. [124], who added 0.4 wt.% CrF_3 to a FLiNaK molten salt melt to assess the impact of doing so on both stainless steels and Ni-based alloys. The addition of CrF_3 resulting in a greater mass loss being observed for both stainless steel and Ni-based alloy. The increase in mass loss was also accompanied by an increase in the depth of corrosive attack as shown in Figure 3.23.

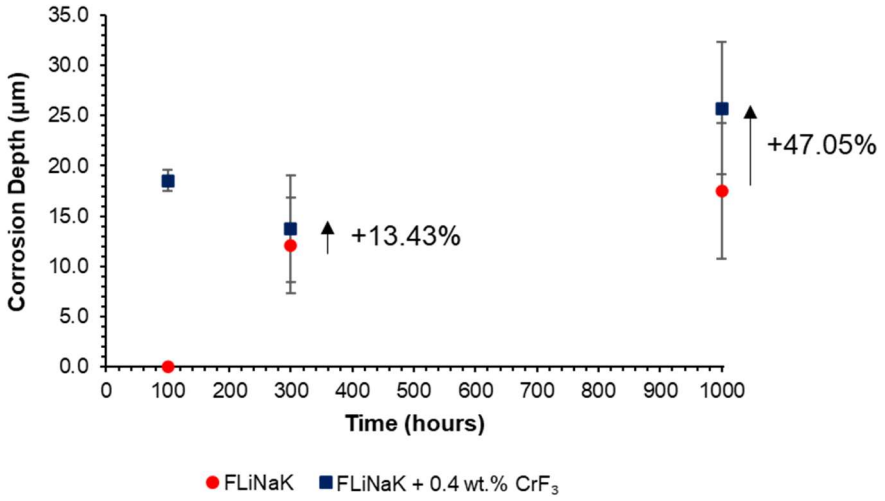


Figure 3.23 – Graph of corrosion depth with respect to time of Hastelloy N in pure FLiNaK salt and FLiNaK salt containing 0.4 wt.% CrF_3 at 700 °C at time intervals of 100, 300 and 1000 hours [124].

The introduction of 0.4 wt.% CrF_3 was observed to increase the corrosion depth of Hastelloy – N by 13.4% and 47.1% after 300 and 1000 hours of exposure, respectively. The study by Yin et al. [124] also investigated the effect of CrF_3 addition on the corrosion behaviour of stainless steel 316L, where similar observations regarding mass change and depletion depth were made. EDX analysis, conducted on cross-sections of stainless steel 316L, presented in Figure 3.24, also showed that Cr, Mn and Fe were all depleted from the grain boundaries during corrosive attack in FLiNaK containing CrF_3.

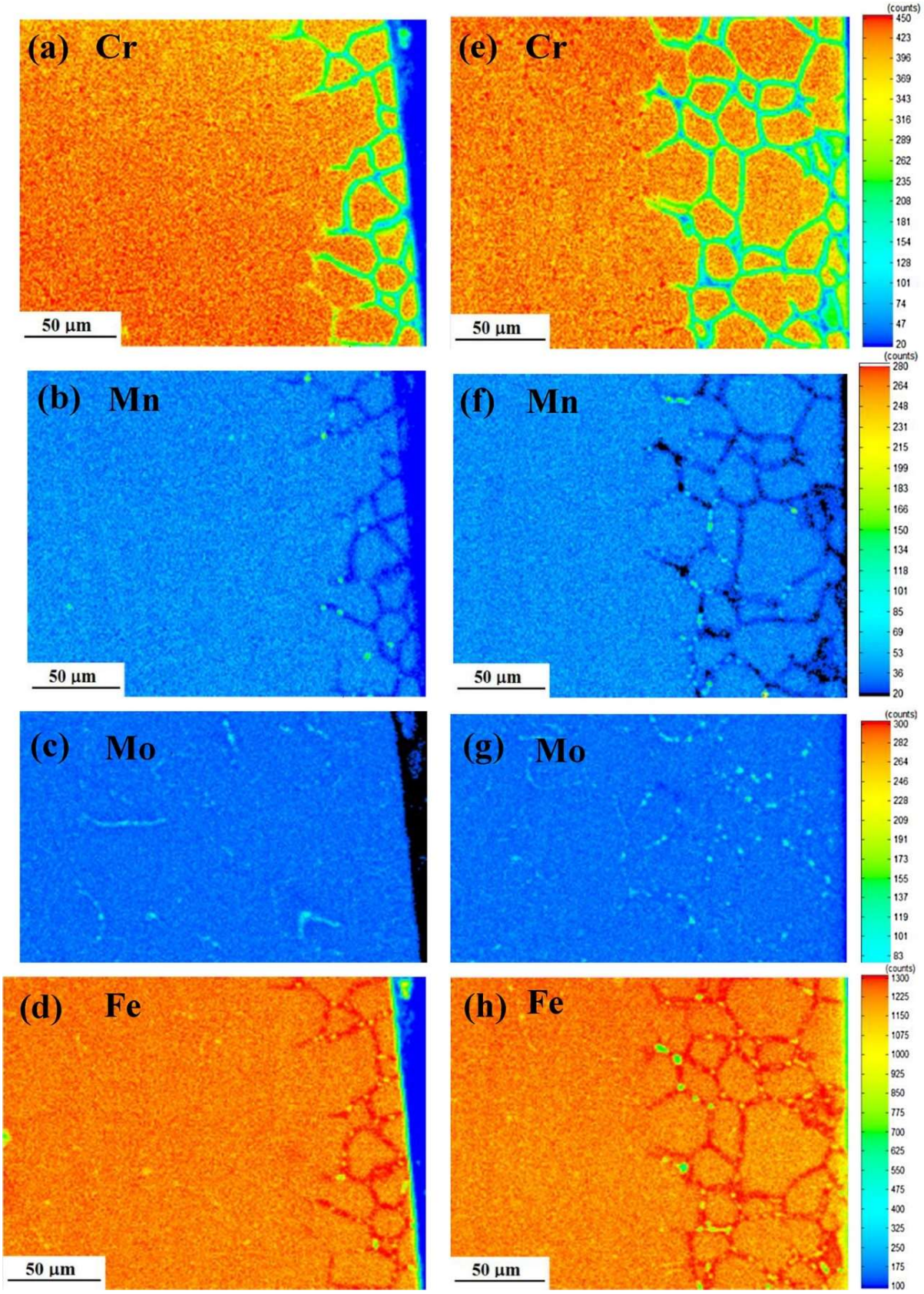


Figure 3.24 – EDX mapping analysis showing depletion of Cr, Mn and Fe from the grain boundaries of 316L after immersion in a) – d) molten FLiNaK salt at 700 °C and e) – h) molten FLiNaK containing 0.4 wt.% CrF_3 for durations of 1000 hours. Image taken from Yin et al. [124].

The depletion of Cr, Mn and Fe observed in Figure 3.24 was attributed to the formation of CrF_2, MnF_2 and FeF_2 by the reaction of these alloying elements with CrF_3 being thermodynamically favourable over other elements such as Ni [53].

3.6.1.2 Introduction of salt contaminants: Moisture

Alongside their research on the impact of fluoride based additives on the corrosion behaviour of metallic materials in molten salt environments, the impact of hydrous and anhydrous CrF_3 was investigated by Pavlik et al. [125]. In their experimental research, 0.5, 1.0, 3.0 and 5.0 mol.% of anhydrous CrF_3 and $CrF_3.3H_2O$ were added to a eutectic FLiNaK molten salt mixture at 680 °C. The same mass change method was used to quantify the corrosion damage of Incoloy 800H coupons as previously.

The specific mass change was observed to be more negative for the hydrated CrF_3 when compared with its anhydrous counterpart. Pavlik et al. [123, 125] proposed that this was due to the formation of hydrogen fluoride (HF), formed by the reaction of salt constituents with H_2O present within the salt mixture. Possible reactions are presented as equations 3.93 and 3.94 [126]:

$$MF + H_2O \xrightarrow{\square} MOH + HF \qquad \textbf{3.93}$$

$$2MF + H_2O \xrightarrow{\square} M_2O + 2HF \qquad \textbf{3.94}$$

where M represents lithium, sodium, or potassium, present in the FLiNaK molten salt. The formed HF is then able to react with the alloy with which it in contact by the following reaction:

$$Me + xHF \xrightarrow{\square} MeF_x + \frac{x}{2}H_2 \qquad \textbf{3.95}$$

where Me can represent any alloying element present within the alloy but is most likely to be an element such as Ni, Cr or Fe.

The production of HF by the reactions described in equations 3.93 and 3.94 were also cited as the reason for material corrosion by Ouyang et al. [127, 128]. To assess the impact of H_2O content on the corrosion behaviour Hastelloy B3 and Hastelloy N Ni-based alloys, Ouyang et al. [127] compared the corrosion behaviour of Ni-based alloys after subjecting them to FLiNaK molten salt containing 1.91 and 3.19 wt.% of H_2O. These quantities of H_2O were achieved using two different heating protocols. Similarly, to previously discussed work, the corrosion behaviour was assessed by measuring the mass change of the coupons and presenting this

mass change per unit area. It was observed that the mass loss increased by a minimum of 195% when the amount of moisture was increase from 1.91 wt.% to 3.19 wt.%, this is shown in Figure 3.25.

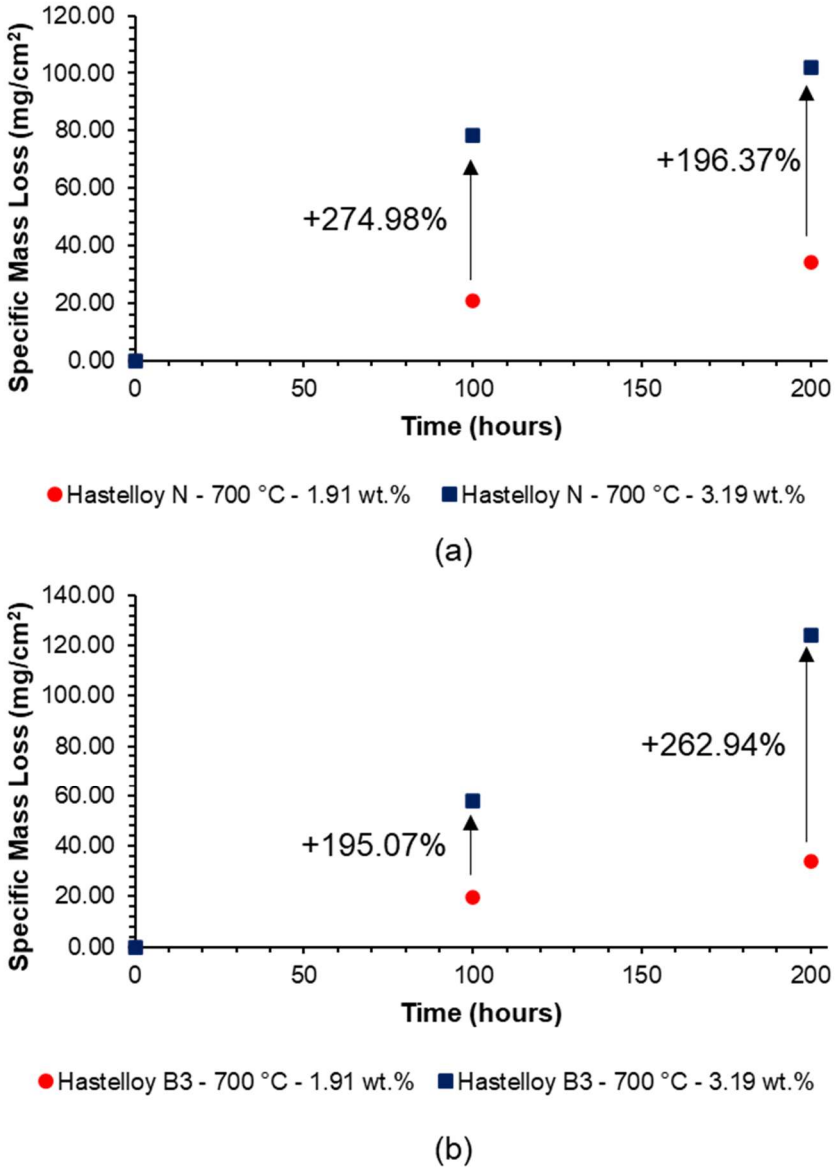


Figure 3.25 – Specific mass loss of a) Hastelloy N and b) Hastelloy B3 Ni-based alloys after immersion in a molten FLiNaK salt environment containing 1.91 and 3.19 wt.% H_2O at 700 °C for 100 and 200 hours. Results, adapted from Ouyang et al. [127], show a drastic increase in the alloy mass loss when H_2O content is increased.

As mentioned, the reason for this increase was believed to be due to the production of a greater concentration of HF by the reactions described by equations 3.93 and 3.94. The production of a greater concentration of HF by these reactions results in a higher activity of F^- within the melt, making the melt more basic and hence more corrosive to materials as per the Lewis acid/base model [46].

Post-experimental analysis of Hastelloy B3 and Hastelloy N samples, immersed in molten salt environments containing moisture was conducted by taking micrographs of corroded coupons. Micrographs of tested coupons, presented in Figure 3.26, shows that increasing the concentration of H_2O within the molten salt, increased both intergranular and intragranular corrosion, with intergranular corrosion being observed by corrosive attack at the grain boundaries. Intragranular corrosion was observed in the form of pitting corrosion.

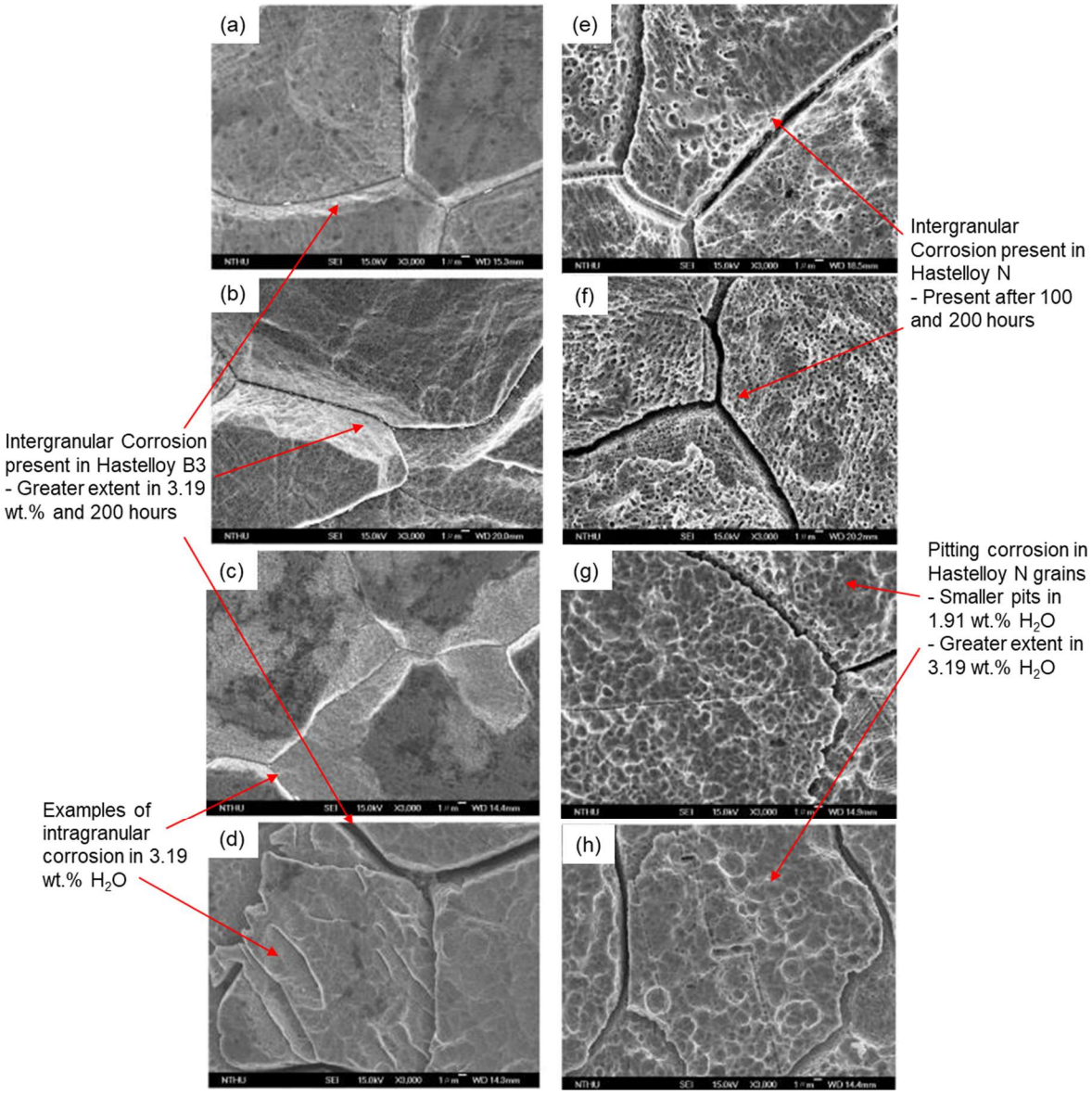


Figure 3.26 – Micrographs of coupons of a) – d) Hastelloy B3 and e) – h) Hastelloy N, immersed in FLiNaK molten salt at 700 °C containing 1.91 wt.% and 3.19 wt.% H_2O for 100 and 200 hours showing both intergranular and intragranular corrosive attack as labelled. Figures taken from experimental study by Ouyang et al. [127].

The impact of H_2O content on the corrosion of Ni-based alloys in molten salt environments has also been researched using electrochemical impedance

spectroscopy (EIS). The research, conducted by Wang et al. [129], involved immersing coupons of GH3535 Ni-based alloy in FLiNaK molten salt at 700 °C. During the study, a comparison was made between the observed corrosion behaviour in molten FLiNaK salt without H_2O and containing 5 wt.% H_2O. Similarly, to studies discussed previously, increasing the concentration of H_2O present in the melt increased the corrosion damage of immersed coupons. The increase in corrosion rate of GH3535 in the melt containing H_2O was reflected by greatly reduced impedance values when compared to the corrosion of GH3535 in the pure FLiNaK salt.

Post experimental analysis was conducted on GH3535 coupons using SEM and EDX analysis. Cross-sections of GH3535 coupons, imaged using SEM, showed that internal voids had formed within the substrate material. This differed from the analysis performed by Ouyang et al. [127], who showed that grains had undergone pitting corrosion. This difference may be attributed to the more aggressive nature of the melt used by Wang et al. [129] who utilised a higher percentage of H_2O. In results similar to those presented in the research conducted by Ouyang et al. [127], the use of a high quantity of H_2O within the melt may result in higher concentrations of HF dissolved within the FLiNaK melt, resulting in a more basic and corrosive melt as per the Lewis acid/base model.

3.6.1.3 Introduction of salt contaminants: Ionic compounds

Although research has focused on the inclusion of H_2O and fluoride-based impurities, the addition of other ionic compounds has also been of interest. The addition of other ionic salts may impact the corrosion behaviour of materials within the melt as per the Lux-Flood and Lewis acid/base models. For example, the material degradation of 316L stainless steel has been assessed in FLiNaK molten salt with the addition of sulphate (SO_4^{2-}) containing salts. The addition of SO_4^{2-} has been of particular interest due to its potential formation during the synthesis of the raw materials of FLiNaK salt [130]. The research, conducted by Qiu et al. [131], involved adding sodium sulphate (Na_2SO_4) to a FLiNaK molten salt mixture in quantities of 100 parts per million (ppm) and 500 ppm. Results from tests containing SO_4^{2-} were compared to those from a pure molten FLiNaK salt mixture. Mass change results showed coupons immersed in molten FLiNaK containing SO_4^{2-} were more heavily corroded than those immersed in a pure FLiNaK salt mixture, with coupons of 316L being immersed in a molten salt environment containing 500 ppm SO_4^{2-} being the most heavily corroded. The corroded surfaces of coupons subjected to 100 ppm of SO_4^{2-} showed corrosion at the grain boundaries, with coupons immersed in FLiNaK with 500 ppm SO_4^{2-} showing a

greater extent of corrosion at the grain boundaries, as well as pitting corrosion. Similar observations were made in the study by Zhu et al. [132] who investigated the effect of SO_4^{2-} inclusion on the corrosion of GH3535 Ni-based alloy. In both cases, the inclusion of SO_4^{2-} within the FLiNaK molten salt caused an increase in the corrosion rate of the immersed material by the dissolution of Cr from the metal matrix. The proposed reaction by which this occurs is included as equation 3.96.

$$Na_2SO_4 + Cr \rightarrow S + Na_2O + Cr_2O_3 \qquad \textbf{3.96}$$

In equation 3.96, the SO_4^{2-} ions are acting as an oxidant, reacting with Cr present in the alloy, forming Cr_2O_3, which can then either form on the substrate material surface, or dissolve into the salt. In the study of GH3535, increasing concentrations of Cr were measured within the salt with increasing quantities of SO_4^{2-}, lending itself to the theory that SO_4^{2-} inclusion leads to the increased dissolution of Cr from the alloy.

However, in the absence of sulphur (S), the addition of O^{2-} ions into the FLiNaK salt melt can limit the dissolution of Cr from the alloy by forming a protective oxide layer, which was illustrated by Ai et al. [133]. In their study, Ai et al. [133] added O^{2-} in quantities of 0 ppm, 200 ppm, 500 ppm, 800 ppm and 1000 ppm by adding varying quantities of lithium oxide (Li_2O) to FLiNaK salt to observe its impact on the corrosion of 316 stainless steel at 650 °C. A comparison was made between the mass changes of 316 stainless steel samples in ordinary FLiNaK and samples immersed in FLiNaK with 1000 ppm of O^{2-}. Results showed that the addition of O^{2-} prevented mass loss, actually causing a mass gain of 0.77 mg/cm^2. This was shown to be caused by the formation of an $LiCrO_2$ corrosion product layer, preventing the dissolution of Cr from the alloy material.

A similarly methodology was deployed by Sankar and Singh [134], who added 0.5 wt.% of Li_2O to FLiNaK molten salt to study the impact of the O^{2-} addition on the corrosion behaviour of Haynes 244, Hastelloy N and 316H stainless steel. Analysis conducted on corroded samples confirmed the presence of a $LiCrO_2$ corrosion product layer, corroborating the observations made by Ai et al. [133]. However, although Cr was no longer being removed from the alloys, Mo was now targeted and being preferentially removed from the corroded samples. This was observed for all three alloys tested when Li_2O was added and resulted in mass losses of all three alloys.

The study by Sankar and Singh [134] was expanded beyond Li_2O to also include NiO and Cr_2O_3 impurities, conducting experiments using 0.1 wt.% and 0.5 wt.% of NiO, as well as using 0.5 wt.% Cr_2O_3. When adding 0.5 wt.% of Cr_2O_3 to FLiNaK

molten salt, no change was noticed in the corrosion behaviour of each alloy compared with the baseline molten FLiNaK salt tests, suggesting the addition of Cr_2O_3 had little to no impact on the corrosion mechanism.

The addition of NiO had a much larger impact on the corrosion behaviour of the three test alloys. The addition of 0.5 wt.% NiO to the FLiNaK melt resulted in an increased corrosion depth in each of the alloys which were achieved through different means. When assessing the corrosion of 316 stainless steel, intergranular corrosion was observed. In Hastelloy N and Haynes 244, the corrosive attack resulted in the formation of micro-voids and the selective dissolution of Cr from the alloy. Similar observations were made when 0.1 wt.% NiO was added to the melt, however, the corrosive damage to each alloy was to a much lesser extent when compared with 0.5 wt.%.

3.6.1.4 Introduction of salt contaminants: Tellurium introduction during nuclear fission

A more current impurity being researched is tellurium (Te) and its impact on material degradation. The phenomena of Te induced intergranular cracking was an issue first observed during the MSRE and was identified by McCoy [17]. McCoy identified that materials had undergone intergranular cracking, and that Te was present within the grain boundaries of the Inconel 600 material used. The theory being that Te was introduced as a product of the nuclear fission process in which U-233 is bombarded with high energy neutrons, causing fission of the U-233 isotope, resulting in the production of heat which can be removed and used in power generation. A potential biproduct of this process is Te. Since the preliminary study conducted during the MSRE, research has been conducted by several authors, who added Te based compounds to different combinations of molten salts to assess the impact of Te addition on the corrosion behaviour of different Ni-based alloys. A summary of such studies, conducted by Ignatiev et al. [43, 135, 136] is provided in Table 3.6.

Table 3.6 – Summary of Te intergranular cracking experimental conditions utilised in the studies of Ignatiev et al. [43, 135] showing the introduction of Te into the salt in the form of Cr_3Te_4.

Test Number	Salt Combination (mol.%)	Specimen Material	T_{max} (°C)	Exposure Time (hours)
Te – 1	LiF – NaF – BeF_2 + Cr_3Te_4 (15-58-27)	HN80M-VI HN80MTY MONICR	700	400
Te – 2	LiF – BeF_2 – ThF_4 – UF_4 + Cr_3Te_4 (73-5-20-2)	HN80M-VI HN80MTY	750	1250
Te – 3	LiF – BeF_2 – UF_4 + Cr_3Te_4 (71-27-2)	HN80M-VI HN80MTY	780	750

In the studies summarised in Table 3.6, the results showed that the HN80MTY material was the most resistant to corrosion and intergranular cracking (IGC) in each of the different salt combinations. This is shown in Figure 3.27 which shows micrographs of alloys after test number Te – 1, defined in Table 3.6.

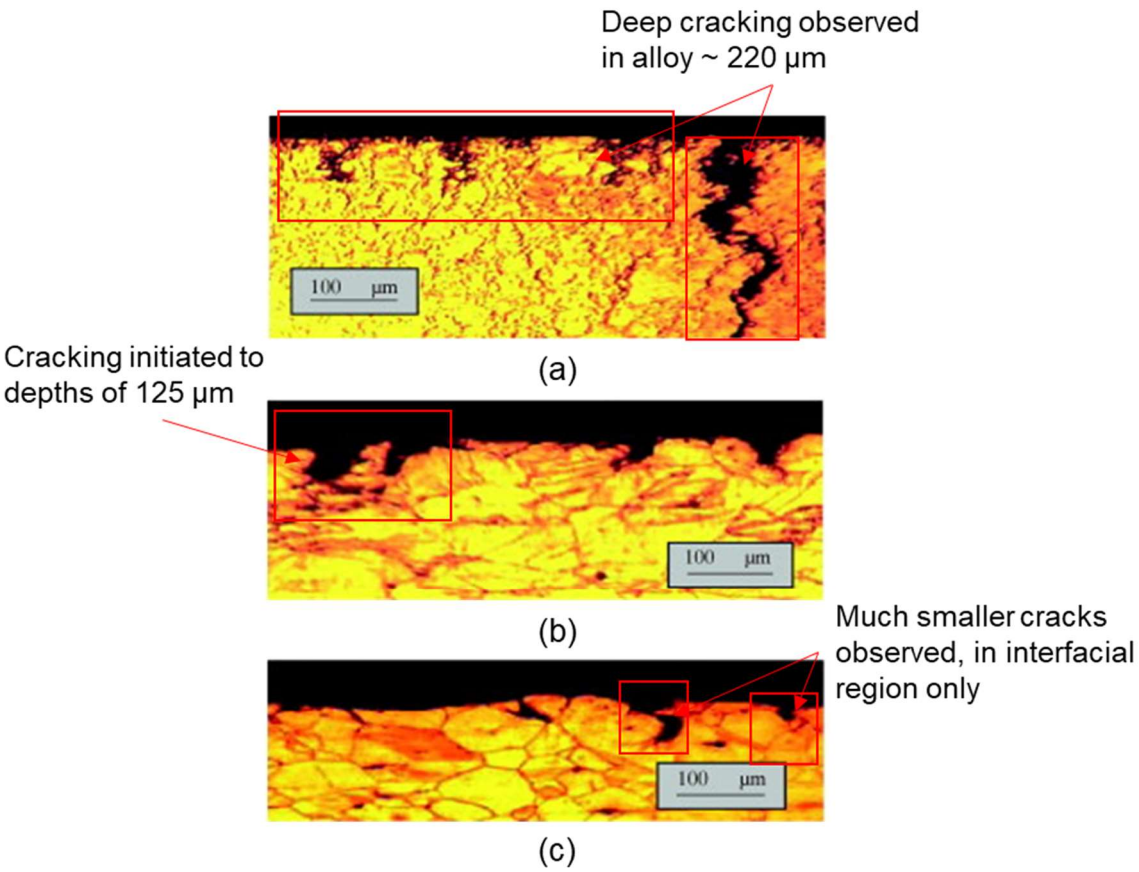


Figure 3.27 – Micrographs of a) MONICR, b) HN80M-VI and c) HN80MTY alloys after immersion in LiF – NaF – BeF_2 molten salt at 700 °C after 240 hours showing that HN80MTY was much less susceptible to IGC than HN80M-VI and MONICR alloys. Figure adapted from [43]

Results presented in Figure 3.27 show that the extent of IGC in the MONICR and HN80M-VI alloys was much more severe than that for HN80MTY, both in terms of the number of cracks initiated and the depth of cracking. This performance by the HN80MTY alloy was attributed to the introduction of Al into the materials composition. A comparison of the materials compositions is presented as Table 3.7.

Table 3.7 – Composition of HN80M-VI, HN80MTY and MONICR alloys used in Te intergranular cracking studies by Ignatiev et al. [43, 135] highlighting the difference in Al concentration as a contributing factor to the improved cracking resistance of HN80MTY.

Alloy	Ni	Cr	Mo	Ti	Fe	Mn	Nb	Si	Al
HN80M-VI	Base	7.61	12.2	0.001	0.28	0.22	1.48	0.040	0.038
HN80MTY	Base	6.81	13.2	0.93	0.15	0.013	0.01	0.040	1.12
MONICR	Base	6.875	15.8	0.026	2.27	0.037	<0.01	0.13	0.02
Alloy	**W**	**Cu**	**Co**	**Ce**	**Zr**	**B**	**S**	**P**	**C**
HN80M-VI	0.21	0.12	0.003	0.003	0.00	0.008	0.002	0.002	0.02
HN80MTY	0.072	0.020	0.003	0.003	0.00	0.003	0.001	0.002	0.025
MONICR	0.16	0.016	0.03	<0.003	0.075	<0.003	0.003	0.003	0.014

The increase in the added concentration of Al into HM80MTY, highlighted in Table 3.7, was believed to be the reason for the decreased susceptibility of HM80MTY to Te intergranular cracking. Analysis of the material microstructures indicated that the introduction of Al to the alloy caused the discontinuation of the carbide phases throughout the microstructure, resulting in a more sparsely distributed carbide phase, making this alloy phase less susceptible to attack by the molten salt.

3.6.1.5 Interactions of dissimilar materials

In the study of molten salt corrosion, the container material used has been shown to impact the corrosion behaviour of alloys being tested, particularly in the case of dissimilar container material and test coupons. Since MSRs are designed to mitigate the effects of dissimilar metal interactions, laboratory experiments should be conducted in a similar fashion to ensure MSR conditions are replicated as much as possible.

A study by Kondo et al. [41] investigated the corrosion behaviour of the ferritic alloy JLF-1 in both FLiBe and FLiNaK salt at temperatures of 500 °C and 600 °C. During the study, crucibles constructed from JLF-1, Ni and Nb were used to understand the impact of crucible material on the corrosion behaviour of the JLF-1 coupons in FLiNaK molten salt. The use of a Ni crucible was observed to increase the mass loss of JLF-1 coupons with an enriched layer of Fe being observed on the Ni crucible surface. In the case of the Nb crucible, a mass gain was observed instead of a mass loss, with surface analysis of coupons indicating the presence of Nb rich layer on the surface of JLF-1 corroded samples.

In many corrosion studies, graphite crucibles have also been used in static immersion tests. One such study by Zheng et al. [74] utilised both graphite and 316L crucibles when assessing the corrosion behaviour of 316L in molten FLiBe salt at 700 °C for durations up to 3000 hours. Similarly, to many studies discussed in this review, the corrosion damage was quantified using a specific mass loss. The mass loss results showed that a greater mass was lost from 316L samples immersed in FLiBe molten salt in graphite crucibles than in crucibles constructed from 316L. The increase in mass loss was also accompanied by an increase in the depth of corrosion attack of 316L coupons as shown in Figure 3.28.

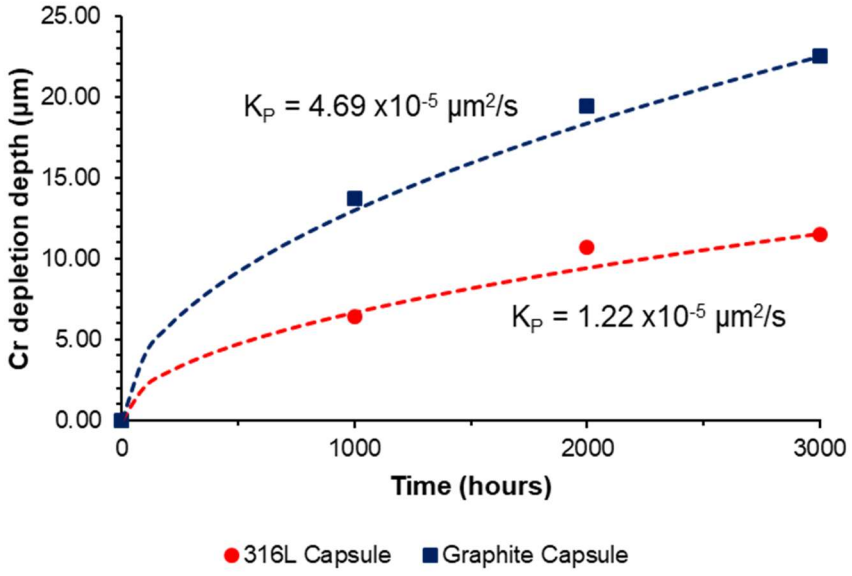


Figure 3.28 – Graphs of a) depth of Cr corrosion attack against time for 316L, corroded in FLiBe molten salt at 700 °C in a 316L crucible and a graphite crucible, with greater corrosion depth being observed after immersion in FLiBe salt in a graphite crucible [74].

The increase in corrosion damage in the graphite crucible was believed to be due to the reaction of C with Cr, forming Cr carbide phases which were shown to be adhered to the graphite crucible. This was supported by Qiu et al. [137] who conducted research investigating the corrosion of pure Cr in FLiNaK molten salt using graphite crucibles. The results of this study showed that Cr_7C_3 particles were deposited around the graphite crucible, potentially formed by the reaction defined as equation 3.97:

$$7Cr + 3C \rightarrow Cr_7C_3 \qquad \textbf{3.97}$$

Other studies investigating the impact of graphite crucible material on the corrosion of Ni-based alloys in FLiNaK salt have shown that Cr – carbides of the structure

$Cr_{23}C_6$ can also form by the reaction of Cr with the graphite crucibles, illustrated by equation [69, 138].

$$23Cr + 6C \xrightarrow{\square} Cr_{23}C_6 \quad \textbf{3.98}$$

Considering equations 3.97 and 3.98, both equations have negative Gibbs free energy changes, hence both reactions are thermodynamically favourable. However, the reaction for the formation of $Cr_{23}C_6$ carbides is more favourable as reaction 3.98 has a more negative free energy change [137]. Therefore, Cr_7C_3 carbides are likely to form by the reaction of $Cr_{23}C_6$ carbides with the graphite crucible, which is a more favourable reaction than reaction 3.97 [69]. This reaction is shown as equation 3.99:

$$7Cr_{23}C_6 + 27C \xrightarrow{\square} 23Cr_7C_3 \quad \textbf{3.99}$$

A separate study conducted by Zheng et al. [138], investigating the impact of dissimilar crucible materials to the test coupon. This study focused on a graphite crucible and a graphite crucible containing a Ni lining. The corrosion behaviour of the testing material, Hastelloy N, was quantified using a mass change technique over a duration of 1000 hours at a test temperature of 700 °C. The mass change results showed mass was lost from the Hastelloy N coupons in both cases, with greater mass losses being observed from Hastelloy N samples immersed in the graphite crucible compared with the graphite crucible containing a Ni lining. In the case of the graphite crucible, 0.165 mg/cm^2 was lost from Hastelloy N coupons compared with 0.124 mg/cm^2 when coupons were immersed in a graphite crucible containing a Ni-liner.

Examination of the corroded samples was conducted using XRD which indicated the presence of Cr_7C_3 on the corroded surfaces. Previous research by Olson et al. [53] suggested that the formation of Cr_7C_3 was formed by the reaction of CrF_2 and C at the molten salt-graphite interface as per equation 3.100:

$$21CrF_2 + 3C \xrightarrow{\square} Cr_7C_3 + 14CrF_3 \quad \textbf{3.100}$$

A key finding from the study by Zheng et al. [138] was the significant depletion of Cr from Hastelloy N after 1000 hours of immersion in the FLiBe salt at 700 °C. As presented earlier when discussing the inclusion of CrF_3 on the corrosion behaviour of Ni-based alloy the inclusion of CrF_3 was observed to aggravate the dissolution of Cr from the material immersed in molten salt by reacting with Cr, oxidising it from Cr to CrF_2 by the reaction defined in equation 3.92. Therefore, the combined impact of the reactions defined in equations 3.92 and 3.100 may explain the increased

degradation of alloys in graphite crucibles that has been observed in numerous molten salt corrosion studies.

3.6.1.6 The effect of temperature and temperature gradients

Due to the design of the MSR, multiple circuits are used to circulate different salts which are maintained at different temperatures. The result of this can be large temperature changes and temperature gradients within the system which may cause different corrosion rates in different locations. It may also result in different corrosion mechanisms being more favourable in different regions. During flow loop testing, conducted at the Oak Ridge National Laboratory [27], different corrosion behaviours were observed in regions with different temperatures. In the flow loop testing, Hastelloy N tubing was used in conjunction with clamshell heaters to induce the desired temperature gradients within the experimental flow loop. The molten salt used within the flow loop was the same as that used in MSRE, described in Section 2.3, which consisted of LiF, BeF_2, ZrF_4 and UF_4 in proportions of 65.0, 29.1, 5.0 and 0.9 mol.% respectively. The experimental set up and resulting corrosion damage of the Hastelloy N tubing is presented in Figure 3.29.

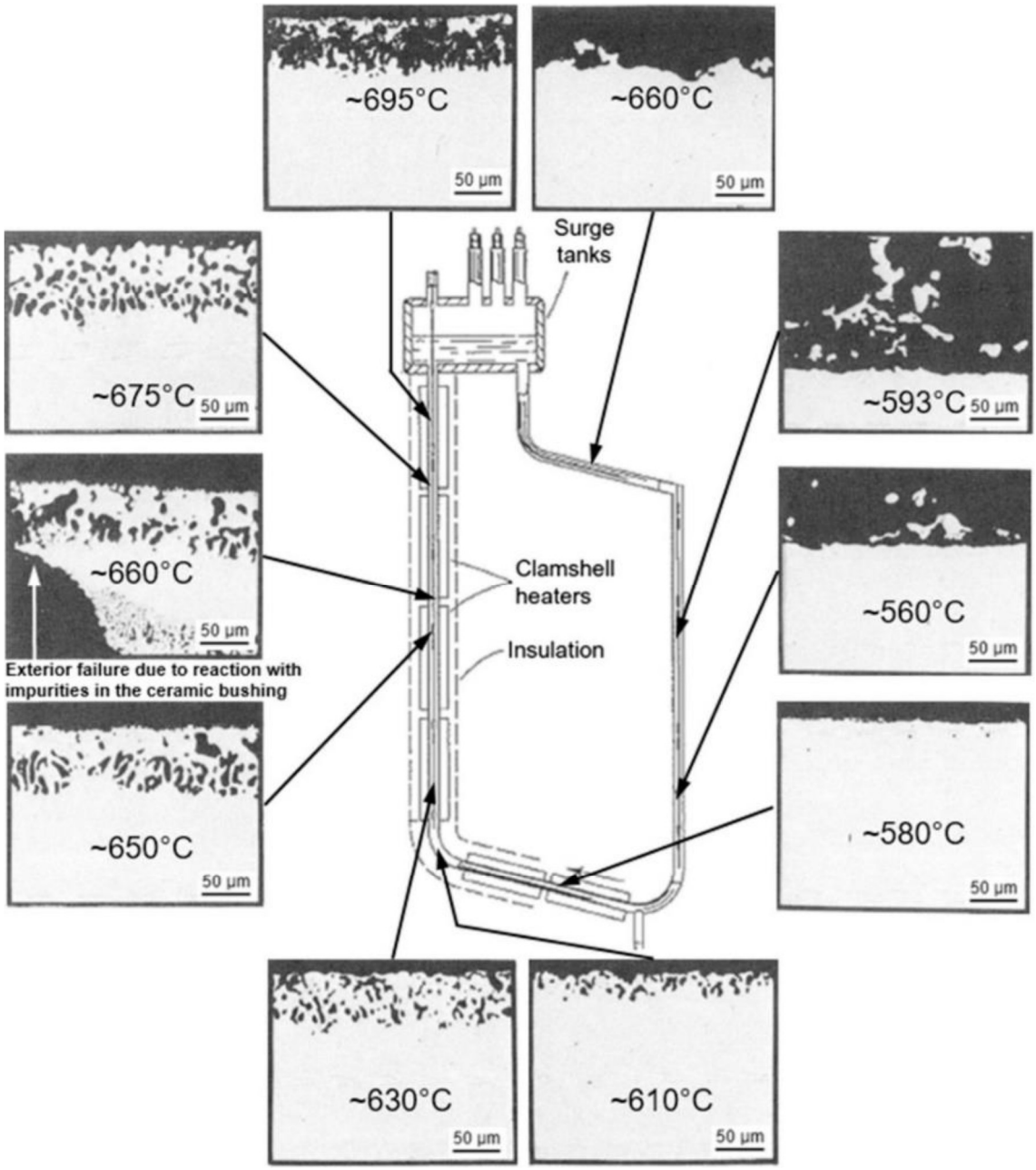


Figure 3.29 – Schematic of the experimental flow loop combined with micrographs taken of Hastelloy N samples taken from each region. Micrographs show the wide range of corrosion behaviour observed at the different operating temperatures [27] .

The result presented in Figure 3.29 show higher level of corrosive attack on Hastelloy N in hotter regions of the system, with material in higher temperature regions having greater mass losses and greater depths of corrosive attack. Material located in cooler regions of the flow loop did not exhibit the same severity of attack, with some regions also having a mass gain due to the formation of a corrosion product layer. It can therefore be concluded that increasing the temperature of the molten salt can greatly aggravate the corrosion behaviour. This is the case due to the increased thermodynamic driving force for Cr dissolution

from the metal alloy [44]. Over time the salt will also be affected by the introduction of impurities into the melt which can aggravate the corrosion of any immersed materials as per the discussion of previous studies in Section 3.6.1.1.

The impact of changing the temperature on the corrosion behaviour of alloys has been studied extensively by many researchers. The effect of temperature was studied by Kondo et al. [41] on the ferritic steel JLF-1. In the study, FLiBe molten salt was used, with samples being immersed at temperatures of 500 °C and 600 °C. The results showed no difference in the mass changes or corrosion depths, however, chemical analysis of the molten salt after testing showed greater concentrations of both Cr and Fe after testing at 600 °C when compared with the salt after testing at 500 °C. Fewer carbide phases were also observed on samples of JLF-1 immersed in FLiBe at 600 °C, suggesting that C had been removed from the samples during exposure. Similar observations were made in the research by Ouyang et al. [127] when assessing the effect of moisture on the corrosion behaviour of two Hastelloy type Ni-based alloys in molten FLiNaK salt. In their study Ouyang et al. [127] conducted experiments at both 600 °C and 700 °C with a moisture content of 3.19 wt.%. The corrosion behaviour, quantified by mass change measurements, showed that greater mass losses were observed when the test temperature was increased. This was shown to be due to a greater extent of intergranular corrosion, as well as pitting corrosion at the elevated temperature.

The previously discussed studies have shown that increasing the temperature of the corrosive medium generally results in an increase in the extent of corrosion damage. However, the precise impact of temperature gradients on the corrosion performance requires more complex investigation. One such study investigated the effect of temperature gradients on the corrosion behaviour of the Ni-based alloy GH3535 and pure Cr in FLiNaK molten salt. The study, conducted by Wang et al. [139] involved inducing temperature gradients of 50 °C and 100 °C by having samples immersed in molten salts in a cold leg and a hot leg which were held at 650 °C and 700 ºC for tests conducted using a temperature gradient of 50 °C and at 600 °C and 700 °C for tests with a temperature gradient of 100 °C. The studies were based on the hypothesis that the effect of inducing temperature gradients was similar to that of galvanic corrosion, in which materials in a cooler region act as a cathode and materials in a hotter region act as the anode. Based on this hypothesis, electrochemical measurement techniques could be applied to measure the effect of inducing a temperature gradient. In the study, potentiodynamic polarisation measurements were made. The open circuit potential (OCP) was also monitored. Galvanic measurements obtained over a 100 °C temperature gradients were larger than those measured over a 50 °C temperature gradient, indicating

that the materials immersed in a system with larger temperature gradients would undergo a greater extent of galvanic corrosion. This finding was corroborated by mass change measurements which showed that both Cr and GH3535 had greater mass losses over a larger temperature gradient, with the materials immersed in the hot leg having the greatest mass loss, hence confirming their function as the anode in the electrochemical cell.

3.6.1.7 Static versus dynamic corrosion conditions

When studying the corrosion of metallic materials in molten salt environments, a static immersion is commonly used. This method involves placing coupons of test material in a static molten salt environment. This can be achieved in two ways. In the first method, test materials are placed in a crucible containing a solid salt mixture. The crucible is then heated until the salt mixture melts, immersing the test materials in the molten salt. Alternatively, a salt mixture is melted prior to the addition of the test materials and then pumped into a secondary system in which it immerses the test materials in molten salt and then remains static.

The method of pumping a molten salt solution into a crucible containing test coupons was achieved by Olson et al. [53] who tested the corrosion behaviour of five alloys Ni-201, Hastelloy N, Hastelloy X, Inconel 617, Haynes 230 and Incoloy 800H in a FLiNaK molten salt solution, held at 850 °C. The test coupons were left in the static system at the test temperature for 500 hours. The test coupons were then removed, cleaned, and had their mass change measured.

Results of this study showed that under static immersion conditions, the specific mass loss increased with increasing Cr content within the alloys for Ni-based alloys. However, as a Fe-based alloy, Incoloy 800H did not follow the same trend indicating that alloy composition plays a key role in the corrosion of alloys in molten salt environments. This may be due to the different mechanism of corrosion of Fe-based alloys in molten salt environments. This will be discussed further in the following section.

Due to the flowing conditions of MSR systems, the study of the corrosion behaviour of alloys under dynamic conditions is equally important as understanding the corrosion behaviour under static conditions. A study by Kondo et al. [140] compared the corrosion of JLF-1 ferritic steel under static and dynamic corrosion conditions in FLiNaK molten salt at 600 °C. To achieve dynamic operating conditions, an impeller was used to achieve a molten salt flow velocity of 0.17 m/s. The corrosion behaviour of JLF-1 was assessed by measuring the mass change after 250 and 1000 hours of testing. Mass loss measurements showed little

difference between the two testing methods, although SEM analysis showed that pits had formed on the exposed surfaces of JLF-1 coupons, with the extent of pitting corrosion being greater on samples tested under static conditions compared with those under flowing conditions. The reason for this was due to the lack of stagnation of impurities at the molten salt – substrate interface under the flowing conditions, with the molten salt being replenished at the corrosion interface.

Additional static immersion studies, conducted by Kondo et al. [71, 141], investigating the corrosion behaviour of a variety of materials, including stainless steels and Ni-based alloys in molten FLiBe salt. These studies focused on stainless steels 304 and 316L as well as Ni-based alloys Hastelloy C276, Inconel 600 and Inconel 625 at temperatures of 500 °C and 600 °C for durations up to 1000 hours. In these studies, the corrosion behaviour was quantified using a mass change technique which was then used to estimate the corrosion rate for each of the materials tested. The results for each material at both temperatures are summarised in Figure 3.30.

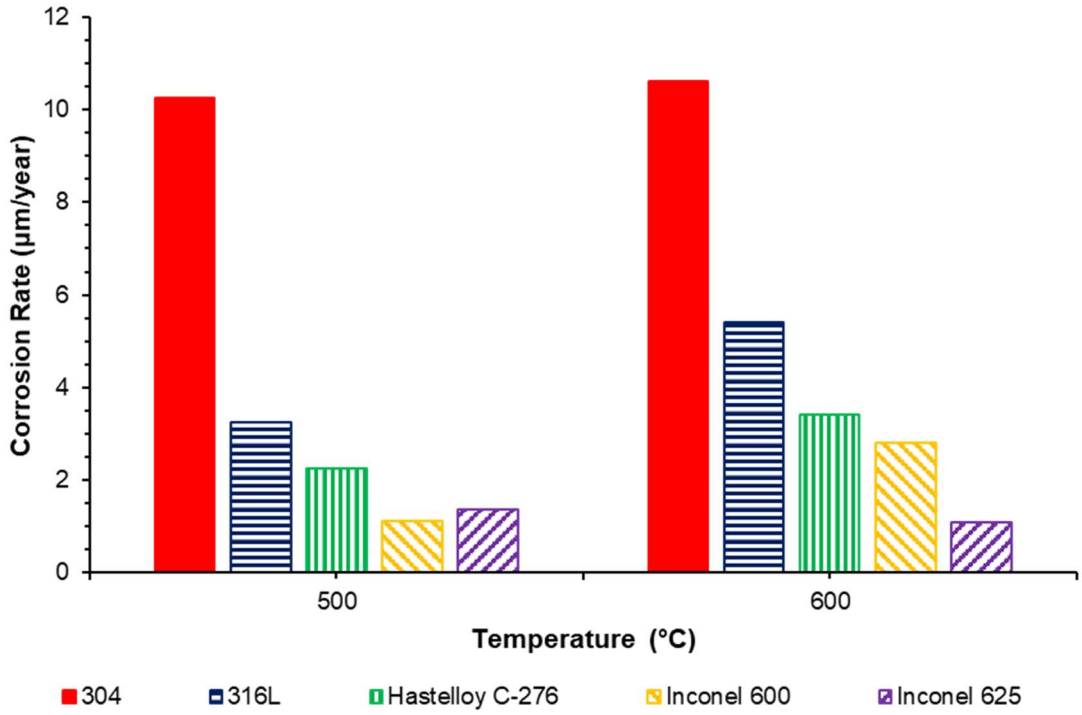


Figure 3.30 – Graph showing corrosion rate against temperature for stainless steels 304 and 316L as well as Ni-based alloys Hsatelloy C276, Inconel 600 and Inconel 625 showing better corrosion resistance of Ni-based alloys in FLiBe molten salt [71, 141].

Generally, Figure 3.30 shows that Ni-based alloys have better corrosion performance in FLiBe salt compared with stainless steels. The difference in observed performance was believed to be due to the compositional and

microstructural differences between the alloys tested. The Ni-based alloys have much higher Ni contents than the stainless steels as well as lower contents of less noble elements such as Fe and Cr that can be preferentially attacked in a molten salt system [6]. However, all five alloys had very similar concentrations of Cr which was shown to be preferentially attacked for all materials. This was observed by EDX analysis which showed Cr depleted regions near the alloy – molten salt interface and by inductive coupled plasma – mass spectroscopy (ICP-MS) which showed that the concentration of Cr present in the FLiBe salt after testing had increased drastically during experimentation.

For applications in CSP storage, the impact of dynamic flow on the corrosion of materials have been more extensively researched than in MSR conditions [142, 143]. However, these studies have focused on the use of nitrate and nitrite salt combinations as the HTF and corrosive medium. Although they have shown potential to be used in CSP systems as an HTF, the use of nitrate salts in MSR systems would not be favourable. Due to the higher operating temperatures of the MSR compared with CSP systems, the HTFs are required to have good high temperature stability. In the temperature ranges of MSR operation, in excess of 700 °C, nitrate salts are not stable enough to ensure efficient operation [144].

Despite the unsuitability of nitrate salts for MSR applications, insight into the impact of molten salt flow conditions on the corrosion of materials may translate to molten fluoride salts in future research. One such study was conducted by Zhang et al. [143], in which stainless steels 316 and 321 were immersed in Solar Salt at 565 °C. A rotating cylinder device was utilised to simulate dynamic corrosion conditions, with experiments taking place at flow velocities of 1 m/s, 2 m/s and 3 m/s. In the study, the corrosion degradation was quantified using specific mass change, with these measurements showing that the weight lost from the coupons increased with flow velocity. It was also observed that the weight loss adhered to a parabolic rate law. This result is presented in Figure 3.31.

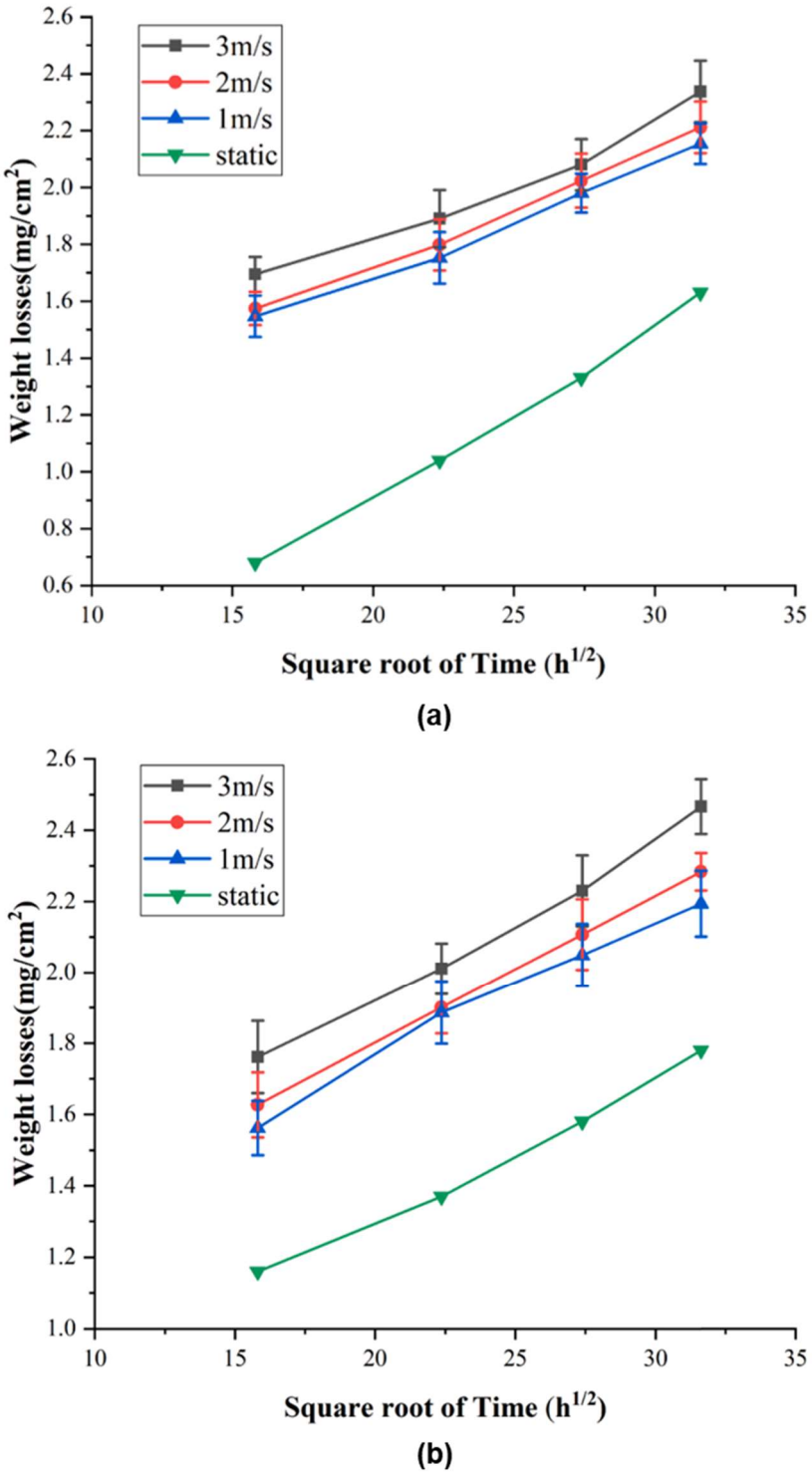


Figure 3.31 – Plots of material loss against the square root of time for the corrosion of stainless steels (a) 316 and (b) 321 in Solar Salt at 565 °C under dynamic molten salt conditions. Results show increasing mass losses when velocity of the melt is increased from 1 m/s to 3 m/s. Since linear trends are observed on these plots, corrosion kinetics were concluded to be parabolic in nature.

Factors contributing to the increased in corrosion degradation were identified by SEM analysis of the corroded samples. Cross-sectional analysis using SEM showed that the corrosion product layers were much thinner than those observed for static corrosion tests. The proposed rationale for the thinning of corrosion product layers was erosion degradation, causing by the dynamic conditions of the molten salt. As a result of erosion, the substrate was exposed to the molten salt environment and corrode at a more rapid rate.

3.6.1.8 The effect of material composition and microstructural properties

As highlighted by Olson et al. [53] in their study of six different metallic alloys, the composition of the alloy can massively influence the corrosion behaviour of each alloy in a molten salt environment.

A comprehensive study investigating the impact of an alloys composition has been conducted by Ghaznavi et al. [73] who have studied the corrosion of numerous Fe – Ni and Fe – Cr - Ni alloys in a ternary molten chloride salt. The molten chloride salt system was composed of lithium chloride, potassium chloride and magnesium chloride (LiCl, KCl and $MgCl_2$ respectively) in proportions of 55 – 40 – 5 mol.%. All molten salt experiments were conducted at a temperature of 350 °C. A summary of each alloy used in molten salt corrosion experiments is presented as Table 3.8.

Table 3.8 - Summary of alloy compositions used in molten chloride salt corrosion studies by Ghaznavi et al. [73] (at.%).

Alloy	Fe Content	Cr Content	Ni Content
Fe30Ni	Balance	-	30
Fe36Ni	Balance	-	36
Fe42Ni	Balance	-	42
Fe48Ni	Balance	-	48
Fe56Ni	Balance	-	56
Fe62Ni	Balance	-	62
Fe68Ni	Balance	-	68
Fe22Cr30Ni	Balance	22	30
Fe22Cr36Ni	Balance	22	36
Fe22Cr42Ni	Balance	22	42
Fe22Cr48Ni	Balance	22	48

After exposure to the molten chloride salt, Fe-Ni and Fe-Cr-Ni alloys showed signs of dealloying. In the case of both alloy types, dealloying was observed when the concentration of Fe exceeded 38 at.%, below which no dealloying mechanism was observed. However, in the Fe-Cr-Ni alloy, the presence of Cr led to the formation of a Cr oxide at the alloy – molten salt interface, formed by the reaction between Cr and impurities within the molten chloride salt. As a result, coarsening of the ligaments was prevented as the Cr_2O_3 layer acted as a diffusion barrier to the corrosive medium.

Although the composition of the testing alloy does have a large impact on its corrosion behaviour, the microstructure of the material also plays a big role in its corrosion behaviour. A study by Wang et al. [145] investigated the corrosion behaviour of Ni-Cr alloys containing 5, 10 and 15 wt.% of Cr. Once formed each alloy had a coarse grain structure with grain sizes ranging from 800 μm to 1500 μm. Each alloy was then heat treated to achieve an equiaxed, fine grain structure with an average grain size of approximately 3 μm.

The corrosion behaviour of the coarse and fine grain structured alloys was assessed in FLiNaK molten salt at a constant 700 °C with assessment of the corrosion behaviour being conducted using potentiodynamic polarisation. The results showed that refining the grain structure promoted the anodic reaction,

resulting in greater dissolution of alloying elements from the alloy, in particular, Cr. This was corroborated by mass change measurements which are presented in Figure 3.32.

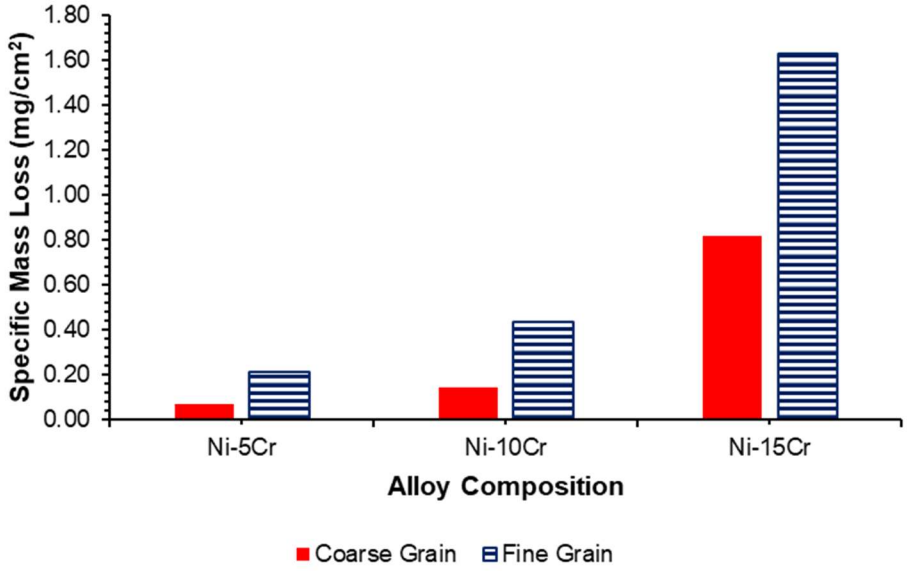


Figure 3.32 – Specific mass change measurements for coarse – and fine – grained Ni-Cr alloys showing an increase in the specific mass changes for fine – grained Ni-Cr alloys when immersed in molten FLiNaK salt at 700 °C.

Specific mass change results presented in Figure 3.32 show a greater mass loss for the alloys with a refined microstructure when compared with those with coarser grains. Greater specific mass losses are also observed for alloys with increasing concentrations of Cr. This is due to the increased rate of Cr dissolution from the alloy due to its higher concentration, hence, increasing the specific mass loss.

A similar result was obtained by Maric et al. [146] when investigating the effect of cold rolling 316L stainless steel on its microstructure and subsequently its corrosion behaviour. In the study, 316L stainless steel was cold rolled until its thickness was reduced by 20% and 30%. Microstructural examination of the samples was conducted and showed lengthening of the grain boundaries in samples that had been cold rolled. Cold rolling was also observed to increase the number of high angle grain boundaries in the 316L stainless steel samples. Samples were immersed in FLiNaK at 650 °C for 300 hours, the results of which showed that cold rolling increase the mass loss that samples exhibited during corrosion testing. Due to the increased number and length of grain boundaries, alloying elements were able to diffuse more readily resulting in their increased depletion from the 316L samples.

A similar result was achieved by Muransky et al. [42] who assessed the corrosion behaviour of three speciality Ni-based alloys, designed for use in the MSR. The three alloys, Hastelloy N, GH3535 and MONICR have similar compositions, however, analysis of the material microstructure showed that Hastelloy N and GH3535 alloys had a greater density of high angle grain boundaries than MONICR. After being immersed in molten FLiNaK salt at 650 °C for time periods of 200, 500 and 750 hours, the MONICR alloys showed the smallest mass loss, as shown in Figure 3.33.

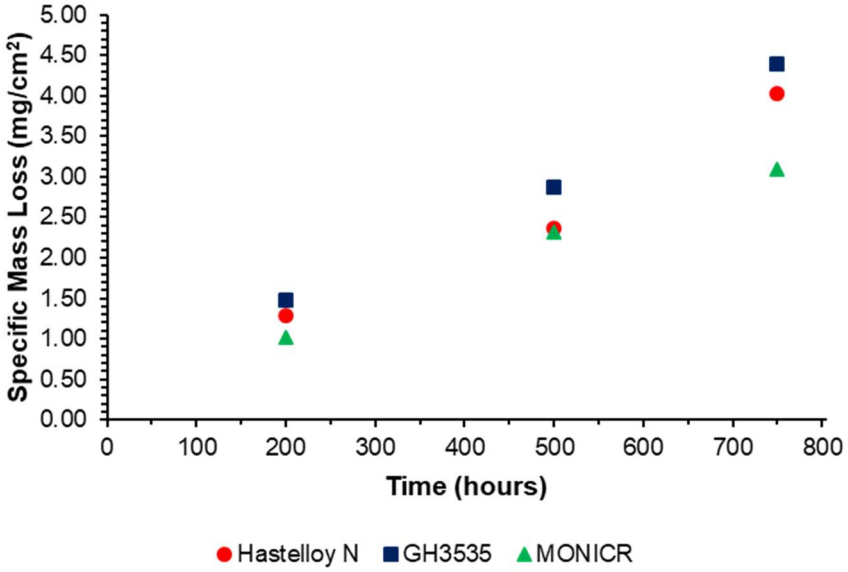


Figure 3.33 – Graph showing material mass loss of Hastelloy N, GH3535 and MONICR alloys in molten FLiNaK salt at 650 °C after 200, 500 and 750 hours of immersion. Results show that MONICR has the best corrosion performance of the three alloys, attributed to its larger grain size and a smaller number of high angle grain boundaries [42].

The reasons for the increased corrosion of Hastelloy N and GH3535 when compared with that of MONICR were largely due to the material microstructures. Due to the MONICR alloys having fewer high angle grain boundaries, intergranular corrosion was reduced, as was alloying element diffusion. Comparison of the compositions themselves also shows that MONICR has smaller concentrations of less noble elements. These elements are highlighted in Table 3.9.

Table 3.9 – Comparison of concentrations of less noble elements present in Hastelloy N, GH3535 and MONICR showing the reduced concentrations of these elements in MONICR when compared with the other alloys. Concentrations provided in wt.% [42].

Element	Hastelloy N	GH3535	MONICR
Cr	7.11	7.03	6.77
Fe	3.71	4.03	0.7
Mn	0.52	0.77	0.059
Si	0.21	0.59	0.162
Al	0.11	0.03	0.005
Ti	< 0.0002	< 0.01	< 0.002

The reduction in the concentration of less noble elements in MONICR, such as Cr and Fe, make it less prone to corrosion in FLiNaK salt by selective dissolution of such elements. Considering the Gibbs free energy of formation of the fluorides of each of the elements in Table 3.9 shows that formation of each of the corresponding metallic fluorides are more favourable than the formation of fluorides by the more noble alloying elements. Therefore, the reduction in the concentration of less noble elements results in reduced metallic fluoride formation by these elements, reducing the susceptibility of MONICR to corrosion in molten FLiNaK.

3.6.1.9 Combined impact of influential factors on corrosion in molten salt environments

In an MSR environment, the influential factors discussed throughout Section 3.6.1 are unlikely to act independently and hence, are more likely to interact to influence the corrosion behaviour of any material interacting with the melt. One such example is the research of Ouyang et al. [127], where both temperature and moisture content were both varied when building an understanding of the corrosion behaviour of Hastelloy B3 and Hastelloy N in FLiNaK molten salt. Within this study, moisture content of the salt was varied to be either 1.91 wt.% or 3.19 wt.%, whilst the temperature was controlled to be either 600 °C or 700 °C. In their research, Ouyang et al. quantified the corrosion degradation by measuring the mass changes over durations of 100 hours and 300 hours at temperatures of 600 °C and 100 hours and 200 hours at temperatures of 700 °C. The results of the study are presented as Figure 3.34.

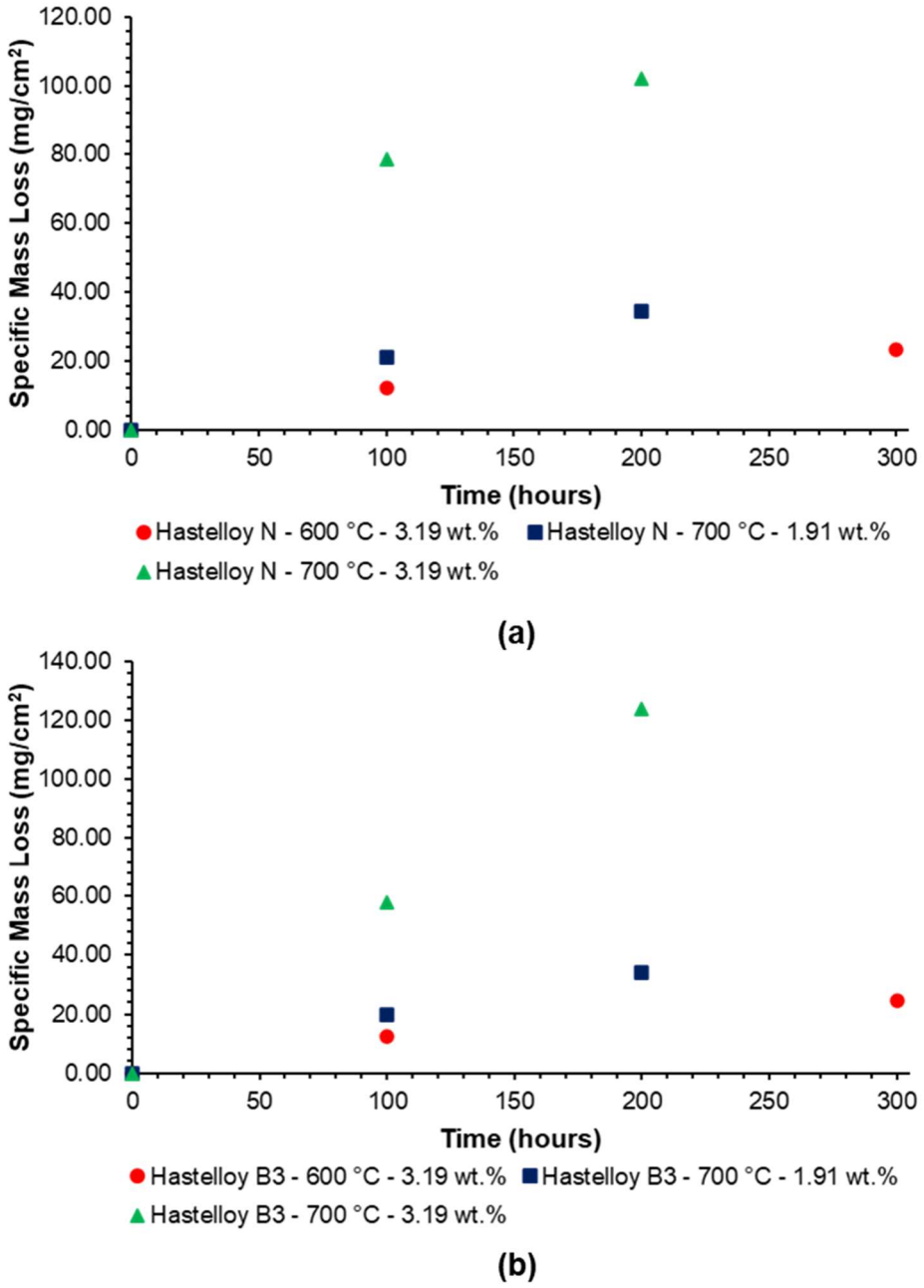


Figure 3.34 – Results presented from study of Ouyang et al. [127], showing specific mass change results obtained at 600 °C and 700 °C for the corrosion of (a) Hastelloy N and (b) Hastelloy B3 in FLiNaK molten salt containing 1.91 wt.% and 3.19 wt.% moisture. Results show that both increasing temperature and moisture concentration increase the extent of material degradation.

The result presented in Figure 3.34 shows that increasing both temperature and moisture concentration increase the extent of material degradation. However, increasing the temperature of the corrosive molten salt environment can be seen to cause a larger increase in the corrosion of the Hastelloy B3 and Hastelloy N alloys than increasing the moisture concentration.

As shown in Figure 3.26, increasing the moisture content of the molten salt environment was shown to increase the extent of both intergranular and pitting corrosion mechanisms of Hastelloy B3 and Hastelloy N. However, increasing the temperature of the molten salt was shown by Ouyang et al. [127] to result in more uniform corrosion across the alloy surface, hence the larger mass changes observed when the temperature was increased when compared with those when moisture content was increased.

Based on literature evidence presented in Section 3.6.1.1 to 3.6.1.4, similar conclusions could be drawn for the interaction of other salt contaminants and increasing temperature. In the case of each salt contaminant, alloying element dissolution or intergranular corrosion were enhanced. Coupling such degradation mechanisms within increasing temperature would result in increased corrosion degradation, as discussed in Section 3.6.1.6 and by the research of Ouyang et al. [127].

Similarly, coupling of corrosion and erosion mechanisms in molten salt environments would also be likely to enhance material degradation i.e. presence of impurities under flowing conditions. The research by Zhang et al. [143] indicated that flowing conditions introduced erosion degradation of the corrosion product layer, resulting in enhanced corrosion mechanisms of the underlying substrate in a pure Solar Salt melt. The introduction of impurities within the melt would be likely to enhance the corrosion of the substrate material after damage to the corrosion product layer, or substrate material, by an erosion mechanism.

In the case of MSR applications, it is critical that interacting degradation mechanisms are understood and mitigated against as far as is reasonably practicable to ensure safe MSR operation.

3.7 Corrosion of irradiated materials in molten salt environments

As a result of the nuclear fission process, impurities can be introduced into the molten salt, as previously discussed with the addition of Te, resulting in enhanced corrosion characteristics of materials. However, the fission process may also impact the materials themselves. The absorption of high energy neutrons by materials during the nuclear fission process can result in the embrittlement of metallic materials. It may also make materials more susceptible to corrosion in molten salt environments by the introduction of voids into the material structure. This section aims to introduce some of the methods used to emulate irradiation damage in a laboratory environment and discuss studies that have used such methods in conjunctions with molten salt corrosion testing.

3.7.1 Irradiation emulation Methods

In laboratory settings, the handling of materials from nuclear reactors is extremely difficult due to the induced radioactivity of materials that have undergone neutron irradiation. Therefore, alternative methods must be used to imitate the irradiation damage that can be induced in materials by neutron irradiation. In an MSR environment, the typical dosage of nuclear irradiation is 200 dpa [38]. Commonly, ion irradiation methods are used to induce damage in materials that is comparable to that induced by neutron irradiation [147]. This process involves bombarding a metallic material with high energy He-ions, or heavier ions, to induce irradiation damage without the associated radioactivity, allowing for the handling of samples in a laboratory setting without additional safety precautions [148]. The ion irradiation process results in the formation of defects within the material which may take the form of vacancies in the microstructure of the material or interstitial defects where atoms occupy an interstitial site in the crystalline material structure. This is illustrated in Figure 3.35.

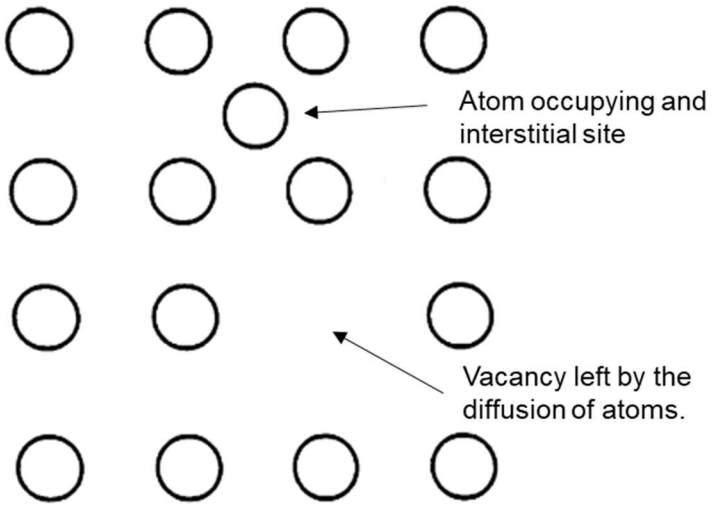


Figure 3.35 – Illustration of atom occupying an interstitial site in a crystalline material structure leaving a vacancy in the material structure. Image adapted from [77].

These defects may then act as nucleation sites for bubble formation. Zhu et al. [149] have previously studied the synergy of helium – ion irradiation and the molten salt corrosion of GH3535 alloy in FLiNaK molten salt at 750 °C. Coupons of GH3535 alloy were irradiated using helium ions with energies up to 30 keV at a rate of 0.2×10^{20} He-ions/m^2/s. To characterise the damage induced in the material by the irradiation process, transmission electron microscopy (TEM) was used. The deployed technique was deployed originally by Jiao et al. [150] which utilises the TEM in under- and over- focused conditions to identify changes bubbles by a change in colour. The result of this TEM technique indicated the presence of

bubbles and voids within the material microstructure, introduced by the helium ion irradiation process as shown in Figure 3.36.

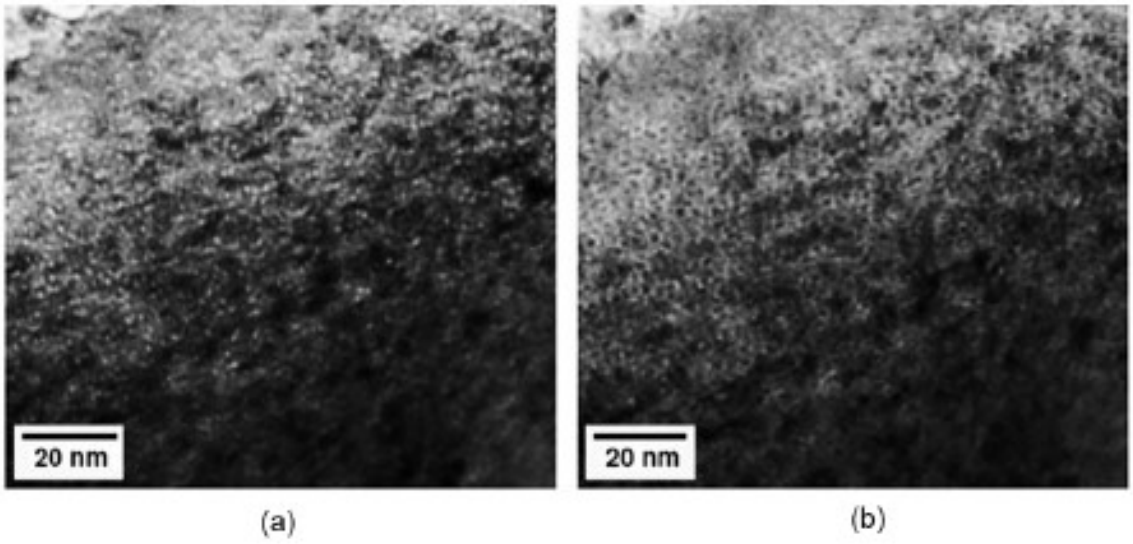


Figure 3.36 – Bubble formation in GH3535 Ni-based alloy after undergoing He-ion irradiation. Bubbles were identified using an over-focused and under-focused technique which identifies bubbles by their change in colour [149, 150].

The introduction of bubbles into the material microstructure can make the alloy more susceptible to corrosive attack. As the exposed surfaces are corroded by the molten salt, the interface between the internal bubbles and the molten salt intersects, which may result in an increase in the exposed surface area, aggravating the corrosion of the alloy. This proposed process is shown schematically in Figure 3.37

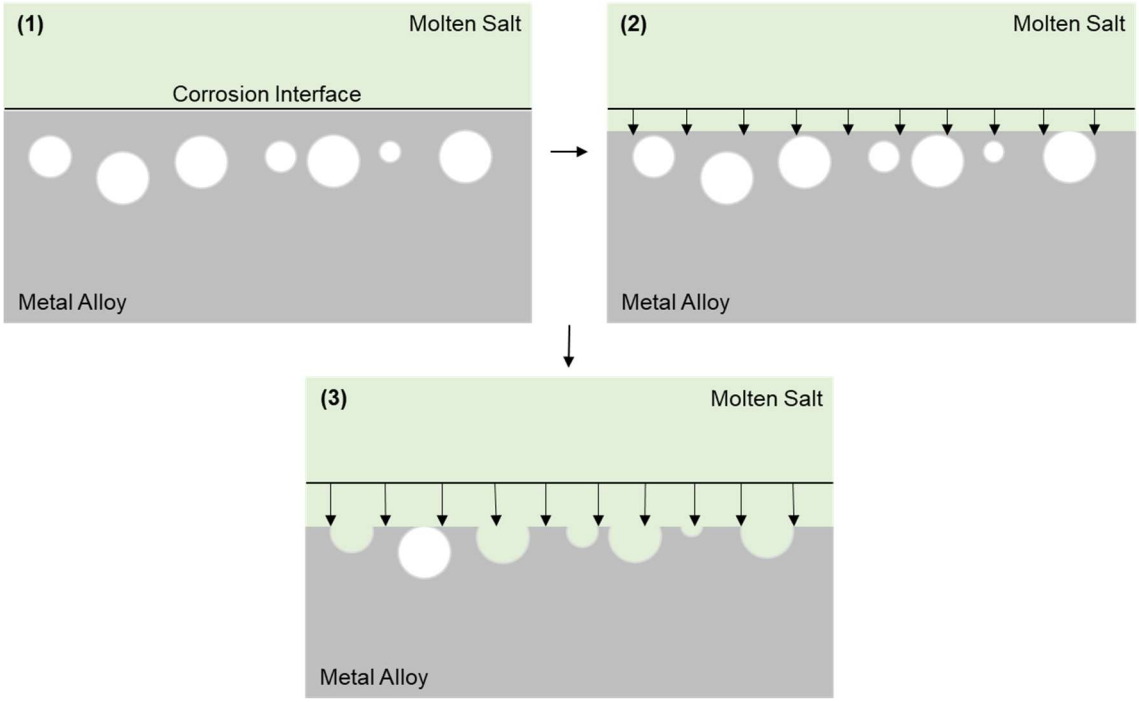


Figure 3.37 – Exposure of increased surface area to molten salt by the intersection of the corrosion interface and bubble layer, aggravating the corrosion mechanism.

Due to the increase in the exposed surface area due to the exposure of bubbles and formation of cavities during molten salt corrosion, the corrosion rate is likely to be increased [151].

3.7.2 Combined irradiation and molten salt corrosion studies

Although the combined study of irradiation and corrosion is a relatively new area of research, literature has been published in which samples are irradiated using a He-ion irradiation technique before being immersed in a molten salt environment. A study by Zhu et al. [149] showed the increased corrosion behaviour of irradiated GH3535 samples in FLiNaK salt at 750 ºC after 200 hours of immersion. The increased corrosion damage manifested in irradiated coupons as increase intergranular corrosion, observed by SEM analysis. The increased dissolution of elements such as Cr and Si was observed which is also indicative of intergranular corrosion. Corrosion was also believed by the aggravated by the diffusion of irradiation defects such as bubbles. During corrosion, bubbles were observed to coalesce, increasing in size from 0.8 nm to 20 nm, resulting in a much larger surface area for corrosive attack.

A more recent study by Zhu et al. [151] compared the impact of irradiation on the molten salt corrosion of GH3535 and Inconel 617 Ni-based alloys. Coupons of each material were tested in unirradiated and irradiated states, with two different

irradiation levels of each material being used. The irradiation dosages received by both alloys were observed to induce helium bubbles within the material microstructure, with the size of these bubbles measuring approximately 3.79 nm and 3.10 nm for Inconel 617 and GH3535 alloys respectively at a depth in the range of 2100 nm – 2300 nm below the irradiated surface. Irradiated samples were then subjected to corrosion in molten FLiNaK salt at 700 °C for 50 hours, with corrosion behaviour being quantified by measuring the depth of corrosive attack. The results for the highest irradiation dosages showed higher depth of corrosive attack for both alloys tested, with Inconel 617 being attacked more aggressively than GH3535. The main corrosion mechanism observed was intergranular corrosion, similar to the result observed by Zhu et al. [149]. However, at lower irradiation dosages, intergranular corrosion was observed to slow when compared with unirradiated samples. This was believed to be due to the self-healing mechanism reported by Zhou et al. [152] who investigated the corrosion of proton irradiated Ni-Cr alloys in FLiNaK molten salt containing europium (III) fluoride (EuF_3). The results of the study by Zhou et al. [152] showed that Cr lost from grain boundaries can be somewhat replenished by the diffusion of Cr and Ni from the bulk material to the grain boundaries. The act of Cr and Ni diffusing to the grain boundaries reduces the rate of intergranular corrosion. At higher irradiation doses this self-healing mechanism was observed to have little effect, with the rate of intergranular corrosion being observed to increase when compared to the corrosion of unirradiated samples.

3.8 Summary of literature review

A comprehensive literature review detailing the key theory and literature regarding the oxidation, molten salt corrosion and irradiation of Ni-based alloys has been covered and highlights the current research gaps within MSR corrosion studies. In the case of the high temperature oxidation of Ni-based alloys, the oxidation rate is regularly quantified, with characterisation of oxidation products also often undertaken using SEM, EDX and XRD techniques among others. However, the inclusion of O_2 in a molten salt environment and its subsequent impact on the molten salt corrosion of Ni-based alloys has rarely been considered. Experiments have been completed by adding O_2 into molten salt mixtures in the form of Li_2O to understanding the impact of this addition on stainless steels and Ni-based alloys, however, these results are not representative of having an abundance of O_2 available within the molten salt from an air atmosphere.

Similarly, current predictive models available for molten salt corrosion focus only on the corrosion mechanism without O_2 which may not be fully representative of the MSR system. Currently, very few mechanistic models exist for predicting the corrosion behaviour of materials in molten salt environments, with ANNs being used most recently to provide mass change predictions without modelling the underlying corrosion mechanisms which are driven by the presence of impurities within the molten salt melt [51]. A similar statement can be made for modelling high temperature oxidation, where empirical models have been developed for predicting oxide growth without predicting the underlying mechanism. For oxidation, this involves diffusion of species from the substrate material which results in oxide growth. Therefore, development of predictive models that capture the full mechanisms of molten salt corrosion and high temperature oxidation are critical in developing predictive models that understand the synergy between the two mechanisms.

To resolve the aforementioned research gaps, a combined experimental and numerical approach will be deployed. Experimentally, the synergy of oxidation and corrosion will be studied in two parts. Initially, an isothermal oxidation study will be undertaken to build a baseline understanding of the high temperature oxidation behaviour of Ni-based alloys, which were shown throughout the literature review to be the most popular material of research for MSR applications. Baseline oxidation experiments will then be followed by a molten salt corrosion study in an air environment. This will then allow for direct comparison of oxidation and molten salt corrosion mechanisms in an air environment with an aim of understanding the synergy between oxidation and corrosion in molten salt environments. To achieve direct applicability to MSR environments, Ni-based alloys will be utilised and temperatures of 700 °C will be used.

These conditions will be replicated in predictive models for high temperature oxidation and molten salt corrosion. In a similar methodology to the experimental research, predictive modelling will be undertaken in two sections. Initially, empirical, and mechanistic models for the high temperature oxidation of Ni-based alloys will be developed. This will allow for the results of empirical and mechanistic models to be directly compared to determine which modelling methodology provides greater insight into oxidation mechanisms. Following this, a molten salt corrosion predictive model will be developed, building on the high temperature oxidation model. The aim of this model will be to combine predictions of element concentration changes with current understanding of the molten salt corrosion mechanism to predict the corrosion of Ni-based alloys in molten salt environments.

Chapter 4 – Materials, Experimental and Numerical Methods

This chapter provides a detailed methodology of the experimental and numerical techniques used for isothermal oxidation and molten salt corrosion of Hastelloy C276. In the case of both oxidation and corrosion testing, static immersion techniques were used to quantify oxidation and corrosion rates, with numerous surface analysis techniques used to characterise products of both processes. Numerical modelling of oxidation and corrosion was undertaken using empirical and mechanistic methods, with the main outputs of these models being elemental distribution changes and rates of oxidation and corrosion.

4.1 Introduction

This section aims to introduce the experimental methodologies, discussing material selection, material preparation and the experimental conditions used throughout this research. This will also include an introduction to the post-experimental analysis that will be undertaken, including SEM, EDX and XRD analysis. Similarly, the numerical methodologies developed to predict the corrosion and oxidation behaviour of Ni-based alloys in molten salt environments are also presented and discussed in detail.

In this study, experimental and numerical methods were combined to investigate and characterise the oxidation and corrosion behaviour of Ni-based alloys in simulated MSR corrosion environments. The primary experimental methodology that has been used when investigating the molten salt corrosion of Ni-based alloys was the static immersion technique as highlighted in Chapter 3. Throughout this study, the static immersion technique for evaluating the corrosion behaviour of Ni-based alloys in molten salt environments was used at conditions similar to the operating conditions of an MSR. A similar technique was deployed to assess the oxidation behaviour of Ni-based alloys in the absence of molten salt. From these experiments, the rates of corrosion and oxidation were assessed using a thermogravimetric method.

This section also discusses the empirical and mechanistic methods that were developed to predict the oxidation and corrosion behaviour of Ni-based alloys. Both types of models were developed within MATLAB. MATLAB is a useful tool due to the extensive number of pre-programmed functions that can be utilised and can be applied to a wide range of applications [153]. The theory associated with empirical and mechanistic modelling has been discussed in Chapter 3, with this chapter

outlining how the theory was applied within MATLAB. When predicting the oxidation behaviour of Ni-based alloys, the main outputs of the empirical and mechanistic models was the specific mass change and the oxidation rate, with the mechanistic model also being utilised to predict elemental concentration changes within the substrate material. When considering the corrosion behaviour of Ni-based alloys in molten salt environments, the mechanistic model was deployed, with the depth of corrosion and corrosion rate being calculated by the model.

4.2 Introduction to High Temperature Oxidation and Molten Salt Corrosion

The research conducted as part of this project is focused on the high temperature oxidation and molten salt corrosion behaviour of Ni-based alloys. The experimental work was conducted using a static immersion technique, in which coupons of Ni-based alloy were immersed in an alumina crucible at a typical MSR operating temperature for durations of 50, 100 and 200 hours. In this study a temperature of 700 °C was used to replicate the high temperatures at which molten salts will reach in an MSR environment. The behaviour of the Ni-based alloys in either an oxidising or corrosive environment is quantified using a thermogravimetric technique which is used to determine rates of oxidation and molten salt corrosion.

Alongside the thermogravimetric method for quantification of the corrosion and oxidation behaviour, characterisation of the corrosion and oxidation processes was conducted using post-experimental analysis techniques. This characterisation protocol included the identification of corrosion and oxidation products, as well as identification of regions of material degradation. Techniques deployed to characterise the corrosion and oxidation products include SEM equipped with EDX, and XRD analysis. A basic outline of the study undertaken in this thesis is presented as Figure 4.1.

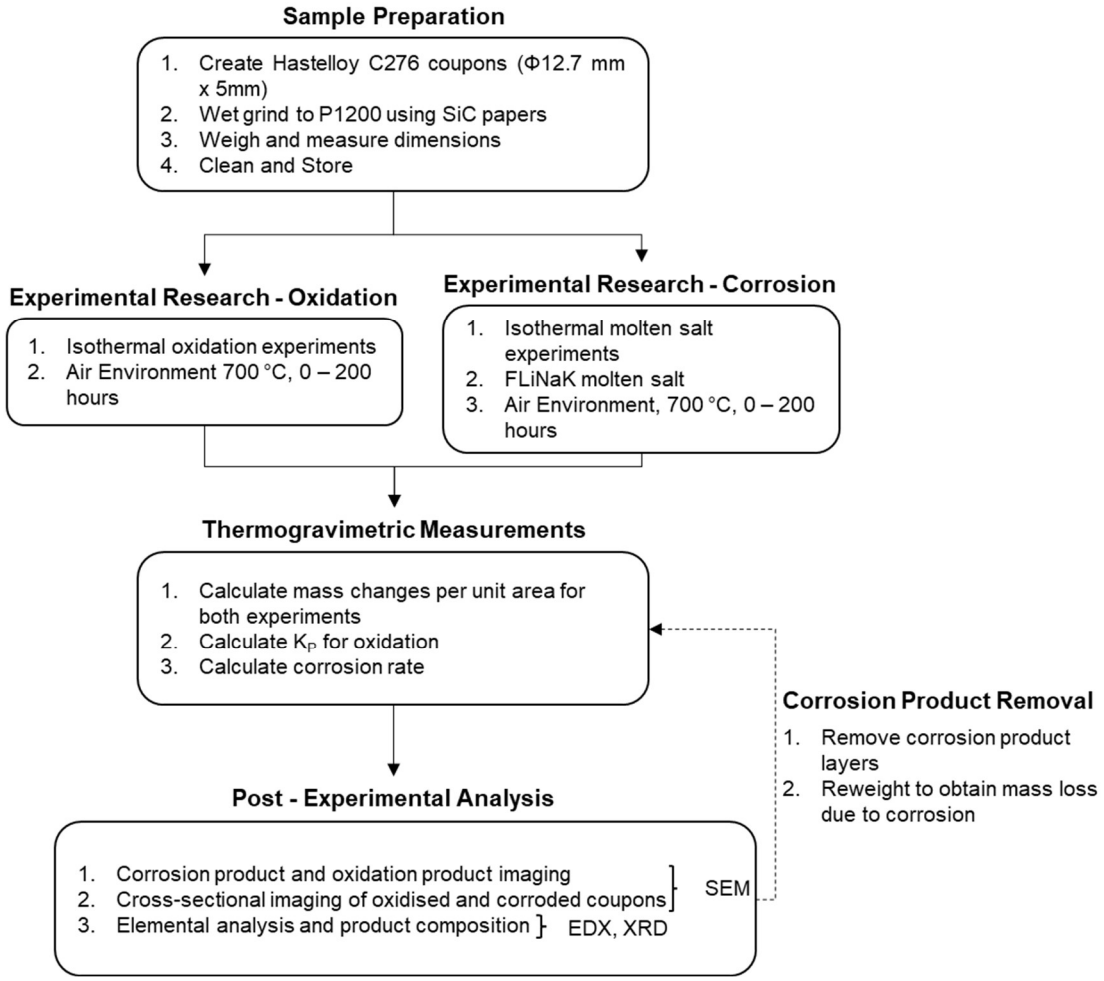


Figure 4.1 - Flow chart of the experimental and subsequent analysis undertaken during this thesis using as-received samples.

4.2.1 Basic Experimental Methodology Description

The experimental aspect of this thesis was conducted using a Carbolite AAF 11/32 high temperature furnace, capable of achieving a maximum temperature of 1100 °C. To conduct experiments, Hastelloy C276 was provided by Goodfellow Cambridge Ltd in the form of round bar. Coupons were then cut from the bar and ground using SiC papers of increasing fineness to achieve a uniform surface finish before being weighed using a mass balance and having their dimensions measured with Vernier callipers. These measurements were taken to calculate the exposed surface area of each coupon. Four coupons of the Hastelloy C276 material were then placed into an LR124 alumina crucible, provided by Almath Crucibles Limited, and placed in the centre of the high temperature furnace. A cross-sectional schematic of the basic test set up is presented in Figure 4.2.

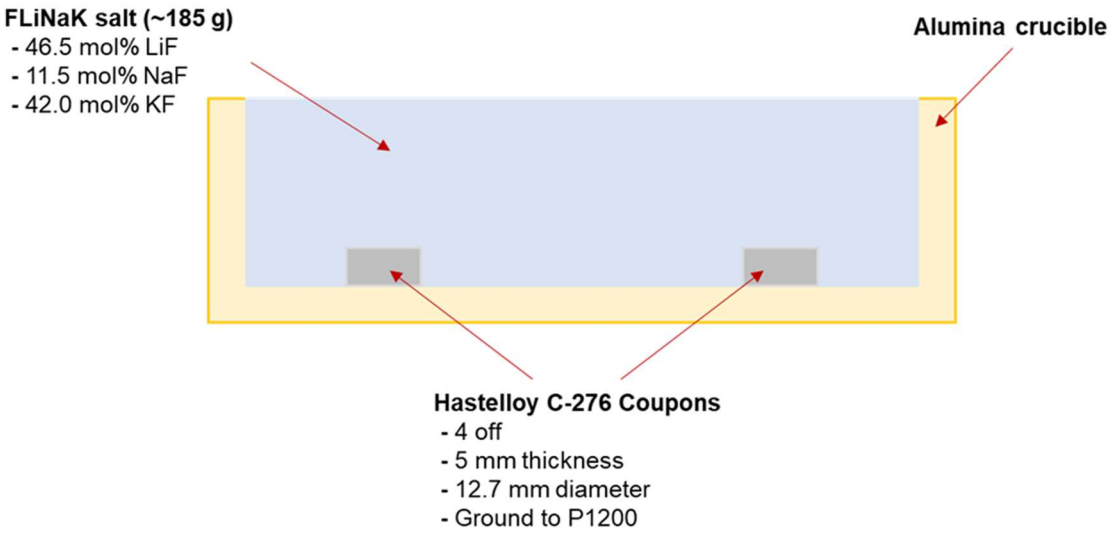


Figure 4.2 – Diagram showing basic test set up used for high temperature corrosion and oxidation testing of Hastelloy C276 with key components of the test set-up labelled.

In the application of a thermogravimetric method for characterising molten salt corrosion or oxidation behaviour, the coupon mass was measured again after the experiment was complete to calculate the mass change per unit area. Following this calculation, plots of the mass change per unit area against time can be generated and used to identify the kinetics of the corrosion and oxidation processes.

4.2.2 Material Selection

Due to the operating conditions of the MSR, materials must be able to operate in high temperature environments with good corrosion resistance to ensure minimal impact of any interactions with any corrosive media that may be present. Specifically, for MSR applications, materials must be able to operate at temperatures in excess of 700 °C due to the temperature of the fuel salt upon leaving the reactor core. Materials must also be resistant to corrosion by fluoride molten salts. Due to these requirements, Ni-based alloys are the preferred materials.

In the case of FLiNaK molten salts, very few materials are fully inert when immersed, although, there is currently research into speciality Ni-based alloys for specific use in MSR environments. However, there are other materials, previously used for nuclear applications, which may perform adequately. One such material is Hastelloy C276, which is defined as a high-temperature and corrosion resistant alloy.

Previous research into the corrosion behaviour of Hastelloy C276 in molten fluoride salts compared its performance against that of Hastelloy X and Inconel 600. In a study by Liu et al. [154], the three alloys were subjected to FLiNaK molten salt at 750 °C, with corrosion performance quantified by the depth of corrosion at time periods of 50, 100, 200 and 300 hours. Results of this study are presented in Figure 4.3.

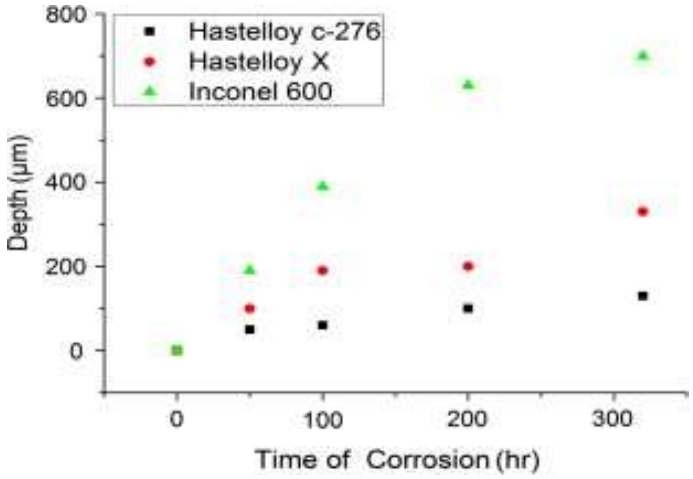


Figure 4.3 – Graph of corrosion depth of Hastelloy C276, Hastelloy X and Inconel 600 after immersion in FLiNaK molten salt at 750 °C for time intervals of 50, 100, 200 and 300 hours. Results indicate that Hastelloy C276 has better corrosion resistance to FLiNaK molten salt over both Hastelloy X and Inconel 600.

Results presented in Figure 4.3 show that Hastelloy C276 had the smallest corrosion depth after 300 hours of exposure to FLiNaK molten salt at 750 °C compared with both Inconel 600 and Hastelloy X, highlighting its greater corrosion resistance to fluoride molten salt in high temperature environments. The improved corrosion resistance highlighted in Figure 4.3 was concluded to be due to the increased concentration of Mo present within the Hastelloy C276 (15.49 wt.%) when compared with that of Hastelloy X (8.29 wt.%) and Inconel 600 (0 wt.%).

In this research, 12.7 mm diameter round bar of Hastelloy C276 was provided by Goodfellows Cambridge. The composition of the supplied material is presented in Table 4.1.

Table 4.1 – Composition of commercial specification for Hastelloy C276 material as received from Goodfellows Cambridge (wt.%).

Element	Ni	Cr	Mo	Fe	W	Co
wt.%	Bal.	14.5 – 16.5	15.0 – 17.0	4.00 – 7.00	3.00 – 4.50	2.50
Element	**Si**	**Mn**	**V**	**C**	**P**	**S**
wt.%	0.08	1.00	0.35	0.02	0.03	0.03

The composition of Hastelloy C276 is shown to have possible variations in the concentrations of key alloying elements such as Cr, Mo, Fe and W which all play a key role in its high temperature and corrosion resistant behaviours. The corresponding microstructure of Hastelloy C276 is presented in Figure 4.4.

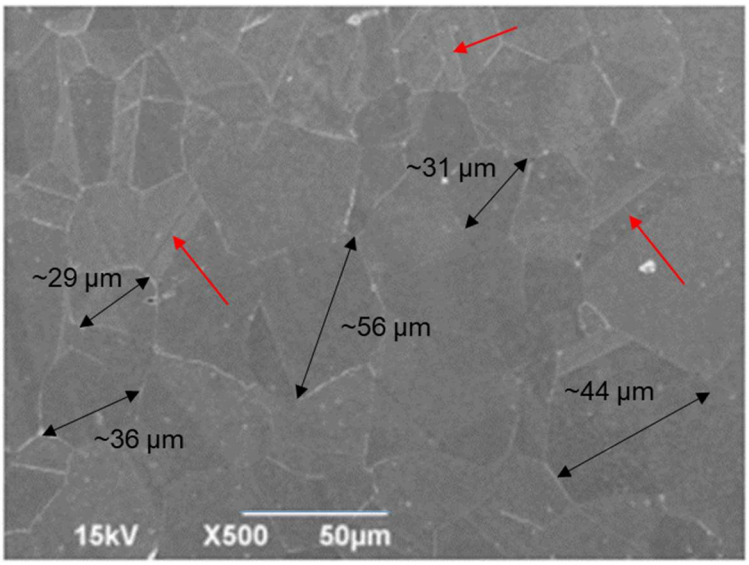


Figure 4.4 – Micrograph of Hastelloy C276 showing equiaxed grain structures with sizes ranging from 30 µm to 60 µm. Examples of annealing twins were observed within the microstructure, and are arrowed red. Micrograph of Hastelloy C276 taken from research by Zhang et al. [100].

The resultant material microstructure, presented in Figure 4.4, shows a γ-phase and Ni-rich matrix, which has been shown to contribute to Hastelloy C276 improved high temperature corrosion and oxidation resistance. The grain size of Hastelloy C276 observed in Figure 4.4 is measured to be between 30 µm and 60 µm with the grain themselves showing an equiaxed structure. Highlighted in Figure 4.4 are annealing twins, which form during recrystallisation of the microstructure during formation of the alloy [155].

4.2.3 Coupon preparation for corrosion and oxidation testing

To conduct experimental work, coupons of Hastelloy C276, 5 mm in thickness, were cut from the 12.7 mm diameter round bar using EDM. Coupons were then ground using a Struers Labopol polishing machine, equipped with SiC grit papers of P240, P600 and P1200, which were deployed in sequence to achieve a uniform surface finish. Ground coupons were then rinsed with distilled water, degreased with acetone and air dried before being stored in a vacuum desiccator until required for testing.

To quantify the rates of corrosion and oxidation, the mass changes of coupons were measured. Coupons were weighed after being prepared to obtain their initial mass, with their diameter and thickness dimensions also being measured to calculate the exposed surface area. The coupons masses were measured to a precision of 0.0001 g, whilst the diameter and thickness measurements were made using a Vernier calliper, with a precision of 0.01 mm. The processes undertaken to prepare samples for experimentation are outlined in Figure 4.5.

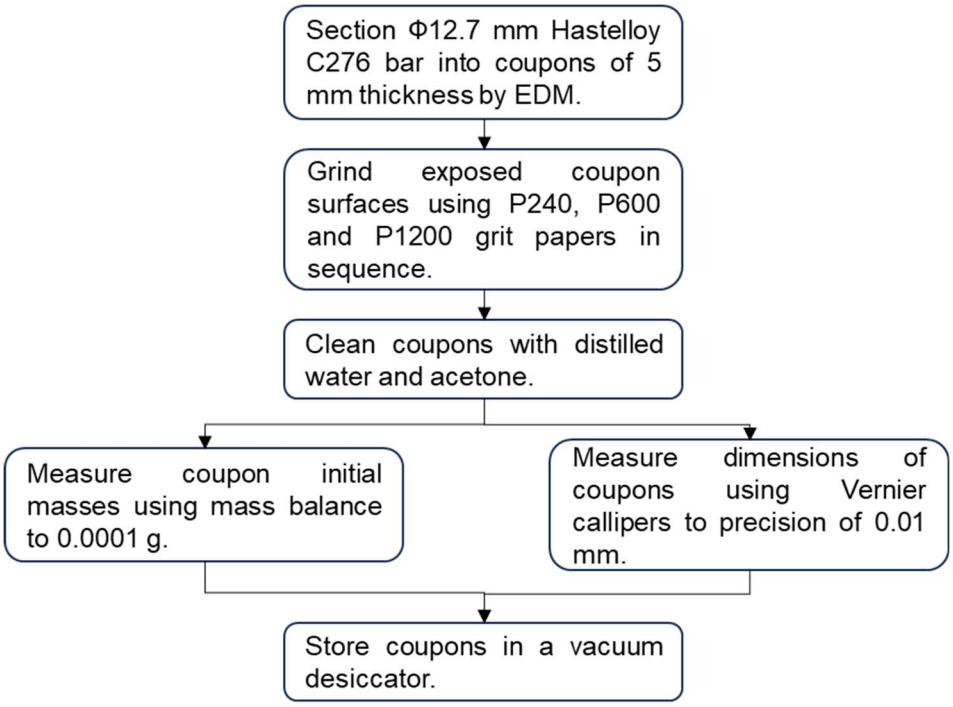


Figure 4.5 – Flowchart of processes undertaken to prepare coupons of Hastelloy C276, ready for studies relating to their high temperature molten salt corrosion and oxidation.

After testing, coupons were re-weighed to obtain their new masses after the corrosion and oxidation processes. The mass change was then determined and subsequently used to calculate the mass change per unit area of coupons. The details of the measuring processes for corrosion and oxidation will be discussed in

more detail in Section 4.2.5. Once weighed, samples were labelled and placed in a vacuum desiccator until required for surface analysis.

4.2.4 Experimental Conditions and Protocols

As previously mentioned, the two main salt combinations used in Generation – IV MSRs are FLiBe and FLiNaK. Currently FLiBe is more commonly used, however, FLiNaK has shown promise of being an effective HTF. Therefore, in this study FLiNaK salt was used in a eutectic mixture of 46.5 – 11.5 – 42.0 mol.%. The salts used were supplied by Alfa Aesar and had purities ≥ 99.0%. In ISO 17245, the standard for the high temperature corrosion testing of metallic materials, a surface area to molten salt volume ratio of 20 is recommended [156]. However, due to the crucible capacity and coupon size, this ratio was not reasonably possible. Based on the maximum crucible volume and salt quantities, a maximum FLiNaK mass of 200 grams was decided upon. Therefore, a surface area to volume ratio of 5 was used in all molten salt corrosion experiments. This volume of salt results in a total salt mass of 182.9 g, consisting of 53.4 g LiF, 21.4 g NaF and 108.1 g KF.

The aim of this research is to understand both the corrosion and oxidation characteristics of Ni-based alloys, hence, two testing protocols were run at a temperature of 700 °C. The oxidation testing protocol consisted of a constant heating phase to achieve 97% of the test temperature. The rate of heating would then be slowed to prevent overshoot of the test temperature. Tests would then be conducted at this temperature for the desired time period of 50, 100 or 200 hours.

Due to the presence of FLiNaK molten salt in the molten salt corrosion experiments, a different heating approach was undertaken. This is shown in Figure 4.6.

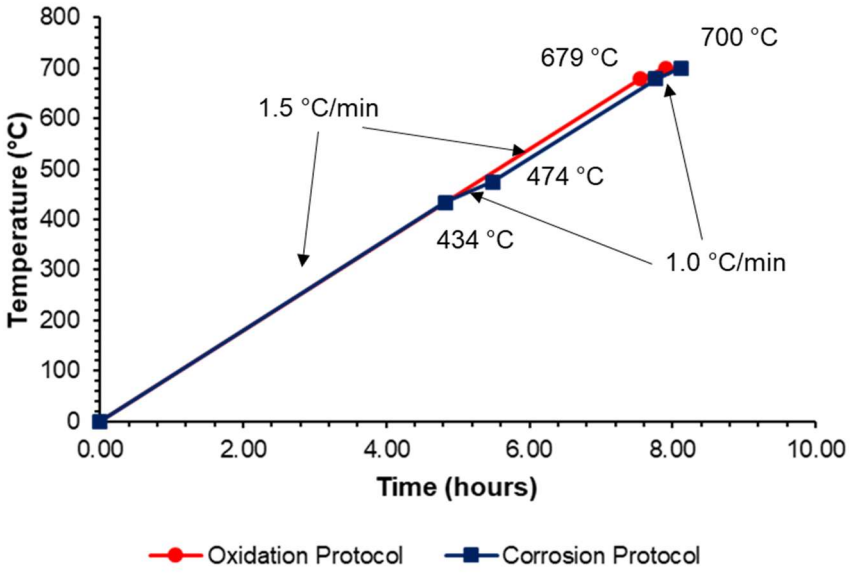


Figure 4.6 – Heating approaches deployed for high temperature isothermal oxidation and corrosion testing of metallic materials as per ISO 21608 and ISO 17245 experimental testing standards [156, 157].

Both heating protocols follow those described in ISO 21608 [157] and ISO 17245 [156] . As shown in Figure 4.6, both heating protocols begin with a constant heating rate of 1.5 °C/min. For the oxidation protocol this heating rate continues up to 97% of the test temperature, at which point the heating rate is reduced to 1 °C/min to ensure the test temperature of 700 °C is achieved and overshoot is minimised.

However, to ensure full melting of the molten salt, the heating rate is reduced to 1.0 °C/min in the region around the melting point of the salt. This is in the region of 434 °C to 474 °C as the melting point of FLiNaK is 454 °C [30]. After 474 °C is reached, the heating rate is raised to 1.5 °C/min until 97% of the test temperature is achieved. The molten salt testing protocol then follows that of the oxidation protocol, with the heating rate reduced to 1 °C/min until 700 °C is achieved.

During the heating protocol for both molten salt corrosion and oxidation experiments, no mass change measurements were taken. This was due to the assumption that mass changes during these times would be negligible. However, this could not be ensured and was not quantified as part of this research. Therefore, presented results may include mass changes due to molten salt corrosion or high temperature oxidation, incurred during heating up and cooling down processes. This may have an impact on the interpretation of the corrosion and oxidation kinetics, determined from the specific mass change measurements obtained experimentally for both processes.

4.2.5 Post – experimental Analysis Techniques

Several compositional and surface analysis techniques were deployed to characterise the corrosion and oxidation products present on exposed surfaces of Hastelloy C276 coupons after testing. These methods included scanning electron microscopy (SEM) equipped with energy dispersive x-ray spectroscopy (EDX) and x-ray diffraction analysis (XRD).

The corrosion and oxidation behaviours were quantified using a thermogravimetric technique, where the coupon mass was measured before and after testing, with coupons being cleaned after testing in accordance with ASTM standard G1-03 [158]. The methodologies and theory behind each of the methods used are described in this section.

4.2.5.1 Thermogravimetric method for quantification of corrosion and oxidation behaviour

A thermogravimetric method was used to determine the mass change of corrosion and oxidised samples. Mass changes of samples were used in conjunction with the samples exposed surface area to calculate the mass change per unit area using equation 4.1.

$$\Delta W = \frac{m_f - m_i}{A} \qquad \textbf{4.1}$$

where ΔW is the mass change per unit area, also called the specific mass change, with units of mg/cm^2, $m_i$and m_f are the initial and final coupons masses, with units of mg, and A is the exposed surface area, with units of cm^2. Coupons of Hastelloy C276, oxidised in a dry air environment were weighed immediately after testing to obtain the specific mass change due to the formation of oxides. However, a more complex process was undertaken for corroded coupons.

After corrosion testing, the final mass of the coupons was measured twice. The first time after rinsing with distilled water to remove any solidified salt from the exposed surfaces of the coupon. This measurement included the corrosion product layer mass in combination with any corrosion damage and was termed the overall specific mass change. The coupons were then cleaned using a diluted hydrochloric acid (HCl) solution, created by mixing 10 mL of 37% HCl with 90 mL of deionised water, to remove the corrosion product layer [158]. The coupon masses were then measured with the new mass measurement only accounting for the corrosion damage to the coupon.

Based on the mass changes associated with the corroded sample, the corrosion rate could also be estimated as per ASTM Standard G1-03 [158]. This ASTM

standard outlines the method for approximating corrosion rate from mass change data using equation 4.2.

$$CR\ (mmpy) = \frac{87600\Delta m}{\rho A t} \qquad \textbf{4.2}$$

Where CR defines the corrosion rate in mmpy, Δm is the mass change of the sample in grams, ρ is the material density in g/cm^3, A is the exposed surface area of the sample in cm^2 and t the corrosion time in hours. The process undertaken for the measuring of the corrosion mass changes is highlighted in Figure 4.7.

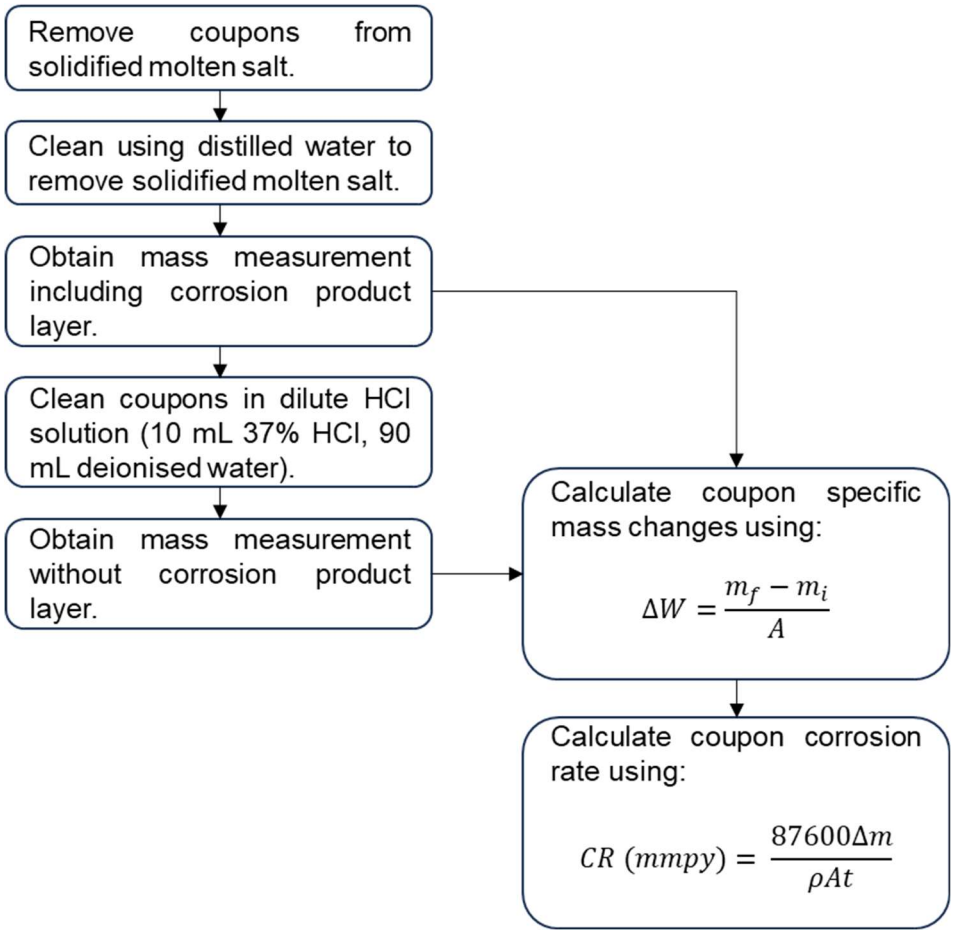


Figure 4.7 – Flowchart illustrating the process undertaken to obtain specific mass changes and corrosion rates of Hastelloy C276 coupons, corroded in molten FLiNaK salt at 700 °C after 200 hours of immersion.

As well as being used for the calculation of corrosion rates, specific mass changes determined from oxidation experiments could be used to calculate the oxidation rate constant. In the case of Ni-based alloys, parabolic oxidation behaviour is commonly observed. Hence the value of K_P can be expressed by:

$$(\Delta W)^2 = K_P t \qquad \textbf{4.3}$$

where K_P is the parabolic rate constant in units of $mg^2/cm^4/s$ and t is the test duration in seconds.

4.2.5.2 Scanning Electron Microscopy (SEM)

SEM is a commonly used tool when analysing corroded or oxidised surfaces and is used in this work to observe corrosion products, oxidation products and corrosion damage due to molten salt that may occur on immersed coupons of Hastelloy C276. Use of the SEM allows for the high-resolution imaging of regions of interest on material coupons post-experimentation. In this research a Carl Zeiss EVO MA15 SEM, depicted in Figure 4.8, was utilised for analysis of oxidised and corroded samples.



Figure 4.8 – Image showing Carl Zeiss EVO MA15 SEM utilised for imaging corroded and oxidised coupons throughout this study [159].

SEM analysis was used for both the analysis of the exposed surfaces of coupons as well as the cross-sections of coupons. In both cases, samples were mounted on a metallic sample holder using carbon tape, with conductivity between the coupon surfaces and the sample holder being achieved by the application of graphite paint. This ensured samples did not electrically charge when being analysed and ensured obtained images were of high quality. In this study, images were taken using the EVO MA15 SEM at magnifications of X500, X1000, X2500 and X5000 using a working distance between 8 mm and 12 mm.

4.2.5.3 Energy Dispersive X-Ray Spectroscopy (EDX)

Commonly used alongside SEM analysis, EDX is a semi-quantitative technique that allows for the identification of elements present in corrosion and oxidation products [160]. In EDX analysis, X-rays, emitted from the sample surface being analysed, are detected. The energy and wavelength of these X-rays can then be identified, and the elements present determined. This is achieved as the energy and wavelength of emitted X-rays correspond to the characteristic values of different elements.

In this research, a variety of EDX techniques, including, point and ID, line scans and elemental maps were all utilised to aid in the identification of elements present on oxidised and corroded surfaces and on cross-sections of tested coupons. In this research EDX allowed for a deeper understanding of how elements were distributed within corrosion and oxidation product layers as well as in the substrate material.

4.2.5.4 X-Ray Diffraction (XRD)

An analysis technique used throughout this thesis is XRD which allows for precise identification of crystalline corrosion and oxidation products without damaging the tested samples. This work was performed on a Siemens Bruker D8 Advance XRD machine over a scan range of $20^{o} < \theta < 80^{o}$ at intervals of 0.016^{o}. An image of the equipment used is presented as Figure 4.9.

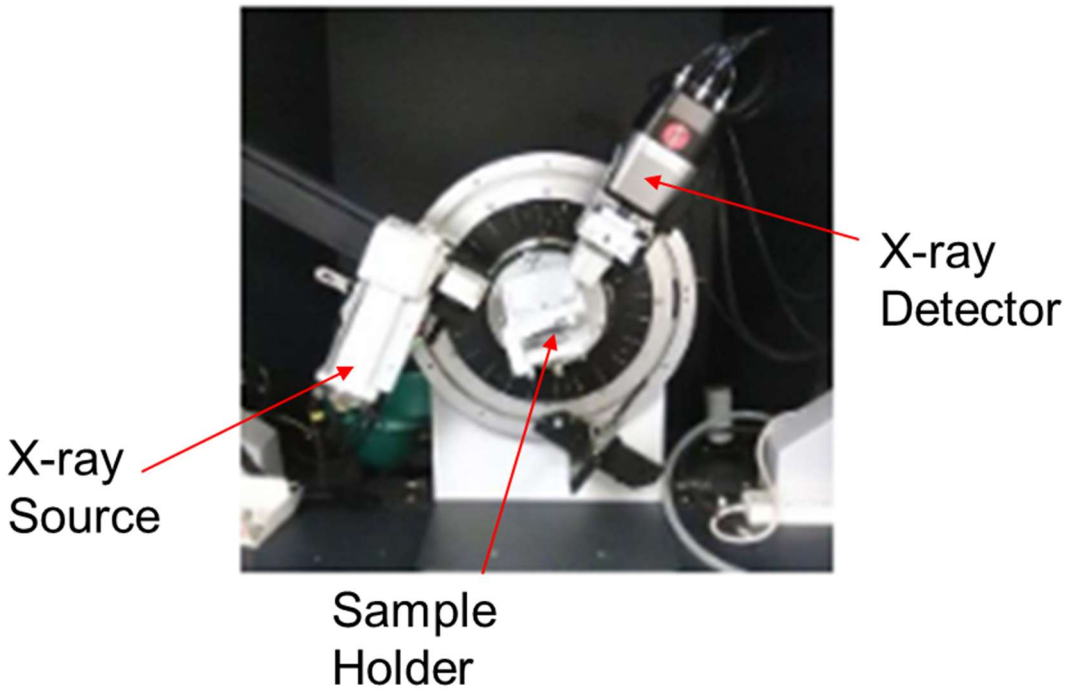


Figure 4.9 – Image of Siemens Bruker D8 Advance XRD machine, used to identify corrosion and oxidation product structures on coupons of Hastelloy C276 after immersion in a dry air environment or in FLiNaK molten salt. Adapted from [65].

When the coupon is being analysed, monochromatic radiation is produced in a cathode tube. The analysed coupons are then bombarded with this radiation, during which, X-ray will be diffracted in accordance with Braggs Diffraction Law, defined below:

$$n\lambda = 2d\sin(\theta) \tag{4.4}$$

Where n is an integer, λ is the wavelength of the beam in m, d is the spacing between diffracting planes in m and θ is the incident angle of the beam in degrees. When a beam is diffracted, it is captured by a detector. The location of the detector provides information regarding the spacing between diffracting planes. The diffraction pattern of the detected beams and their peak intensities provide insight into the quantity of X-ray diffraction occurring which in turn can be interpreted into how much of a given phase is present on the analysed sample. All analysis of XRD results was completed using Xpert Highscore XRD software, which was used to identify the oxidation and corrosion products present on corroded and oxidised samples by comparing the known diffraction patterns of metallic oxides to those observed in XRD analysis.

4.2.6 Use of experimental results as validation evidence

Experimental results obtained throughout this work will be used as validation evidence for predictions made by the empirical and mechanistic modelling methodologies. A key output from both molten salt corrosion and oxidation modelling will be the specific mass changes associated with both processes. Hence, experimentally determined specific mass change measurements, obtained using the methodologies described throughout Section 4.2, will be used in the validation of model predictions. Differences observed between experimental and predicted specific mass change results will be expressed as percentage differences, which will subsequently be used in the discussion of whether predicted and experimental results agree.

To further validate the mechanistic model, comparisons of K_P values, derived from specific mass change predictions, will be made to experimental data presented in literature. This additional validation will use data over a temperature range of 450 °C up to 800 °C using the research of Li et al. [99] and Park et al. [161], who conducted high temperature oxidation experiments on Hastelloy C276. This validation will be presented after the results of the sensitivity study, the aim being to show that the decided upon modelling parameters show good agreement with published literature data.

In the modelling of high temperature oxidation, oxide layer thicknesses will be another key output. Experimentally, oxide layer thickness measurements will be obtained by deploying SEM analysis of coupon cross-sections after exposure to a dry air environment at 700 °C at time intervals of 50, 100 and 200 hours. These measurements will then be used to validate the predictions of oxide layer thicknesses provided using both empirical and mechanistic modelling methodologies under the same conditions. Similarly, to the comparison of specific mass changes, differences between experimental and predicted oxide layer thicknesses will be presented as percentage differences to allow for agreement between the data sets to be discussed.

Similar analysis will be conducted on corroded coupons of material, exposed to FLiNaK molten salt at 700 °C for time periods of 50, 100 and 200 hours, to measure the depth of corrosive attack. These measurements will subsequently be used to validate predictions of corrosion depth obtained using the mechanistic modelling methodology described in this thesis during Section 4.4, with the same method of comparison being used to discuss agreement between data sets.

4.3 Use of empirical model for oxide growth prediction

Empirical modelling is a commonly used tool for predicting oxidation behaviour of super alloys, using published data to determine relationships between oxidation behaviour and an alloys composition. Published work by Sato et al. [87] focused on the development of an empirical model for predicting the growth of alumina (Al_2O_3) during the oxidation of Ni-based super alloys. The developed model, discussed in Section 3.3 was used to predict oxide layer thicknesses for Rene N5 and SCA425+ super alloys at temperatures of 900 °C and 980 °C for durations up to 100 hours. This section aims to outline how the underpinning theory of the alumina forming model was applied into a novel empirical model for chromia forming alloys such as Hastelloy C276.

4.3.1 Development of empirical model – Application of theory

As previously discussed in Section 3.3 of this thesis, it was assumed by Sato et al. [87] that Al_2O_3 behaves as an n-type semiconductor to allow for simplification of the underlying physics behind their empirical model. As a result of this assumption, it was concluded that the theoretical background for modelling the growth of Al_2O_3 would be directly applicable to other n-type semiconductors such as chromia (Cr_2O_3) which is a commonly observed oxidation product of Cr containing Ni-based alloys. Hence, the modelling of Cr_2O_3 growth could be achieved using the same underpinning theory as the model presented by Sato et al. [87].

Therefore, equation 3.47 was changed to reflect the formation of Cr_2O_3 as shown below:

$$U = \sum_{i=1}^{n} [(z_i - z_{Cr}).x_i]\,\Delta G_{f,Cr_2O_3} \qquad \textbf{4.5}$$

where z_{Cr} is the valence of Cr and ΔG_f is the Gibbs free energy of formation of Cr_2O_3 instead of Al_2O_3.

When calculating the effective valence, Sato et al. [87] deployed a microsegragation method to determine the quantities of different elemental oxides were acting as impurities in the alumina layer. However, the presented concentrations of elemental impurities within the oxide layer closely matched the composition of the alloy. To confirm that utilising the composition of the alloy to calculate the effective valence was valid, a study was conducted in which the calculations of effective valence were performed and compared to the results of the work by Sato et al. [87]. The results of the calculation performed by Bensch et al. [88] is presented as Table 4.2.

Table 4.2 - Calculation of effective valence, performed by Bensch et al. using microsegragation method [88].

Test	Elemental contaminants (wt.%)						Val^{eff}
	Co	Cr	Mo	W	Al	Ta	
SCA425+ 1000 °C 300 hours	4.86 ± 0.02	15.12 ± 0.08	1.01 ± 0.04	3.85 ± 0.07	4.64 ± 0.02	8.49 ± 0.11	-0.5751 ± 0.0016
	5.06 ± 0.03	15.58 ± 0.08	0.97 ± 0.04	4.13 ± 0.08	4.54 ± 0.06	7.87 ± 0.29	-0.5760 ± 0.0019
	5.06 ± 0.04	15.46 ± 0.11	0.97 ± 0.07	4.18 ± 0.10	4.55 ± 0.05	7.58 ± 0.30	-0.5808 ± 0.0027
	4.90 ± 0.11	15.61 ± 0.46	0.96 ± 0.06	4.12 ± 0.07	4.59 ± 0.12	7.66 ± 0.58	-0.5777 ± 0.0035
	4.93 ± 0.15	15.54 ± 0.62	1.14 ± 0.45	3.94 ± 0.19	4.60 ± 0.10	8.04 ± 0.49	-0.5729 ± 0.0063
	5.03 ± 0.11	15.47 ± 0.25	1.03 ± 0.02	3.93 ± 0.19	4.54 ± 0.24	8.06 ± 0.20	-0.5775 ± 0.0039
	5.05 ± 0.06	15.53 ± 0.07	0.97 ± 0.01	4.01 ± 0.12	4.50 ± 0.07	8.09 ± 0.13	-0.5772 ± 0.0023
	5.07 ± 0.02	15.69 ± 0.31	0.99 ± 0.05	3.98 ± 0.10	4.46 ± 0.10	7.89 ± 0.50	-0.5789 ± 0.0049
	5.03 ± 0.12	15.50 ± 0.13	0.95 ± 0.12	3.86 ± 0.12	4.51 ± 0.12	8.30 ± 0.15	-0.5775 ± 0.0025

The average effective valence, as calculated by Bensch et al. [88] was -0.57707. Using the composition of SCA425+ to determine the effective valence yielded a value of -0.5665. The calculation steps taken to achieve this value are presented in Table 4.3.

Table 4.3 – Calculation of effective valence for SCA425+ using nominal alloy composition and calculation method described by Bensch et al. [88] using theory introduced by Sato et al. [87].

Element	Weight Percent (wt.%)	MR (kg/mol)	Z_i	$Z_i - Z_{Cr}$	Nº of Atoms	Atomic Percent (at.%)	Val^{eff}
Ni	61.85	58.693	2	-1	$3.173x10^{22}$	62.64	-0.6264
Co	5.00	58.933	2	-1	$2.555x10^{21}$	5.04	-0.0504
Cr	15.50	51.996	3	0	$8.976x10^{21}$	17.72	0.0000
Mo	1.00	95.95	6	3	$3.138x10^{20}$	0.62	0.0186
W	4.00	183.84	6	3	$6.551x10^{20}$	1.29	0.0388
Al	4.55	26.982	3	0	$5.077x10^{21}$	10.02	0.0000
Ta	8.00	180.948	5	2	$1.331x10^{21}$	2.63	0.0526
Hf	0.10	178.486	4	1	$1.687x10^{19}$	0.03	0.0003
Si	0.00	28.085	4	1	0	0.00	0.0000
				TOTAL	$5.065x10^{22}$	100.00	**-0.5665**

The discrepancies between the two methods were deemed minor, with there being a difference of 1.83% between the two different methods. This small difference was deemed to be acceptable, hence the effective valence was calculated using the nominal alloy composition throughout this work.

Following the validation of this method for determining the effective valence, modelling was completed using different variations of the composition of Hastelloy C276. As defined by Haynes International, the concentration of elements within Hastelloy C276 is allowed to be within certain limits as defined in Table 4.4.

Table 4.4 – Element concentration limits for Cr, Mo, Fe and W present in Hastelloy C276 as defined in material specification.

Element	Lower Conc. Limit (wt.%)	Upper Conc. Limit (wt.%)
Cr	14.5	16.5
Mo	15.0	17.0
Fe	4.0	7.0
W	3.0	4.5

A preliminary analysis of the effect of these ranges of values on the effective valence indicated that the concentrations of Cr and Mo had the largest impact. Therefore, test cases where variations in the Cr and Mo concentrations were devised. The test cases used in the modelling work are presented in Table 4.5.

Table 4.5 – Modelling cases for variations in the composition of Hastelloy C276 covering minimum, nominal and maximum concentrations of Cr and Mo.

Test Case	Cr concentration (wt.%)	Mo concentration (wt.%)	U (kJ/mol)
1	14.5	17.0	165.32
2	15.5	16.0	176.70
3	16.5	15.0	188.07

The test cases described in Table 4.5 were used to provide upper and lower limits of the Cr_2O_3 predictions based on the calculated values of U for each case. In the presentation of results from the empirical model, these upper and lower limits are presented as error bars to show the full range of the prediction.

4.3.2 Development of empirical model – Calculation of Gibbs free energy change of Cr_2O_3

The empirical model by Sato et al. [87] was developed for alumina forming Ni-based alloys. However, with the underpinning theory applied to Cr_2O_3 forming Ni-based alloys, shown in equation 4.5, a method of calculating the Gibbs free energy change of Cr_2O_3 was required in order to complete the calculation of the kinetic parameter, U. In the calculation of the Gibbs free energy change of formation of Cr_2O_3, it remains important to ensure minimal errors are introduced into the empirical model. Since the calculated Gibbs free energy change of Cr_2O_3 directly impacts the kinetic parameter U, it also impacts the empirical relationship between U and K_P, with the value of K_P being larger or smaller depending on whether the calculated Gibbs free energy change is larger or smaller than the actual value. Therefore, it is important to select a method of calculation that has been validated and shows minimal errors between the calculated and actual values for the Gibbs free energy change of Cr_2O_3.

Therefore, the Gibbs free energy change of Cr_2O_3 was calculated using the validated approach of Ziemniak et al. [162], who developed an empirical relationship between the Gibbs free energy of formation of Cr_2O_3 and temperature. This involved taking high temperature heat capacity, C_p, and entropy measurements over a temperature range of 250 K up to 1373 K. The C_p values were subsequently fit to the extended Maier – Kelly formulation which takes the form:

$$C_p = A + BT + CT^2 + DT^{-0.5} - ET^{-2} \quad \textbf{4.6}$$

Following this, the molar entropy can be calculated from its thermodynamic relationship with heat capacity, as shown below:

$$S^0(T) = S^0(298) + \int_{298}^{T} \frac{C_p}{T} dT \quad \textbf{4.7}$$

By substitution of equation 4.6 into equation 4.7, an equation for the molar entropy in the form of the Maier – Kelly formulation can be found:

$$S^0(T) = S^0(298) + A \ln T + BT + \left(\frac{C}{2}\right) T^2 - 2DT^{-0.5} - \left(\frac{E}{2}\right) T^{-2} - F \quad \textbf{4.8}$$

where F is the constant of integration and takes the value of the integral of C_p/T when the temperature is 298.15 K.

Using a similar method, the change in enthalpy for the formation of Cr_2O_3 can be determined using the following thermodynamic relationship:

$$\Delta_f H^0(T) = \Delta_f H^0(298) + \int_{298}^{T} \Delta_f C_p dT \quad \textbf{4.9}$$

Again, substituting equation 4.6 into 4.9 gives the following result:

$$\Delta_f H^0(T) = \Delta_f H^0(298) + AT + \left(\frac{B}{2}\right) T^2 + \left(\frac{C}{3}\right) T^3 + 2DT^{0.5} - ET^{-1} - G \quad \textbf{4.10}$$

where G is the constant of integration and takes the value of the integral of C_p when the temperature is 298.15 K.

Combining equations 4.8 and 4.10 in the form of the equation for the Gibbs free energy change, presented as equation 4.11, gives the equation for the Gibbs free energy change as presented as equation 4.12.

$$\Delta_f G^0(T) = \Delta_f H^0(T) - T\Delta_f S^0(T) \quad \textbf{4.11}$$

$$\Delta_f G^0(T) = \Delta_f G^o(298) - (T - 298.15)\ \Delta_f S^o(298) - g - aT(\ln T - 1) - \left(\frac{b}{2}\right) T^2 - \left(\frac{c}{6}\right) T^3 + (4d) T^{0.5} - \left(\frac{e}{2}\right) T^{-1} + fT \quad \textbf{4.12}$$

The values of each of the parameters required to calculate the Gibbs free energy change of Cr_2O_3 formation using equation 4.12 are presented in Table 4.6.

Table 4.6 – Coefficients used when calculating the Gibbs free energy change of Cr_2O_3, defined in equation 4.12 [162].

$\Delta S^0(298)$	a	b	c (x10^{-6})	d
-272.511	49.275	-0.00601	-15.4989	-660.534
e (x10^{-5})	**f (J/mol/K)**	**g (J/mol)**	**$\Delta G^0(ref)^*$ (kJ/mol)**	
3.09151	353.036	-9560.6	840.58	

*The reference temperature for Gibbs free energy of Cr_2O_3 formation was 1100 °C

Based on equation 4.12 and the test temperature of 700 °C utilised in this study, the Gibbs free energy of formation of Cr_2O_3 was calculated to be -872.24 kJ/mol.

4.3.3 Development of empirical model – Relationship between U and K_P

To complete the empirical model, a relationship between the value of the kinetic factor, U, and the value of K_p need to be determined. Sato et al. [87] stated that the relationship between K_p and U follows the general form of the Arrhenius equation:

$$K_p = A.e^{b.U} \quad \textbf{4.13}$$

where A and b are temperature dependent constants. To determine the values of these constants, K_p values for Ni-based alloys were taken from literature, with values of U being calculated for each of the alloys for which data was collected. If the data used did not have data points for 700 °C, these values were interpolated or extrapolated from the available data using the Arrhenius form of the equation for K_p:

$$K_p = K_0 e^{-\frac{Q}{RT}} \quad \textbf{4.14}$$

Alloys were chosen for this study by evaluating the oxidation products of the alloys at the temperatures quoted. Based on this analysis, if Cr_2O_3 was a main product, it was included in the preliminary study dataset. In total, thirteen Ni-based alloys were considered within the study. A summary of each alloy's composition is presented in Table 4.7, whilst a summary of K_P values for each alloy is included as Table 4.8.

Table 4.7 – Summary of alloy compositions considered for use in the empirical model study [99, 101, 163-168] [169-171].

Material	Element (wt.%)																			
	Ni	Cr	Mo	Fe	Si	Mn	Co	W	Al	Ti	V	Ta	Hf	Zr	Nb	Cu	C	P	S	B
Hastelloy C22	57.36	21.20	13.30	3.80	0.03	0.25	0.93	2.90	-	-	-	-	-	-	-	-	0.002	0.007	0.004	-
GH202	66.45	20.39	4.08	-	-	-	-	5.62	1.38	2.02	-	-	-	-	-	-	0.06	-	-	-
GH738	58.78	19.48	3.99	0.45	-		12.9	-	1.4	2.95	-	-	-	-	-	-	0.055	-	-	-
GH586	54.14	19.00	8.00	-	-	-	11.00	3.00	1.60	3.20	-	-	-	-	-	-	0.06	-	-	-
GH3535	70.06	7.00	16.00	4.00	0.40	0.50	-	-	-	2.00	-	-	-	-	-	-	0.04	-	-	-
RR1000	52.3	15.00	5.00	-	-	-	18.50	-	3.00	3.60	-	2.00	0.50	0.06	-	-	0.027	-	-	0.015
Astroloy	55.41	15.00	5.00	-	-	-	17.00	-	4.00	3.50	-	-	-	-	-	-	0.06	-	-	0.03
Waspaloy	58.48	19.50	4.00	-	-	-	13.50	-	1.40	3.00	-	-	-	0.05	-	-	0.06	-	-	0.0065
Udimet 720	55.16	18.00	3.00	-	-	-	15.00	1.25	2.50	5.00	-	-	-	0.04	-	-	0.02	-	-	0.035
Hastelloy C276	54.97	15.80	16.20	6.50	0.06	-	1.90	4.20	-	-	0.3	-	-	-	-	-	0.007	0.035	0.025	-
IN718	52.50	19.00	3.00	18.50	0.20	0.20	-	-	0.60	0.80	-	-	-	-	5.20	-	-	-	-	-
IN625	61.90	21.20	9.30	3.50	0.20	-	0.10	-	0.20	0.20	-	-	-	-	3.70	-	-	-	-	-
Haynes 282	55.23	19.00	9.50	1.50	0.15	0.30	10.00	-	1.70	2.55	-	-	-	-	-	-	0.06	-	-	0.005

Table 4.8 – Summary of Ni-based alloy K_p data at 700 °C used to generation plots of LN(K_P) against U.

Material	Parabolic rate constant, K_P ($mg^2/cm^4/s$)	Method of calculation	References
Hastelloy C22	$5.76x10^{-9}$	Linear Extrapolation	[163]
GH202	$2.07x10^{-8}$	Linear Extrapolation	[164]
GH738	$1.37x10^{-9}$	Linear Extrapolation	[165]
GH586	$1.34x10^{-7}$	Linear Extrapolation	[166]
GH3535	$8.20x10^{-9}$	Data Available in source	[167]
RR1000	$3.23x10^{-9}$	Data Available in source	[101]
Astroloy	$5.31x10^{-9}$	Linear Extrapolation	[168]
Waspaloy	$2.78x10^{-9}$	Linear Extrapolation	
Udimet 720	$1.17x10^{-8}$	Linear Extrapolation	
Hastelloy C276	$1.27x10^{-7}$	Linear Extrapolation	[99]
IN718	$7.40x10^{-8}$	Linear Extrapolation	[169]
IN625	$1.90x10^{-8}$	Linear Extrapolation	[170]
Haynes 282	$7.69x10^{-8}$	Linear Extrapolation	[171]

Based on the K_P data presented in Table 4.8, a plot of LN(K_P) against U was generated to identify if a trend existed between the values of K_P and U for the full collection of Ni-based alloys.

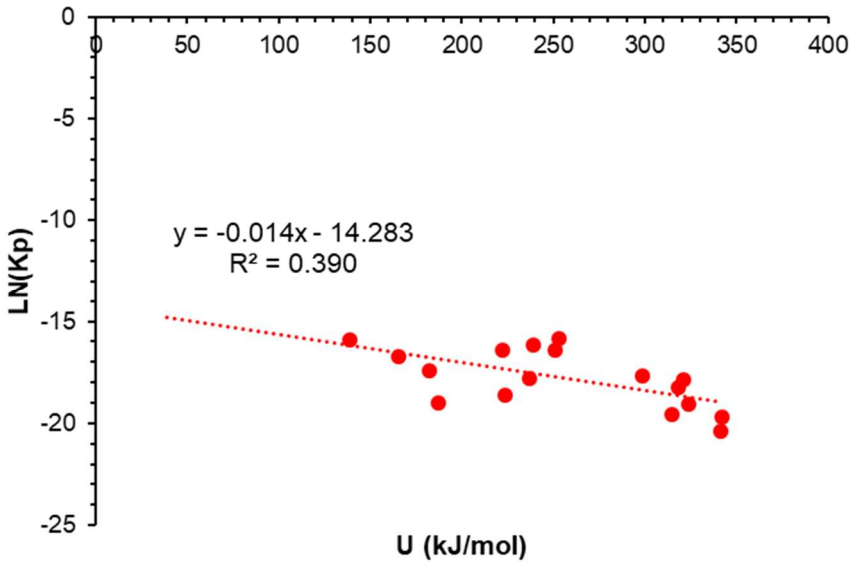


Figure 4.10 – Plot of the natural logarithm of K_P against U for alloy data presented in Table 4.8. A calculated R^2 value of 0.390 indicates that no correlation exists between the K_P and U data for the selected alloys.

Due to the lack of data correlation observed in Figure 4.10, further material down selection was undertaken to develop a more robust relationship between K_P and U. Firstly, the data sets used to calculate values of K_P for each alloy were interrogated and sets with fewer than three data points were removed. Similarly, data sets where the presented data had to be manually interpreted were also considered for removal due to the potential to introduce significant errors into the model if interpreted incorrectly.

After interrogation of the data sets, the composition of each alloy was assessed to remove alloys with compositions too dissimilar to that of Hastelloy C276, with concentrations of Ni and Cr being the main focus for sample removal. This Ni-based alloy down selection process left six alloys with compositions similar to Hastelloy C276 and robust data sets that could be used in this study. These alloys include GH568, GH202, Hastelloy C276, Udimet 720, Waspaloy and Astroloy. The resultant plot of the natural logarithm of K_P against U for these six alloys is presented as Figure 4.11.

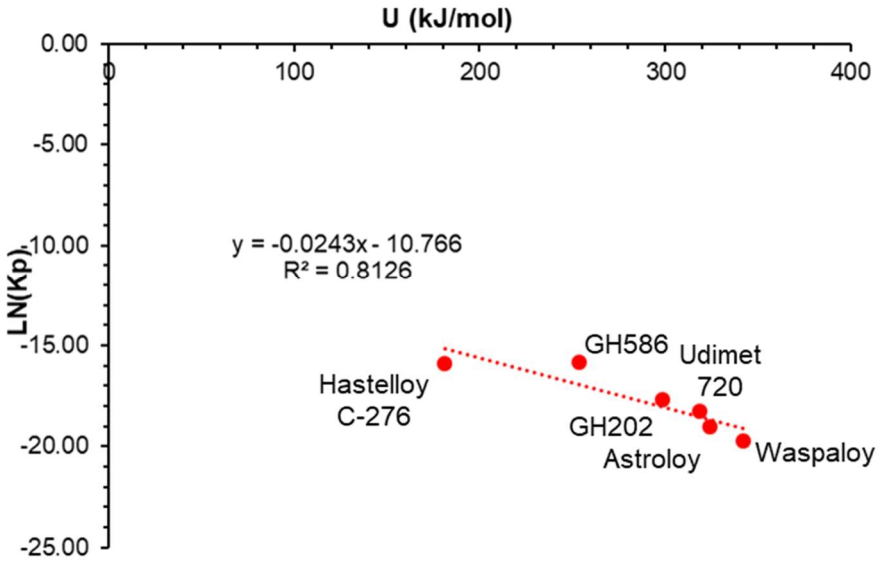


Figure 4.11 – Plot of LN(K_P) against U for alloys of GH586, GH202, Hastelloy C276, Udimet 720, Waspaloy and Astroloy [99, 164, 166, 168] . Plot shows improved relationship between LN(K_P) against U for these alloys, with a calculated R^2 of 0.8126.

Based on the linear equation presented in Figure 4.11 the values of A and b present in equation 4.13 are 2.11×10^{-5} and -0.0243 respectively, resulting in the equation for K_P shown below.

$$K_p = 2.11 \times 10^{-5} e^{-0.0243U} \quad \textbf{4.15}$$

Based on the values of U presented in Table 4.5 and equation 4.15, K_P values of 2.19×10^{-7}, 2.88×10^{-7} and 3.80×10^{-7} $mg^2/cm^4/s$ were calculated for the oxidation of Hastelloy C276. Based on these values of K_P, the mass change per unit area was predicted for the oxide in the range of 0 to 200 hours. In future sections, results will be presented using a K_P value of 2.09×10^{-7} $mg^2/cm^4/s$, with the minimum and maximum values being used to present error bars.

4.3.4 Development of empirical model – Predicting oxide layer thickness

Based on the predicted specific mass change, the oxide layer thickness was calculated. This was done on the assumption that the predicted oxide layer was primarily composed of Cr_2O_3, with any other alloying elements within the oxide layer being negligible/ acting as a small amount of impurity. This is a very similar assumption to that made for the underpinning mathematics of the model and was therefore deemed to be a valid assumption for the calculation of the oxide layer thickness.

Considering the following metal oxidation reaction,

$$\frac{x}{y}M + \frac{1}{2}O_2 \rightarrow \frac{1}{y}M_xO_y \quad \textbf{4.16}$$

where M is the metallic element and x, and y are constants in the chemical equation. The rate of the reaction presented as equation 4.28, can be expressed as follows:

$$\frac{d\xi}{dt} = f(t) \quad \textbf{4.17}$$

where ξ represents the extent of the reaction. At any time of t, the extent of the reaction can be shown to be equal to the formation of reaction products or the loss of the reactants:

$$d\xi = dn_{M_xO_y} = -\frac{dn_M}{x} = -\frac{2dn_{O_2}}{y} \quad \textbf{4.18}$$

where n is the number of moles of the specified species. In the case where no metal volatilization occurs, the mass change of the sample,ΔW can be related to the mass change of oxygen at the surface. It therefore follows that:

$$-2dn_{O_2} \times AW_{O_2} = \Delta W \quad \textbf{4.19}$$

where $AW_{O_2}$is the atomic weight of oxygen (~16 g/mol). It can therefore be said that:

$$-2dn_{O_2} = \frac{\Delta W}{16} \quad \textbf{4.20}$$

$$-2dn_{O_2} = \frac{\Delta W}{16} = ydn_{M_xO_y} = -\frac{y}{x}dn_M \quad \textbf{4.21}$$

In oxidation testing, the standard is to present the mass change as a function of the sample are. Applying this, gives the following result:

$$-2\frac{dn_{O_2}}{A} = \frac{1}{16}\frac{\Delta W}{A} = y\frac{dn_{M_xO_y}}{A} = -\frac{y}{x}\frac{dn_M}{A} \quad \textbf{4.22}$$

Based on the mass change due to oxygen at the interface between the sample and the air, the amount of oxide formed at the surface can then be calculated using the following equation:

$$\frac{\Delta W_{M_xO_y}}{A} = \frac{MW_{M_xO_y}}{16y}\frac{\Delta W}{A} \quad \textbf{4.23}$$

where $MW_{M_xO_y}$is the molecular weight of the oxide. To then determine the thickness of the oxide layer, the following equation was derived.

$$X_{M_xO_y} = \frac{MW_{M_xO_y}}{16\rho_{M_xO_y}y}\frac{\Delta W}{A} \quad \textbf{4.24}$$

where $X_{M_xO_y}$represents the thickness of the oxide layer and $\rho_{M_xO_y}$ is the density of the formed oxide. Applying this equation to the result of the empirical model allowed for the prediction of the thickness of the chromia scale. Using the following chemical equation:

$$\frac{2}{3}Cr + \frac{1}{2}O_2 \rightarrow \frac{1}{3}Cr_2O_3 \quad \textbf{4.25}$$

The thickness of the chromium oxide scale was deduced to be equal to:

$$X_{Cr_2O_3} = \frac{MW_{Cr_2O_3}}{48\rho_{Cr_2O_3}}\frac{\Delta W}{A} \quad \textbf{4.26}$$

4.4 Use of MATLAB functions in predicting corrosion and oxidation behaviour

MATLAB [153] is a commonly used calculation tool in the field of engineering due to its extensive library of functions that can be applied to different engineering scenarios. However, in the fields of molten salt corrosion and oxidation of alloys, the deployment of MATLAB has not been seen for predictive models. In relation to this research, MATLAB allows for the predictions of element distribution changes within alloys during oxide growth or element depletion processes in corrosive environments. Typically, changes in elemental distribution and the precise make up of corrosion products is not entirely known. However, being able to predict changes in an alloy due to oxidation and molten salt corrosion processes is useful in fully understanding the mechanisms of molten salt corrosion and oxidation of alloys. Combined with the use of compositional and surface analysis techniques, a much more robust understanding of corrosion and oxidation of alloys was achieved.

4.4.1 Overview of MATLAB partial differential equation solver

The MATLAB partial differential equation solver is a tool that can be used when looking to solve one- and two-dimensional partial differential equations which are of the form shown in equation 4.27:

$$c\left(x,t,u,\frac{\partial u}{\partial x}\right)\frac{\partial u}{\partial t} = x^{-m}\frac{\partial}{\partial x}\left(x^m f\left(x,t,u,\frac{\partial u}{\partial x}\right)\right) + s\left(x,t,u,\frac{\partial u}{\partial x}\right) \quad \textbf{4.27}$$

In equation 4.27 there are a number of user defined input arguments that are defined within the code. This is achieved by using both MATLAB scripts and specific MATLAB functions associated with the partial differential equation solver. The partial differential equation solver requires three input functions, the first being the equation function (pdefun), the second the initial condition function (icfun) and the boundary condition function (bcfun). The formulation of each of these functions will be discussed throughout this section.

4.4.2 Development of a mechanistic model in MATLAB – Predicting element distribution

The MATLAB partial differential equation solver was used throughout this thesis to predict elemental changes to Hastelloy C276 in high-temperature environments both with and without molten salt. The main stages in using the MATLAB partial differential equation solver are presented in Figure 4.12.

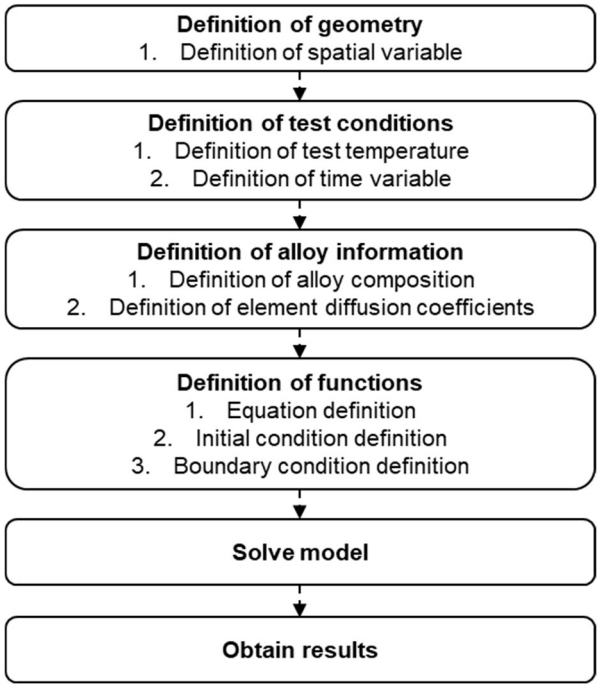


Figure 4.12 – Stages involves in developing a diffusion-based model using the MATLAB partial differential equation solver.

As described in Figure 4.12, there are three main functions that are used to run the partial differential equation solver in MATLAB. These three functions are the equation definition, initial conditions, and boundary conditions functions. The equation definition function defines the partial differential equation to solve. In this case the equation being solved is Fick's second law of diffusion, presented as equation 4.28.

$$\frac{\partial C}{\partial t} = D\frac{\partial^2 C}{\partial x^2} \qquad \textbf{4.28}$$

In the context of this model, Fick's second law of diffusion is applicable as elemental concentration changes need to be modelled in terms of a spatial term to understand the distribution of elements within the substrate material. The concentration changes also need to be modelled over a number of time intervals in order for the full kinetics of oxide growth to be captured.

When defining the equation, it must be defined using the standard form that the solver in MATLAB expects. The expected form is that of equation 4.27. In this form, x is the spatial variable, t is the time variable, u is the dependent variable that is being differentiated with respect to x and t whilst du/dx is the partial spatial derivative. In the case of this research, the dependent variable, u, is the concentration of the different species being modelled.

The values of c, f and s are therefore the coefficients of each of these terms, with the value of m being defined as the symmetry constant. The value of m can take a value of 0, 1 or 2 depending on whether 1-D Cartesian coordinates, 2-D cylindrical coordinates or 3-D spherical coordinates are being used. In this research, the value assigned to the symmetry constant is zero, hence the model is developed in 1-D Cartesian coordinates. This is achieved using the simplified geometry utilised in this work, shown in Figure 4.13.

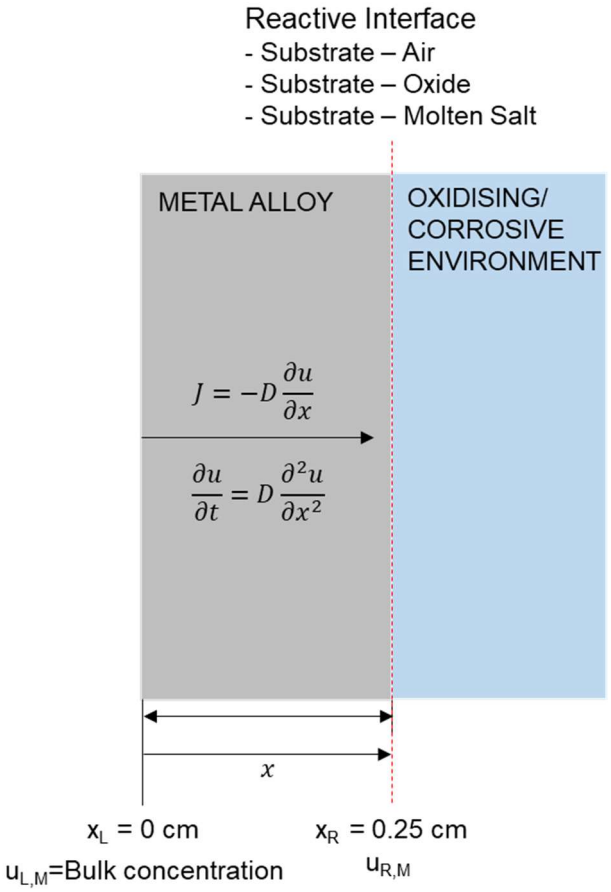


Figure 4.13 – Diagram of simplified modelling geometry, allowing for the modelling of elemental changes in a coupon of Hastelloy C276 in 1-D Cartesian coordinates.

To improve the model accuracy and complexity, the model could be developed as a 3-D model. However, in the case of this research, the diffusion of alloying elements was modelled in one dimension, with the concentration changes then applied in each direction to each surface of the coupon expose to the oxidising or corrosive environment. Modelling the diffusion processes in this way has previously been shown to provide accurate prediction capabilities whilst achieving a simplified modelling geometry which is much less computationally expensive [93].

Since all equations being modelled need to be re-written in the form defined by equation 4.27, Fick's second law of diffusion can be written as shown in equation 4.29:

$$\frac{1}{D}\frac{\partial C}{\partial t} = \frac{d}{dx}\left(\frac{\partial C}{\partial x}\right) \qquad \textbf{4.29}$$

Based on the form in which Fick's second law of diffusion is presented in equation 4.29, the values associated with the coupling, flux and source terms can be determined. The input values for each of these terms as well as the symmetry constant are presented in Table 4.9.

Table 4.9 – Constant values for standard form required by MATLAB's partial differential equation solver.

Coefficient	Description	Value
c	Coupling term	1/D
f	Flux term	$\frac{\partial u}{\partial x}$
s	Source term	0
m	Symmetry constant	0

A key parameter in solving Fick's second law is the diffusion coefficient of the alloying elements within the alloy matrix. For this, diffusion coefficients for each constituent element in Hastelloy C276 in a Ni solute were found in literature. For many elements, multiple diffusion coefficients were used within the model, with the individual results for each element then being averaged. The utilised diffusion coefficients were taken within a temperature range as close to the test temperature as possible. In some cases, this data was not available and hence was extrapolated from several data points. The overall minimum and maximum values for the specific mass change were then presented using error bars. A summary of the diffusion coefficients used for each constituent alloying element of Hastelloy C276 is presented in Table 4.10.

Table 4.10 – Summary of all diffusion coefficient data used from literature for each alloying element.

Element	Diffusion Coefficient (cm^2/s)	References
Ni	1.17×10^{-15} 8.65×10^{-16}	[82, 172, 173]
Cr	4.24×10^{-15} 3.51×10^{-15}	[119, 174]
Mo	2.77×10^{-16} 9.16×10^{-16}	[174, 175]
Fe	4.77×10^{-16} 2.36×10^{-16}	[82, 173, 176]
W	1.22×10^{-16} 2.01×10^{-16}	[174, 177]
Co	6.70×10^{-16} 2.12×10^{-15}	[82, 173]
Mn	3.58×10^{-13} 6.40×10^{-15}	[82, 120, 173]
V	1.01×10^{-15}	[173]
Si	3.02×10^{-14}	[178]
C	1.04794×10^{-11}	[93]

In Table 4.10 some large variations in the diffusion coefficients quoted in literature can be observed, with the greatest variation being observed in the diffusion coefficients of Mn. Based on these differences, a minimum and maximum prediction of the mass change per unit area was possible. Based on these values, an average at each time point was calculated.

For modelling simplicity, it is assumed that the diffusion coefficient of each alloying element within the substrate remains constant over time. In reality, diffusion coefficient may change over time with changes in concentration which may have a direct impact on the oxidation kinetics being modelled. However, due to the relatively short time periods and small concentrations changes being predicted by this model, the assumption of constant diffusion coefficients was deemed valid.

A key area of interest in this model is the movement of element ions within an alloy and how the element distribution changes with time. This is important to understand the outward diffusion of alloying elements to the substrate – air or

substrate – molten salt interface as this will determine the rate of growth of oxide layers or growth of corrosion products.

To achieve this using the partial differential equation solver, the initial and boundary conditions need to be defined. The initial condition for each element within an alloy is the initial concentration of the element within the alloy. For this work, the concentration of each element within the alloy was defined. This was achieved by converting the weight percentage of each element into an elemental mass by multiplying the weight percentage by the sample mass. Dividing the elemental mass in g by the molecular weight of the element in units of g/mol allowed for the determination for the concentration of the elements in mol as shown in equation 4.30:

$$mol = \frac{M}{MR} \qquad \textbf{4.30}$$

The initial concentrations in moles for each alloying element based on the calculation performed using equation 4.30, present in Hastelloy C276 are defined in Table 4.11.

Table 4.11 - Initial concentration values for each element modelled in MATLAB.

Element	Concentration (wt.%)	Concentration (mol)
Ni	57.000	0.054684
Mo	16.000	0.009390
Cr	15.500	0.016785
Fe	5.500	0.005546
W	3.750	0.001149
Co	2.500	0.002389
Mn	1.000	0.001025
V	0.350	0.000387
Si	0.080	0.000160
P	0.025	0.000045
C	0.010	0.000047
S	0.010	0.000018

To solve the model, a number of assumptions and boundary constraints were defined in a function. Similarly, to defining the equation to be solved, boundary constraints were defined in the format desired by the MATLAB solver. In this case the constraints were defined in the form defined by equation 4.31.

$$p(x,t,u) + q(x,t)f\left(x,t,u,\frac{\partial u}{\partial x}\right) = 0 \quad \textbf{4.31}$$

Boundary conditions were defined as prescribed by the MATLAB function. They are defined at the left-hand side and the right-hand side of the geometry. In order to achieve this and reduce the computational demand, a simplified geometry was used. Considering a coupon of Hastelloy C276 sat in a crucible, as shown in Figure 4.2**,** it was assumed that the movement of alloying elements at each surface was uniform i.e. that alloying elements would diffuse the same amount in each direction. This included the surface that was in contact with the crucible, meaning a line of symmetry could be drawn through the centre of the coupon in both the x and y directions, as depicted in Figure 4.14.

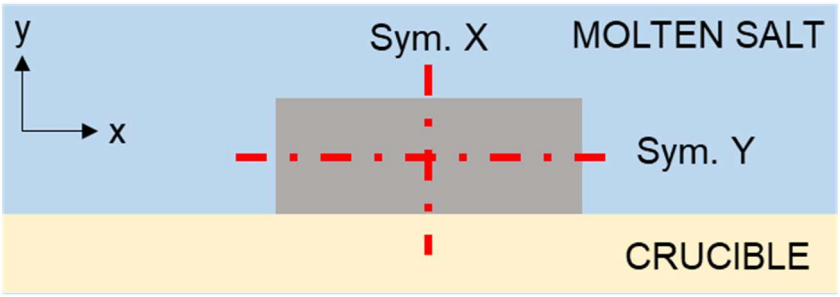


Figure 4.14 – Depiction of symmetry conditions in x and y directions through the centre of the Hastelloy C276 coupon.

Within the modelling geometry, boundary conditions were defined at the left- and right-hand sides of the geometry. In this case the left-hand side of the geometry was taken to be the centre of the geometry and the right-hand side the substrate – air interface. Therefore, at the left-hand side of the modelling geometry, it is assumed that the concentration of each alloying element will remain the same as its initial concentration for the duration being modelled. This can be expressed as:

$$u(0,t) = uConc \quad \textbf{4.32}$$

where u(0,t) is the concentration of the alloying element being assessed, at the left-hand side of the geometry in units of mol and uConc is the initial concentration of the same alloying element in units of mol. As shown in equation 4.31, all boundary conditions must be expressed so that they equal zero. The boundary condition at the left-hand side of the modelling geometry is therefore expressed as:

$$uL - uConc = 0 \quad \textbf{4.33}$$

At the right-hand side of the modelling geometry, the alloying element concentration will reduce due to the loss of elements into the oxide layer. The boundary condition can therefore be expressed as:

$$u(x,t) + D\frac{du}{dx} = 0 \qquad \textbf{4.34}$$

where u(x,t) is the concentration of the alloying element at the right-hand side of the geometry in units of mol, du/dx is the concentration gradient of the alloying element across the modelling geometry and D is the diffusion coefficient of the alloying element in units of cm^2/s.

4.4.3 Development of a mechanistic model in MATLAB – Predicting mass changes due to oxide growth

Once elemental changes have been calculated by the MATLAB solver, changes in concentration can be converted to mass changes due to the growth of oxide. Due to the presence of oxygen when undergoing an oxidation process, elements at the surface of the substrate will react with oxygen to form their most stable metallic oxides. Based on the reaction equations for each element, an estimate of the mol of oxide formed can be made and subsequently, their mass determined.

For this to be achieved, each oxide forming reaction must be defined for each of the metallic element's present in Hastelloy C276. These reactions are summarised in Table 4.12.

Table 4.12 - Summary of oxide forming reactions taking place between metallic species and oxygen to form metallic oxides.

Alloying Element	Oxide Forming Reaction	Equation Number
Ni	$Ni + \frac{1}{2}O_2 \xrightarrow{\square} NiO$	4.35
Mo	$Mo + \frac{3}{2}O_2 \xrightarrow{\square} MoO_3$	4.36
Cr	$2Cr + \frac{3}{2}O_2 \xrightarrow{\square} Cr_2O_3$	4.37
Fe	$Fe + \frac{1}{2}O_2 \xrightarrow{\square} FeO$	4.38
W	$W + \frac{3}{2}O_2 \xrightarrow{\square} WO_3$	4.39
Co	$Co + \frac{1}{2}O_2 \xrightarrow{\square} CoO$	4.40
Mn	$Mn + O_2 \xrightarrow{\square} MnO_2$	4.41
Si	$Si + O_2 \xrightarrow{\square} SiO_2$	4.42
V	$2V + \frac{5}{2}O_2 \xrightarrow{\square} V_2O_5$	4.43

Based on the mol of metal ions involved in each reaction, the number of mol of oxide produced can be determined by dividing by the number of mol of metal and multiplying by the number of mol of oxide, for example, in the reaction of Cr with O to form Cr_2O_3, 2 moles of Cr react with 1.5 moles of O_2 to form 1 mol of Cr_2O_3. For this reaction, the concentration of Cr depleted from the substrate can be divided by 2 and multiplied by 1 to calculate the mol of Cr_2O_3 produced. Following this, the mass of oxide can be determined by multiplying the number of mol of oxide by the molecular weight of the oxide:

$$M = MR \times mol \tag{4.44}$$

where M is the mass in grams, MR the molecular weight of the oxide in g/mol and mol the concentration in mol. Assuming each metal oxide forms simultaneously, the total mass increase due to oxide growth can be calculated by summing these values. However, the convention in literature is to present results as a mass change per unit area, i.e. the specific mass change. Since the mass change was assumed to be uniform at each surface, the total mass change per unit area was calculated using the following equation:

$$\Delta W = \frac{\Delta M}{\pi r^2} + \frac{\Delta M}{\pi dh} \tag{4.45}$$

Where ΔW is the specific mass change of the coupons and ΔM is the mass change predicted for each oxide by equation 4.44. In equation 4.45, the parameter r is the radius of the Hastelloy C276 coupons, d the diameter of the coupons and h the height. These parameters took values of 6.35 mm, 12.7 mm, and 5 mm, respectively.

Upon growth of the metallic oxide layers, diffusion of alloying elements ions through the metallic oxide layers to the oxide - air interface would become the mechanism controlling the oxidation rate of the alloy. However, this model assumes that metallic ions at the substrate – air interface are continuously oxidised to their metallic oxide at this interface and does not account for diffusion of metallic ions through the formed oxide layer. To fully capture the oxidation mechanism, diffusion of metallic ions through the oxide layer to the oxide layer – air interface would need to be added to the model.

4.4.4 Development of a mechanistic model in MATLAB – Predicting elemental depletion depths and depletion depth due to corrosion.

Based on the results calculated for concentration changes of elements within the alloy, the depletion depth of elements could be calculated within MATLAB. This was achieved by determining the position of the first value that did not equal the initial concentration within the solution vector. Determining this position at each time interval allows for the depletion depth to be modelled as a function of time.

Based on the situation being modelled, the total corrosion depth was calculated. This was achieved by modelling the corrosion process in three parts, intrinsic corrosion, active corrosion, and internal oxidation. This concept has been used previously by Li et al. [121] who described intrinsic corrosion as the corrosion behaviour due to impurities in the salt and active corrosion as the corrosion behaviour due to pure salt. In the scenario being investigated in this work, oxidation is a key factor in material degradation. However, oxidation can occur internally if oxide is able to diffuse into the material substrate. This results in metallic oxides being formed within the substrate instead of the substrate – salt interface.

4.4.4.1 Development of mechanistic model for fluoride salt corrosion

As discussed previously in Section 3.5.3, Li et al. [121] have used the theories of intrinsic and active corrosion previously when predicting the corrosion behaviour of stainless steels. Li et al. [121] developed a model to predict the corrosion behaviour of stainless steels in the nitrate salt combination Solar Salt, composed

of 60 wt.% sodium nitrate ($NaNO_3$) and 40 wt.% potassium nitrate (KNO_3), which is a leading candidate for use in concentrating solar power plants as a HTF [179]. Due to the presence of oxygen within the molten salt, the model used by Li et al. [121] described the total oxide thickness as the sum of the oxide thicknesses due to intrinsic and active corrosion.

$$h_{tot} = h_{ic} + h_{ac} \quad \textbf{4.46}$$

where h_{tot} is the total oxide thickness, and h_{ic} and h_{ac} are the oxide thicknesses due to intrinsic and active corrosion, respectively. However, in molten salt environments, previous studies have shown that many oxides are soluble in molten FLiNaK salt, hence the substrate material would remain exposed to attack from the molten fluoride salt. Therefore, in this work, h_{tot} will represent the total corrosion depth with h_{ic} and h_{ac} representing the corrosion depth due to intrinsic and active corrosion.

The original model by Li et al. [121], base the underlying mathematics of the model on a four-step active corrosion process which is based on the movement of $FeCl_2$, as discussed in Section 3.5.3. However, in this work the most prominent impurity in fluoride molten salts is hydrogen fluoride (HF), formed by the reaction of fluoride salts with water present in the molten salt [127]. Hence, the active corrosion process will be based on the movement of HF. The intrinsic corrosion process will be based on the movement of the metallic fluoride chromium (II) fluoride (CrF_2) which is formed by the reaction of the substrate with the FLiNaK molten salt.

Since the rate active and intrinsic corrosion are governed by the diffusion of the two aforementioned species, it follows that the molar flux of either species can be expressed as per Fick's first law, either as a function of the diffusion coefficient or concentration of the species. Following the mathematics for CrF_2 gives the following result:

$$J_{CrF_2} = -D_{CrF_2} \frac{dC_{CrF_2}}{dh_{ic}} \quad \textbf{4.47}$$

$$J_{CrF_2} = -C_{CrF_2} \frac{dh_{ic}}{dt} \quad \textbf{4.48}$$

The rate of corrosion depletion, defined as dh/dt can be expressed by combining equations 4.47 and 4.48 and making dh/dt the subject:

$$\frac{dh_{ic}}{dt} = D_{CrF_2} \frac{1}{C_{CrF_2}} \frac{dC_{CrF_2}}{dh_{ic}} \quad \textbf{4.49}$$

where D_{CrF_2} is the diffusion coefficient of CrF_2 in the oxide, and C_{CrF_2} is the concentration of CrF_2 within the oxide layer. When the reactions reach an equilibrium, it can be said that:

$$\frac{dh_{ic}}{dt} = D_{CrF_2}\frac{1}{C_{CrF_2}}\frac{\Delta C_{CrF_2}}{h_{ic}} \quad \textbf{4.50}$$

where ΔC_{CrF_2} represents the differences in CrF_2 concentration between the molten salt/ oxide and oxide/substrate interface. The concentration of oxidized CrF_2 is assumed to be negligible, hence:

$$\Delta C_{CrF_2} = C_{CrF_2}^{in} \quad \textbf{4.51}$$

where $C_{Cr\ _2}^{in}$ represents the concentration of CrF_2 at the oxide/substrate interface, assuming that all of the fluorine in the reaction is transformed into CrF_2, it follows that:

$$C_{CrF_2}^{in} = C_{F_2}^{in} \quad \textbf{4.52}$$

where $C_{F_2}^{in}$ represents the concentration of F_2 at the oxide/substrate interface. However, the change in concentration across the oxide scale has not been fully understood. In the model by Li et al. [121], a linear relationship was chosen for the diffusion process across the oxide. Using this relationship gives:

$$C_{F_2}^{in} = \gamma\varphi(F^-) \quad \textbf{4.53}$$

where γ is a linear coefficient and $\varphi(F^-)$ is the concentration fraction of F^- in the molten salt melt. Combining equations 4.50 - 4.53 gives the following expression:

$$\frac{dh_{ic}}{dt} = D_{CrF_2}\frac{1}{C_{CrF_2}}\frac{\gamma\varphi(F^-)}{h_{ic}} \quad \textbf{4.54}$$

Which can then be rearranged and integrated with respect to t to give an expression for h_{ic}:

$$h_{ic} = \sqrt{D_{CrF_2}\frac{1}{C_{CrF_2}}\gamma\varphi(F^-)t} \quad \textbf{4.55}$$

Using MATLAB, the value of t can be changed iteratively to obtain the depletion depth due to active corrosion as a function of time. Following these same steps for active corrosion, where instead of monitoring the movement of CrF_2, HF will be monitored, the depletion depth due to active corrosion with respect to time can be calculated, with the total depletion depth being calculated finally as per equation 4.46. The depletion depths calculated using this method will be presented in Chapter 6 and compared to experimentally determined depletion depths.

Based on the theory implemented for the diffusion base model, discussed in Section 4.4.2, parabolic kinetics of corrosion are assumed. In this case, this was deemed to be a valid assumption as the corrosion of Ni-based alloys in molten salt environments is caused by the outward diffusion of alloying elements and the inward diffusion of impurities to generate a dealloying corrosion mechanism which then leads to the dissolution of less noble alloying elements, such as Cr, from the substrate.

In the case of CrF_2 and HF, the diffusion coefficients for both species in a molten FLiNaK salt environment are required for the calculation of the active and intrinsic corrosion depths. They are also required to predict the concentration changes of each species throughout the molten salt. The diffusion coefficients used within this model were obtained from literature and are detailed in Table 4.13.

Table 4.13 – Diffusion coefficients for CrF_2 and HF in molten salt environments, obtained from literature sources [180-182].

Species	Diffusion Coefficient (cm^2/s)	Reference
CrF_2	$3.78x10^{-5}$	[180, 181]
HF	$3.40x10^{-5}$	[182]

Table 4.13 shows a faster diffusion coefficient for CrF_2 within a molten FLiNaK salt medium when compared with that of HF. In this case, diffusion coefficients in literature for CrF_2 were initially for 600 °C. Therefore, $3.78x10^{-5}$ cm^2/s was calculated using the Arrhenius equation, utilising the activation energy of diffusion of Cr^{2+} in chloride salt from Yang et al. [181] to derive the full Arrhenius expression, which is presented as equation 4.56:

$$D_{CrF_2} = 1.13 \times 10^{-3} e^{-\frac{27.5\ (\frac{kJ}{mol})}{RT}} \qquad \textbf{4.56}$$

4.4.4.2 Inclusion of oxygen impurity in molten fluoride salt

In this study, the incorporation of oxygen within the molten salt must also be considered. Oxygen was introduced into the molten salt system due to the experimental research taking place in an air environment. Therefore, its diffusion through the molten salt, and its subsequent impact on the corrosion behaviour at the molten salt – substrate interface must be considered.

To consider the impact of oxygen inclusion within the molten salt system, it was assumed that any oxidation product would be fully dissolved in the molten salt. This assumption was made as studies have shown that metallic oxides such as Cr_2O_3

and NiO are soluble in molten FLiNaK salt [30, 50]. As a result, the introduction of O_2 into the system can accelerate the depletion of alloying elements from the substrate material [133, 183]. Within the molten salt system, it will therefore be treated in the same way as CrF_2 and HF.

The diffusion coefficient of O_2 in a molten salt system has been investigated and estimated to be $2.26x10^{-5}$ cm^2/s at 700 °C [184]. Once the concentration of the O_2 at the molten salt interface has been calculated, the depth of O_2 penetration can be calculated. This requires a second diffusion coefficient for O_2 in a Ni substrate, which was calculated to be $1.24x10^{-13}$ cm^2/s based on the experimental data of Whittle et al. [185].

4.5 Summary of research methods

Within this study, numerous experimental and numerical methods will be deployed to conduct a robust investigation into the corrosion and oxidation behaviour of the Ni-based alloy Hastelloy C276. The key experimental technique that will be used in the quantification of the corrosion and oxidation behaviour of Hastelloy C276 will be a static immersion technique as defined for molten salt corrosion and oxidation testing by ISO 17426 and ISO 21608 [156, 157]. Characterisation of corrosion and oxidation product morphology will be conducted using SEM analysis, with EDX being used to identify elements present within the products and XRD deployed to identify the structures of corrosion and oxidation products.

In the case of oxidation prediction, empirical and mechanistic models were created based on underpinning electrochemical and diffusion theory from literature for the specific test case of Hastelloy C276. The two methods were deployed in MATLAB with the main outputs of both models being the specific mass change and the oxide layer thickness. The mechanistic model was also able to predict elemental changes within the material microstructure due to it being based on the diffusion behaviour of alloying elements in a Ni-matrix. Since the mechanistic model was able to predict elemental changes in the material substrate at high temperatures, the mechanistic model was developed further using the corrosion modelling methodology of Li et al. [121] for corrosion of stainless steels in Solar Salt.

Since key outputs from each modelling methodology included the specific mass change, oxide layer thickness and corrosion depth, experimentally determined results for each of these values were used to validate the numerical model. Validation of each model was also supported by published data from sources of literature.

Chapter 5 – Results I

High Temperature Oxidation of Hastelloy C276: Experimental and numerical approaches

High temperature oxidation of Hastelloy C276 is of great interest for molten salt reactor applications due to its impact on material in high temperature corrosive and oxidising environments. High temperature oxidation studies have been conducted on numerous Ni-based alloys to understand the rates of oxidation and the formation of oxidation products over time. Numerical modelling approaches were adopted to develop a predictive model to characterise the oxidation of Hastelloy C276, as well as provide an understanding of changes to the elemental distributions within the alloy in high temperature air environments.

5.1 Introduction

The high temperature oxidation of metallic alloys can be either detrimental to alloy performance or aid in its protection against aggressive environments [77]. In the case of Ni-based alloys for molten salt applications, the introduction of oxygen may change the behaviour of Ni-based alloys by adjusting melt basicity as per the acid/ base models discussed in Section 3.5.2. Therefore, it is important to initially understand how the Ni-based alloy proposed in this research, Hastelloy C276, behaves in an oxidising environment and characterise its oxidation behaviour.

To understand the oxidation behaviour of Hastelloy C276, the experimental and numerical approaches presented in Chapter 4 were deployed. The use of these techniques allowed for the oxidation behaviour to be characterised using empirical and mechanistic modelling methods whilst also using experimental results to validate the results of the developed models. The use of the experimental and numerical approaches allowed for the following objectives to be completed:

- Prediction of the oxidation behaviour of Hastelloy C276 in oxidising environments using empirical and mechanistic modelling approaches.
- Completion of static oxidation tests involving Hastelloy C276 coupons at 700 °C, quantifying the oxidation behaviour using a thermogravimetric technique.
- Characterisation of the oxidation behaviour of Hastelloy C276 in an oxidising environment by analysis of oxidised samples using SEM, EDX and XRD analysis techniques.

- Validation of the empirical and mechanistic models using experimental results obtained in this study and using data available in literature.

5.2 Prediction of oxide growth – Empirical Model

5.2.1 Empirical Model – Model Description

The empirical model developed was created in MATLAB using the processes described in Section 4.3. The deployed methodology includes the use of compositional and oxidation data from literature for a variety of Ni-based alloys in order to predict the specific mass change of Hastelloy C276 coupons at 700 °C. This prediction allows for the determination of the oxidation kinetics and the establishment of a parabolic rate constant for the oxidation of Hastelloy C276 at 700 °C.

The developed model is based on determining the relationship between a compositional parameter, denoted as U, and the oxidation behaviour of the alloy, quantified by a parabolic rate constant, K_P. In the development of the empirical model, it was assumed that the main oxidation product would be Cr_2O_3, with all other oxides being treated as an impurity within the main Cr_2O_3 layer, as per the model on which this study was based, developed by Sato et al. [87] and Bensch et al. [88]. In reality this would not be the case as previous literature has indicated that many Ni-based alloys form a multi-oxide layer containing several different metallic oxides, particularly NiO, Cr_2O_3 and $NiCr_2O_4$ are commonly observed for Ni-based alloys [165].

The methodology deployed in this work is based on the model used by Sato et al. [87] and Bensch et al. [88] which was originally developed for predicting the oxidation behaviour of alumina forming alloys. To make the methodology relevant for the application of Cr_2O_3 formation, adaptations were made to the original model, which have been described in Section 4.3.1. The modelling adaptations included the selection of relevant alloys to build a robust empirical relationship between K_P and U for Cr_2O_3 formation.

5.2.2 Empirical Model – Oxide growth prediction

As described throughout Section 4.3, an empirical model was developed to predict the specific mass change of Hastelloy C276 coupons, exposed to dry air at 700 °C. The empirical model was used to predict the oxidation behaviour of Hastelloy C276 over a 200-hour time period to match the experimental conditions utilised

within the rest of this research. The resulting specific mass change prediction is presented as Figure 5.1.

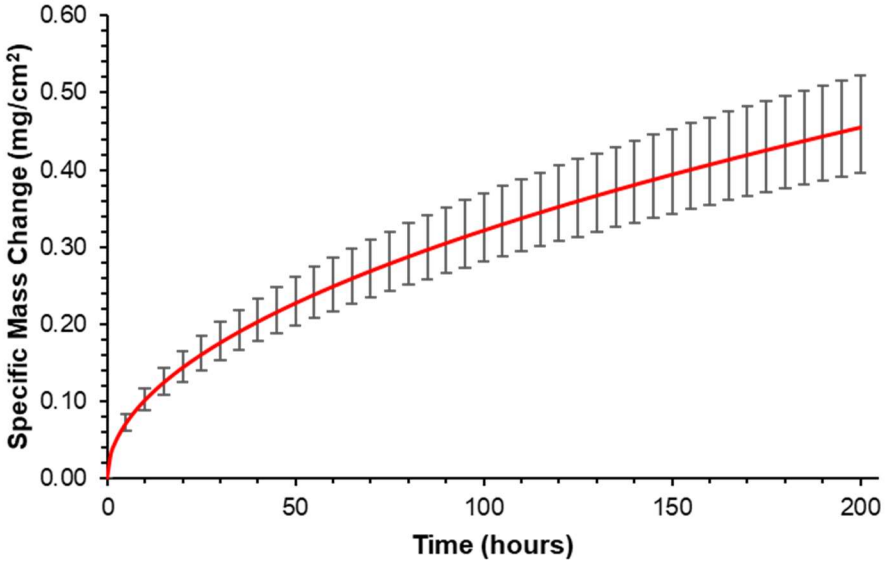


Figure 5.1 – Prediction of specific mass change of Hastelloy C276 over a 200-hour test duration at a constant temperature of 700 °C using the empirical modelling methodology. Specific mass change of 0.4555 mg/cm^2 for Hastelloy C276 was predicted at the specified temperature and duration.

Due to the literature data which suggested that the oxidation kinetics would follow a parabolic trend for Hastelloy C276, parabolic rate constants were used within the empirical model and hence a parabolic result was obtained. A specific mass change of 0.4555 mg/cm^2 was obtained from the model, as shown in Figure 5.1. Conversion of this specific mass change to a K_P yielded a value of 2.88×10^{-7} mg^2/cm^4/s.

The error bars presented in Figure 5.1 represent the minimum and maximum specific mass change predictions based on the minimum and maximum values of U presented in Table 4.5. The minimum and maximum values can also be expressed using parabolic rate constants of 2.19×10^{-7} and 3.80×10^{-7} mg^2/cm^4/s, respectively.

5.2.3 Empirical Model – Oxide Layer Prediction

Based on the specific mass change prediction presented in Figure 5.1, the predicted thickness of the oxide layer was determined using the theory presented in Section 4.3.3 in which equation 4.26 was derived. The prediction of oxide layer thickness is given in Figure 5.2.

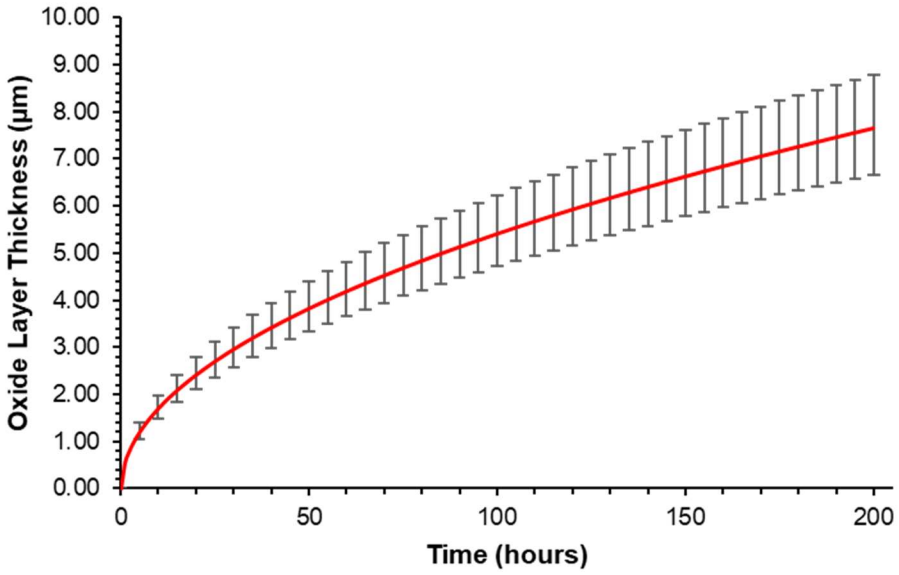


Figure 5.2 – Prediction of oxide layer thickness, calculated from specific mass change results obtained from the developed empirical modelling methodology. Oxide layer thickness is predicted to be 7.66 µm after 200 hours of exposure of Hastelloy C276 to dry air at 700 °C.

Based on the specific mass change results of the empirical model, the oxide layer should increase to a thickness of 7.66 µm over a 200-hour time period. This result can be expressed by a K_P value due to the parabolic nature of the oxide layer growth. The value of K_P determined for the oxide layer growth is 8.15×10^{-5} µm^2/s. Lower and upper limits of oxide layer thickness represented by error bars can be characterised using the same methodology to the specific mass changes as presented in Figure 5.1. The upper and lower limited were defined by parabolic rate constants of 6.18×10^{-5} and 1.07×10^{-4} µm^2/s.

5.3 Predictions of oxide growth and element depletion – Diffusion Based Model

5.3.1 Diffusion Based Model – Model Description

The diffusion-based model developed in this research was also developed in MATLAB using the partial differential equation solver. Utilising this solver removed the requirement to develop a finite difference problem within MATLAB, reducing the complexity of the code developed. In the case of this work, it was assumed that oxide growth was uniform in each direction, therefore symmetry conditions were applied so the model was only solved in one direction. The results were then scaled

over the whole sample area based on a sample 12.7 mm in diameter and 5 mm thick. The density of Hastelloy C276 was also taken to be 8.89 g/cm^3 [186].

Using this method reduced computational demand without limiting the models' predictive capabilities. Due to these symmetry conditions, boundary conditions were applied at the centre of the sample and the top surface exposed to a dry air environment. It was assumed that there would be no change in the concentration at the centre of the sample, this assumption was shown in a similar work conducted by Karunaratne et al. [93]. At the surface it was assumed that the concentration of elements would decrease based on the concentration gradient present between the centre of the sample and the exposed surface.

Mass changes to samples were then calculated by assuming elements present at the surface would react with oxygen to form their most thermodynamically stable respective oxides as per the equations shown in Table 4.12.

5.3.2 Diffusion Based Model – Sensitivity Study

In element-based models, the results can be influenced by the coarseness of the mesh being used. In this case, the number of elements is defined by the combination of the number of modelling nodes used in the geometry i.e. the number of nodes distributed between 0 and 0.25 cm as shown in Figure 4.14, and the number of time steps used, i.e. how many intervals are used between 0 and 200 hours, which is defined by the time step. To determine the impact of the number of modelling nodes on the final result, a time step of 1 hour was used and the number of modelling nodes varied from 1001 up to a maximum value of 250001. As part of the study, two results were monitored with respect to the number of modelling nodes. These values were the specific mass change and the depletion depth of Cr from the alloy. The results obtained for these two parameters are presented in Figure 5.3.

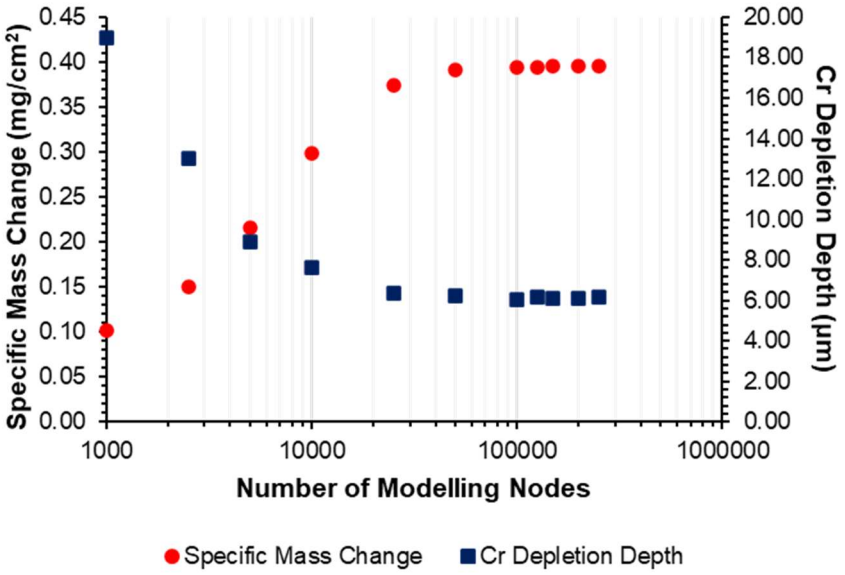


Figure 5.3 - Specific mass change prediction against the number of modelling nodes for Hastelloy C276 exposed to a dry air environment at 700 °C for durations up to 200 hours. Result shows specific mass change result converges around 25001 modelling nodes using a time interval of 1 hour.

In both cases, increasing the number of modelling nodes from 1001 up to 250001 causes a large change in the results, after which point, both specific mass change and Cr depletion depth results are observed to converge, with results changing from this point onwards by less than 1%. However, closer analysis of the raw data showed true convergence is achieved when using in excess of 125001 modelling nodes.

To understand the impact of changing the time interval, five-time intervals were used whilst using 125001 nodes to observe any changes in the obtained results. Similarly, to the study of the number of modelling nodes, the specific mass change and the Cr depletion depth were monitored with respect to the number of time intervals. The results of this study are summarised in Figure 5.4 and Figure 5.5 respectively.

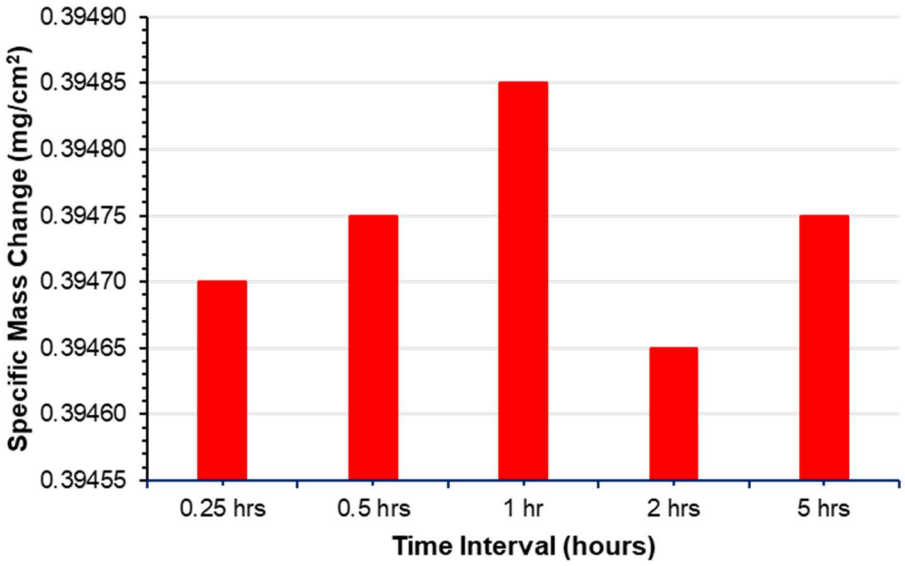


Figure 5.4 – Specific mass change prediction when using time intervals of 0.25, 0.50, 1.00, 2.00 and 5.00 hours when using 125001 modelling nodes. Results indicate a difference of 0.05% between the minimum and maximum specific mass change predictions, suggesting that the number of modelling nodes has a bigger influence on the result than the time interval.

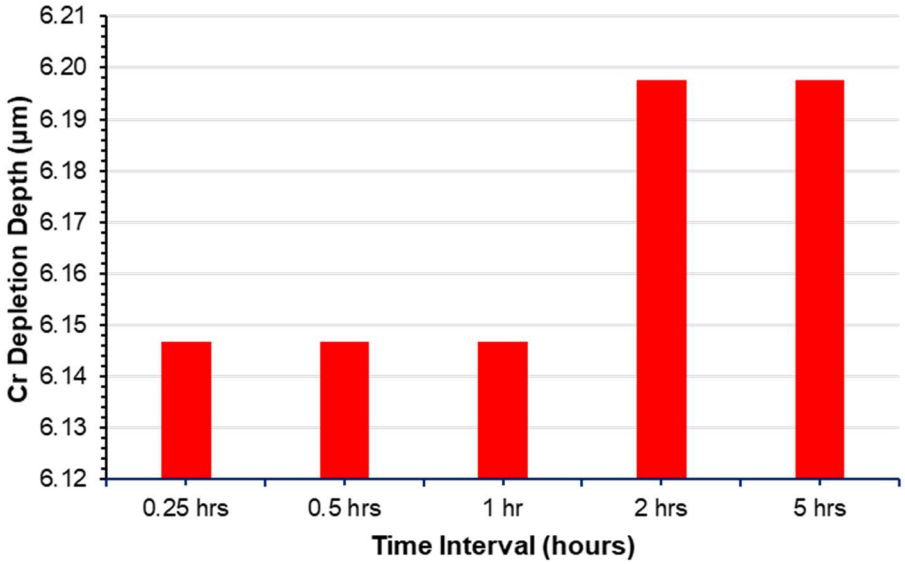


Figure 5.5 – Cr depletion depth prediction when using time intervals of 0.25, 0.50, 1.00, 2.00 and 5.00 hours and 125001 modelling nodes. Results show a maximum difference of 0.82% between the minimum and maximum Cr depletion depth predictions at the different time intervals, indicating that the number of modelling nodes influences the result more heavily.

The results presented in Figure 5.4 and Figure 5.5 show that the time interval used has very little impact on the obtained result, with the maximum difference between results being calculated to be 0.05% and 0.82% for specific mass change and

depletion depth predictions respectively. Changing the time interval over which the model was solved was also observed to impact the computation time, as shown in Figure 5.6.

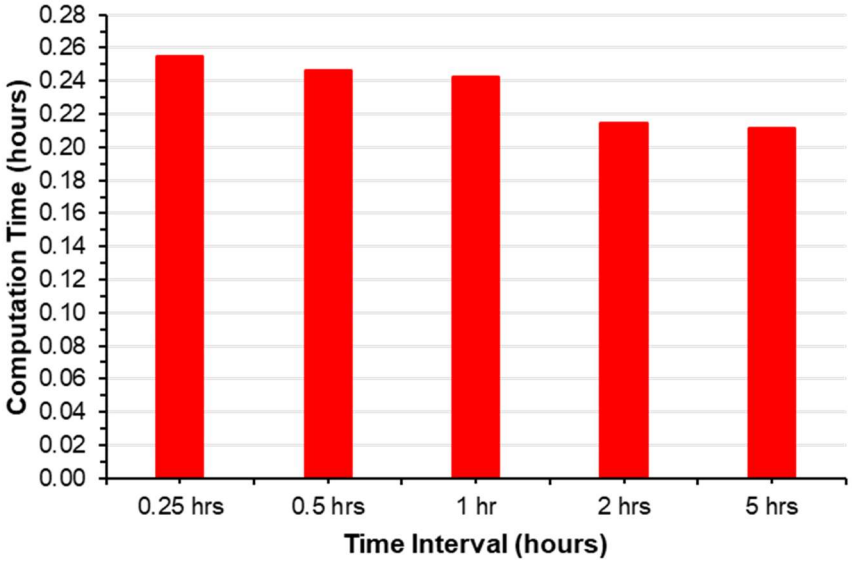


Figure 5.6 – Computation time of mechanistic model when using time intervals of 0.25, 0.50, 1.00, 2.00 and 5.00 hours and 125001 modelling nodes. Result show decreasing computation time with increasing time intervals.

The result presented in Figure 5.6 shows that increasing the time interval used decreases the overall computation time. This is expected due to the reduction in the overall number of elements being solved for. However, the reduction in the computation time is minimal compared with the reduction in the number of elements as shown in Table 5.1.

Table 5.1 – Percentage reduction in time interval versus percentage reduction in modelling elements used to obtain oxidation prediction, showing very small reductions in time interval compared with reduction in modelling elements.

Time Interval (hrs)	Modelling Elements	% Reduction in modelling elements	Computation Time (hrs)	% Reduction in computation time
0.25	$1.00x10^8$	**Baseline**	0.2548	**Baseline**
0.50	$5.00x10^7$	50.0	0.2467	3.18
1.00	$2.50x10^7$	75.0	0.2429	4.67
2.00	$1.25x10^7$	87.5	0.2142	15.9
5.00	$5.00x10^6$	95.0	0.2115	17.0

As shown in Table 5.1 a 95% reduction in the number of modelling elements results only in a 17.0% reduction in the computation time. Based on this result, it was concluded that to obtain appropriate results, any time step tested could be used alongside a minimum of 100001 modelling nodes in order to achieve a converged result. However, using, and increased number of modelling nodes used within the MATLAB model also increased the computational demand and hence, the computation time. Therefore, a compromise exists between the computation time and the desired output from the model that required investigation.

Assessing the trade-off between the computation time and the number of modelling nodes were performed using a time interval of 1 hour, with the number of modelling nodes being varied from 1001 up to 250001. The computation time with the increasing number of modelling nodes was recorded with the result presented in Figure 5.7.

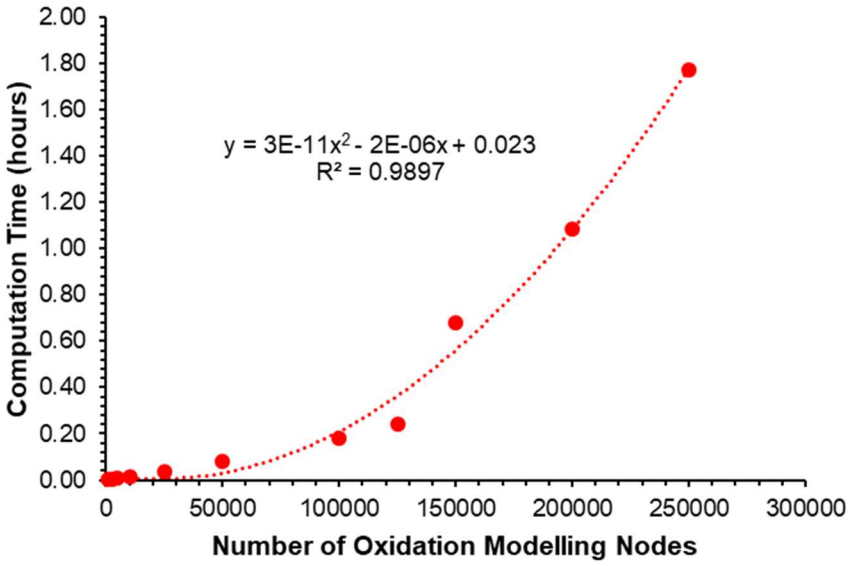


Figure 5.7 – Graph of computation time against the number of modelling nodes shows a roughly squared relationship in the range of 1001 to 250001 nodes with a drastic increase in computation time being observed when in excess of 125001 modelling nodes are used.

The results of this study show that the computation time increases in an approximately squared relationship with respect to the number of modelling nodes. When comparing with the result showing decrease in computation time with an increase in the time interval, this result shows that the number of modelling nodes used impacts the computation time much more greatly than the time interval being used.

Previous results have shown that changes in the results of both the specific mass change and the depletion depth of Cr are observed to marginally increase when modelling nodes in excess of 100001 are used for this study. Comparison between the changes in the predicted specific mass changes, the Cr depletion depth and the associated increase in the computation time are shown in Figure 5.8.

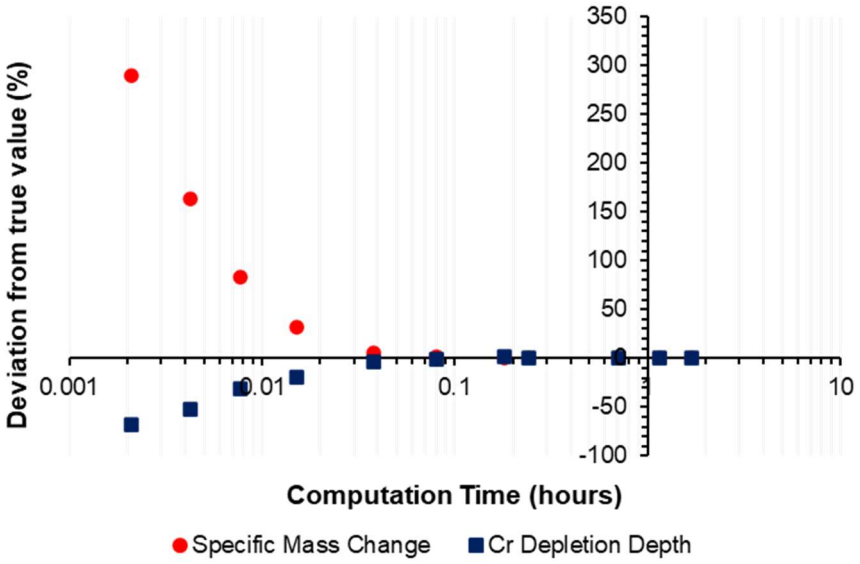


Figure 5.8 – Graph of the computation time and the percentage deviation in the average specific mass change and the Cr depletion depth showing decreasing deviation of both monitored parameters with increasing computation time. Graph shows very little change in the two monitored parameters past 0.2 hours of computation time (100001 nodes).

Figure 5.8 shows very little change in the result past a computation time of approximately 0.2 hours, where 100001 nodes were used within the model, suggesting that the number of modelling nodes used could be reduced to reduce computational demand whilst obtaining a converged solution. Based on the percentage changes in the results and the computation time, it was concluded that for this test case, 125001 modelling nodes should be used to predict the oxidation behaviour of Hastelloy C276 in dry air at 700 °C for durations up to 200 hours.

5.3.3 Diffusion Based Model – Validation of Mass Change Prediction against Literature

Based on the results of the sensitivity study a smaller set of test cases were decided upon for use in the validation study. To validate the mechanistic model, the previously discussed work by Li et al. [99] was used, in which isothermal oxidation experiments at temperatures of 450, 500 and 550 °C were conducted for durations of 240, 240 and 1000 hours respectively. The research outcomes included values of K_P at each test temperature to which the results from the mechanistic model are compared.

When considering the number of test cases to use in the validation study of the model, the maximum number of elements was used to determine the maximum number of modelling nodes that could be implemented at each time step.

Performing this analysis allowed for certain time steps to be eliminated from consideration as too few modelling nodes could be used to solve the numerical model. A summary of this analysis is presented in Table 5.2.

Table 5.2 – Summary of time intervals and maximum number of modelling nodes when modelling test durations of 240 and 1000 hours, as per the tests of Li et al. [99].

Time Step (hours)	Time Intervals for 240 hours	Maximum number modelling nodes	Time Intervals for 1000 hours	Maximum number modelling nodes
0.25	960	130208	4000	31250
0.50	480	260416	2000	62500
1.00	240	520833	1000	125000
2.00	120	1041666	500	250000
5.00	48	2604166	200	625000

Based on the analysis in Table 5.2, time steps of 0.25 and 0.50 hours could not be used when modelling the 1000 hour test at 550 °C as the maximum number of modelling nodes falls below the 125000 modelling nodes required, as shown in Section 5.3.2. However, comparison of the results obtained using time periods of 240 and 1000 hours for 550 °C showed very little difference in their prediction. Therefore, time steps of 1.00, 2.00 and 5.00 hours could be used in the validation study in combination with the 125001 modelling nodes. To ensure good resolution of the results obtained, the use of a time interval of 1.00 hours was deemed preferable.

In order to provide a realistic comparison between the mechanistic model and the results of Li et al. [99], the sample dimensions and alloy composition were changed to match those used in the original study. Instead of using circular coupons, rectangular samples, measuring 14 mm x 14 mm x 6 mm were used. The composition of the Hastelloy C276 material used by Li et al. [99] is presented in Table 5.3.

Table 5.3 - Composition of Hastelloy C276 used in the study by Li et al. [99] when investigating the oxidation behaviour of Hastelloy C276 at temperatures of 450, 500 and 550 °C.

Element	Ni	Mo	Cr	Fe	W	Co
wt.%	Bal.	16.2	15.8	6.5	4.2	1.9
Element	**Si**	**V**	**C**	**P**	**S**	
wt.%	0.06	0.3	0.007	0.035	0.025	

To provide validation of the mechanistic model, the parabolic rate constants obtained experimentally by Li et al. [99] were extracted and converted from units of $mg^2/cm^4/hr$ to $mg^2/cm^4/s$ to ensure consistency between the experimental and predictive results. A summary of these results is presented in Table 5.4.

Table 5.4 – Summary of temperature and K_P data obtained for Hastelloy C276 in a dry air environment by Li et al. [99].

Temperature (C)	Test Duration (hours)	K_P ($mg^2/cm^4/s$)
450	240	$6.86x10^{-12}$
500	240	$8.39x10^{-11}$
550	1000	$7.11x10^{-10}$

Alongside the research of Li et al. [99], the higher temperature oxidation study of Park et al. [161] was also used. In this study, the oxidation behaviour of Hastelloy C276 foils were characterised using a mass change method with varying temperatures and concentrations of O_2. The data set taken from the study by Park et al. [161] and used for validation is presented in Table 5.5.

Table 5.5 – Summary of data collected from study by Park et al. [161] into the oxidation of Hastelloy C276 foils at temperatures of 600, 700 and 800 °C using O_2 concentrations of 100%.

Temperature (°C)	Test Duration (hours)	Specific Mass Change (mg/cm^2)	K_P ($mg^2/cm^4/s$)
600	72	0.010	$2.01x10^{-10}$
700	24	0.035	$7.04x10^{-9}$
800	16	0.085	$6.30x10^{-8}$

Plots of LN(K_P) against the reciprocal of temperature (1/T) were generated using the validation cases to obtain a linear relationship as per equation 3.54. The generated relationships could then be compared with those calculated using the

mechanistic model. A complete summary of the validation data is presented in Figure 5.9

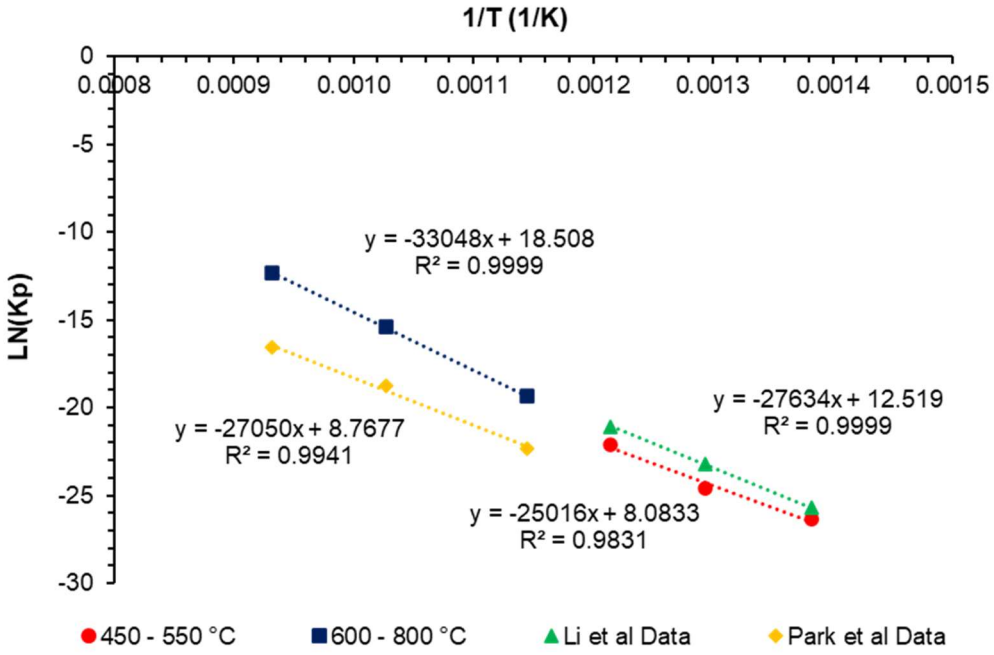


Figure 5.9 – Plot of LN(K_P) against 1/T showing developed relationship for the oxidation of Hastelloy C276 using experimental results of Li et al. [99] and Park et al. [161]. The developed relationships indicate activation energies, Q, for the oxidation of Hastelloy C276 of 207995.53 J/mol and 274777.60 J/mol in the temperature regions of 450 °C to 550 °C and 600 °C to 800 °C, respectively.

The result presented in Figure 5.9 shows good agreement between all the mathematical predictions and the experimental results of Li et al. and Park et al. [99, 161]. A comparison of the predicted activation energies for the oxidation reaction and the pre-exponential constants using each time interval and the experimental results of Li et al. and Park et al. [99, 161] is presented in Table 5.6.

Table 5.6 – Comparison between values, predicted by the developed mechanistic model and experimental results obtained from literature, of oxidation reaction activation energy, Q, in temperature ranges of 450 °C to 550 °C and 600 °C to 800 °C and their corresponding data sets from literature [99, 161]. Predictions made using 125001 modelling nodes and a time interval of 1.00 hours.

Study	Q (kJ/mol)	Percentage Difference (%)
Li et al.	229765.30	**Baseline**
Prediction (450 °C – 550 °C)	207995.53	9.95
Park et al.	224907.23	**Baseline**
Prediction (600 °C – 800 °C)	274777.60	20.0

The comparison between results predicted using the mechanistic model and accepted experimental results, taken from literature sources, presented in Table 5.6 show good agreement with literature data in the temperature range of 450 °C to 550 °C, with the difference being approximately 10%. In the higher temperature range a wider difference of 20.0% is observed. Reasons for this may include the data set against which the prediction was compared. The data from Park et al. [161] was collected in an atmosphere of 100% O_2 which differs from the environment in which the oxidation prediction was made i.e. a dry air environment containing approximately 20% O_2. Combining the two data sets, as shown in Figure 5.10 shows that the prediction bisects the two sets of data from literature.

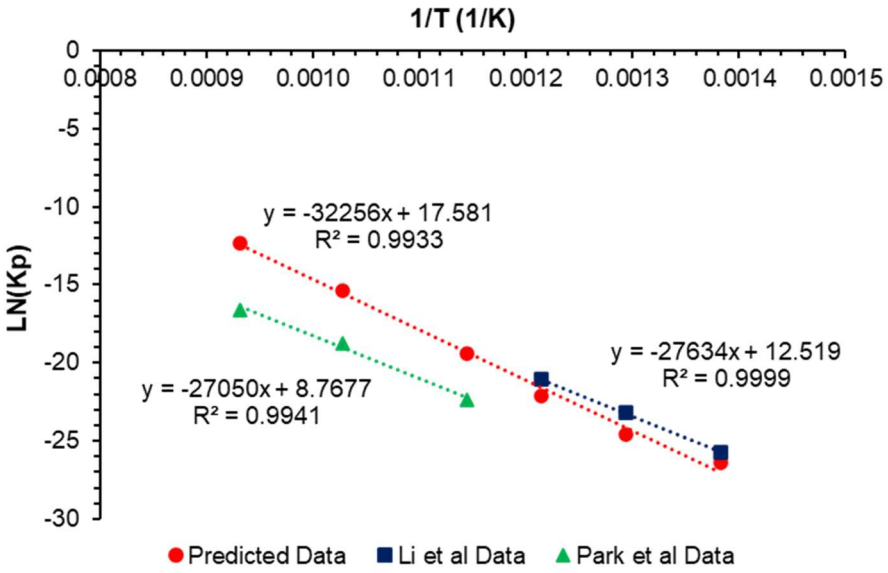


Figure 5.10 – Combined prediction of the fully temperature range showing that the predicted data bisects the two sets of data from literature. This prediction yields an activation energy of 268192.51 J/mol.

The result presented in Figure 5.10 yields an activation energy of 268192.51 J/mol which differs from the results of Li et al. [99] by 15.4% and the results of Park et al. [161] by 17.6%. Overall, these differences were deemed to be acceptable for the purpose of this model.

5.3.4 Diffusion Based Model – Oxide growth prediction

A main output of the diffusion-based model was the prediction of oxide growth. This includes both the specific mass change and the oxide layer thickness. Prediction of the specific mass change was achieved by using element change predictions and metallic oxide formation reactions described in Section 4.4. The prediction for the specific mass change of Hastelloy C276 is presented as Figure 5.11.

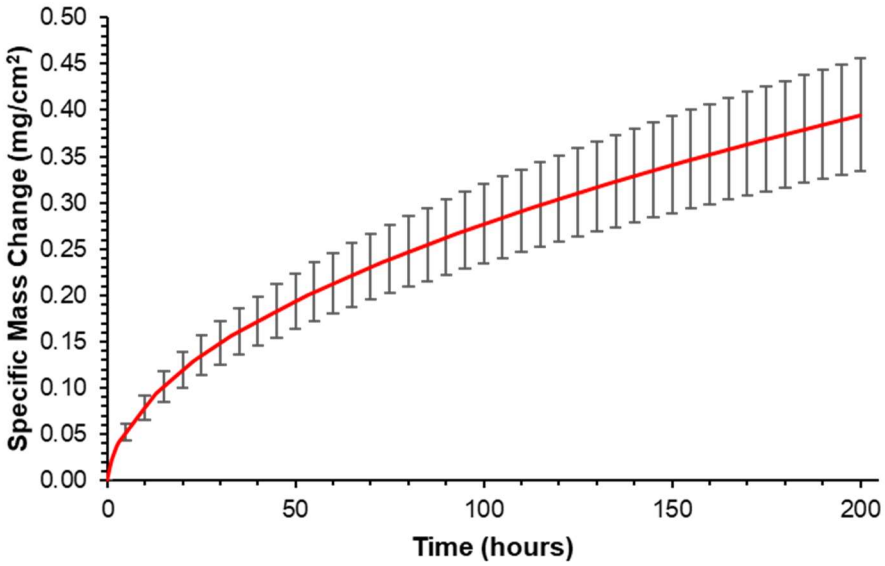


Figure 5.11 - Diffusion based prediction of specific mass change of Hastelloy C276 at 700 °C, over the time interval of 0 to 200 hours. Result shows parabolic oxidation behaviour of Hastelloy C276, characterised by a specific mass change of 0.3948 mg/cm^2 and K_P value of 2.17x10^{-7} mg^2/cm^4/s.

The result presented in Figure 5.11 shows a specific mass change of approximately 0.3948 mg/cm^2 over a 200-hour time period, with a calculated K_P value of 2.17x10^{-7} mg^2/cm^4/s. Considering the full range of results, the K_P value varied between a minimum of 1.55x10^{-7} and a maximum of 2.88x10^{-7} mg^2/cm^4/s. When comparing this to the result of the empirical model, the diffusion-based model predicts a less positive specific mass change than the empirical model, with the empirical model predicting a greater specific mass change by 0.0607 mg/cm^2. The comparison of the results is shown in Figure 5.12.

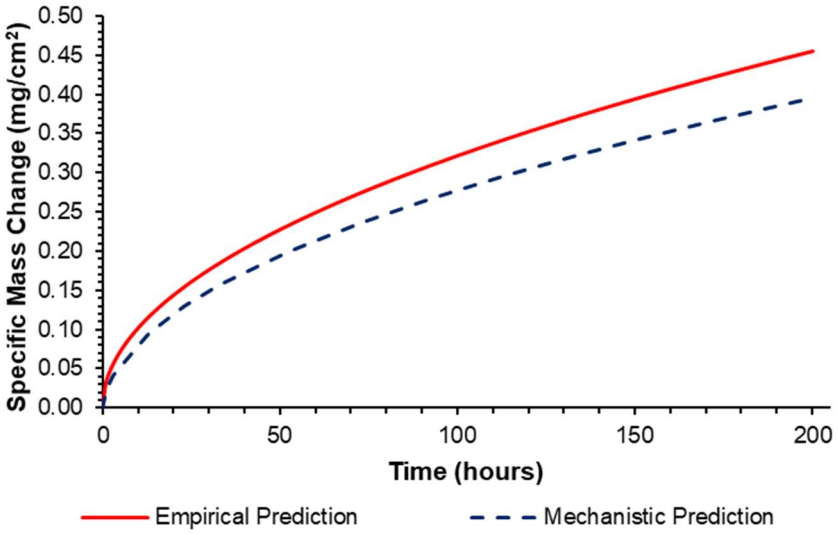


Figure 5.12 – Comparison of specific mass change predictions for the oxidation of Hastelloy C276, oxidised in dry air at 700 °C for 200 hours, using empirical modelling and mechanistic modelling methodologies. The empirical modelling methodology predicted a specific mass change of 0.4555 mg/cm^2. This prediction is 14.3% greater than the prediction of 0.3948 mg/cm^2 made by the diffusion-based model.

When examining results of the empirical modelling methodology, a K_P value of 2.88×10^{-7} mg^2/cm^4/s was predicted for the oxidation of Hastelloy C276 at 700 °C. This is approximately 33% greater than the prediction made by the diffusion-based model of 2.17×10^{-7} mg^2/cm^4/s. The empirical model can be concluded to be predicting faster parabolic oxidation kinetics as well as a greater amount of metallic oxide being produced compared to the prediction made by the mechanistic model.

As illustrated in Figure 5.1 and Figure 5.11, both models predict minimum and maximum values of specific mass changes. In these figures the minimum and maximum predictions are presented in the form of error bars. Analysis of the spread of the data suggests that there is a 27.5% difference between the minimum and maximum values presented by the empirical model and 30.7% difference between the minimum and maximum specific mass change values predicted by the mechanistic model. These differences in both models were due to the wide range of input data used in both models, this being the parabolic oxidation data in the empirical model and diffusion coefficient data in the mechanistic model.

The diffusion-based model also predicted the total oxide layer thickness, which was achieved by summing the individual oxide layer thicknesses, calculated from the calculated mass changes due to the growth of each metallic oxide being formed. This result is presented as Figure 5.13.

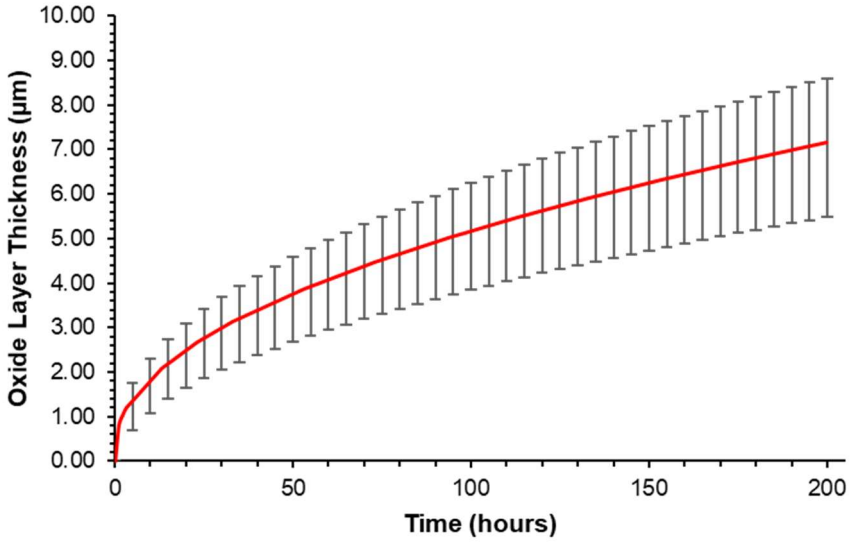


Figure 5.13 – Prediction from the mechanistic model of oxide layer thickness formation over 200 hours of Hastelloy C276, exposed to a dry air environment at 700 °C. An oxide layer thickness of 7.13 µm was obtained.

A parabolic relationship is observed for the oxide layer thickness, meaning the rate of oxide growth can be expressed with a value of K_P in units of $\mu m^2/s$. The value of K_P for the oxide layer growth is 7.06×10^{-5} $\mu m^2/s$. A comparison between the predictions of oxide layer thickness from the mechanistic and empirical models are also presented in Figure 5.14.

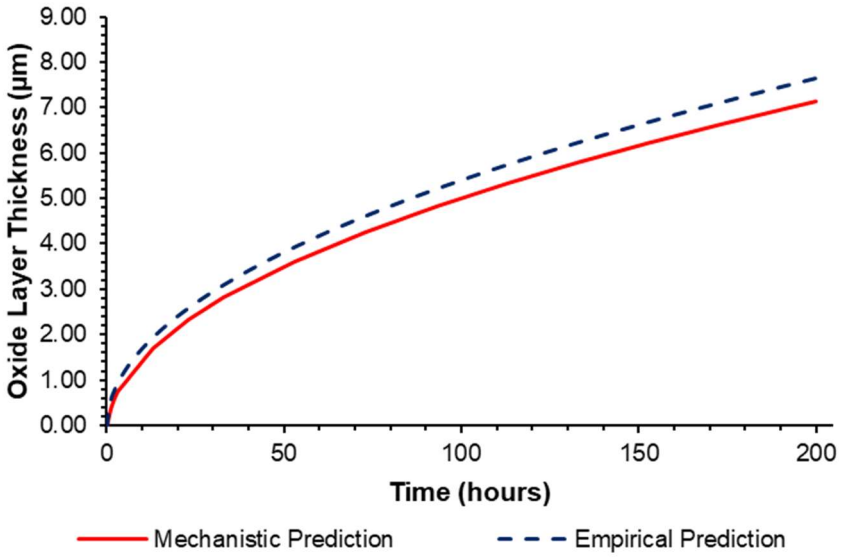


Figure 5.14 – Comparison of predictions of oxide layer thickness formation over 200 hours of Hastelloy C276, exposed to a dry air environment at 700 °C from empirical modelling and mechanistic modelling methodologies. The empirical and mechanistic modelling methodologies predicted oxide layer thicknesses of 7.66 µm and 7.13 µm, respectively.

The comparison of the predicted oxide layer thicknesses presented in Figure 5.14 shows a difference of 7.17% between the predicted values after 200-hours, with the empirical model predicting a thicker oxide layer than the mechanistic model. This difference in the result can be attributed to the difference in the methodologies used to calculate the oxide layer thickness, with the empirical model using a theoretical calculation whilst the mechanistic model uses the individual predicted oxide growth data. The observed result is also expected due to the faster parabolic oxidation kinetics predicted by the empirical model when compared with the mechanistic model as presented in Figure 5.12.

5.3.5 Diffusion Based Model – Elemental Distributions

As the mechanistic model is able to capture the diffusion characteristics of each alloying element, the concentration changes and subsequently, the depletion depth, or each alloying element can be predicted. Therefore, the elemental distributions of the key oxide forming alloying elements such as Cr, Mo and Fe were assessed in the near surface region to observe their depletion behaviour. As the major elemental constituent in Hastelloy C276, the distribution of Ni was also assessed.

The depletion depths of each of the elements described were all predicted by examining the concentration changes of each element, with the depletion depth

being taken as the depth at which the concentration of each element no longer matches the nominal concentration of that element within the substrate. A plot for the depletion depths with respect to time for Ni, Cr, Mo, and Fe is presented as Figure 5.15.

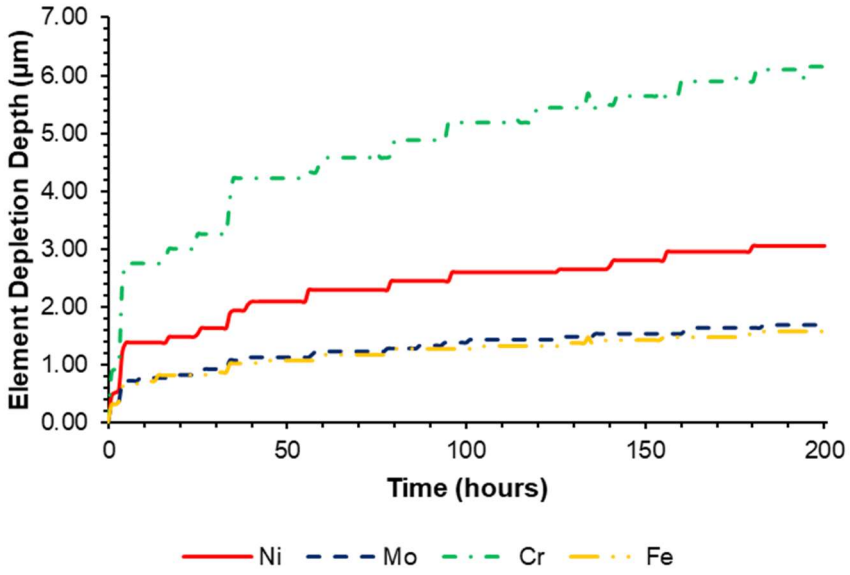


Figure 5.15 - Calculated depletion depths of Ni, Cr, Mo and Fe based on concentration changes presented in Figure 5.16 to Figure 5.19 showing depletion depths of 3.05 µm, 1.68 µm, 6.15 µm and 1.57 µm for alloying elements of Ni, Mo, Cr and Fe respectively after 200 hours of exposure to a dry air environment at 700 °C.

The result presented in Figure 5.15 shows that the most mobile element, Cr, has the greatest depletion from the substrate, with Ni, Mo and Fe all having predicted depletion depths of approximately 1.50 – 3.00 µm.

The distributions of these elements within the substrate and at the substrate – air interface was predicted at each time interval. However, for comparison to the experimental results, results from time intervals of 50, 100 and 200 hours are presented. The concentration distribution of Ni in the near surface region is presented in Figure 5.16.

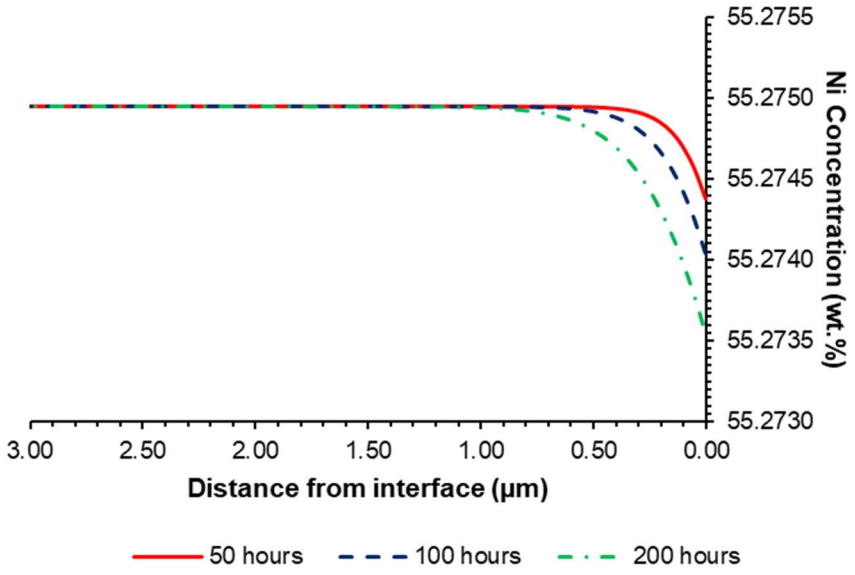


Figure 5.16 – Elemental distribution profile of Ni in the near surface region next to the substrate – air interface showing predicted depletion behaviour at time intervals of 50, 100 and 200 hours after exposure to dry air at 700 °C.

The elemental distribution of Ni in the near surface region, shown in Figure 5.16, shows the concentration of Ni within the near surface region decreasing with respect to time. The decrease in the elemental concentration is accompanied by an increase in the depth of Ni depletion increasing from 2.08 µm to 3.05 µm when the exposure time is increased from 50 to 200 hours. This result is consistent with other results observed in literature for Ni-based alloys. The concentration of Ni is observed to drop from 55.2745 wt.% in the substrate to approximately 55.2735 wt.% at the interface between the material and air after 200 hours of exposure. A similar depletion trend was observed for Cr as shown in Figure 5.17.

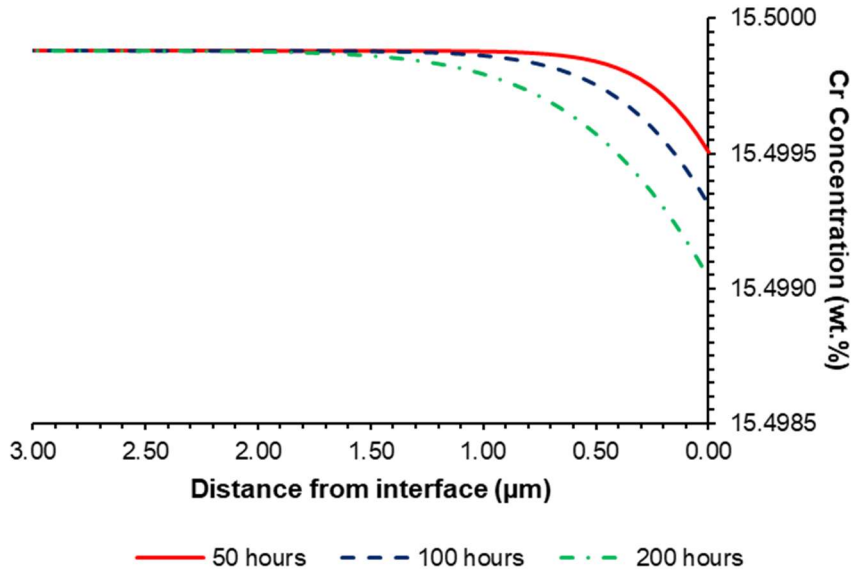


Figure 5.17 - Elemental distribution profile of Cr in the near surface region next to the substrate – air interface showing predicted depletion behaviour at time intervals of 50, 100 and 200 hours after exposure to dry air at 700 °C.

Similarly, to that of Ni, the elemental distribution of Cr shows both increased depletion depth and greater change in concentration at the interface as a function of time, with the depletion depth increasing from 4.22 µm to 6.15 µm and the concentration decreasing from the substrate concentration of 15.500 wt.% to a minimum of approximately 15.499 wt.% after 200 hours. The increased depletion depth of Cr was attributed to its larger diffusion coefficient in Ni when compared with the self-diffusion coefficient of Ni. Due to its smaller diffusion coefficient in Ni, much smaller depletion depths were observed for Mo as shown in Figure 5.18.

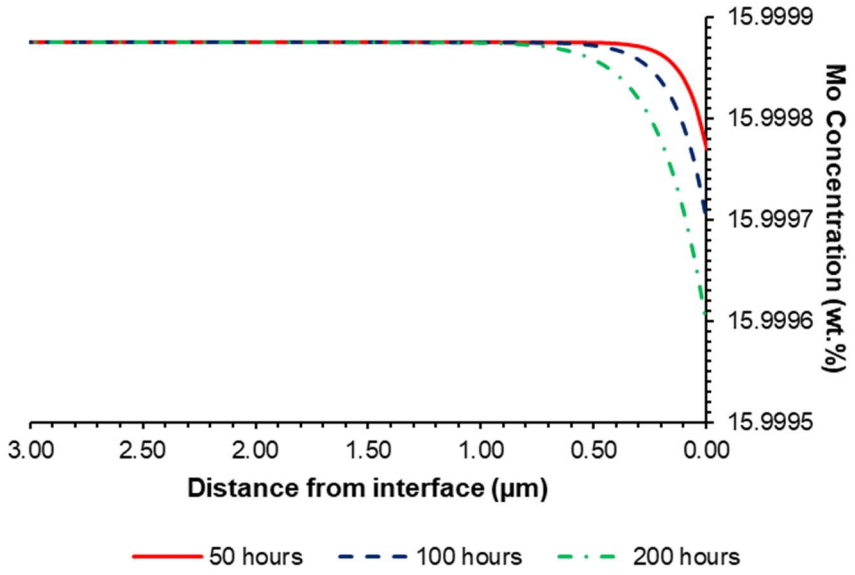


Figure 5.18 - Elemental distribution profile of Mo in the near surface region next to the substrate – air interface showing predicted depletion behaviour at time intervals of 50, 100 and 200 hours after exposure to dry air at 700 °C.

The depletion depth of Mo at the interface is observed to increase from 1.12 µm to 1.68 µm with very little change, approximately 1.8×10^{-4} wt.%, in the concentration at the substrate – air interface being observed. Smaller depletion depths were observed again when examining the elemental distribution of Fe as shown in Figure 5.19.

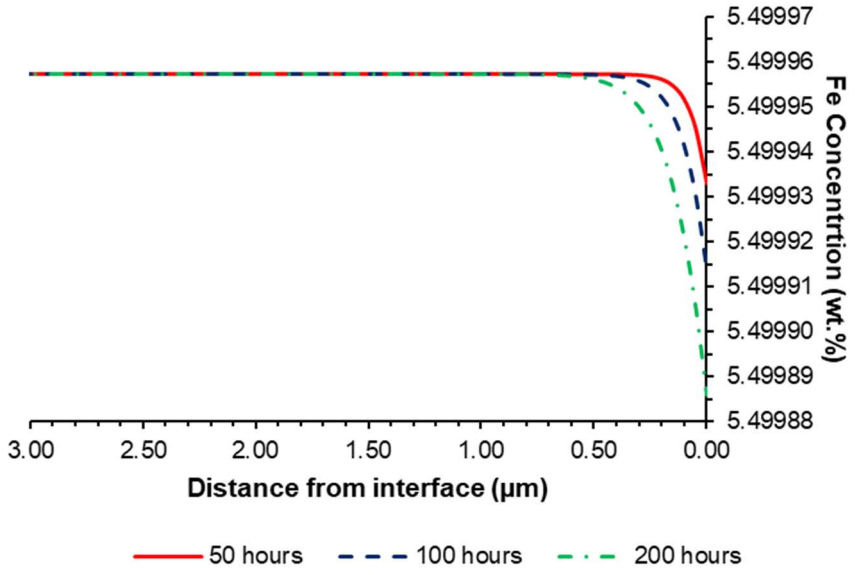


Figure 5.19 - Elemental distribution profile of Fe in the near surface region next to the substrate – air interface showing predicted depletion behaviour at time intervals of 50, 100 and 200 hours after exposure to dry air at 700 °C.

The depletion depth of Fe is observed to increase from 1.07 μm after 50 hours to 1.57 μm after 200 hours of exposure to dry air. Similarly, to Mo, the concentration of Fe at the interface between the substrate and air is observed to drop very marginally, from approximately 5.49996 wt.% to 5.49989 wt.%. This may be a result of their much smaller diffusion coefficients when compared with more mobile elements such as Cr.

5.4 Experimental Results and Oxide Layer Characterisation

To develop a full understanding of the oxidation behaviour of Hastelloy C276, including quantification of the oxidation kinetics and characterising the oxidation products formed, an experimental protocol was developed to establish a baseline for the oxidation behaviour of Hastelloy C276 in a dry air environment at 700 °C for durations up to 200 hours. The results of this study are presented throughout this section of the study.

5.4.1 Experimental Methodology

Oxidation testing was completed using a high temperature furnace, capable of reaching 1100 °C, using an isothermal oxidation technique. A test temperature of 700 °C was used to align the experimental studies with conditions observed in nuclear applications. To conduct experiments, coupons of Hastelloy C276 were placed in alumina crucibles at room temperature after being ground, weighed and measured as per the protocol defined in Section 4.2.3. The whole system was then heated together as shown in Figure 4.6.

The oxidation behaviour of Hastelloy C276 was then quantified using a thermogravimetric method, with mass change measurements being taken after 50, 100 and 200 hours of oxidation. The use of these time intervals allowed for the identification of the oxidation kinetics and subsequent calculation of a rate constant for the oxidation of Hastelloy C276.

5.4.2 Experimental Results – Mass Change Measurements

As discussed in Section 4.2, the mass of Hastelloy C276 coupons were taken after isothermal test durations of 50, 100 and 200 hours, with tests being conducted at 700 °C. Measurements of coupon masses were made using a balance with a precision of ±0.0001 g. The mass change per unit area was then calculated as per equation 4.1. The calculated mass change per unit area result is presented in Figure 5.20.

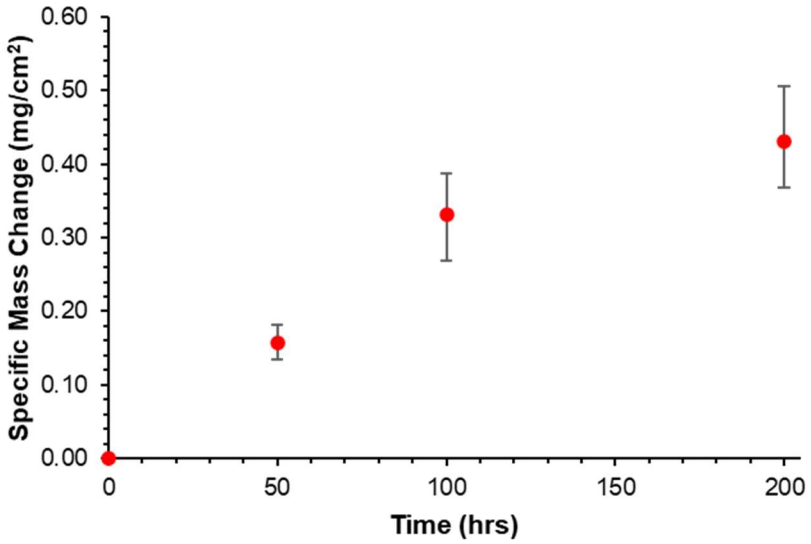


Figure 5.20 - Experimentally determined specific mass change results of Hastelloy C276 coupons, oxidised in a dry air environment at 700 °C for a duration of 200 hours. A final mass change of 0.4300 mg/cm^2 was measured after 200 hours of exposure.

The result presented in Figure 5.20 shows an increased rate of oxidation in the region of 0 – 50 hours, followed by a slowing of this rate over the remaining test duration. Based on this result, Hastelloy C276 shows parabolic type oxidation kinetics. To confirm this observation the square of the specific mass change was plotted against time, with a well-fitting linear relationship confirming the parabolic nature of Hastelloy C276 at 700 °C during the time period of 0 – 200 hours. This plot is presented as Figure 5.21.

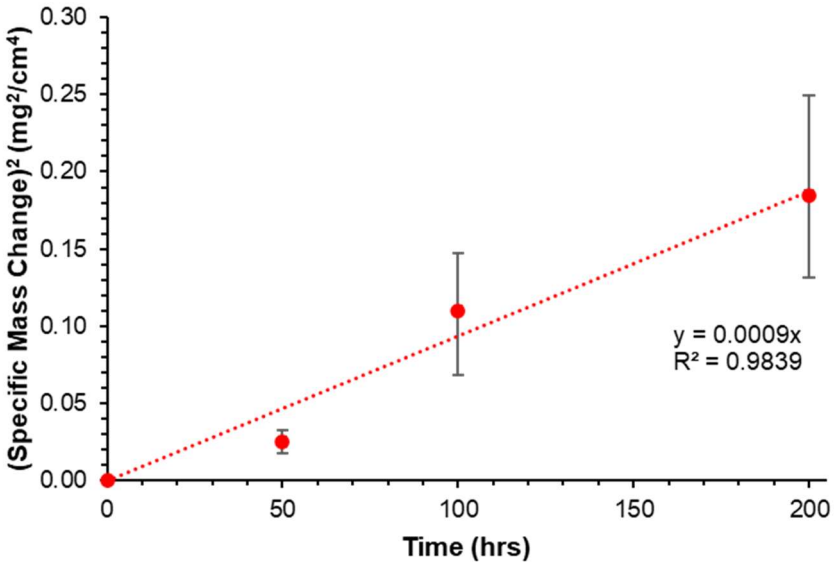


Figure 5.21 – Plot of square of specific mass change of Hastelloy C276 coupons, oxidised in dry air at 700 °C for a duration of 200 hours using an experimental methodology, against time. Result shows linear trend with an R^2 value of 0.9646.

The linear result presented in Figure 5.21 confirms the parabolic nature of the oxidation kinetics of Hastelloy C276, with a K_P value of 2.57×10^{-7} $mg^2/cm^4/s$ being calculated for the oxidation of Hastelloy C276 at 700 °C in the duration of 0 to 200 hours.

5.4.3 Characterisation of Oxide Layer – SEM analysis

After mass measurements were taken and specific mass change results calculated, SEM and EDX analysis were conducted on the oxide layers formed during testing. SEM imaging was used to take high resolution images of the oxidised surfaces to allow for identification of any key features of the oxide layer. EDX was conducted in conjunction with SEM imaging to identify elements present within the oxide layer. This analysis was conducted on both the exposed surfaces and on cross-sections of oxidised coupons.

When imaging the exposed surfaces of experimental coupons, micrographs were taken at a magnification of X5000. Coupons were taken from isothermal tests after exposure to dry air for 50, 100 and 200 hours. A comparison of the exposed surfaces after these durations is presented in Figure 5.22.

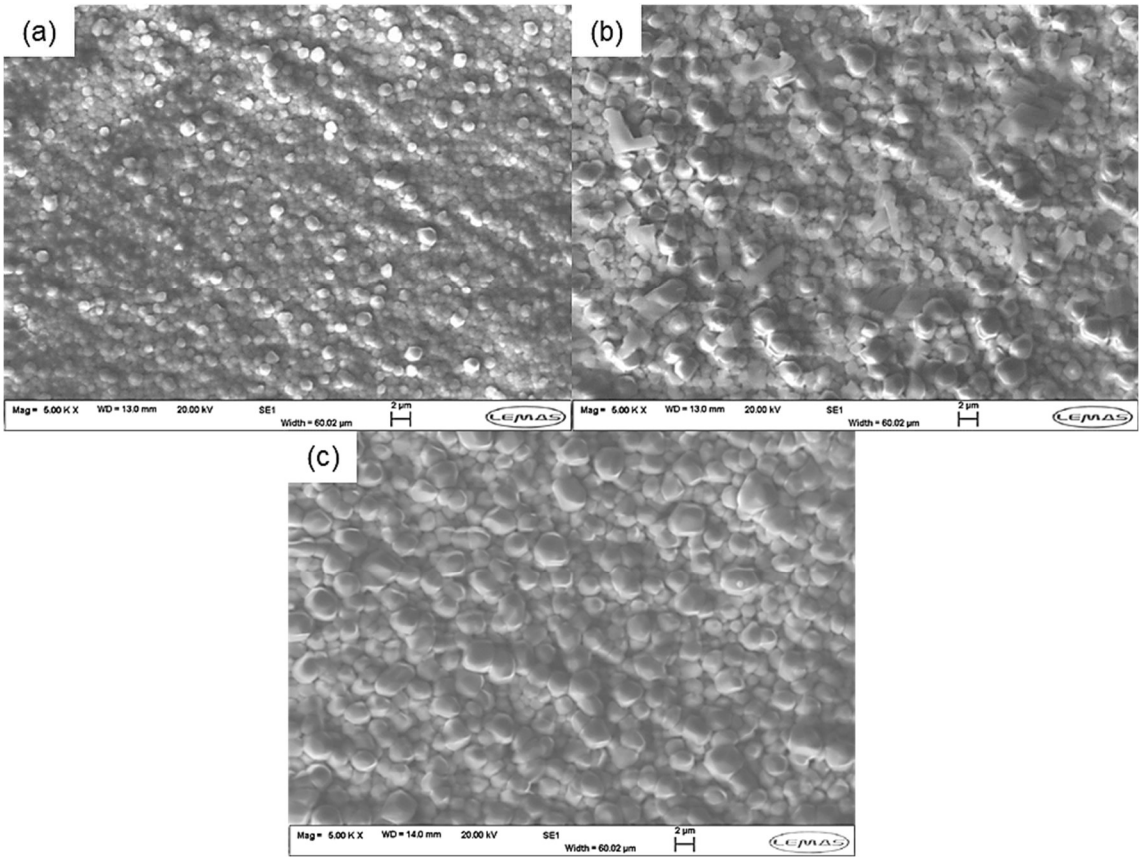


Figure 5.22 - Micrographs of oxidised surfaces of Hastelloy C276 coupons, taken at a magnification of X5000, after a) 50 hours, b) 100 hours and c) 200 hours of exposure to a dry air environment at 700 °C with average oxide crystal size labelled.

Similar images were taken of cross-sections of samples, exposed to a dry air environment for durations of 50, 100 and 200 hours. A comparison of the cross-sections is presented in Figure 5.23.

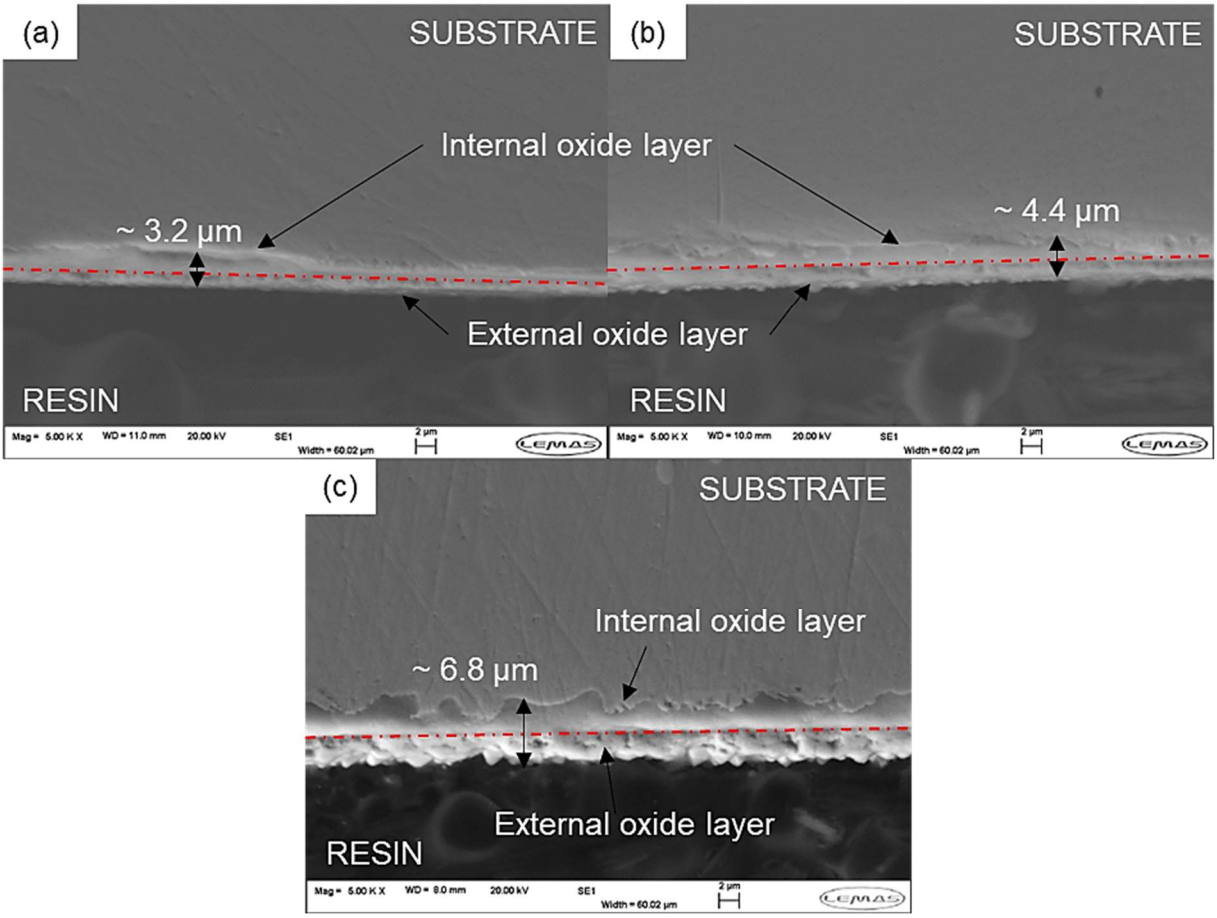


Figure 5.23 – Micrographs of cross-sections of Hastelloy C276 coupons, exposed to a dry air environment at 700 °C for durations of a) 50 hours, b) 100 hours and c) 200 hours. The substrate – oxide interface in each case is shown in red, with internal and external oxide layers labelled. Average total oxide layer thicknesses are also labelled.

Key observations of the micrographs presented in Figure 5.22 and Figure 5.23 include the increasing oxide layer growth and increasing oxide crystal size as a function of time. Both the oxide layer thickness and oxide crystal sizes were measured, with a layer thickness or crystal size being calculated at each time interval. The resultant measurements are presented in Figure 5.24.

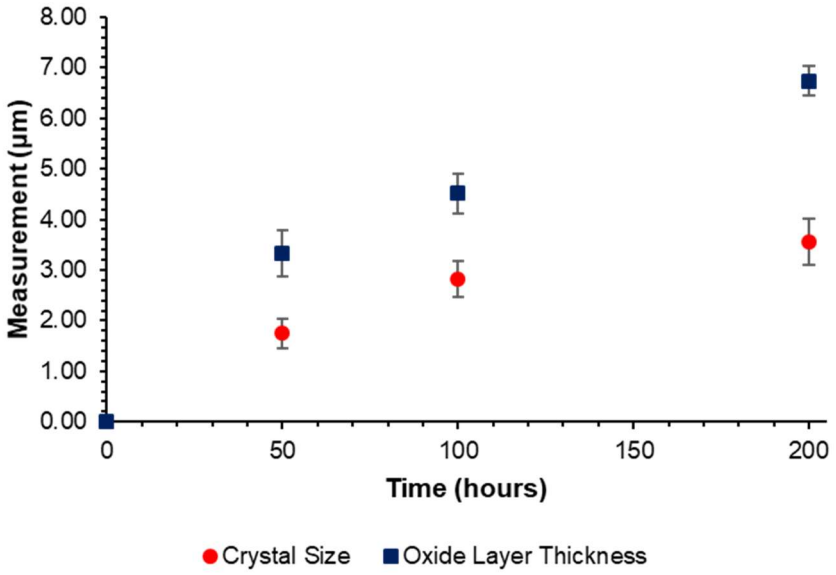


Figure 5.24 – Average oxide crystal size and oxide layer thickness, measured on Hastelloy C276 coupons after exposure to a dry air environment, held at 700 °C for durations of 50, 100 and 200 hours.

Similarly, to the specific mass change results, both oxide crystal size and layer thickness growth appear to follow a parabolic growth law, with the oxide layer thickness increasing to a maximum of 6.74 µm after 200 hours of exposure to a dry air environment. A plot of the measurements squared against time is presented as Figure 5.25 to confirm the growth kinetics.

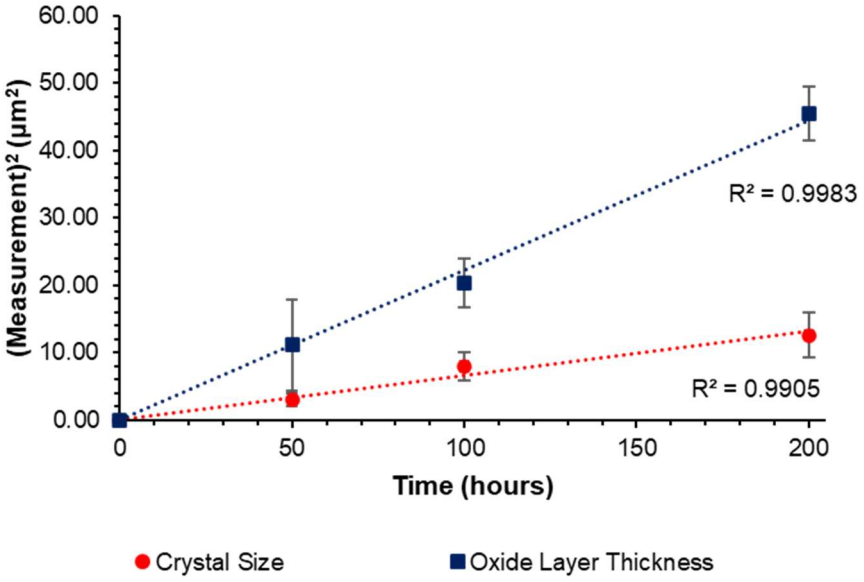


Figure 5.25 – Plot of the square of oxide crystal size and oxide layer thickness measurements against time, showing a linear relationship for both sets of measurements, confirming parabolic growth law of both oxide crystal size and oxide layer thickness.

The linear relationships observed between the square of each measurement against time confirms the parabolic nature of the growth of both the oxide crystals and the oxide layer thickness.

5.4.4 Characterisation of Oxide Layer – EDX analysis

When conducting EDX analysis, three main methods were used. Point and ID analysis was conducted on regions of interest to identify elements present in crystal structures or other artefacts. EDX maps were created to identify elements present over an area of the oxidised surface. Finally, EDX line scans were used on cross-sections to examine the distribution of elements within the oxide layer and at the interface between the oxide layer and the substrate material.

To identify the elements, present in the oxide layer, EDX maps were taken of the oxidised regions presented in Figure 5.22, with Point and ID analysis being conducted on the crystal structures. The EDX maps are presented in Figure 5.26.

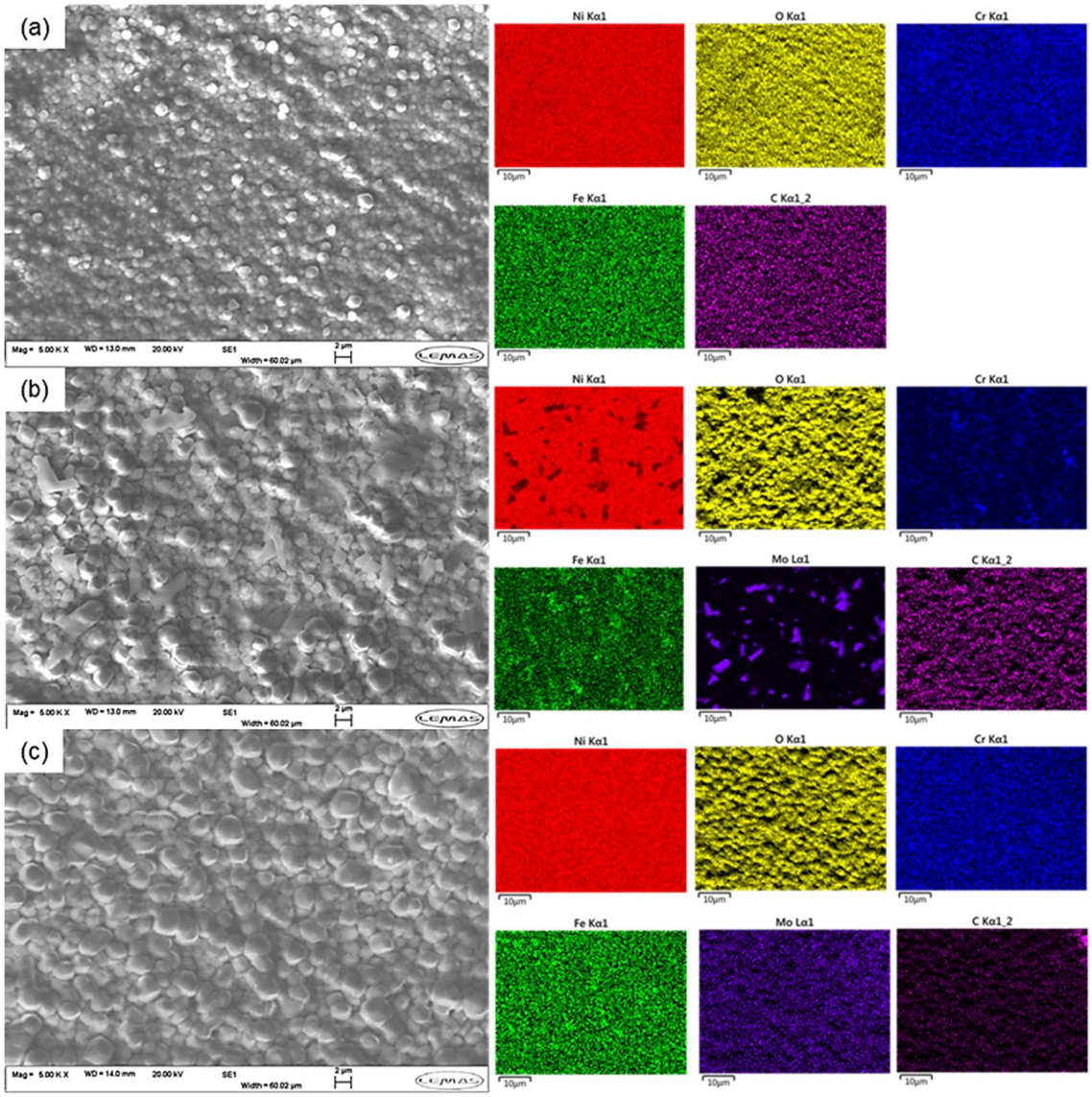
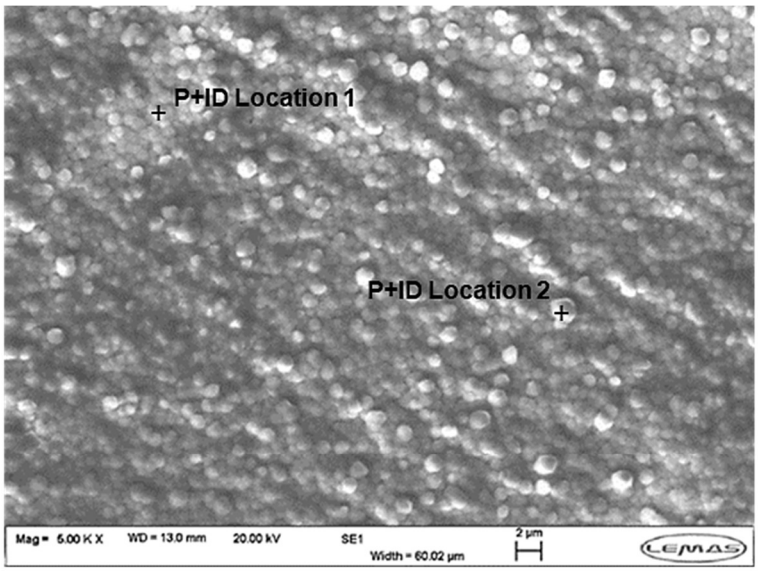


Figure 5.26 – EDX maps of micrographs of oxidised surfaces of Hastelloy C276 coupons, presented in Figure 5.22, after a) 50 hours, b) 100 hours and c) 200 hours of oxidation in a dry air environment at 700 °C.

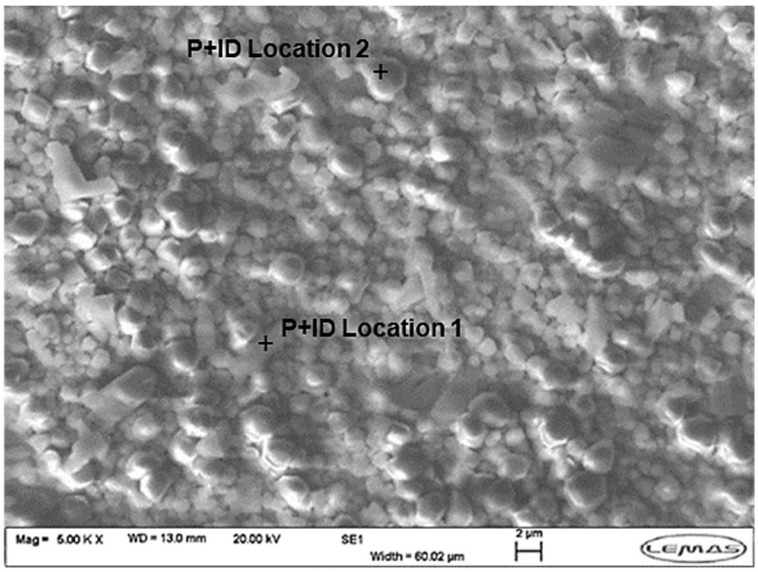
After 50 hours of exposure to air at 700 °C, the oxide layer is observed to be composed of Ni, Cr, Fe and O, although the intensity of Cr and Fe is observed to be less than that of Ni and O. This suggests that the oxide layer is primarily composed of a Ni-oxide. This was corroborated by Point and ID analysis which showed individual crystals contained high concentrations of Ni and O, with much smaller concentrations of Cr and Fe, as shown in Figure 5.27.



Element	P+ID Location 1 (wt.%)	P+ID Location 2 (wt.%)
C	2.98	6.99
O	16.07	25.47
Cr	3.23	1.14
Fe	1.61	0.61
Ni	76.11	65.79

Figure 5.27 – Point and ID analysis of individual oxide crystals, formed on Hastelloy C276 coupons after 50 hours of exposure to dry air at 700 °C, showing high concentrations of Ni and trace amount of Cr and Fe.

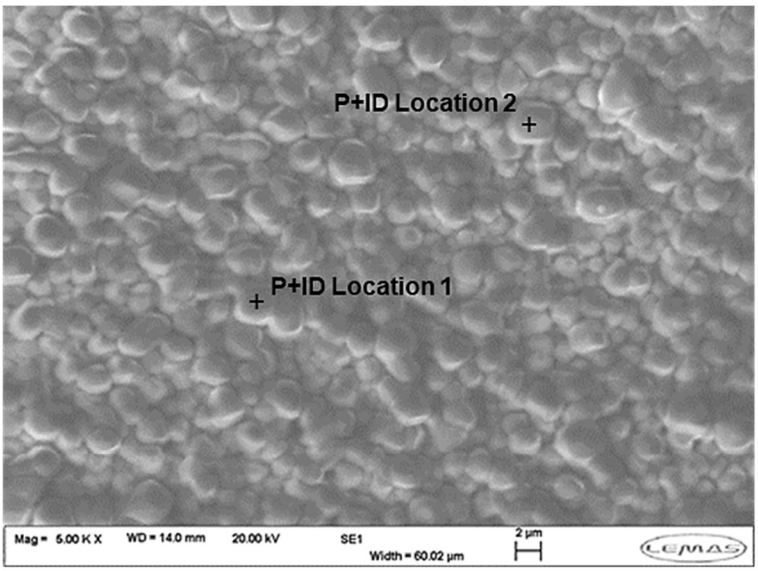
After 100 hours of exposure, the intensity of Cr and Fe are observed to decrease, suggesting an increase in the thickness of the Ni-based oxide forming at the air – oxide interface. Also observed in the EDX maps were regions enriched in Mo, which were likely to be due to the precipitation of Mo-carbide phases from the material microstructure. Again, Point and ID analysis was conducted on the exposed surface and the results used to corroborate the findings presented in Figure 5.26. The results of the Point and ID analysis are presented in Figure 5.28.



Element	P+ID Location 1 (wt.%)	P+ID Location 2 (wt.%)
C	7.12	5.11
O	29.63	22.58
Cr	0.79	1.09
Mn	0.73	0.00
Fe	0.46	0.62
Ni	25.85	70.61
Mo	31.38	0.00
W	4.04	0.00

Figure 5.28 – Point and ID analysis of individual oxide crystals, formed on Hastelloy C276 coupons after 100 hours of exposure to dry air at 700 °C, showing high concentrations of Ni and reduced amounts of Cr and Fe. Regions of Mo enrichment was also observed.

An increase in the coverage of both Cr and Fe is observed in Figure 5.26c after 200 hours with no observable change in the intensity of Ni and O, suggesting that the most outer oxide layer is still predominantly a Ni-based oxide. This is supported by the EDX analysis presented in Figure 5.29.



Element	P+ID Location 1 (wt.%)	P+ID Location 2 (wt.%)
C	5.79	5.89
O	25.48	21.21
Cr	1.15	1.16
Fe	0.55	0.65
Ni	70.78	71.08

Figure 5.29 – Point and ID analysis of oxide crystals, formed on Hastelloy C276 coupons after 200 hours of exposure to dry air at 700 °C, showing similar concentration of both Cr and Fe as well as Ni and O.

The increased coverage of the sample observed of both Cr and Fe suggest that Cr and Fe have been able to diffuse through the oxide layer to the air-oxide interface where that have the potential to be oxidised.

To confirm the observations described previously regarding the composition of the oxide layer, EDX line scans were made on cross-sections of Hastelloy C276 coupons, exposed to dry air at 700 °C for durations of 50, 100 and 200 hours. The line scans are presented in Figure 5.30.

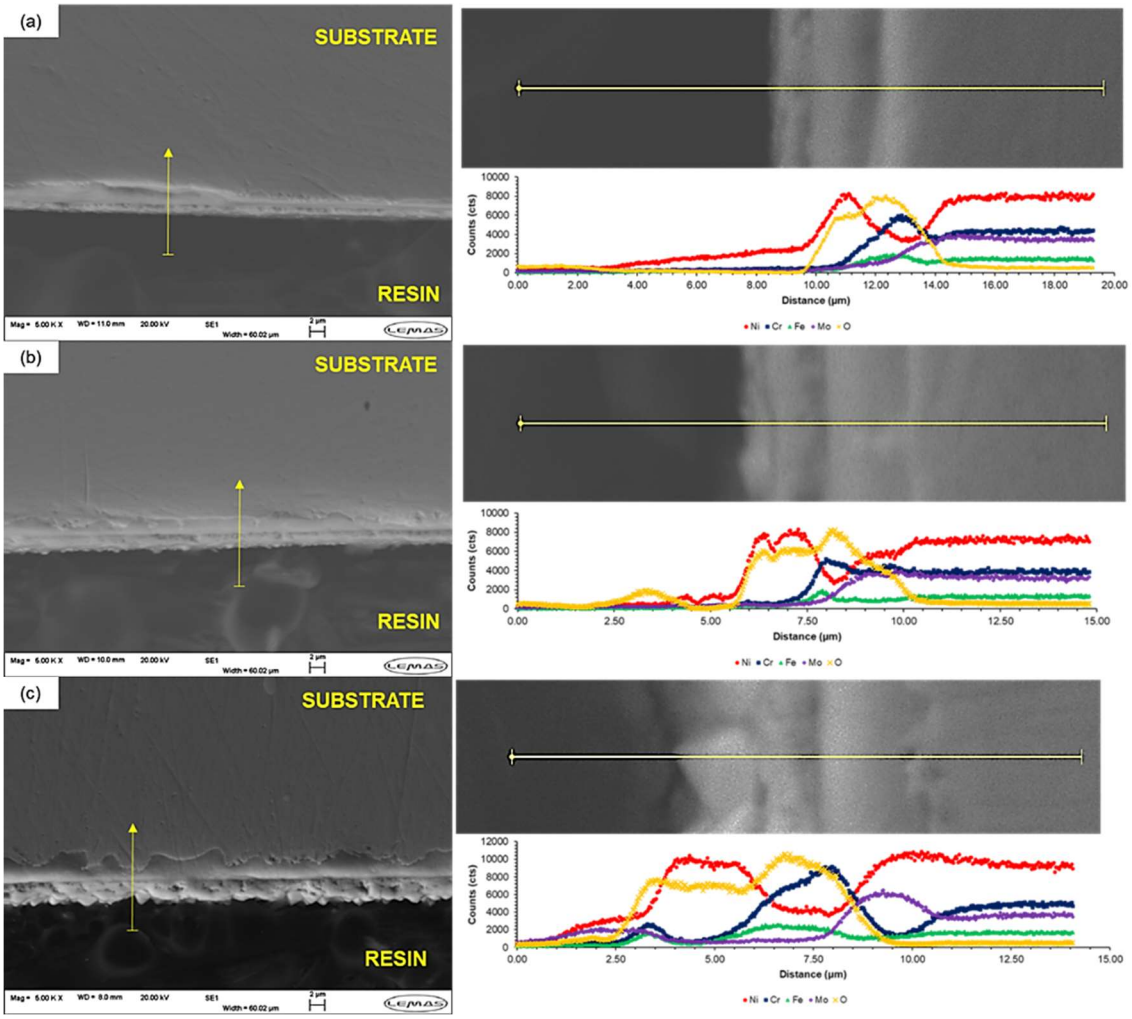


Figure 5.30 – EDX line scans conducted on cross-sections of Hastelloy C276 coupons after exposure to dry air at 700 °C for durations of a) 50 hours, b) 100 hours and c) 200 hours. Results show increasing depletion of Cr from the substrate material as well as continuous growth of the oxide layer.

After 50 hours of exposure, the composition of the most outer oxide layer can be observed to be primarily Ni-based. However, in the oxide – substrate interface region, Ni is depleted, and Cr and Fe are slightly enriched, suggesting the formation of a multi-layer oxide structure. This corroborates the EDX maps presented in Figure 5.22 as Ni was observed to have the greater response, with Cr and Fe being present but having lower intensities. The thickness of the Ni-enriched oxide is observed to increase in Figure 5.30b, with Cr and Fe still being enriched in the oxide-substrate interface region. No additional Cr or Fe enrichment is observed at the air-oxide interface; hence they have not yet been able to diffuse through the oxide layer. This observation agrees with the observations made regarding Figure 5.22b. Up to 100 hours, a multi-layer oxide scale is possible, constructed of several metallic oxides.

The biggest changes in the element distribution of the oxide layer are observed after 200 hours of exposure. This thickness of the Ni-enriched oxide is observed to increase again; however, peaks of Cr and Fe are now observed in this region also. This shows that Cr and Fe have been able to diffuse through the oxide layer to the air-oxide interface. Within the rest of the oxide structure, Cr is observed to be enriched within the oxide layer itself but now depleted at the oxide-substrate interface. This observation can also be made for Fe, but to a lesser extent. Due to the introduction of Cr and Fe into the enriched Ni-based oxide, the formation of a spinel-oxide is possible in conjunction with the continued growth of separate metallic oxide layers. In order to fully characterise the oxide structures, an additional technique was needed.

5.4.5 Characterisation of Oxide Layer – XRD analysis

Although many of the elements within the oxide layer were identified by EDX analysis, the oxide structures themselves could not be identified. Therefore, XRD analysis was conducted on coupons of Hastelloy C276 to identify the oxides present within the oxide layer. The results of the XRD analysis are presented in Figure 5.31.

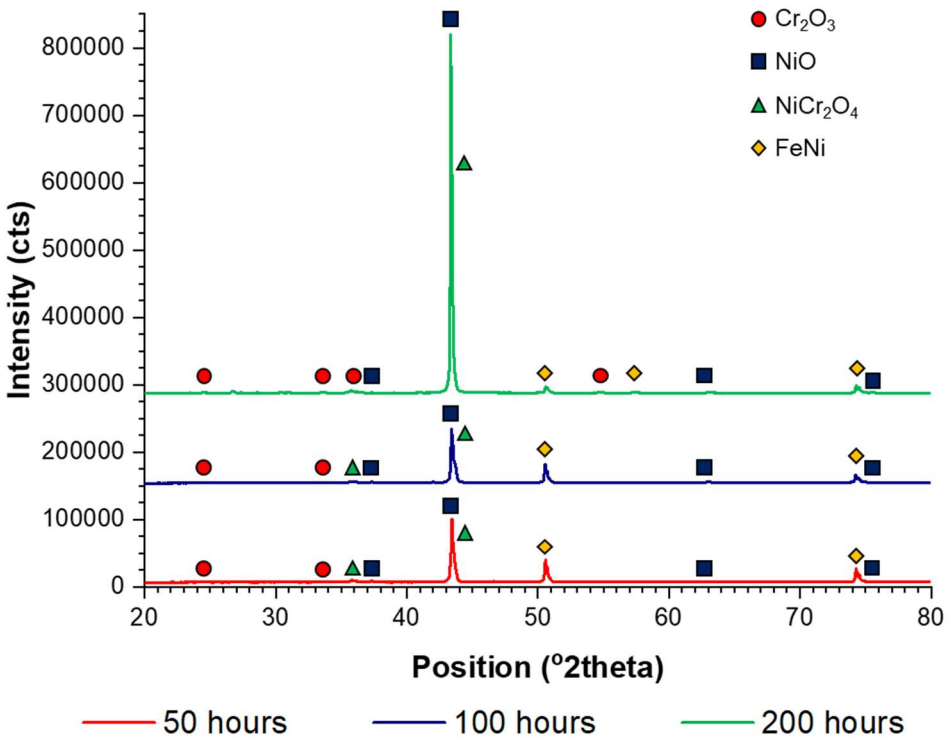


Figure 5.31 – XRD analysis conducted on coupons of Hastelloy C276 after exposure to dry air at 700 °C for durations of 50, 100 and 200 hours. Peaks were identified using Xpert Highscore software and have been labelled as per their designated structure.

The identified peaks, labelled on Figure 5.31, correspond to oxide structures formed during the oxidation of Hastelloy C276 at 700 °C after durations of 50, 100 and 200 hours. After 50 hours of oxidation, the identified structures include NiO and Cr_2O_3 along with peak corresponding to the substrate material. After 100 hours of oxidation, both NiO and Cr_2O_3 were identified again, however, peaks corresponding to the spinel oxide $NiCr_2O_4$ were also identified. The formation of $NiCr_2O_4$ is achieved by the reaction of NiO and Cr_2O_3 as shown equation 5.1.

$$NiO + Cr_2O_3 \rightarrow NiCr_2O_4 \quad \textbf{5.1}$$

After 200 hours of exposure to a high temperature oxidising environment, the same peaks were identified as 100 hours of exposure. However, the intensity of the NiO and Cr_2O_3 peaks are observed to decrease whilst the intensity of the $NiCr_2O_4$ peak is observed to increase, indicating that the formation of $NiCr_2O_4$ is the predominant oxidation mechanism after longer oxidation durations.

5.5 Experimental Results versus Numerical Predictions

In this work both experimental and numerical approaches were undertaken to capture the oxidation behaviour of the Ni-based alloy Hastelloy C276 at 700 °C. This included the development of empirical and mechanistic modelling methodologies and conducting isothermal oxidation testing. In all cases, the specific mass change of Hastelloy C276 coupons due to being oxidised was a key result. A comparison between the experimentally determined result and numerical predictions is presented in Figure 5.32.

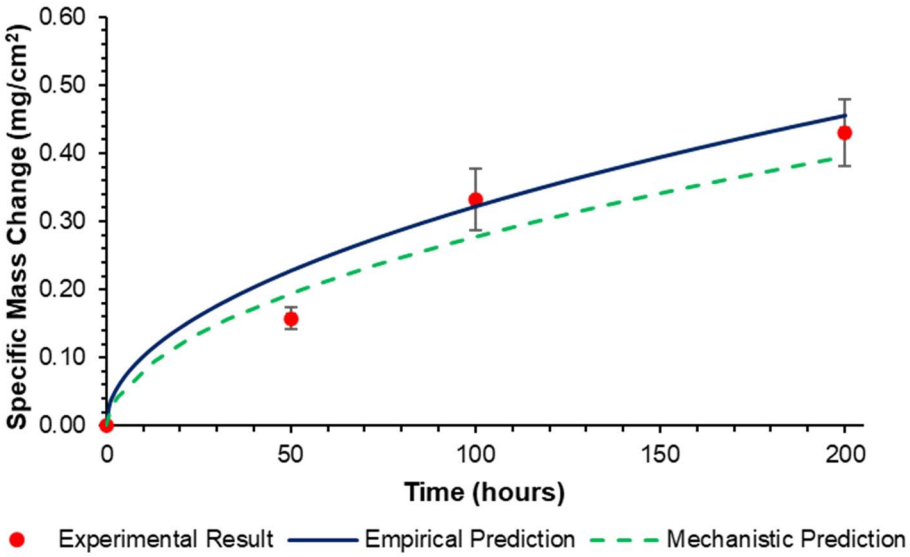


Figure 5.32 – Comparison of experimentally determined specific mass changes of Hastelloy C276 coupons, exposed to dry air environment at 700 °C for durations of 50, 100 and 200 hours and numerical predictions of specific mass change for the same conditions. Numerical predictions were made by empirical modelling and mechanistic modelling methodologies developed in this thesis.

On first observation, good agreement is observed between both models and the experimentally determined specific mass change results. Interestingly, the specific mass change predicted by the empirical model shows better agreement to the experimental result, differing by 5.76%, whereas the mechanistic model prediction differs by 8.54%. However, both predictions are acceptable in this case, with predictions being inside the range of experimental error at both 100 and 200 hours shown in Figure 5.32.

Although the empirical model shows better numerical agreement with the experimentally determined result, the empirical model is based on data available in literature, and therefore may be volatile to the addition or subtraction of data points from the model. The empirical model is also based on the formation of Cr_2O_3 only, with other oxides being treated as impurities with the oxide layer. This means that the result obtained from the empirical model represents an over-prediction of Cr_2O_3 formation for the Hastelloy C276 alloy. Experimental results, both in this study and in literature, have showed that multiple oxides form during the oxidation of Ni-based alloys in a multi-layer oxide structure [99, 101, 104]. Therefore, a model which does not fully capture the growth of each oxide is limited in its applicability.

In contrast, the mechanistic model is capable to predicting the growth of each oxide individually based on the concentration changes of each element at the air-

substrate interface. Therefore, a much deeper level of understanding can be achieved using a mechanistic model over the empirical counterpart. This includes an understanding of the oxide layer thicknesses as well as their compositions. A comparison between the measured and predicted oxide layer thicknesses are presented in Figure 5.33.

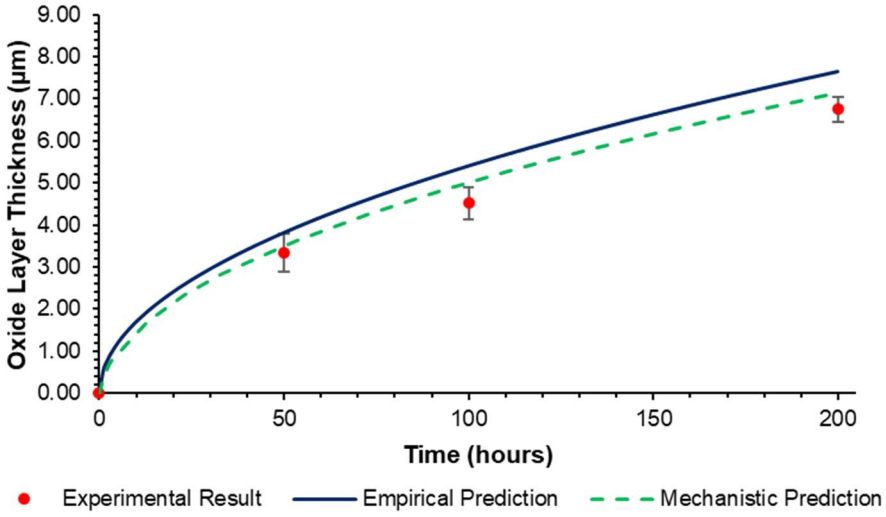


Figure 5.33 – Comparison of oxide layer thicknesses determined by exposure of Hastelloy C276 coupons to a dry air environment at 700 °C for durations of 50, 100 and 200 hours to numerical predictions from empirical and mechanistic models developed in this research.

In this case, the mechanistic model shows the best agreement with experimental measurements, with the mechanistic model overpredicting the oxide layer thickness after 200 hours of exposure by 5.62%. Whereas the prediction provided by the empirical model overpredicts the oxide layer thickness more and differs from the experimental measurements by 12.8%. The prediction made by the mechanistic model is acceptably close to the experimentally determined values, with the result falling within the range of error shown for the measurement of the oxide layer thickness in Figure 5.33. The overall results obtained by the mechanistic model indicate a much deeper level of understanding due to the inclusion of element diffusion behaviour and the chemistry of individual oxide growth. Therefore, the use of the mechanistic model may be more favourable than the empirical model.

5.6 Summary of Results

To summarise, the research results presented in this chapter stem from the deployment of experimental and numerical modelling methodologies, applied to a

high temperature oxidising environment. This has involved developing empirical and mechanistic models for the oxidation of Hastelloy C276. The results from these studies were validated with results from literature and in-house experimental mass change measurements.

Experiments conducted were used to quantify the oxidation kinetics of Hastelloy C276, showing parabolic oxidation kinetics, characterised by a K_P value of 2.57×10^{-7} $mg^2/cm^4/s$. The oxidation layer morphology was visualised using SEM analysis, which showed an increase in the oxide crystal size, as well as their coverage over the oxidised surface, with respect to time. EDX analysis confirmed the presence of Cr, Ni and Fe within the oxide layer, with XRD analysis confirmed the oxide structures of NiO and Cr_2O_3. An $NiCr_2O_4$ oxide structure was identified after longer oxidation durations. Peaks corresponding to the substrate material were also identified.

Empirical and mechanistic modelling methodologies also predicted oxidation kinetics, with the predicted K_P values being 2.88×10^{-7} $mg^2/cm^4/s$ and 2.17×10^{-7} $mg^2/cm^4/s$, respectively. These values differ from the experimental results obtained in this study by 11.4% and 16.9%, respectively. Despite these differences between the experimental and predicted K_P values for Hastelloy C276, the results were deemed to be acceptable. As shown in Figure 5.32, the predictions made using empirical and mechanistic modelling techniques fall within the error observed in mass change measurements after 200 hours of exposure. Smaller experimental errors were observed in measurements taken after 50 and 100 hours of exposure to dry air. However, differences of less than 10% were observed between predicted and experimentally measured values of specific mass change of Hastelloy C276 in a dry air environment. Good agreement was also observed between the numerical methods and data obtained from literature, particularly the works of Li et al. [99] and Park et al. [161] where differences of approximately 10% and 20% were observed between the predicted activation energies and the experimentally derived values of Li et al. [99] and Park et al. [161] respectively.

Due to the good agreement of the mechanistic model with both experimental specific mass changes and oxide layer thicknesses, the mechanistic model will be utilised in the corrosion study and developed further. This choice was made due to the capability of the mechanistic model to predict the concentration profiles of alloying elements, meaning that their changes in concentration can be utilised in the calculation of the corrosion behaviour as per the described corrosion model in Section 4.4.

Chapter 6 - Results II

Corrosion of Hastelloy C276 in molten salt environments: Experimental and numerical approaches

In the previous chapter, the high temperature oxidation of Hastelloy C276 was investigated using both experimental and numerical methods. The results of the previous chapter showed that Hastelloy C276 exhibited parabolic oxidation kinetics, indicating that its oxidation is controlled by the diffusion of species across the formed oxide layer. This was corroborated by numerical modelling methods, the first an empirical method and the second a mechanistic model which captured the diffusion behaviour of elements within the Ni-based alloy.

The research conducted in this chapter therefore builds upon the high temperature oxidation studies by investigating the corrosion behaviour of Hastelloy C276 in molten FLiNaK salt in an air environment. The mechanistic model developed for predicting the high temperature oxidation of Hastelloy C276 will also be expanded to provide predictions of specific mass changes due to corrosion and depths of corrosive attack.

6.1 Introduction

Corrosion of metallic alloys within molten salt systems remains a serious issue to nuclear reactor longevity and performance. For MSR applications, Ni-based alloys have been the material of choice due to their good high temperature performance and corrosion resistant properties. However, even these materials have been shown to undergo corrosive attack in molten salt environments. In order to develop an improved understanding of the performance of Ni-based alloys in molten salts applicable to the MSR, the mechanisms by which these materials degrade need to be fully investigated.

To aid in the development of this improved understanding of how Ni-based alloys behave in molten fluoride salt environments, experimental methods were deployed to investigate and characterise the corrosion behaviour of Hastelloy C276 in molten FLiNaK salt. A numerical model was also developed, utilising the mechanistic model developed for the oxidation of Hastelloy C276, to predict the corrosion behaviour of Hastelloy C276 in a FLiNaK molten salt environment. Deploying both experimental and numerical modelling techniques allowed for the following research objectives to be completed:

- Predict the corrosion behaviour of Hastelloy C276 in molten salt environments containing FLiNaK, building upon the mechanistic oxidation modelling approach detailed in Chapter 5.
- Complete static corrosion tests involving Hastelloy C276 coupons and molten FLiNaK salt at 700 °C to quantify the corrosion behaviour using a thermogravimetric technique.
- Characterise the corrosion behaviour of Hastelloy C276 in a corrosive molten salt environment by analysis of corroded samples using SEM, EDX and XRD analysis techniques.
- Validate the developed mechanistic model using both experimental results obtained in this study and data available from the literature.

6.2 Prediction of corrosion – Mechanistic Model

The corrosion model developed in this chapter builds upon the mechanistic oxidation model developed and discussed in Chapter 5. The mechanistic oxidation model allowed for prediction of the elemental concentration changes within the substrate material based on the diffusion behaviour of alloying elements at a temperature of 700 °C during the 200-hour test duration. This result directly applies to the methodology deployed throughout this chapter to predict the corrosion behaviour of Hastelloy C276 in a molten salt environment, in which changes in element concentration between the bulk and interface are used.

6.2.1 Diffusion Based Model - Model Description

The corrosion model developed throughout this chapter builds directly upon the mechanistic oxidation model discussed in Chapter 5. In the numerical modelling methodology deployed in this chapter, the predicted concentration changes for Cr at the substrate – molten salt interface were utilised to predict the corrosion behaviour of Hastelloy C276 in a molten FLiNaK salt environment at 700 °C as a function of time. This was achieved using an adaptation of the model developed by Li et al. [121] for predicting the molten salt corrosion of 316L in a nitrate molten salt environment. This model will therefore capture material loss due to corrosion and the depth of corrosion attack due to the interactions between molten FLiNaK salt and the Hastelloy C276 test material.

6.2.2 Diffusion Based Model - Sensitivity Study

Since the corrosion model developed in this research builds directly upon the mechanistic oxidation model presented in Chapter 5, a sensitivity study for

assessing the convergence of element concentration profiles throughout the corroding alloy as a function of time was not completed. Instead, the ideal conditions found in the sensitivity study presented in Section 5.3.2 were used.

However, the development of the corrosion model did require a further study due to the inclusion of the corrosive species HF, CrF_2 and O_2 within the predictive model. To include each of these species, their diffusion behaviour was predicted within the molten salt as a function of time using their diffusion coefficients as presented in Section 4.4.4. This allowed for their concentrations at the substrate – molten salt interface to be predicted.

In this case, the sensitivity study was conducted in the molten salt region of the model geometry and not the substrate material. Therefore, the diffusion distance modelled was 0.37 cm, which related to the distance from the air – molten salt interface to the molten salt – substrate interface. This is illustrated in Figure 6.1.

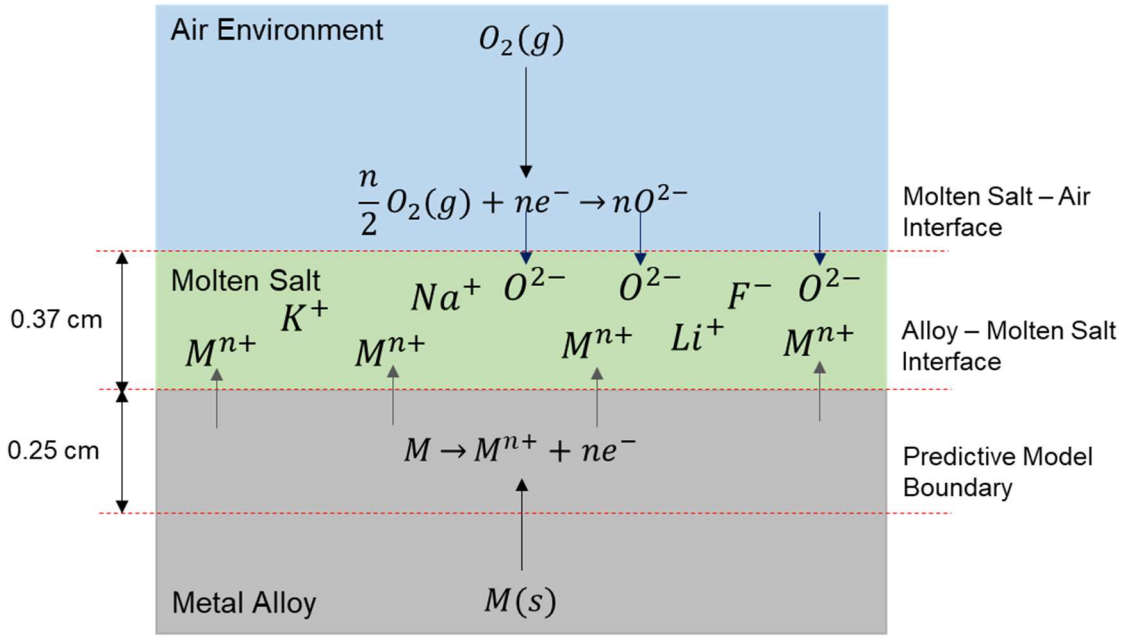


Figure 6.1 – Illustration of corrosion system, in which the diffusion of corrosive species HF, CrF_2 and O_2 was predicted.

The diffusion distance presented in Figure 6.1 was calculated from the volume of salt added to the crucible for each experiment and the volume of the alumina crucibles being used. As described previously when discussing the modelling methodology for the corrosion of Hastelloy C276 in FLiNaK molten salt, diffusion coefficients for HF, CrF_2 and O_2 in molten fluoride salts were taken from literature and used within this study [180-182, 184].

Similarly, to the sensitivity study of the mechanistic model presented in Section 5.3.2, a sensitivity study was conducted, monitoring the concentration changes of

CrF_2, HF and O_2 at the substrate – molten salt interface to determine how many modelling nodes were required in the corrosion portion of the model to achieve a mesh independent solution of the concentration of each species. This result is presented in Figure 6.2:

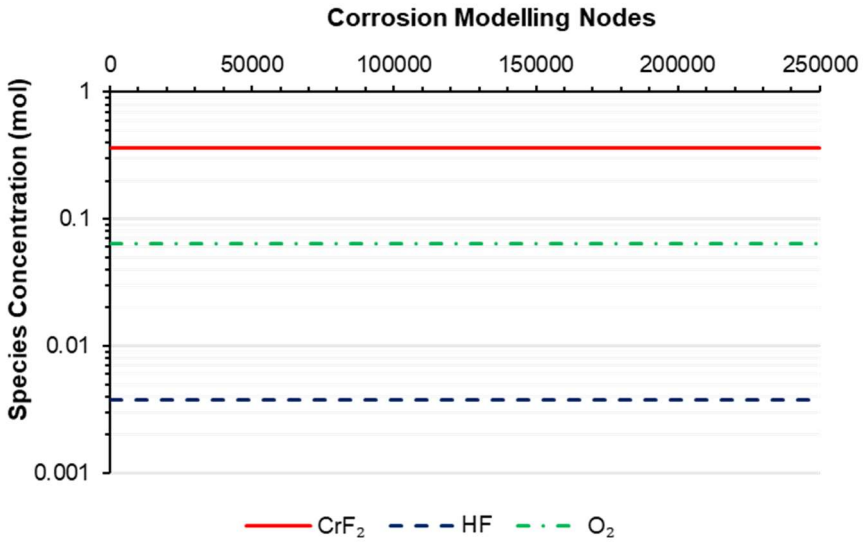


Figure 6.2 – Changes in concentrations of HF, CrF_2 and O_2 at the molten salt – substrate interface with varying number of modelling nodes showing that increasing the number of modelling nodes has no impact on the predicted concentrations of the investigated species.

The result presented in Figure 6.2 shows that changing the number of modelling nodes from 101 up to 250001 for the prediction of the concentration profiles of CrF_2, HF and O_2 has no impact on the result. This was observed due to the rapid diffusion kinetics of CrF_2, HF and O_2 diffusion within a molten FLiNaK salt environment, meaning changes in concentration are almost instantaneous. This is highlighted in Figure 6.3 which shows extremely rapid concentration changes of the CrF_2, HF and O_2 species with respect to time.

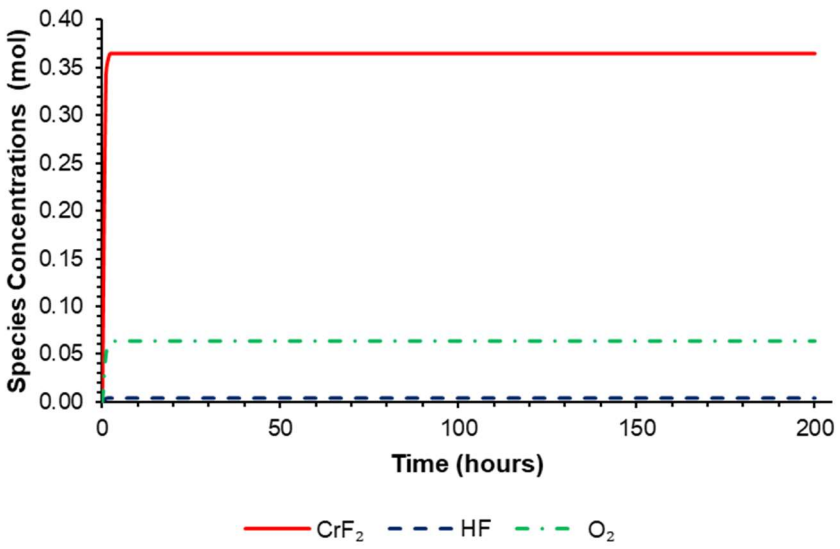


Figure 6.3 – Concentration predictions of CrF_2, HF and O_2 at the substrate – molten salt interface at 700 °C in the time period of 0 to 200 hours. Due to the faster diffusion kinetics of these species, rapid changes are initially observed before reaching a constant value.

Since the number of modelling nodes had very little impact on the concentrations of CrF_2, HF and O_2, the number of modelling nodes could be reduced as much as possible in order to reduce the computational demand and thus decrease the computation time.

Therefore, a study was conducted to understand the influence of the number of modelling nodes on the computation time. The computational time at each number of modelling nodes is presented in Figure 6.4.

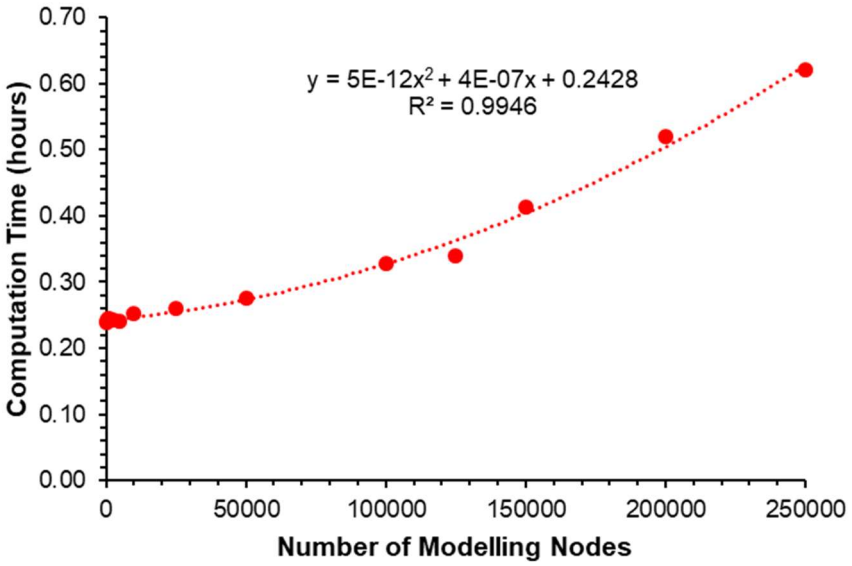


Figure 6.4 – Graph showing the computation time with varying number of modelling nodes used for the prediction of concentration changes of CrF_2, HF and O_2 within the corrosion model.

The result for the change in the computation time with respect to the number of modelling nodes presented in Figure 6.4 shows that the number of modelling nodes in the corrosion portion of the model has a much smaller impact on the computation time than the number of modelling nodes used in the oxidation portion of the model. The computation time for the corrosion model was observed to increase from 0.24 hours to 0.62 hours. When compared with the oxidation model, an increase of 0.38 hours is less than the increase observed for the oxidation model, where the computation time increased from 0.0029 hours to 1.77 hours when the number of modelling nodes is increased from 1001 to 250001. Similarly, to the oxidation model, the computation time is observed to increase in a quadratic relationship with the number of modelling nodes.

Since the number of modelling nodes fails to have any impact on the concentration of the HF, CrF_2 and O_2 species at the molten salt – substrate interface, the computation time can be minimised as much as possible by choosing the minimum number of modelling nodes. Therefore, the number of modelling nodes chosen was 101 to reduce the computation demand whilst maintaining a mesh independent solution for the concentration profiles of each of the required species.

To ensure that a final mesh independent result is obtained, the intrinsic corrosion depth was also monitored. The intrinsic corrosion depth was monitored with increasing numbers of modelling nodes in the oxidation model as the intrinsic corrosion depth calculation was dependent on the concentrations of Cr predicted by the oxidation mechanistic model. As part of the study, the active corrosion depth

was not monitored as its result was independent of the results of the mechanistic oxidation model. Therefore, the result of the intrinsic corrosion depth sensitivity study is presented in Figure 6.5.

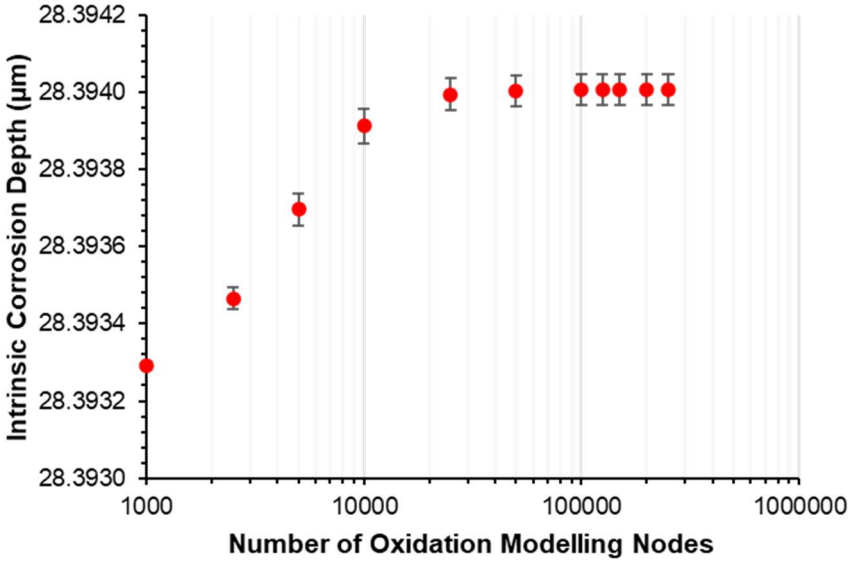


Figure 6.5 – Intrinsic corrosion depths with respect to the number of modelling nodes used in the corrosion model. This result shows convergence of the intrinsic corrosion depth when increasing the number of modelling nodes from 1001 to 250001 within the corrosion model whilst using 125001 modelling nodes within the oxidation mechanistic model. Convergence is observed when in excess of 25001 modelling nodes are used in the corrosion model.

The result presented in Figure 6.5 shows that the intrinsic corrosion depth of Hastelloy C276 changes very little with increasing the number of modelling nodes in the oxidation model, with an increase of 0.0006 µm being observed from 1001 modelling nodes up to 250001 modelling nodes. The active corrosion depth is observed to converge at a value of 28.3940 µm when using in excess of 25001 modelling nodes. This is much less than the number required to achieve convergence in elemental changes predicted as part of the oxidation model. Therefore, to achieve convergence in both the corrosion and oxidation models, 125001 modelling nodes are used for the calculation of a solution that is fully independent of the mesh. Similarly, to match the mechanistic oxidation model and remove the need for post-processing of the species data developed in this section of the model, a time interval of 1 hour will be used.

6.2.3 Diffusion Based Model - Corrosion Predictions

Following the sensitivity study presented in Section 6.2.2, 101 modelling nodes were used in the model to predict the concentrations of HF, CrF_2 and O_2 at the

molten salt – substrate interface. These concentrations were then used within the model described in Section 4.4 to predict the corrosion behaviour of Hastelloy C276 in molten FLiNaK salt. The first result predicted by the model is the corrosion depth of Hastelloy C276 after immersion in molten FLiNaK salt. This result is presented in Figure 6.6.

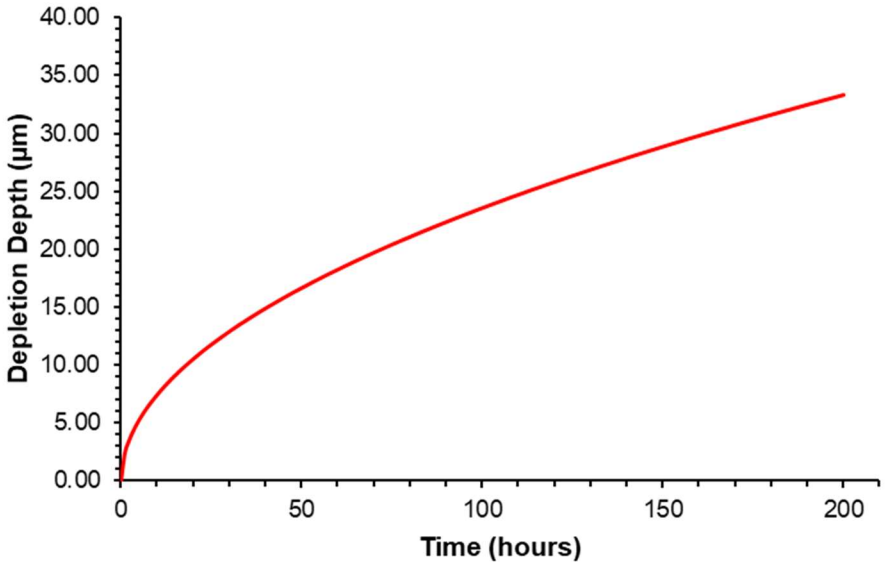


Figure 6.6 - Graph of predicted corrosion depth due of Hastelloy C276 after immersion in FLiNaK molten salt at 700 °C for time periods up to 200 hours, with a maximum corrosion depth of 33.34 µm being predicted up to 200 hours of immersion.

The corrosion depth prediction presented in Figure 6.6 shows the corrosion depth increases in a parabolic fashion, with a maximum depletion depth of 33.34 µm being observed after 200 hours of exposure. The corrosion depth was converted into a mass change, with the result of this calculation being presented in Figure 6.7.

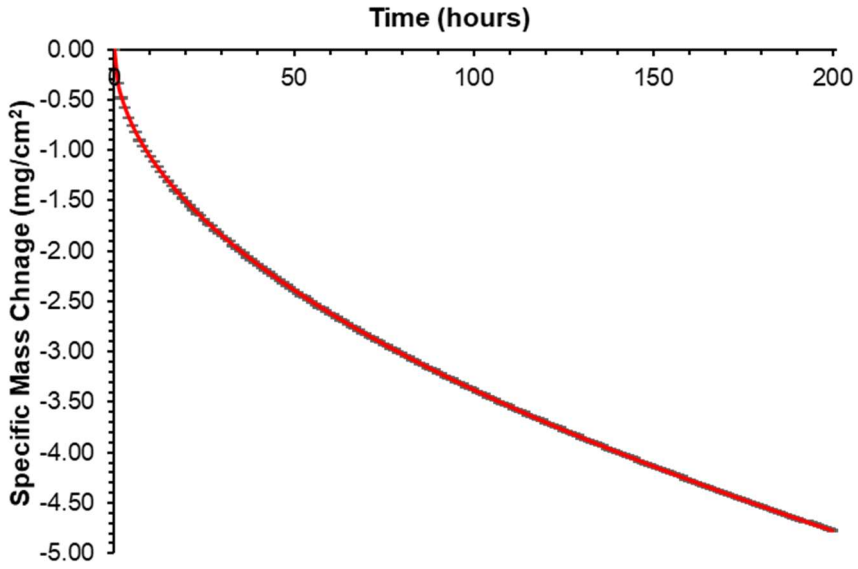


Figure 6.7 - Graph of mass change per unit area prediction of Hastelloy C276 coupons after immersion in molten FLiNaK salt at 700 °C for time periods up to 200 hours showing a specific mass loss of approximately 4.77 mg/cm^2.

Figure 6.7 indicates a specific mass loss from corroded coupons of Hastelloy C276 of 4.77 mg/cm^2. This value was calculated assuming that Cr was dissolved from the substrate material. The specific mass change predictions presented in Figure 6.7 were then used to predict corrosion rates of Hastelloy C276 coupons in a molten FLiNaK salt environment using equation 4.2. The predicted corrosion rates are presented in Figure 6.8.

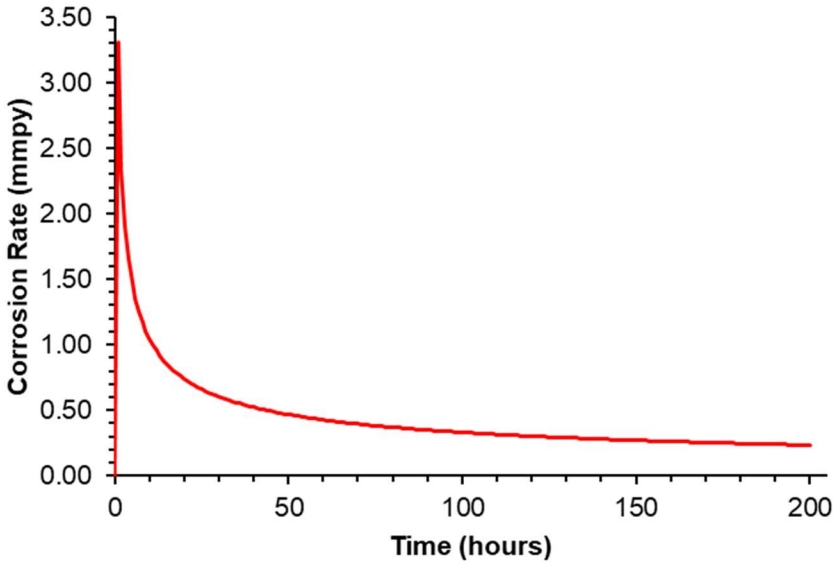


Figure 6.8 – Predicted corrosion rate of Hastelloy C276 coupons immersed in a molten FLiNaK salt environment, containing oxygen at a temperature of 700 °C for a duration of 200 hours. Result shows an initial spike in the corrosion rate to approximately 3.50 mmpy before rapidly dropping below 0.5 mmpy within 50 hours of immersion.

The result presented in Figure 6.8 shows an initially high corrosion rate of approximately 3.50 mmpy before decreasing corrosion over the 200-hour test duration and lowering to 0.23 mmpy. This is consistent with the results presented in Figure 6.6 and Figure 6.7 which show initially large increases in the corrosion depth and the specific mass change with respect to time before slowing. This prediction indicates the initial rapid formation of an oxide film that will form due to the large corrosion rate of 3.50 mmpy. This oxide film will aid in mitigating against further corrosion and is then able to protect the underlying substrate from corrosive attack from the corrosive molten salt.

6.3 Experimental Results and Corrosion product characterisation

To fully characterise the corrosion behaviour of Hastelloy C276 coupons in a FLiNaK molten salt environment, a static immersion technique was deployed with a thermogravimetric method being used to quantify the corrosion damage and corrosion product formation. Characterisation of the corrosion products and the corrosion damage was then undertaken using analysis techniques such as SEM, EDX and XRD to identify the corrosion products formed and to analyse the corroded substrate to identify the mechanism by which corrosion takes place.

The aforementioned techniques have been utilised in many previous molten salt corrosion studies in which coupons of material were immersed in molten FLiNaK salt, with corrosion behaviour being quantified using a thermogravimetric method, hence were deemed to be suitable for the purposes of this research.

6.3.1 Experimental Results - Mass change measurements

The corrosion damage of Hastelloy C276 coupons, immersed in FLiNaK salt at 700 °C was quantified using a thermogravimetric technique, with the final result being defined as a specific mass change. Corrosion rates were also calculated from the specific mass changes using equation 6.1, as specified in ASTM G1-03 for evaluating corrosion test specimens [158]:

$$CR\ (mmpy) = \frac{87600\Delta m}{\rho A t} \qquad \textbf{6.1}$$

Similarly, to the oxidation study of Hastelloy C276 presented in Chapter 5, mass change measurements were made after 50, 100 and 200 hours of static immersion in molten FLiNaK salt at 700 °C.

To obtain a preliminary understanding of whether any corrosion product had formed during the corrosion of Hastelloy C276 in a molten salt environment, mass change measurements were made after removal of any residual solidified salt and before thorough cleaning to remove any corrosion product layers. The measurement of these mass change would allow for multiple results to be identified. One being an indication of whether a corrosion product layer would grow on the exposed surfaces of Hastelloy C276 within a harsh molten salt environment and another being the kinetics of the corrosion product layer growth as a function of time. Mass change measurements obtained at this stage would also allow for the comparison of results before and after corrosion product removal to draw conclusions regarding the synergy of corrosion product growth and corrosion of the underlying substrate material. This mass change results obtained before corrosion product removal are presented in Figure 6.9.

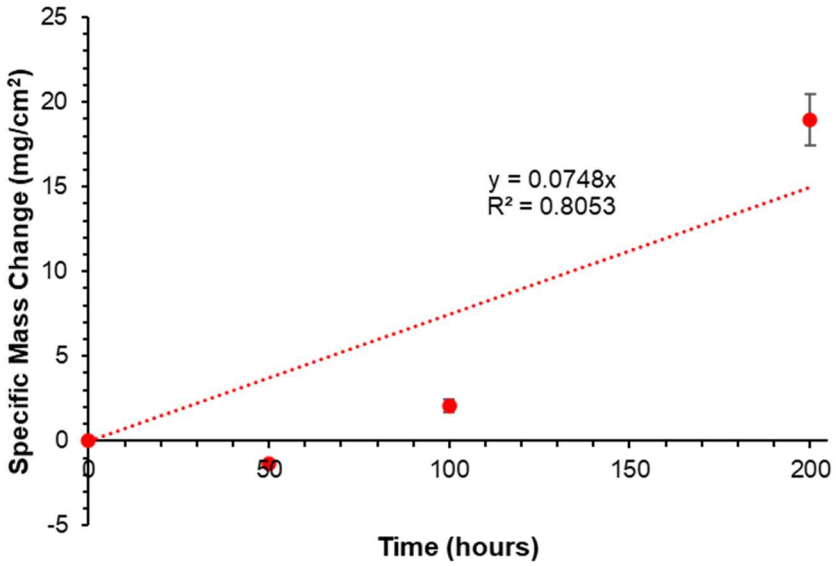


Figure 6.9 – Specific mass change of Hastelloy C276 coupons, corroded in FLiNaK molten salt at 700 °C for up to 200 hours showing overall mass gain due to corrosion product growth.

The result presented in Figure 6.9 shows an initial specific mass loss after 50 hours of exposure before specific mass gains at 100 hours and 200 hours of immersion. In this case the specific mass change has contributions from both corrosion product growth and material removal due to corrosion. As a result, the synergy existing between corrosion product formation and corrosion damage can be discussed.

Figure 6.9 shows that after 50 hours, an initial mass loss was observed which is indicative of corrosion of the substrate material dominating the reaction kinetics. However, after 100 and 200 hours of immersion, mass increases are observed which may be attributed to the formation of a corrosion product layer within the molten salt environment. This is likely to be due to the reactions taking place between alloying elements and oxygen present within the molten salt at the substrate – molten salt interface. The growth of a corrosion product layer may indicate that its formation is the dominating reaction. However, this cannot be confirmed without mass change measurements taken after the corrosion product is removed.

Therefore, following the establishment of the specific mass changes of Hastelloy C276, coupons were cleaned to remove the corrosion product and identify the mass change of Hastelloy C276 coupons in the absence of the corrosion product. The mass change measurement for this study is presented as Figure 6.10.

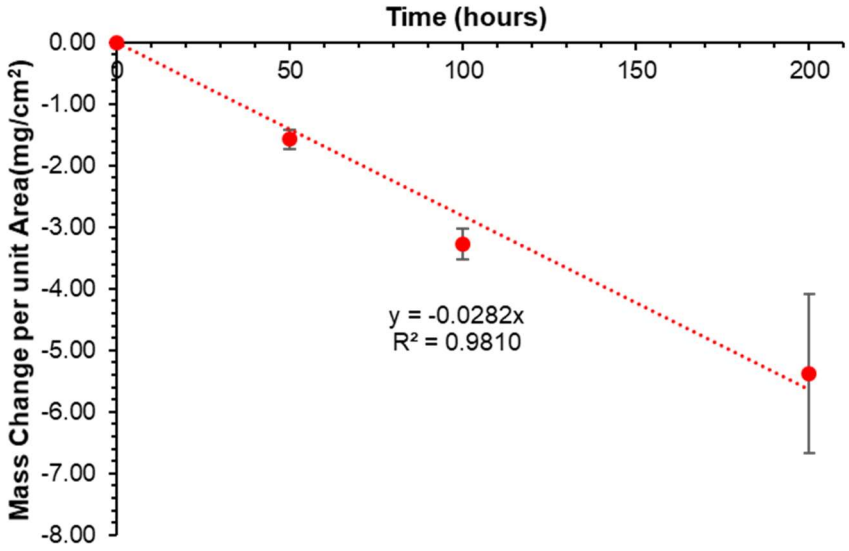


Figure 6.10 - Mass change per unit area measurements made on Hastelloy C276 coupons after immersion in molten FLiNaK salt at 700 °C, with measurements being taken after 50, 100 and 200 hours of static immersion.

The measurements presented in Figure 6.10 show that mass was continuously lost over the 200-hour duration. Comparing this result to the oxidation study presented in Chapter 5, a significant mass loss was observed when compared with the mass gain that was observed in the oxidation study of Hastelloy C276. In an oxygen containing molten salt environment, this is likely to be caused by the formation of a non-protective oxide layer which may be soluble in the corrosive salt, resulting in the continued corrosive attack to the immersed material by the FLiNaK molten salt. This has been observed by many authors, most recently by Liu et al. [183] who added O^{2-} in the form of Li_2O to FLiNaK molten salt to understand its impact on the corrosion of Hastelloy N. Results shows that the presence of O^{2-} led to the formation of insoluble $LiCrO_2$ which was non-protective and hence did not slow the corrosion of the Hastelloy N substrate.

The mass change measurements show a linear trend, suggesting a constant corrosion rate of the substrate material in the FLiNaK molten salt. This was observed by the calculation of the corrosion rate of Hastelloy C276 in molten FLiNaK salt from the specific mass change measurements presented in Figure 6.10. The corrosion rate measurements of Hastelloy C276 at time intervals of 50, 100 and 200 hours in FLiNaK molten salt are presented in Figure 6.11.

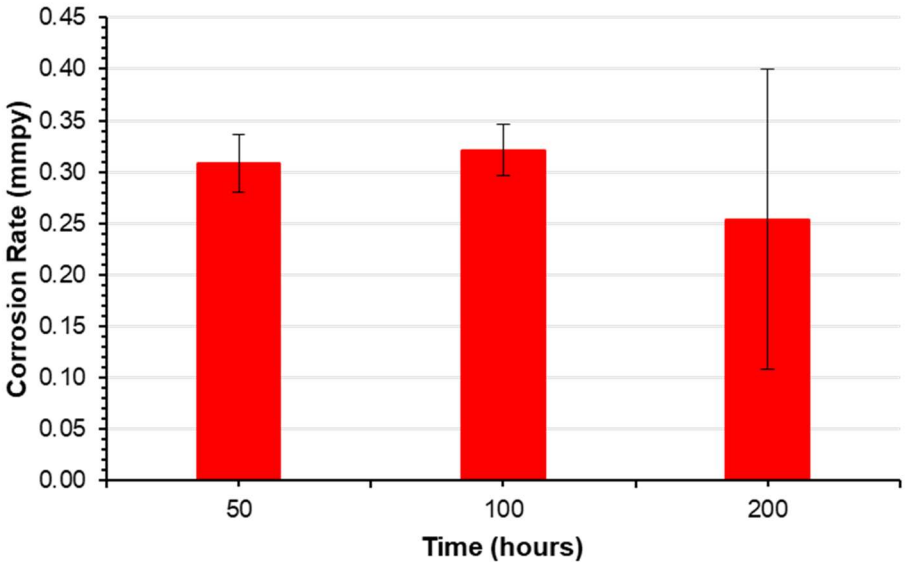


Figure 6.11 - Corrosion rate of Hastelloy C276, calculated from mass change measurements at time intervals of 50, 100 and 200 hours. Results show a consistent corrosion rate over time, with a maximum difference of 23.4% between corrosion rates measured after 100 and 200 hours of immersion.

The results presented in Figure 6.11 show a relatively constant corrosion rate over 200 hours of exposure, with there being a maximum difference of 23.4% between the average calculated corrosion rate obtained after 100 and 200 hours of immersion in molten salt. The extremities of errors bars presented in Figure 6.11 represent the maximum and minimum corrosion rates calculated from specific mass change measurements made on coupons immersed in molten FLiNaK salt after 50, 100 and 200 hours of immersion. As can be seen, large error bars are observed for corrosion rates calculated after 200 hours of immersion. However, the data presented in Figure 6.11 indicates that the corrosion rate remains approximately constant over the 200-hour test duration.

The constant corrosion rate observed in Figure 6.11 suggests that the corrosion product layer being formed is not providing sufficient protection to the underlying substrate material to protect the exposed surfaces and reduce the corrosion rate of the Hastelloy C276 coupons immersed in the molten FLiNaK salt.

Although the corrosion product layer may not be protective, its formation may be the dominant reaction taking place within the molten salt system. Based on the mass change measurements presented in Figure 6.9 and Figure 6.10 a comparison between the mass change before and after corrosion product removal is presented in Figure 6.12.

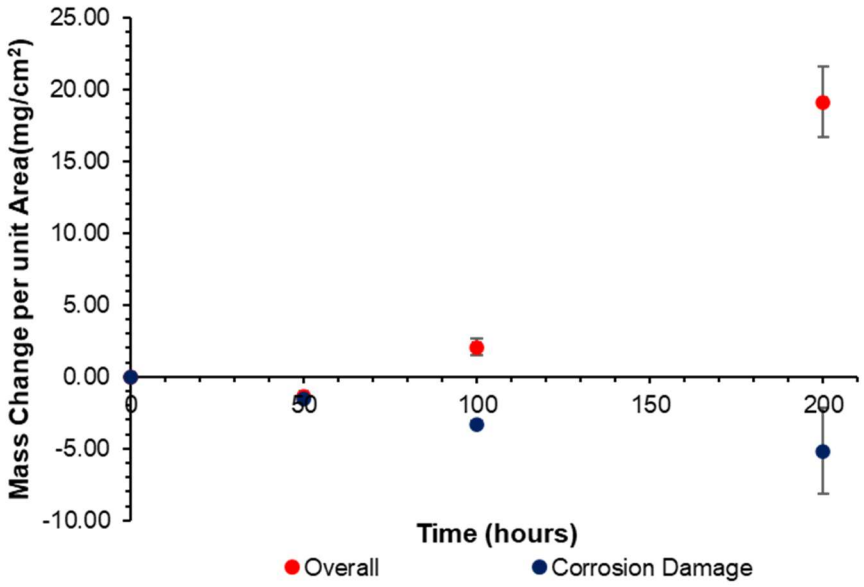


Figure 6.12 – Comparison of measured specific mass changes before and after corrosion product removal, showing synergy of corrosion product formation and corrosion, indicating change in kinetics of corrosion product layer as a function of time.

The results presented in Figure 6.12 shows that at 50 hours of immersion, the corrosion of Hastelloy C276 may be the dominant reaction taking place, with a mass loss being observed from the substrate material. A difference of 14.8% is observed between specific mass changes before and after corrosion product removal, indicating that very little corrosion product is present on the exposed surfaces after 50 hours of immersion and that after 50 hours, corrosion product formation kinetics are slow.

After 100 and 200 hours of immersion in a molten salt environment, a positive specific mass change is observed, indicating that the corrosion product growth is greater than the quantity of material removed by corrosion. Assuming that the difference between the overall specific mass change and the specific mass change due to corrosion is equal to the specific mass change of the corrosion product, the kinetics of corrosion product growth can be assessed, with a comparison being presented in Figure 6.13.

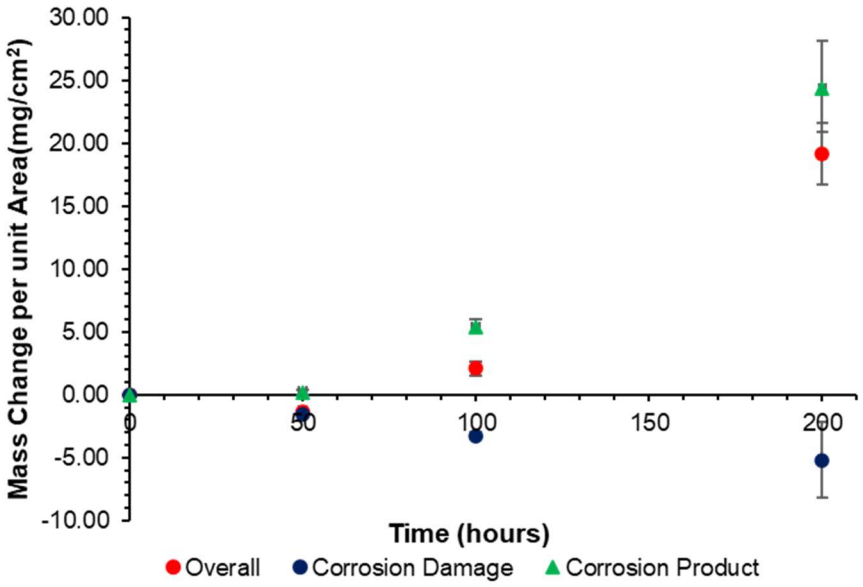


Figure 6.13 – Comparison of specific mass changes for Hastelloy C276 in molten FLiNaK salt, including overall specific mass change, specific mass change due to material loss and specific mass change due to corrosion product formation.

The specific mass change due to corrosion product formation presented in Figure 6.13 shows very similar kinetics to the overall specific mass change, with the kinetics of corrosion product formation increase with time. This is a peculiar result as the quantity of corrosion product formed is not proportional to the mass lost from the substrate material within the molten salt environment. However, to fully understand the formation of any corrosion products, additional analysis must be performed to characterise the corrosion products present on exposed surfaces after corrosion testing.

6.3.2 Characterisation of corrosion products – SEM analysis

After specific mass change measurements were made, analysis of the corrosion products and any corrosion damage to the substrate material was undertaken using SEM analysis, which was conducted on both the exposed surfaces and on cross-sections of corroded samples immersed in FLiNaK salt at 700 °C for 50, 100 and 200 hours.

SEM micrographs taken of corroded coupons of Hastelloy C276 after immersion in molten FLiNaK salt revealed distinct regions of both corrosion product and substrate on the exposed surfaces of samples. These regions were observed on coupons after each time interval and are presented in Figure 6.14.

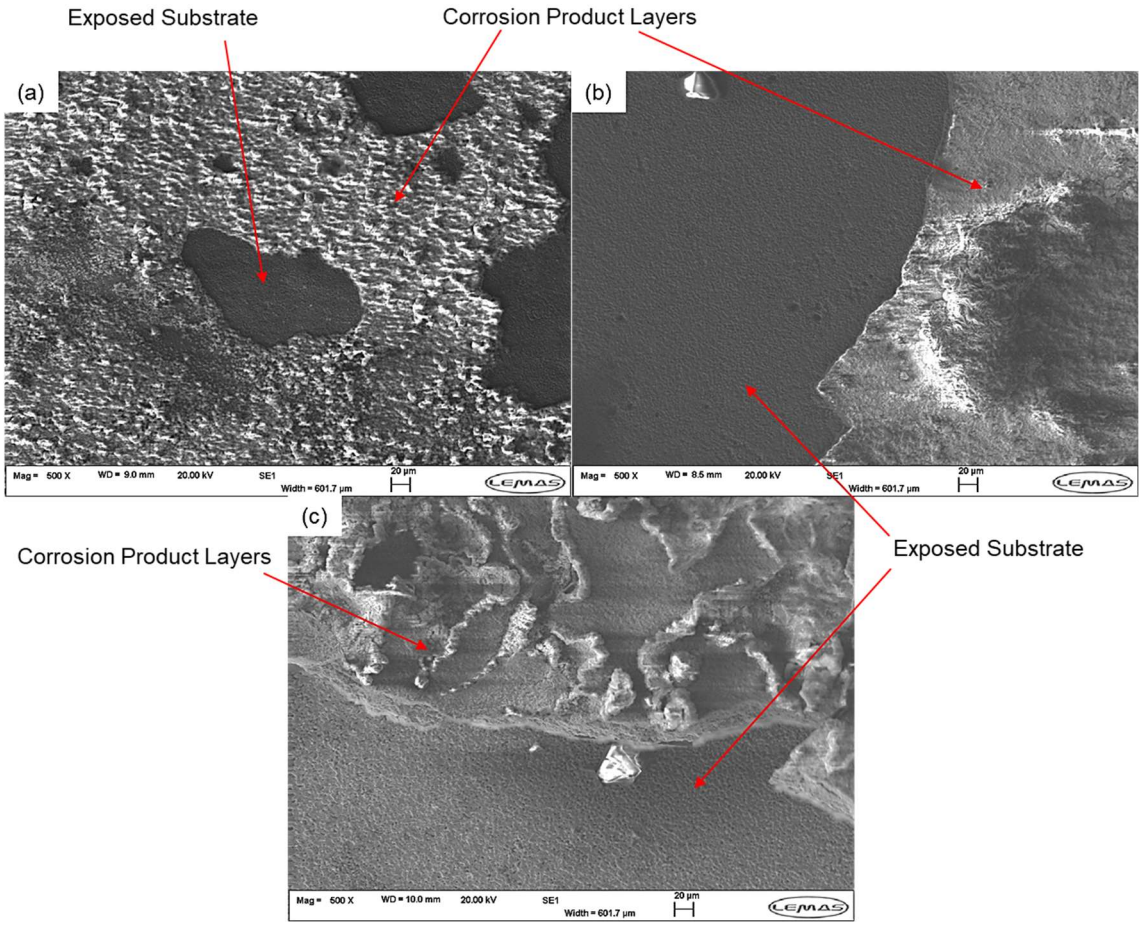


Figure 6.14 – Micrographs of the exposed surfaces of Hastelloy C276 coupons, immersed in molten FLiNaK salt for a) 50 hours, b) 100 hours and c) 200 hours at 700 °C in an air environment. Regions of corrosion product and exposed substrate are labelled.

The observed regions of exposed substrate material may be due to corrosion product removal by either dissolution of the corrosion product layer or by the physical removal of non-adherent portions of the corrosion product. Due to the thermodynamic stability of the most thermodynamically favourable corrosion product, $LiCrO_2$, physical removal of non-adherent portions of the corrosion product layer is the more likely result [133, 134]. However, if the corrosion product is Cr_2O_3, removal of the corrosion product by its dissolution into the molten FLiNaK salt may be more favourable [50].

The micrographs presented in Figure 6.14 clearly show an evolution of the corrosion product morphology as the time increases from 50 to 200 hours. To examine these changes more closely, higher magnification images of the corrosion product regions were taken. The obtained micrographs are presented in Figure 6.15.

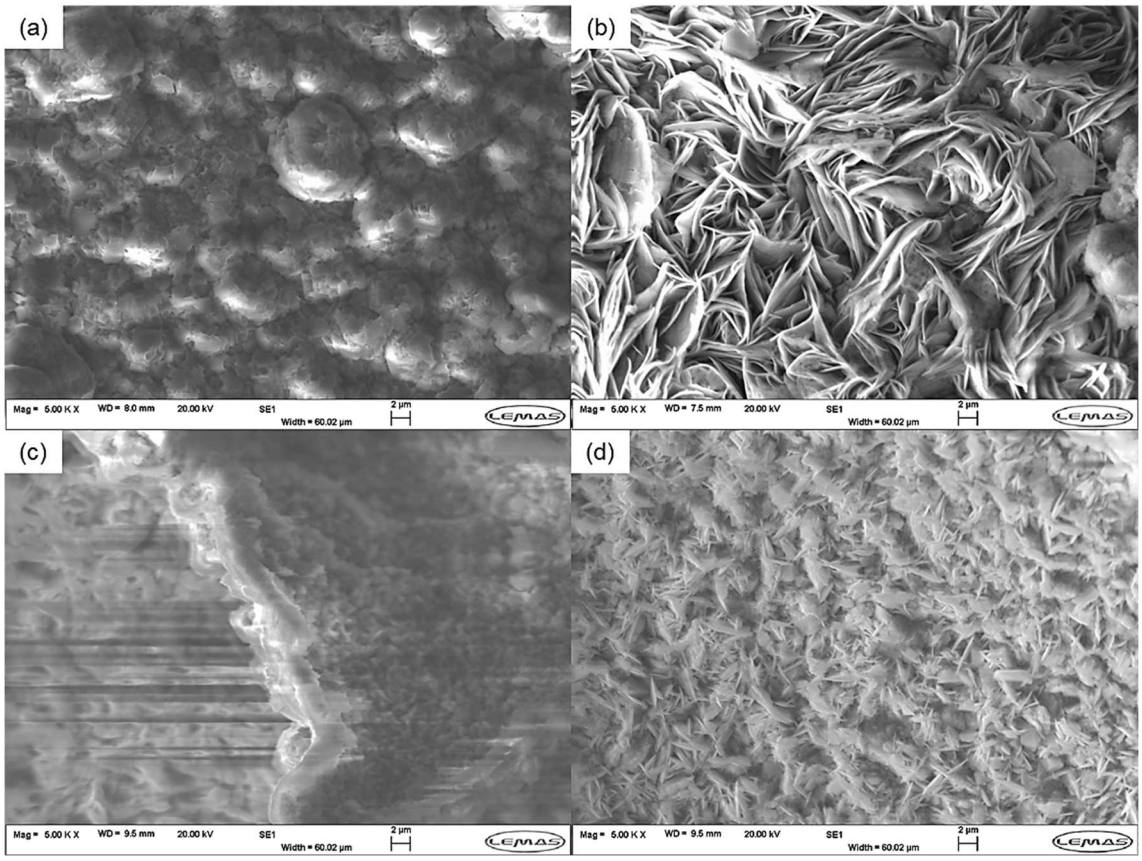


Figure 6.15 – SEM images of regions of corrosion product on the exposed surfaces of Hastelloy C276 coupons, identified after a) 50 hours, b) 100 hours, c) and d) 200 hours of immersion in molten FLiNaK salt at 700 °C in an air environment.

The SEM images presented in Figure 6.15 highlight the evolution of corrosion product layer from crystalline corrosion product to a predominantly wispy product on top of the crystalline layer, to a more compacted layer of a needle like corrosion product after 200-hours of exposure to FLiNaK molten salt. As well as the needle like corrosion product, regions of raised crystalline corrosion product formed a network surrounding the needle like corrosion product. This is consistent with formation of corrosion products at the grain boundaries of the material, where dissolution of alloying elements can be greatly accelerated during corrosion by a molten salt medium [74]. Corrosion product formation can then be facilitated by the reaction between alloying elements and O_2 at the interface between the corrosion product layer and the molten salt.

Within the corrosion product layer were the regions of exposed substrate also identified in Figure 6.14. Initial observation of the exposed substrate showed heavy corrosion damage, with a dealloying corrosion mechanism being proposed as the main form of corrosion. Images taken on coupons after 50, 100 and 200 hours of exposure are presented in Figure 6.16.

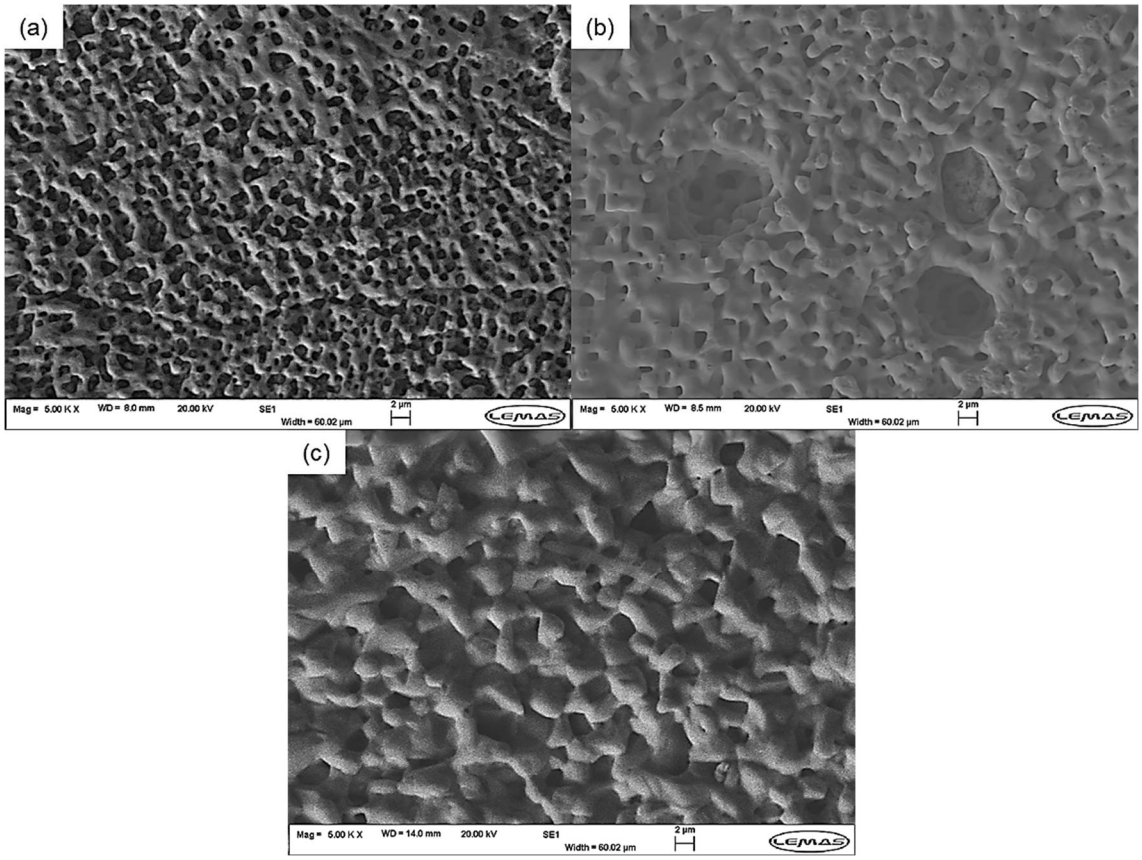


Figure 6.16 – SEM images of regions of corroded substrate, exposed by the loss of corrosion products, of Hastelloy C276 coupons, identified after a) 50 hours, b) 100 hours and c) 200 hours of immersion in molten FLiNaK salt at 700 °C.

The micrographs present in Figure 6.16 shows evidence of dealloying of the substrate material, with micrographs showing consistency with the evidence of dealloying presented by Ghaznavi et al. [44, 73] in molten chloride salt systems. Alongside evidence of dealloying, micrographs also showed much larger voids within the substrate interface which may be regions of a more aggressive corrosion mechanism, such as pitting corrosion. To examine the corrosion damage of the Hastelloy C276 coupons further, cross-sections were taken to identify any underlying corrosion damage. These cross-sections were examined using SEM, with images shown in Figure 6.17.

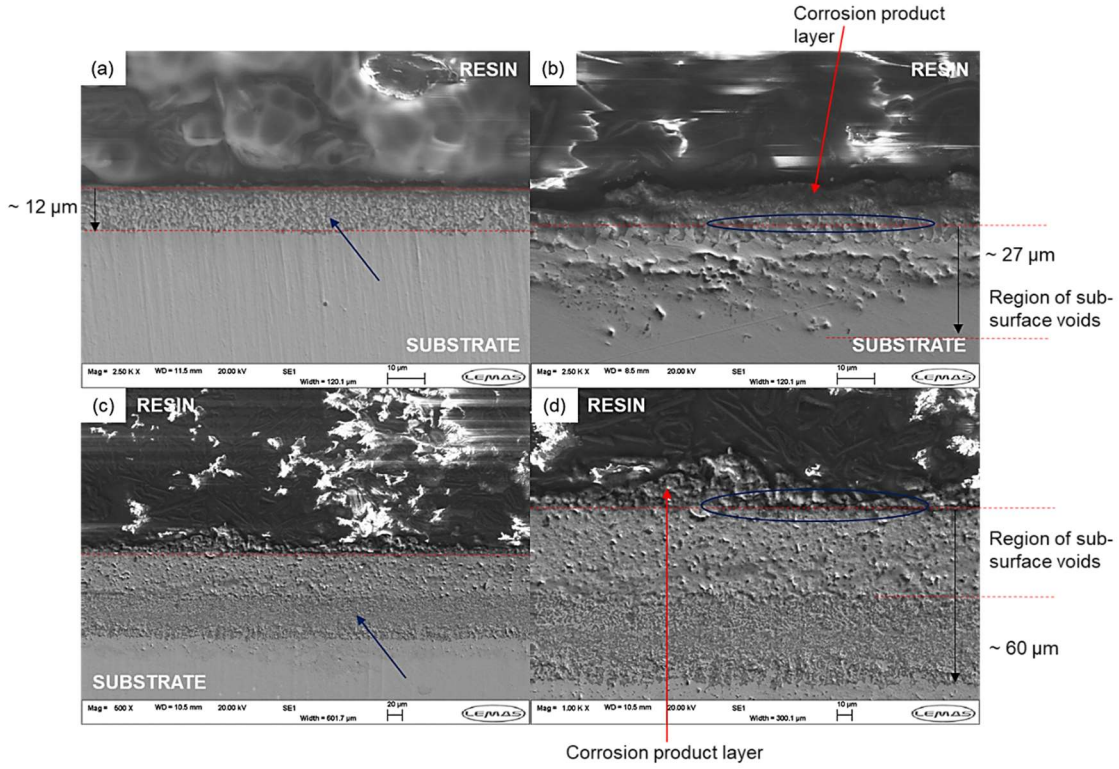


Figure 6.17 – SEM images of cross-sections of corroded Hastelloy C276 coupons after a) 50 hours, b) 100 hours and c) and d) 200 hours of immersion in molten FLiNaK salt at 700 °C at 500 and 1000X magnifications respectively. In each case, the substrate – molten salt interface is presented by a dashed red line. Corrosion product layers are labelled, with their defects circled in blue. Corrosions depths, measured from the substrate – molten salt interface is labelled, with any element depletion zones being arrowed blue.

Cross-sectional images shown in Figure 6.17 showed increasing depth of corrosive attack as well as the formation of voids within the corroded region of substrate material after 100 hours of exposure to molten FLiNaK salt. After 200 hours, sub-surface voids are observed again which is consistent with dealloying of the substrate material in molten FLiNaK. Based on the cross – sectional images, the corroded regions were measured to understand the relationship between the depth of corrosive attack and the immersion time. This result is presented in Figure 6.18.

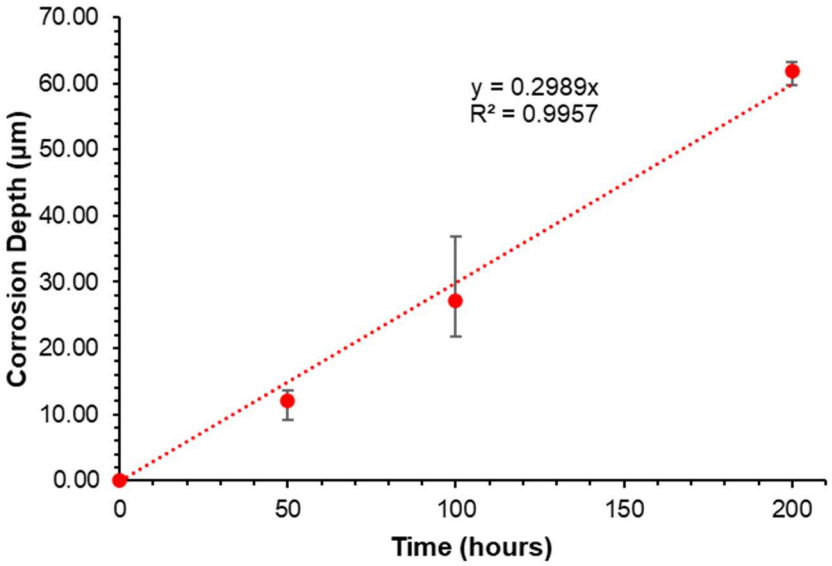


Figure 6.18 – Depth of corrosive attack with respect to time, measured from the thickness of the corrosion interfaces presented in Figure 6.17, showing a linear trend similar to that observed for the specific mass change of Hastelloy C276 coupons presented in Figure 6.10.

Measurements of corrosion depth, presented in Figure 6.18, indicate a linear relationship between the corrosion depth and time, indicating that the substrate material is being corroded at a constant rate. This corroborates corrosion rate measurements presented in Figure 6.11. This result also supports the hypothesis that the corrosion product layer formed is unprotective to the substrate material in a molten salt environment.

On coupons exposed to FLiNaK salt for 100 and 200 hours, regions of corrosion product were also observed on the cross-sectional images of the exposed surfaces presented in Figure 6.17. However, these corrosion product layers were discontinuous with regions of the underlying substrate remaining exposed to the FLiNaK molten salt due to defects such as voids and cracks within the layers. To develop a deeper understanding of the impact of corrosion on the substrate material, the regions of corrosion product and substrate presented in Figure 6.15, Figure 6.16 and Figure 6.17 were analysed using EDX analysis.

6.3.3 Characterisation of corrosion products – EDX analysis

Alongside SEM analysis, EDX analysis was performed to identify elements present in the regions of corrosion products and the regions of corrosion damage presented in Section 6.3.2. When examining corroded surfaces, point and ID, element mapping and element line scans were used to observe any elemental changes.

EDX maps of the corrosion product regions shown previously in Figure 6.16 are presented in Figure 6.19.

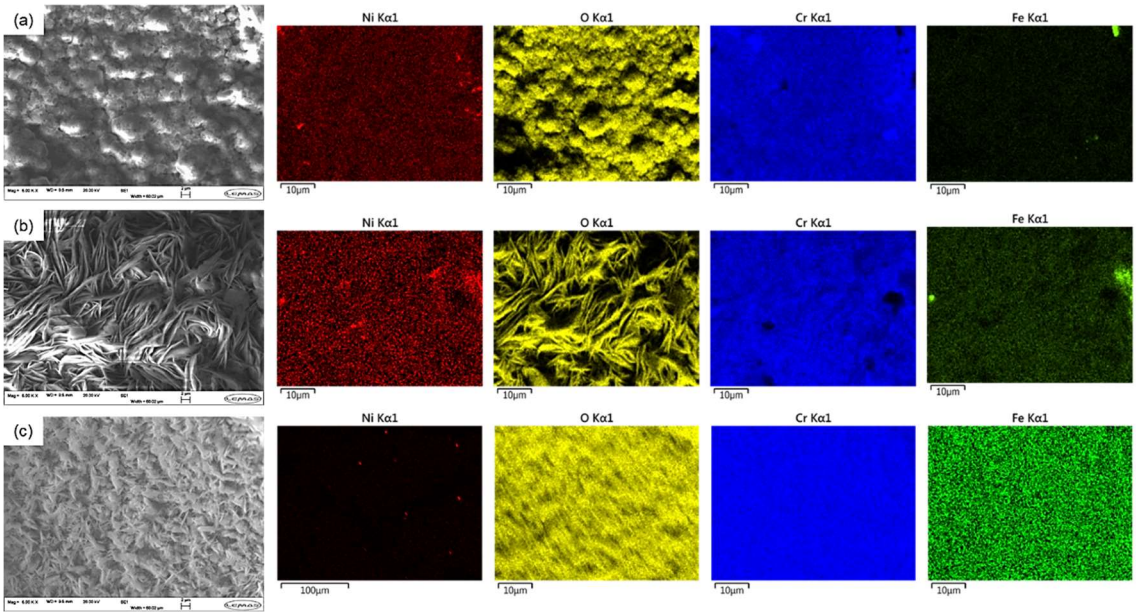


Figure 6.19 – EDX analysis of corrosion product layer after a) 50 hours, b) 100 hours and c) 200 hours of exposure of Hastelloy C276 coupons to FLiNaK molten salt at 700 °C.

Analysis of the corrosion product layers presented in Figure 6.19 show that Ni becomes depleted from the corrosion product layer with increasing exposure duration whilst Cr is consistently present along with O_2. The corrosion product layer also becomes enriched with Fe as the exposure time of Hastelloy C276 coupons increases from 50 to 200 hours due to the diffusion of Fe to the molten salt – corrosion product interface through the corrosion product layer. In this case, the increased presence of Fe may also be due to the properties of the corrosion product layer, with many corrosion products being susceptible to dissolution in a molten FLiNaK salt environment [50].

Similarly, to the EDX maps presented for the corrosion product layer shown in Figure 6.19, EDX maps were also generated for regions of corroded substrate material identified in Figure 6.16. This analysis is presented in Figure 6.20.

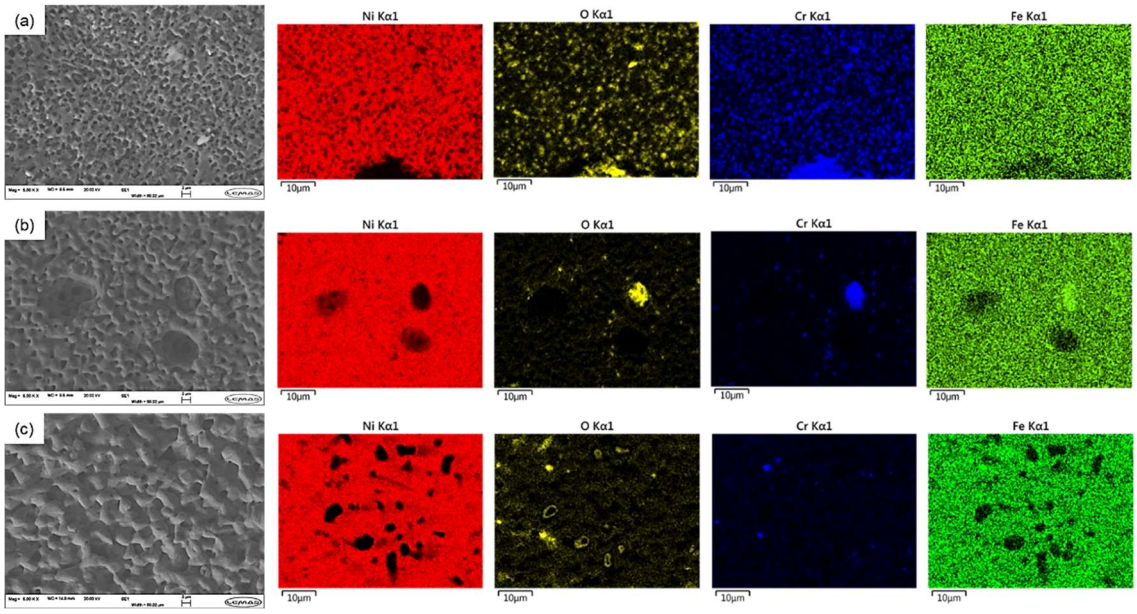
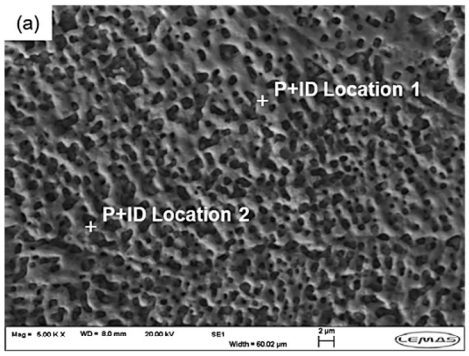
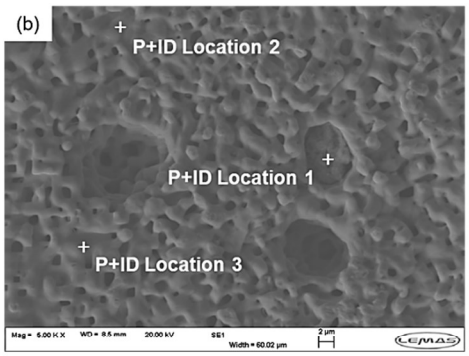


Figure 6.20 – EDX analysis of corroded substrate material after a) 50 hours, b) 100 hours and c) 200 hours of exposure of Hastelloy C276 coupons to FLiNaK molten salt at 700 °C showing consistent concentrations of Ni and Fe with depleted concentrations of Cr and O.

In Figure 6.20, the continuous depletion of Cr is observed as the exposure time increases from 50 to 200 hours. This finding was corroborated by the EDX point and ID analysis presented in Figure 6.21 which show a large reduction in the Cr concentration within the substrate material when the test durations was increased from 50 to 100 hours. After 200 hours the Cr concentration at the substrate – molten salt interface was negligible.



Element	P+ID Location 1 (wt.%)	P+ID Location 2 (wt.%)
C	0.80	1.25
O	1.66	5.93
Cl	1.81	0.24
K	0.32	0.56
Cr	9.06	12.81
Fe	2.12	1.78
Ni	83.72	76.88
Mo	0.52	0.55
Total	100.00	100.00



Element	P+ID Location 1 (wt.%)	P+ID Location 2 (wt.%)	P+ID Location 3 (wt.%)
C	0.56	0.09	
O	22.61	0.11	0.06
Si	0.26		0.02
K	0.88		
V	0.50		
Cr	57.59	2.44	1.93
Mn	1.27		0.24
Fe	6.08	3.35	3.36
Ni	10.24	93.35	94.30
Mo		0.66	0.09
Total	100.00	100.00	100.00

Figure 6.21 – EDX point and ID analysis showing large reduction in the Cr concentration present when the test duration increases from a) 50 hours to b) 100 hours. At the substrate – molten salt interface, the average Cr concentration was observed to drop from 10.94 wt.% to 2.19 wt.% with the increase in exposure time. The region corresponding to high Cr concentration in Figure 6.20b was shown to have much larger concentrations of Cr and O.

Despite showing the trend that the concentration of Cr within the substrate material decreases as a function of time, the micrographs presented in Figure 6.20 also indicate some small regions of enriched Cr within a Ni enriched matrix, particularly after 50 and 100 hours of immersion. These regions of Cr enrichment were observed to also correspond to regions of O enrichment. An example of such a region is presented in Figure 6.21b as Point and ID Location 1, which contains 57.6 wt.% Cr and 22.6 wt.% O_2.

The highlighted regions of internal Cr and O_2 enrichment are likely to be due to the formation of an internal oxide layer, formed by the inward diffusion of O_2 through the molten salt to the substrate – molten salt interface and outward diffusion of Cr to the same interface. The formation of an internal Cr – oxide layer was also observed during the high temperature oxidation of Hastelloy C276 presented in Chapter 5 which was achieved by the inward diffusion of O_2 through the Ni-matrix.

The consistent concentrations of Ni and Fe at the substrate – molten salt interface observed in Figure 6.20 and Figure 6.21 with a corresponding decrease in Cr was preferentially removed from the substrate is consistent with a dealloying corrosion mechanism, in which the role of metallic fluorides plays a vital role [70]. In a molten

salt system, the formation of NiF_2 and FeF_2 is common. Previous studies have shown that these fluorides are able to react with Cr present in the corroding material for form CrF_2, reducing Ni and Fe from 2+ oxidation state to 0, resulting in the deposition of Ni and Fe at the interface of the reaction [126]. These reactions are presented in equations 6.2 and 6.3 respectively.

$$Cr + NiF_2 \rightarrow CrF_2 + Ni \quad \textbf{6.2}$$

$$Cr + FeF_2 \rightarrow CrF_2 + Fe \quad \textbf{6.3}$$

The substitution type reactions presented in equations 6.2 and 6.3 between Cr and Ni and Fe fluorides occur due to the thermodynamic stability of CrF_2, where CrF_2 is the most stable metallic fluoride, as shown in Table 6.1. Since CrF_3 is also less thermodynamically stable than CrF_2, the reaction of CrF_3 with Cr can also aggravate the corrosion process, forming CrF_2 as shown in equation 6.4.

$$2CrF_3 + Cr \rightarrow 3CrF_2 \quad \textbf{6.4}$$

Thermodynamic analysis presented in Table 6.1 shows that CrF_2 is much more stable than other metallic fluorides that may form during the reaction of Hastelloy C276 with molten FLiNaK salt, including NiF_2 and FeF_2.

Table 6.1 – Gibbs free energy changes of metallic fluorides that may form during the reactions between Ni-based alloy and FLiNaK molten salt at 727 °C, showing that CrF_2 is more thermodynamically stable than other metallic fluorides [29].

Species	ΔG (kJ/mol)
CrF_2	-312.13
CrF_3	-302.50
NiF_2	-237.02
FeF_2	-278.236

This observation supports the continuous depletion of Cr observed from the material substrate whilst Ni and Fe become enriched at the interface between molten salt and substrate material.

To further investigate the observed depletion of Cr from the substrate material, as well as develop a further understanding of the movement of elements through the substrate material and corrosion product layer, EDX line scans were conducted on the cross-sections taken of Hastelloy C276 coupons. The results of these line scans are presented in Figure 6.22.

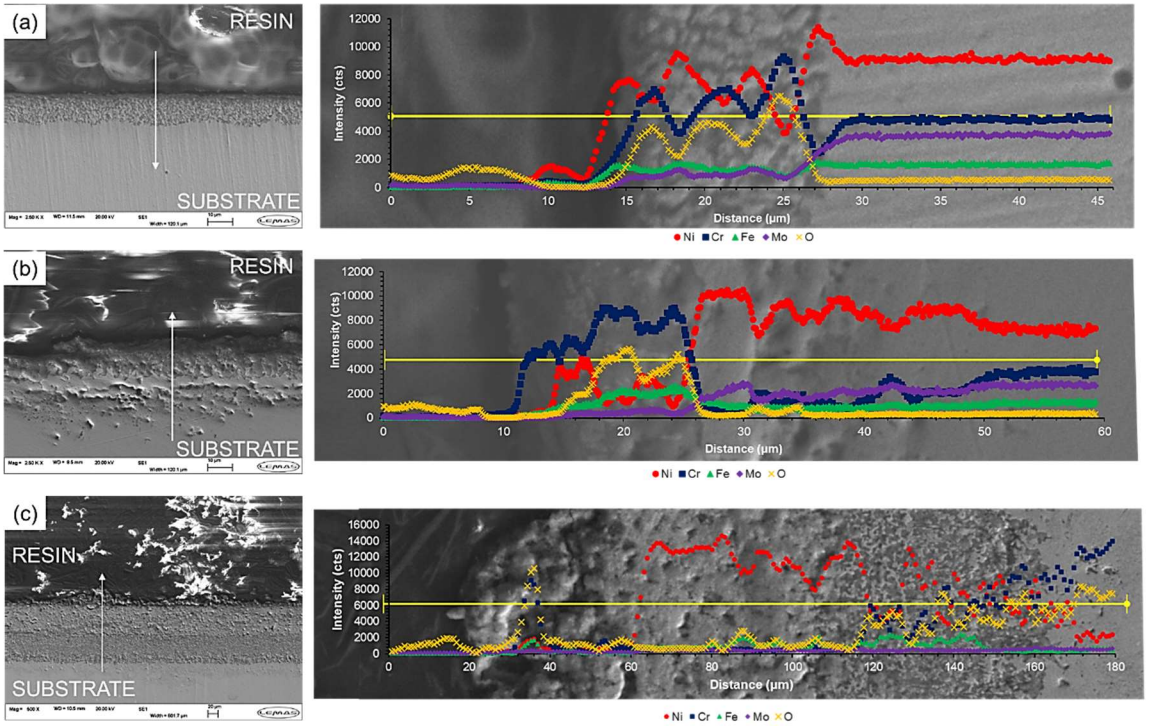


Figure 6.22 - EDX line scan analysis showing evolution of element distribution throughout the formed corrosion product layer and substrate of Hastelloy C276 exposed to FLiNaK salt for a) 50 hours, b) 100 hours and c) 200 hours at 700 °C.

The EDX line scans presented in Figure 6.22 show the evolution of the elemental distributions within the substrate and corrosion product layer when present with the distributions of Ni, Cr, Fe and Mo being monitored. After 50 hours of exposure, a region of Cr enrichment is observed within the corroded region, close to the substrate – molten salt interface. These regions of Cr enrichment are interspersed with regions of Ni depletion. The Cr enriched regions also correspond to regions of O_2 enrichment, supporting the earlier hypothesis that Cr is oxidised within the substrate material. At the molten salt – substrate interface, Ni appears to be enriched whilst Cr is depleted to a depth of approximately 2 µm, with Fe also being depleted from the bulk concentration.

After 100 hours of exposure, a region of approximately 15 µm is observed to be enriched with both Cr and O_2 which is indicative of an externally formed Cr – oxide layer, within which Ni is depleted and Fe is slightly enriched. This differs from the results at 50 hours, in which the internal oxidation of Cr was observed to be the main way in which Cr was oxidised. After 100 hours, both internal and external oxidation of Cr is observed, however, external oxidation of Cr is observed to be greater as shown in Figure 6.23.

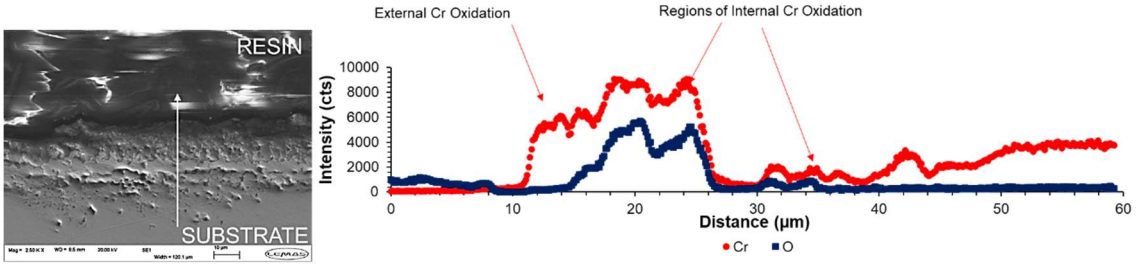


Figure 6.23 – EDX line scans of cross – section of Hastelloy C276 after 100 hours of immersion showing both internal and external oxidation of Cr. However, the result shows that the external oxidation of Cr is greater than that that occurs internally.

The greater extent of external Cr oxidation compared to internal is likely to be due to the faster outward diffusion kinetics of Cr through the corrosion product layer to the corrosion product – molten salt interface than the inward diffusion of O_2 to the substrate – corrosion product layer and hence into the Ni-based alloy. If this were the case, the Cr would be present at the corrosion product – molten salt interface where it could react and continue to form a Cr – rich corrosion product. The formation of this corrosion product then acts as a diffusion barrier to O_2 trying to diffuse through and oxidise Cr internally. Below this region of Cr and O_2 enrichment, a region of Cr depletion is observed, indicating that Cr has been removed from the alloy and reacted with O_2 within the molten salt to form a Cr – based oxide layer. Within the internal Cr depleted zone, Ni is enriched as it has been transported from the bulk to the substrate – oxide interface.

In comparison to the results obtained for 100 hours, the Cr depleted zone before the substrate – oxide interface was observed to be much larger after 200 hours of exposure, with the depletion depth being approximately 50 µm from the substrate interface. Within this Cr depleted region, Ni was enriched. Similarly, to the results obtained for 100 hours, a Cr – rich corrosion product was observed to have formed as an external corrosion product by the reaction of outwardly diffusing Cr with the inwardly diffusing O_2. However, in a result similar to that shown for 50 hours of corrosion, regions of Cr enrichment were observed below the region of Cr depletion at a depth of approximately 50 µm. The regions of internal Cr enrichment were also enriched with O_2 and depleted of Ni which is indicative of Cr oxidation within the substrate material.

In each time period, a Cr – rich corrosion product has been identified. However, in order to fully characterise the corrosion product, additional techniques alongside EDX are required. Therefore, XRD analysis of the corrosion product was performed.

6.3.4 Characterisation of corrosion products – XRD analysis

EDX analysis conducted on coupons of Hastelloy C276 allowed for the identification of elements present within the corrosion product layer and at the interface between the molten salt and the substrate material. To confirm the structures of any oxide products, present within the corrosion product layer, XRD analysis was undertaken. The diffraction peaks are presented in Figure 6.24.

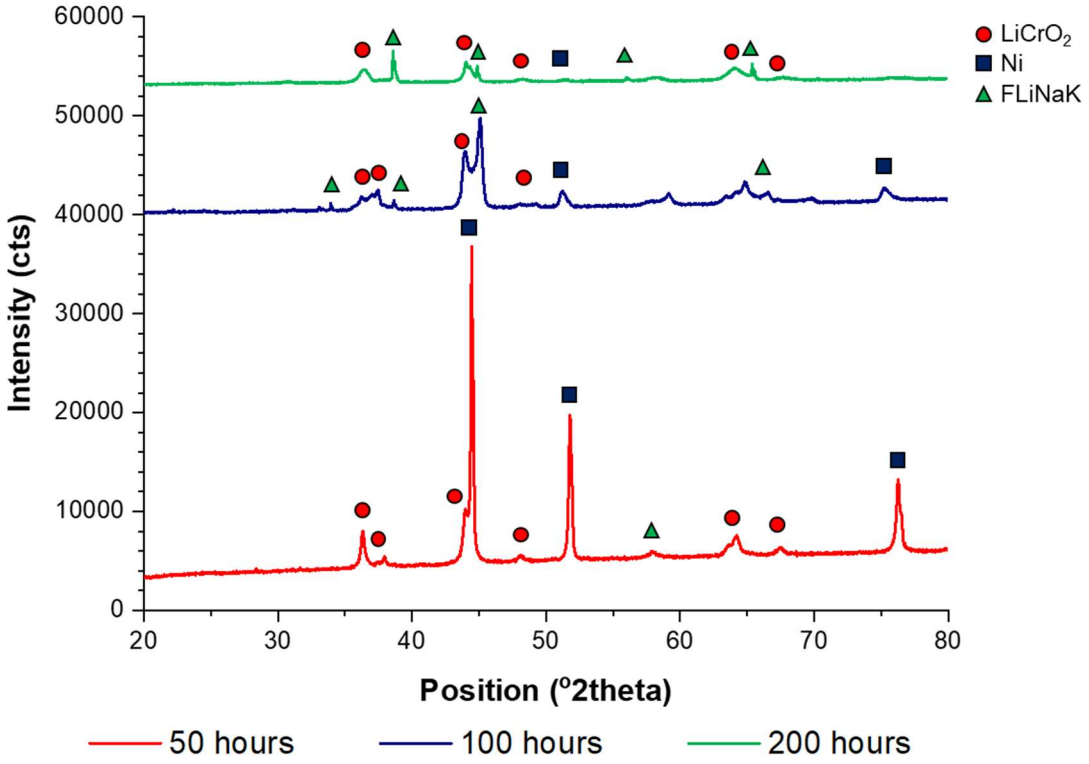


Figure 6.24 – XRD analysis conducted on coupons of Hastelloy C276 after exposure to molten FLiNaK salt at 700 °C for experimental durations up to 200 hours.

The XRD analysis presented in Figure 6.24 indicates the presence of an oxide comprised of Li and Cr. XRD peaks indicate that the Li and Cr oxide is of the structure $LiCrO_2$. This differed from the oxidation products that were observed to form in the oxidation study presented in Chapter 5. Due to the introduction of alkaline metals such as Li, Na and K, complex oxides containing these elements are able to form, as shown by the presence of $LiCrO_2$ from the XRD analysis. An oxide such as $LiCrO_2$ has been shown to form on the exposed surfaces of Ni-based alloys in molten salt environments containing O_2.

At each time interval peaks corresponding to $LiCrO_2$ were observed. The result presented in Figure 6.24 suggests that the oxide layer is being dissolved into the

molten salt layer as the intensity of the peaks associated with $LiCrO_2$ are decreasing with time.

The presence of Li within the oxide layer differs from previous EDX analysis presented throughout this chapter, as previous analysis does not show the presence of Li. This may be due to the lightweight nature of the Li atoms which, when excited by an electron, will not release a photon with a higher enough energy to be detected by EDX analysis [187]. Other peaks observed in Figure 6.24 correspond to the substrate material, which is exposed due to the dissolution of the corrosion product layer into the molten FLiNaK salt.

6.4 Experimental Results versus Numerical Predictions

Throughout this research into the molten salt corrosion of Hastelloy C276, both experimental and numerical approaches have been deployed. These methods were deployed for FLiNaK molten salt corrosion at a temperature of 700 °C. A comparison between specific mass change results obtained experimentally and predicted by the mechanistic model is presented in Figure 6.25.

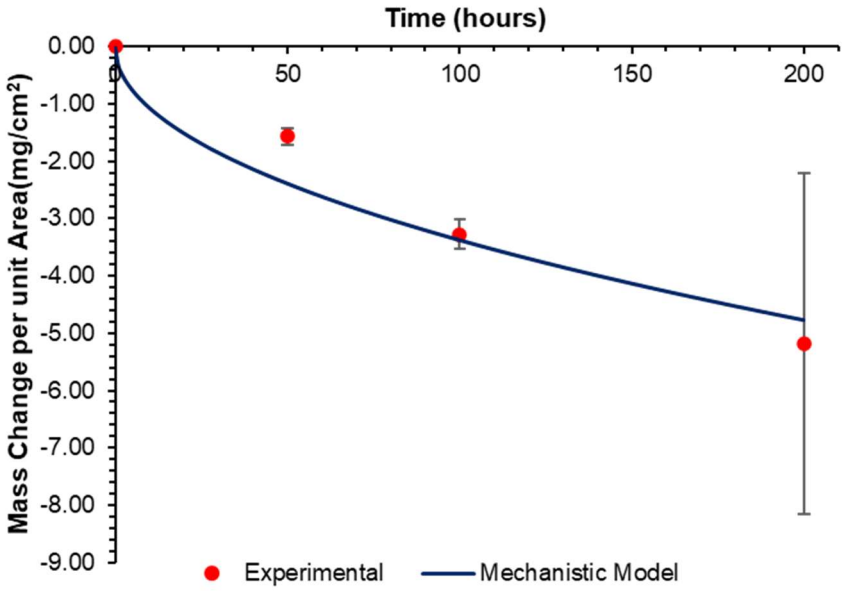


Figure 6.25 – Comparison between experimentally determined and numerically predicted mass changes for the Ni-based alloy Hastelloy C276 in molten FLiNaK salt at 700 °C for exposure times up to 200 hours.

As shown in Figure 6.25, there are some discrepancies between the predicted and experimentally determined specific mass loss at each time interval. The maximum difference between the experimental and predicted specific mass changes are observed to be at a time interval of 50 hours, where the difference is approximately

34 %. However, good agreement is observed at 100 and 200 hours of exposure, where the differences between experimental and predicted values are 2.81% and 8.71% respectively which were deemed to agree. The large error observed at 50 hours of exposure between may be due to the formulation of the predictive model assuming that the mass loss will change in a parabolic form, whereas the mass losses observed experimentally follow a linear trend.

Specific mass change measurements presented in Figure 6.25 were converted to corrosion rates in units of mmpy using equation 6.1. A comparison between corrosion rates, predicted using the mechanistic model and determined experimentally are presented in Figure 6.26.

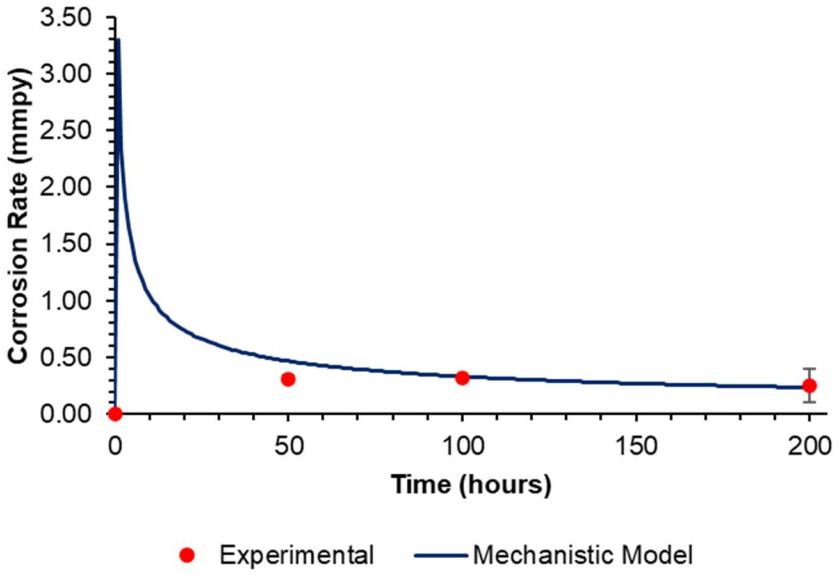


Figure 6.26 - Comparison between experimentally determined and numerically predicted corrosion rates of Hastelloy C276, exposed to a molten FLiNaK molten salt environment at 700 °C for a duration of 200 hours.

As shown in Figure 6.26, the predicted and experimentally determined values for the corrosion rate agree well at the time intervals tested, with a maximum difference of 41.0% being calculated between the experimental and prediction made by the mechanistic model at 50 hours of exposure. However, the prediction includes a large initial corrosion rate followed by a reduction as an equilibrium is achieved. This portion of the prediction has not been validated, and therefore represents a limitation of the mechanistic model. In order to fully validate the predictions made by the mechanistic model, data should be gathered at shorter time intervals to determine the initial corrosion kinetics.

As discussed previously in Section 6.2, the mass changes and corrosion rates were calculated from the predicted corrosion depths. A comparison between the

predicted and experimentally measured corrosion depths are presented in Figure 6.27.

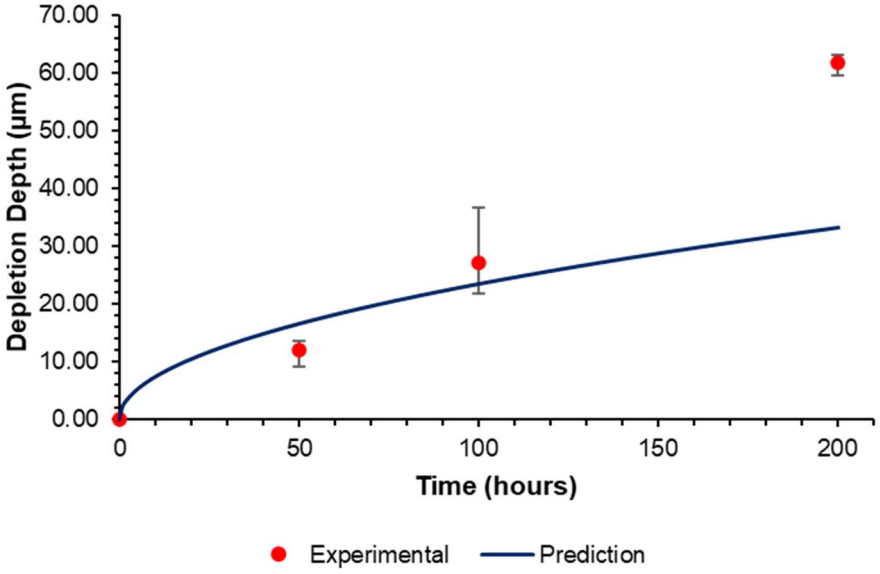


Figure 6.27 – Comparison between experimentally determined and numerically predicted corrosion depth of Hastelloy C276 coupons using the mechanistic model, exposed to a molten FLiNaK molten salt environment at 700 °C for a duration of 200 hours, showing good agreement between predicted and experimentally determined corrosion depths at 50 and 100 hours, with a large discrepancy being observed after 200 hours of immersion.

The predicted and experimentally determined values of corrosion depth presented in Figure 6.27 show good agreement at time intervals of 50 and 100 hours, with the predicted values falling within the observed experimental errors. Although good agreement is observed, the maximum difference between experimental and predicted values is observed after 200 hours of immersion, with a difference of 60.0% being calculated between the average experimental corrosion depth and the corrosion depth predicted by the empirical model.

The large discrepancy may be due to the kinetics utilised within the mechanistic model as the model is heavily based on a parabolic relationship between mass changes and the time for the oxidation portion of the model. This assumption is also consistent with Wagner's theory [75, 76], in which corrosion should be controlled by the diffusion of Cr from the substrate to the corrosion product – molten salt interface. However, this was not observed experimentally as linear kinetics have been identified.

6.5 Summary of Results

To summarise, the research results presented in this chapter are the result of experimental and numerical modelling methodologies, applied to a high temperature, FLiNaK molten salt environment. This has involved the development of the mechanistic model from Chapter 5 into a predictive model for the corrosion of Hastelloy C276 in a molten salt environment containing air.

The experiments conducted within this research were used to quantify the corrosion behaviour of Hastelloy C276, with results being expressed as a corrosion rate in units of mmpy. Results showed that the corrosion rate of Hastelloy C276 in a molten FLiNaK salt environment were consistent across the full time period of 200 hours at approximately 0.3 mmpy. The consistency of the corrosion rate across the full 200-hour experimental duration is indicative of a non-protective corrosion product layer.

This was corroborated by SEM analysis which showed distinct regions of exposed substrate material combined with regions that were covered by the corrosion product layer. SEM analysis of cross-sections also confirmed that he underlying substrate had undergone corrosion attack, with voids being observed to form at increasing corrosion depths within increasing time. EDX line scans also confirmed the dissolution of alloying elements, particularly Cr from the underlying substrate material. The mechanism for this elemental dissolution was dealloying which has been commonly observed for Ni-based alloys, particularly in halogenated salt environments.

Mechanistic modelling of the FLiNaK molten salt system was also conducted, from which predictions of corrosion rate and corrosion depth were predicted. This was achieved by developing the predictive model presented in Chapter 5 to capture the corrosion behaviour of Ni-based alloys in molten salt environments. The agreement between predicted and experimental results is good in some cases, however, the difference in kinetics between the oxidation and corrosion behaviour may be a reason as to why results of specific mass change, corrosion depth and corrosion rate differ.

Chapter 7 – Discussion

High temperature molten salt corrosion and oxidation of Hastelloy C276

In this chapter, the key findings from the results of the experimental and numerical modelling studies conducted and presented in Chapter 5 and Chapter 6 are discussed. In particular, the mechanisms by which the high temperature oxidation of Ni-based alloys occurs and the effect of oxide layer growth on the oxidation kinetics will be discussed. With regards to the molten salt corrosion of Ni-based alloys in FLiNaK salt, the mechanisms by which molten salt corrosion occurs will be discussed as well as the impact of corrosion product formation on the corrosion behaviour of Ni-based alloys.

7.1 Introduction

High temperature oxidation and molten salt corrosion experiments have been performed to develop a more robust understanding of the behaviour of Hastelloy C276 in these environments and to understand the synergy between these processes in an oxygen containing environment. Findings from this research have direct implications for the nuclear industry and provides unique insight into the material degradation mechanisms that structural materials may undergo in MSR environments.

The high temperature oxidation and molten salt corrosion behaviour of Hastelloy C276 were completed in Chapter 5 and Chapter 6. High temperature oxidation tests, performed at 700 °C showed parabolic oxidation kinetics for Hastelloy C276 over the time period of 0 to 200 hours. In a molten FLiNaK salt environment at 700 °C, specific mass losses followed a linear trend due to corrosion, with a non-proportional increase in the mass of corrosion product being observed with respect to time. The presented results in the aforementioned chapters will be discussed throughout this chapter. This will include a discussion on the oxidation and corrosion behaviours individually, before discussing the correlations that exist between the two degradation processes.

To accompany the experimental work, numerical methods were deployed to predict the high temperature oxidation and molten salt corrosion characteristics of Hastelloy C276. Similarly, to the experimental studies, the results of these models were presented in Chapter 5 and Chapter 6. This section will discuss the results

obtained from the empirical and mechanistic models and provide reasoning for their agreement with the experimental results obtained throughout this research. This chapter also aims to discuss whether the empirical and mechanistic modelling methodologies used are effective in predicting the corrosion and oxidation behaviour of Ni-based alloys. In summary, the objectives of this chapter were to discuss:

- The oxidation kinetics of Hastelloy C276 and how they are influenced by oxide layer growth.
- The mechanisms by which metallic oxides are observed to grow in an air containing environment and how this growth influences specific mass changes.
- The success of using numerical modelling approaches in predicting the diffusion of alloying elements, oxidation, and corrosion behaviour of Ni-based alloys in molten salt environments.
- The mechanisms of molten salt corrosion and the impact of molten salt corrosion on material degradation
- The significance of corrosion product layer formation on the corrosion behaviour of Hastelloy C276 in molten fluoride salt environments.

7.2 High temperature oxidation mechanism of Hastelloy C276

To enhance understanding of the high temperature oxidation mechanism of Hastelloy C276, isothermal high temperature oxidation experiments have been conducted on coupons of Hastelloy C276 in a dry air environment at 700 °C. Experimental trials have been conducted over time periods of 50, 100 and 200 hours, with experimental results being supported by the development of predictive models using empirical and mechanistic methods under the same temperature and time conditions. In each case, the oxidation rate was quantified by measuring or predicting the mass change due to oxide growth as a function of time. Similarly, the total oxide layer thicknesses were measured or predicted to enhance the understanding of oxide layer growth over time.

The experimentally determined mass changes showed that the oxidation kinetics of Hastelloy C276 slowed with respect to time, indicating that the oxidation rate could be characterised using a parabolic rate law, with a corresponding K_P value. This same result was observed for the predictive models. A summary of the oxidation rates for Hastelloy C276 in a dry air environment, calculated using the experimental and predictive methods, are provided in Table 7.1.

Table 7.1 – Summary of experimentally determined and numerically predicted values of specific mass change, K_P and oxide layer thickness for Hastelloy C276 in a dry air environment at 700 °C after 200 hours of exposure.

Calculation Method	Specific Mass Change (mg/cm^2)	K_P ($mg^2/cm^4/s$)	Total Oxide Layer Thickness (μm)
Experimental	0.4300	$2.57x10^{-7}$	6.74
Empirical Model	0.4555	$2.88x10^{-7}$	7.66
Mechanistic Model	0.3948	$2.17x10^{-7}$	7.15

As presented in Chapter 5, differences of 5.76% and 8.54% were observed between the experimental specific mass change measurements and predictions made by the empirical and mechanistic models, respectively. Differences were observed to be larger between K_P values with differences of 11.4% and 16.9% being observed between experimentally derived K_P values and those predicted by empirical and mechanistic models.

Experimental and predictive modelling results indicated that the high temperature oxidation of Hastelloy C276 followed parabolic oxidation kinetics and is controlled by the growth of the oxide layer and the diffusion of species through the oxide layer. This could be related to the outward diffusion of metallic ions to the oxide – air interface, or the inward diffusion of ions to oxidise alloying elements within the oxide layer, at the substrate – oxide interface or internally within the substrate. Therefore, understanding the processes by which the oxide layer grows, is key to developing a mechanistic understanding of the oxidation process.

7.2.1 Effect of oxide layer formation on oxidation kinetics

In the case of metal oxidation, oxide layer formation is dependent on the transport of species to the interface between the substrate and the oxidising environment. For oxidation to occur, the proposed reactions of oxide formation must also be thermodynamically favourable. However, for parabolic oxidation kinetics, over time, the oxidation rate becomes dependent on the diffusion of the species to the oxide – air interface, where species must diffuse through the oxide scale. Due to the oxide scale, which acts as a diffusion barrier, the rate of diffusion of species to the oxide - air interface determined the rate of oxidation. The diffusion of species to the oxide – air interface reduces as the diffusion barrier increases, and hence the oxidation rate is observed to slow over time. This process is presented schematically in Figure 7.1.

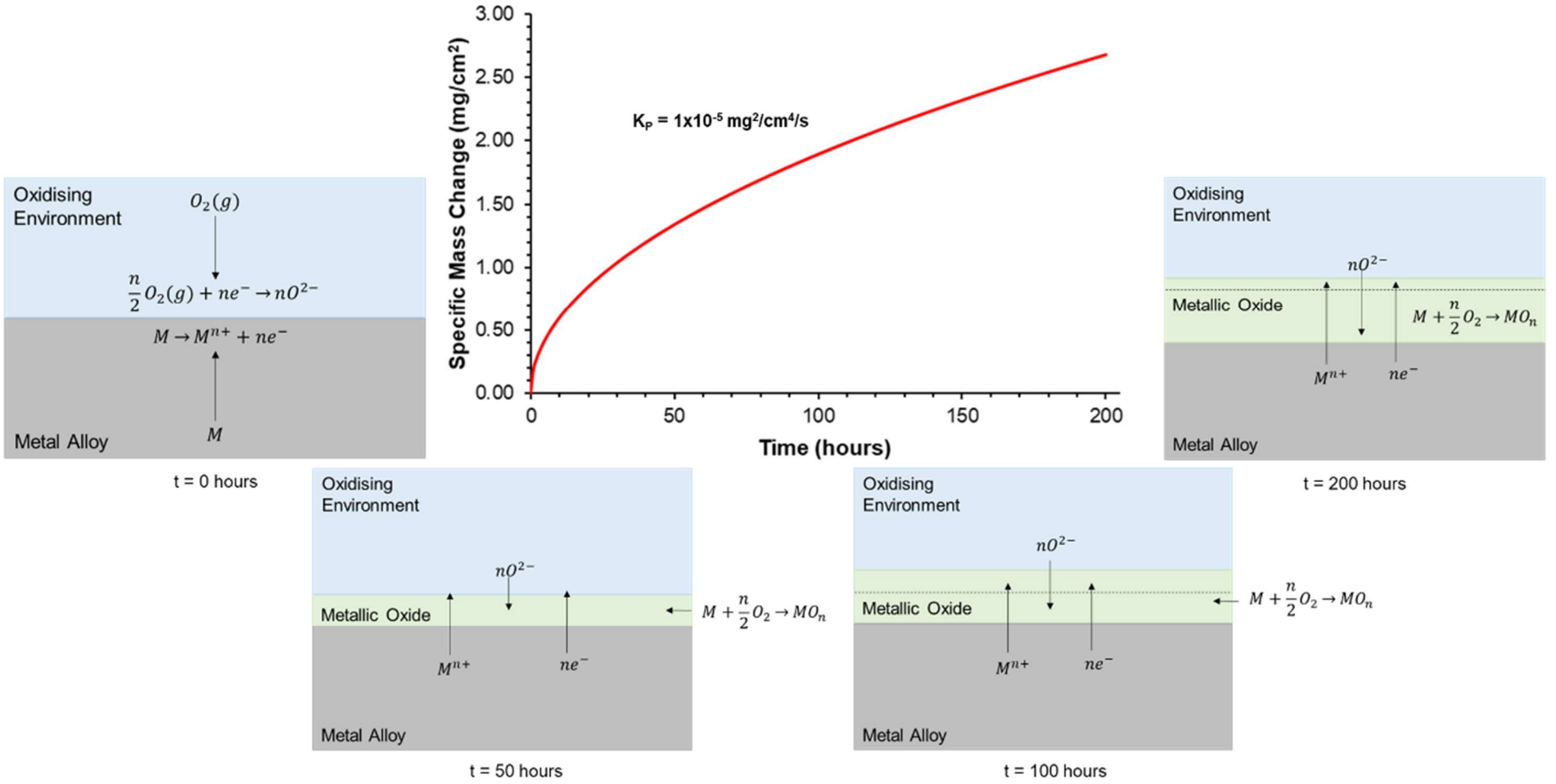


Figure 7.1 – Schematic showing process of alloy oxidation in high temperature environment, illustrating changes in the oxidation rate with increasing oxide layer thickness using an arbitrary K_P value of 1x10^{-5} mg^2/cm^4/s.

Figure 7.1 shows the outward diffusion of the alloying elements to the oxide – air interface, resulting in their reaction with O_2 to form a metallic oxide layer. Figure 7.1 also illustrates the inward diffusion of O_2 through the oxide layer to the substrate – oxide interface where oxidation of alloying elements can also occur.

When assessing the composition of the formed oxide layer, diffusion of Ni in a predominantly NiO layer is faster than Cr, which is shown by its greater diffusion coefficient in Table 7.2.

Table 7.2 – Diffusion coefficients for Ni and Cr in a NiO layer at 700 °C, showing the faster diffusion kinetics of Ni [188, 189].

Species	Diffusion Coefficient in NiO (cm^2/s)	Reference
Ni	$1.42x10^{-15}$	[188]
Cr	$3.20x10^{-16}$	[189]

As a result of its greater diffusion coefficient, shown in Table 7.2, Ni will diffuse to the oxide – air interface faster than Cr will, hence the outer layer is most likely to be NiO. This observation is corroborated by experimental analysis undertaken in this thesis and presented in Figure 7.2, which shows a NiO outer oxide layer at each time interval of 50, 100 and 200 hours, with a Cr_2O_3 inner layer.

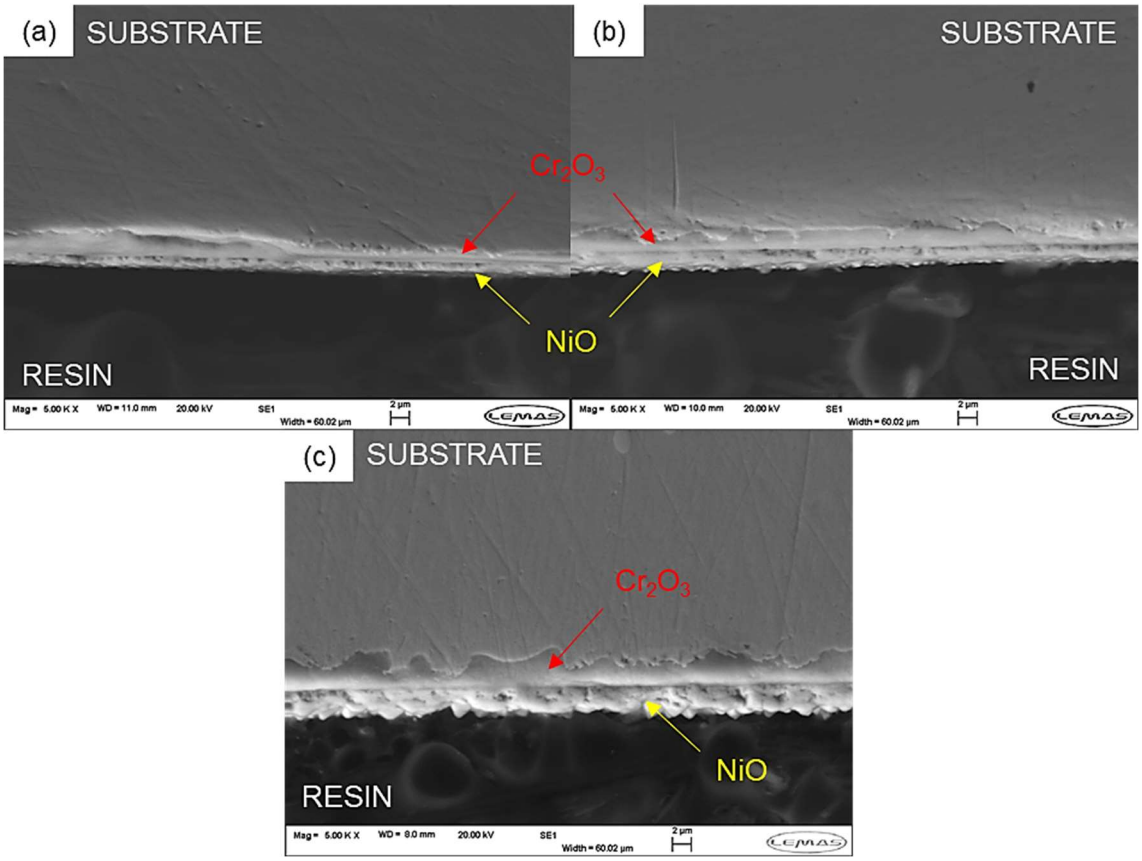


Figure 7.2 – SEM analysis of cross-sections of Hastelloy C276 exposed to a dry air environment at 700 °C for durations of 50, 100 and 200 hours, highlighting the different oxides present within the oxide layer showing a NiO outer layer and Cr_2O_3 inner layer with a $NiCr_2O_4$ layer being observed at longer time intervals.

Figure 7.2 shows that Cr_2O_3 formation is achieved by internal oxidation i.e., oxidation of Cr within the substrate material. This is corroborated by EDX line scans which show oxygen present within the substrate material. Internal oxidation occurs when the concentration of species at the oxide – air interface is lower than the critical concentration required for an oxide to form. This occurs as a result of the slower diffusion kinetics of species through the substrate material to the substrate – air interface when compared with the diffusion kinetics of O_2 through the same substrate [190].

As well as the continuous growth of the external NiO layer, the inner layer of Cr_2O_3 is also observed to increase in thickness. This is achieved by the inward diffusion of oxygen through the oxide layer, towards the substrate – air interface as shown in Figure 7.1. This results in the oxidation of alloying elements at this interface. In a similar way to the diffusion of species to the oxide – air interface, the growth of the oxide layer also impacts the diffusion of oxygen to the substrate – oxide interface, resulting in a slowing of the oxidation rate.

7.2.2 Effect of diffusion behaviour on oxide layer growth

As shown throughout Chapter 5, the oxides formed during the oxidation of Hastelloy C276 were composed predominantly of Ni and Cr. It has been theorised that this is due to their faster diffusion properties when compared with other alloying elements. In the case of Hastelloy C276, Ni and Cr have been shown to diffuse faster within the Ni-matrix of Hastelloy C276 than other alloying elements such as Fe and Mo [82, 173-176]. This results in a greater concentration of these species being present at the interface with air where they can be oxidised.

This was supported during the predictive modelling of concentration changes of Hastelloy C276 as a function of time using the mechanistic modelling approach. The diffusion properties of alloying elements were identified in literature and used to predict compositional changes within the alloy. Differences in the concentrations of alloying elements between the bulk material and the substrate – air interface were expressed as a concentration deviation and plotted against the distance from the substrate – air interface. The concentration deviation was calculated as defined by equation 7.1, where the defined concentrations were obtained from the regions as shown in Figure 7.3.

$$Concentration\ Deviation = \frac{C_b - C_i}{C_b} \qquad \textbf{7.1}$$

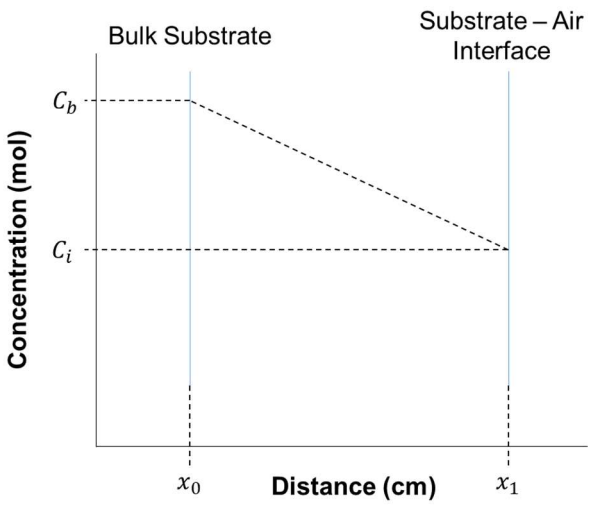


Figure 7.3 – Schematic showing concentration changes of an arbitrary alloying element within an alloy, with defined concentrations relating to the concentration deviation calculation defined in equation 7.1, with C_{BS} and C_i representing the bulk and interfacial concentrations of an arbitrary alloying element.

The concentration deviations of Ni, Cr, Fe and Mo were the main focus of this study as they are the main constituents of the Hastelloy C276 alloy. Their concentration deviations are compared at time intervals of 50, 100 and 200 hours in Figure 7.4

and show that the concentrations of Ni and Cr differ the most from their respective initial concentrations when compared with Fe and Mo.

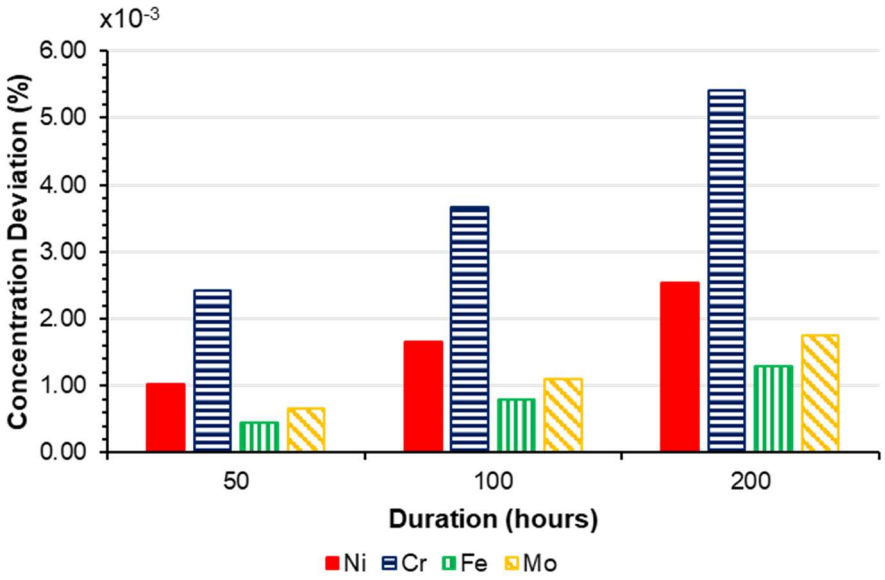


Figure 7.4 – Bar chart showing concentration deviation from initial concentration, highlighting the concentration changes of Cr and Ni are greater than those of Fe and Mo.

This finding is also corroborated by predictions of elemental depletion depth, shown by Figure 7.5 which shows concentration deviation from the initial concentration present in the alloy for Ni, Cr, Fe and Mo at distances from the substrate – air interface.

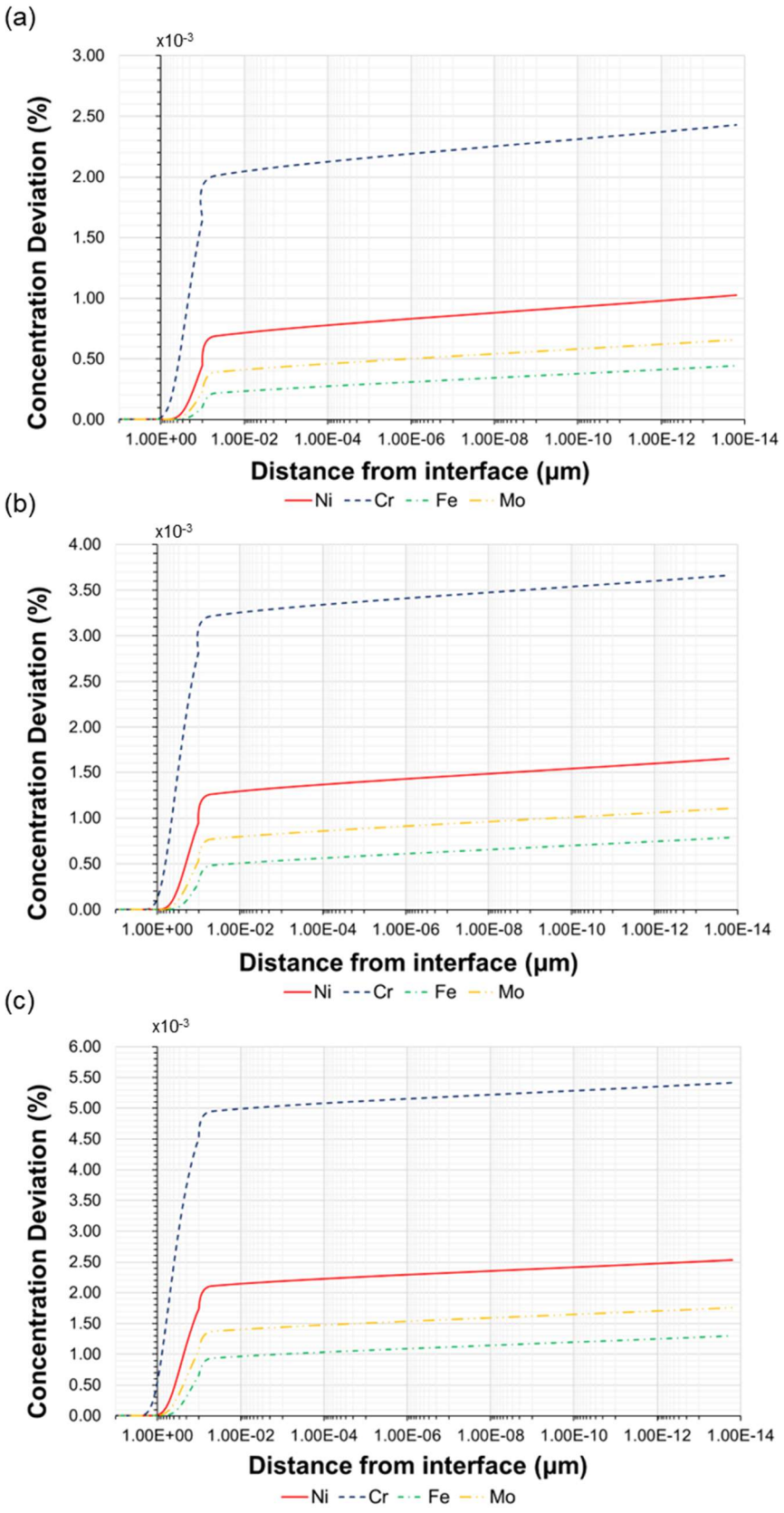


Figure 7.5 – Comparison of concentration changes of Ni, Cr, Fe and Mo as a function of distance from the substrate – air interface, showing Ni and Cr are more greatly depleted from the substrate when compared with Fe and Mo at time intervals of a) 50 hours, b) 100 hours and c) 200 hours.

The result presented in Figure 7.5 shows that as well as having the greatest concentration deviation, Cr and Ni also diffuse more rapidly to the substrate – air interface, with both elements having to diffuse from deeper within the substrate material then Fe and Mo. This can be attributed to their faster diffusion properties in a Ni-matrix compared with Fe and Mo.

Over time, the factor limiting oxide growth becomes the diffusion of species within the oxide layer and their transport to the oxide – air or the substrate – oxide interface. When investigating the growth of the Cr_2O_3 layer, cross-sectional analysis of oxidised coupons showed that Cr was enriched at the substrate – oxide interface, along with O. Ni is also observed to be enriched externally as previously discussed. This is suggestive of Cr oxidation within the substrate material, where Cr_2O_3 is formed by internal oxidation. As a result, it may be concluded that the oxidation of Cr to Cr_2O_3 is governed by the inward diffusion of O_2 to the substrate – oxide interface, where there is an abundance of Cr due to its fast diffusion properties in a Ni-matrix. This is shown by the concentration changes predicted by the mechanistic model in Figure 7.5, which shows Cr diffuses most rapidly to the substrate – air interface.

An example of this is shown in Figure 7.6, which shows inward diffusion of O_2 to the substrate – oxide interface. The oxidation of Cr is also observed after 100 hours of exposure to a dry air environment at 700 °C, where Cr is observed to be enriched at the substrate – oxide interface.

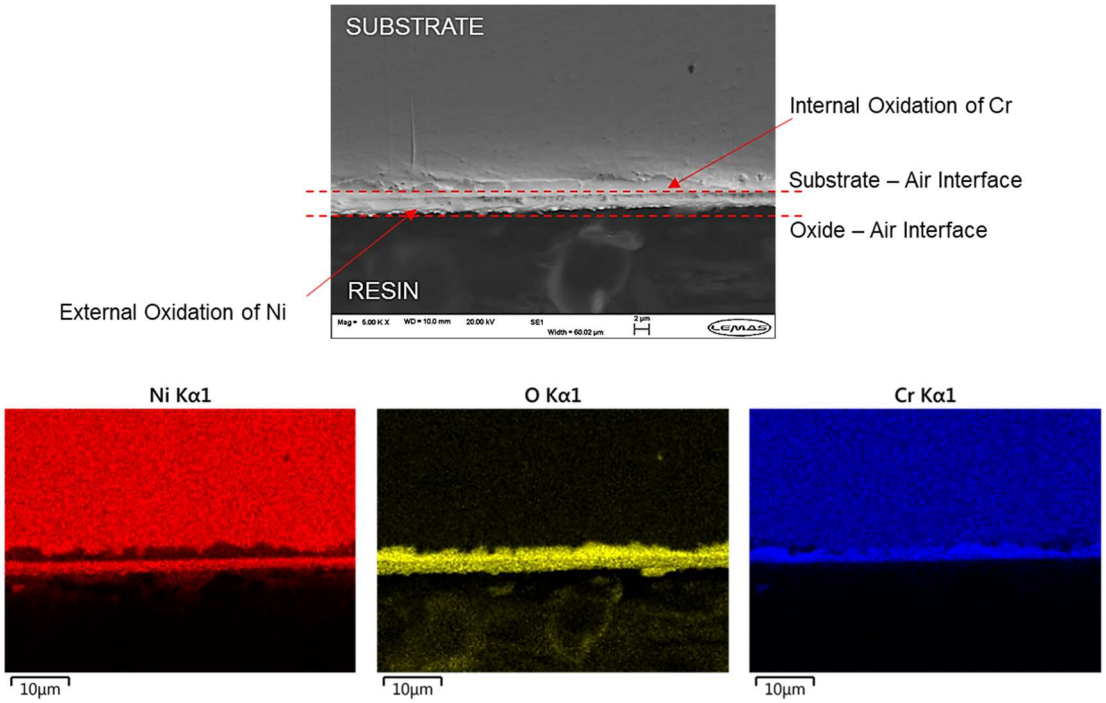


Figure 7.6 – EDX maps of cross-section of Hastelloy C276 exposed to a dry air environment for duration of 100 hours with key interfaces labelled showing internal oxidation of Cr to Cr_2O_3 and external oxidation of Ni to NiO.

The findings presented in Figure 7.6 were also corroborated by EDX line scans which highlight the movement of elements throughout the substrate and the oxide layer. EDX line scans showing the profiles of Ni, Cr and O after 100 hours of exposure of Hastelloy C276 to a dry air environment are presented in Figure 7.7 and shows the presence of O within the substrate material within a region of Cr enrichment at the substrate – air interface.

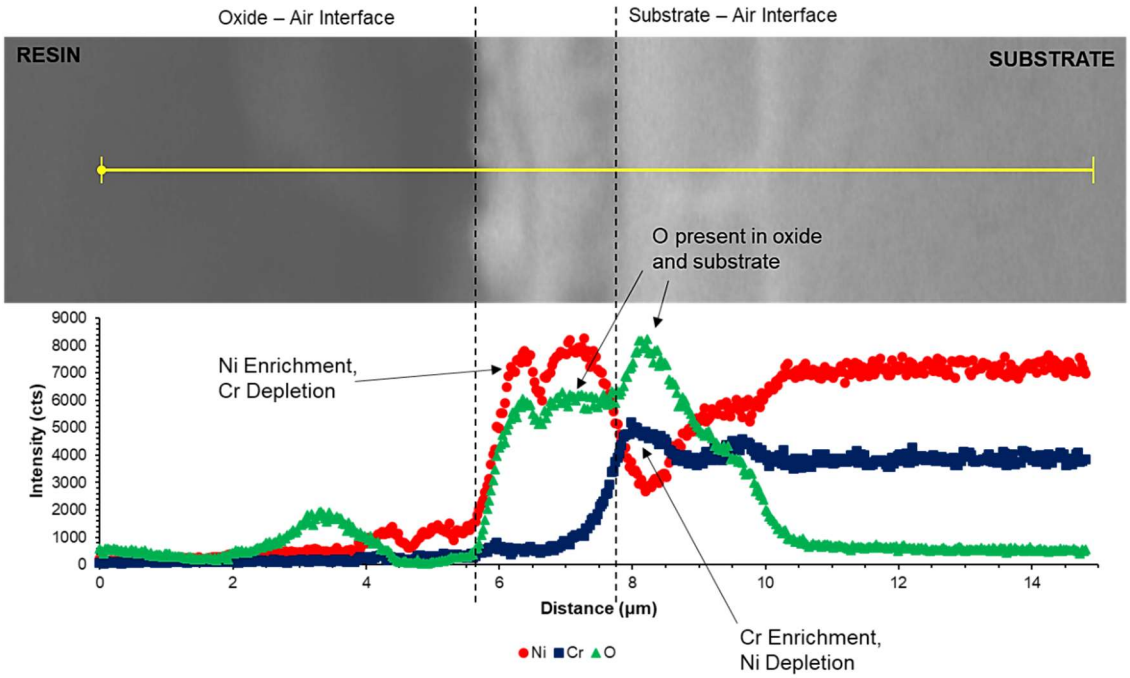


Figure 7.7 – EDX line scans of cross-section of Hastelloy C276 exposed to a dry air environment after 100 hours of exposure showing diffusion of O into the substrate, enrichment of Cr at the substrate – air interface and enrichment of Ni within the external oxide layer.

Line scans presented in Figure 7.7 show regions of O enrichment, both within the oxide layer, corresponding to the region of Ni enrichment, and within the substrate material at the substrate – air interface. This result shows that Ni has diffused outward from the substrate material to form an external oxide scale from its reaction with O. The region of Cr enrichment is within the substrate material at the substrate – oxide interface, with no Cr being observed within the oxide layer. This confirms that Cr is internally oxidised by its reaction with O which reaches the substrate – oxide interface by the process of inward diffusion. The rates of oxide growth with therefore be determined by the diffusion of Ni and O through the oxide layers.

To determine the rates of oxide growth, the thicknesses of the NiO and Cr_2O_3 layers presented were measured at each time interval. Measurements of the oxide layer thicknesses, presented in Figure 7.8, showed that the thickness of Cr_2O_3 increases by 107.8% from 50 to 200 hours of exposure and NiO by 101.4%.

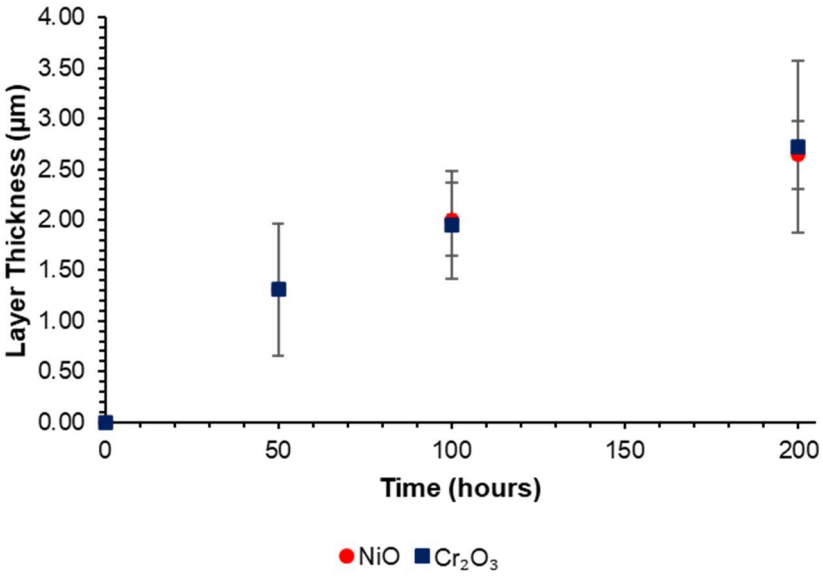


Figure 7.8 – Graph showing growth of Cr_2O_3 and NiO layers as a function of time, with Cr_2O_3 thickness increasing by 107.8% from 1.31 µm to 2.72 µm and NiO by 101.4% from 1.31 µm to 2.64 µm.

Figure 7.8 shows that the growth of both oxides follows a parabolic relationship and grow at very similar rates. The parabolic nature of the oxide growth is expected as the formation of both types of oxide are controlled by the diffusion of species to either the substrate – oxide interface for Cr_2O_3 growth or the oxide – air interface for NiO growth. Parabolic oxidation kinetics were confirmed by plotting the square of oxide layer thickness against time. This is shown in Figure 7.9.

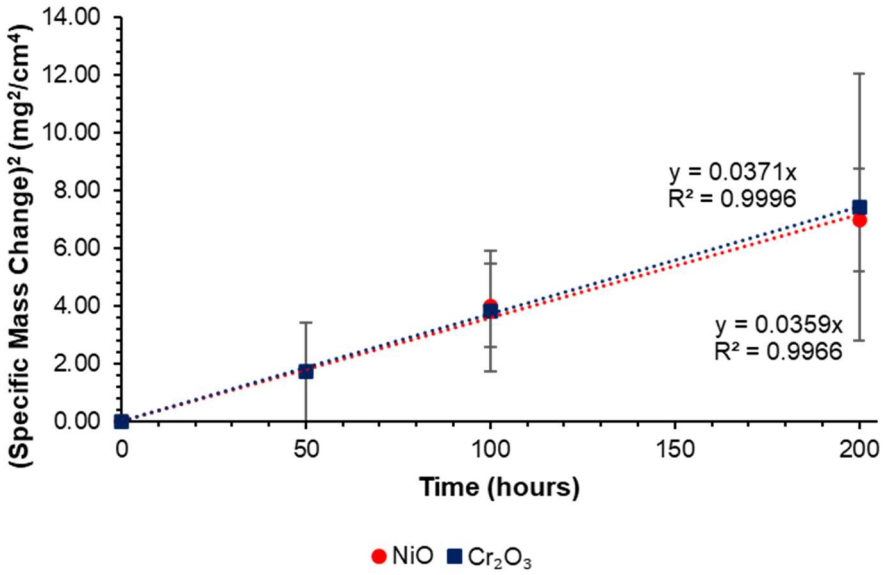


Figure 7.9 – Plot of square of oxide layer thicknesses for NiO and Cr_2O_3 against time, showing strong linear relationships, confirming parabolic oxidation kinetics of both oxide layers. Growth of oxides can be characterised by K_P values of 7.20×10^{-5} and 7.61×10^{-5} $\mu m^2/s$ for NiO and Cr_2O_3, respectively.

Although the thicknesses of each layer only differ by 3.07% after 200 hours of exposure to a dry air environment at 700 °C, the result presented in Figure 7.8 suggests that Cr_2O_3 grows at a faster rate than NiO as a greater increase in the thickness of Cr_2O_3 is observed when compared with the NiO layer. The similarity in oxide layer thicknesses observed experimentally were also observed within the mechanistic model, which showed similar specific mass changes as a function of time, as shown in Figure 7.10, which compares experimentally determined and predicted layer thicknesses of Cr_2O_3 and NiO, assuming that the respective oxide layers are non-porous and completely cover the exposed coupons.

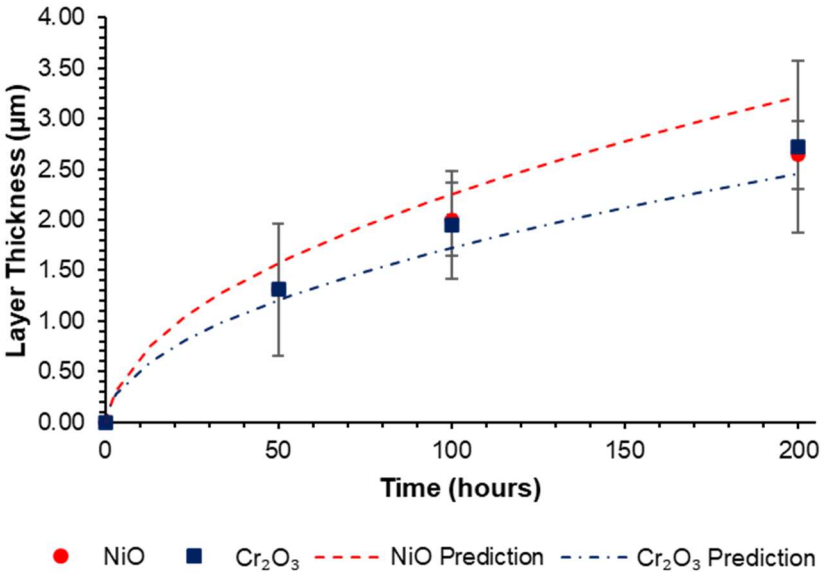


Figure 7.10 – Comparison of experimentally measured Cr_2O_3 and NiO layer thicknesses and those predicted by the mechanistic model showing similar oxidation kinetics of both oxides. Mechanistic model predictions are observed to fall within experimental errors.

The predictions of Cr_2O_3 and NiO thickness follow the same trend as the experimental values, with predictions presented from the mechanistic model lying inside the experimental errors presented using error bars for the measured layer thicknesses for Cr_2O_3 and NiO in Figure 7.10.

The results presented in Figure 7.9 and Figure 7.10 would indicate that the different rates of oxidation are due to the different diffusion behaviours of Ni, Cr and O_2 within the oxide layer. Comparison of the diffusion characteristics of Cr, Ni and O_2 in the oxide layer is presented in Figure 7.11.

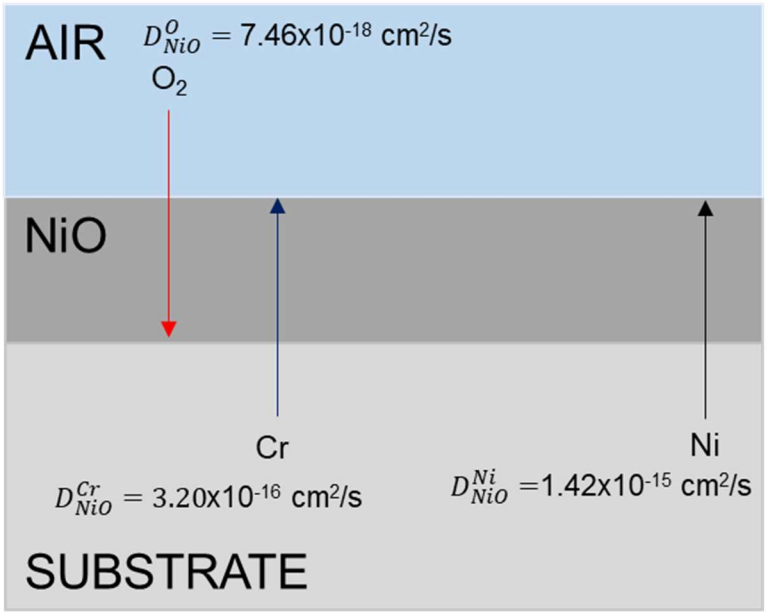


Figure 7.11 – Schematic showing the diffusion coefficients of Ni, Cr and O_2 within a NiO layer at 700 °C showing that diffusion coefficients of O_2 and Cr are smaller than that of Ni by several orders of magnitude.

Within the NiO layer, Ni is shown in Figure 7.11 to have the fastest diffusion kinetics, hence, Ni will diffuse fastest to the oxide – air interface where it can be oxidised. In the case of oxide formation, diffusion of O_2 to the substrate – air interface will limit the oxidation of Cr to Cr_2O_3 and the diffusion of Ni to the oxide – air interface will limit the oxidation of Ni to NiO. Diffusion of O_2 to the substrate – oxide interface limits the oxidation of Cr as diffusion of Cr has been shown to occur more quickly than Ni by the results of the mechanistic model, resulting in an enriched region of Cr at the substrate – air and substrate – oxide interface.

Despite the fast diffusion kinetics of Ni to the oxide – air interface, experimental results presented in Figure 7.8 and Figure 7.9 show that the rate of oxide formation of NiO and Cr_2O_3 is constant. Therefore, species diffusion must not be the only consideration when discussing oxide growth, hence, additional factors must be considered. Two potential factors that should be considered are the reaction kinetics for oxide formation and the potential short circuit diffusion of O_2 across the NiO layer.

7.2.3 Considering reaction kinetics for oxide formation

For the rates of Cr_2O_3 and NiO growth to be identical, as observed in Figure 7.9, the rate constants for each reaction and the concentrations of species involved in each reaction need to be considered. In general terms, the reaction rate, R, can be expressed as:

$$R = k[Reactants]^n \quad \textbf{7.2}$$

where k is the reaction constant, and [Reactants] is the concentration of reactants involved in the reaction. The value of n is the order of the reaction and is determined from the reaction equation. For the formation of Cr_2O_3 and NiO, the equations for R can be defined as shown in equations 7.3 and 7.4 respectively:

$$R_{Cr_2O_3} = k_{Cr_2O_2}[Cr]^{\frac{2}{3}}[O_2]^{\frac{1}{2}} \quad \textbf{7.3}$$

$$R_{NiO} = k_{NiO}[Ni][O_2]^{\frac{1}{2}} \quad \textbf{7.4}$$

Thermodynamically, it can be shown that $k_{Cr_2O_2}$ is much greater than k_{NiO} by calculating the standard Gibbs free energy change for each reaction and calculating their associated equilibrium constants. Hence, for R to be equal for the formation of both oxides, the concentrations of Ni involved in the reaction must be greater than Cr involved in the formation of Cr_2O_3. This was shown to occur by the mechanistic model, which shows that there is a greater concentration change for Ni as there is for Cr. This is the case due to the greater concentration of Ni present within the Ni-based alloy Hastelloy C276.

7.2.4 Short circuit diffusion of O_2 in NiO layers

As discussed previously, in this study it is believe that the outer NiO layer grows by the outward diffusion of Ni, whilst the inner Cr_2O_3 layer grows by the inward diffusion of O_2. However, due to the faster diffusion behaviour of Ni than O_2 within the NiO layer, the growth rate of an external NiO layer would be expected to be greater than that of an internal Cr_2O_3 layer. This differs from the obtained result which shows that the two rates of oxide growth are almost identical.

For this to be achieved, the rate of O_2 diffusion inward to the substrate – oxide interface must be occurring at a faster rate than quoted in Figure 7.11, which shows that O_2 diffusion in NiO is slower than Ni by a minimum of 10^3 cm^2/s. This faster rate of O_2 diffusion to the substrate – oxide interface can be achieved by short circuit diffusion pathways such as grain boundaries and dislocations and has been discussed in previous studies in which multi-oxide layers formed [191].

7.3 Use of modelling techniques for the prediction of high temperature oxidation kinetics

As discussed in Chapter 5, the predictive modelling of high temperature oxidation was completed using empirical and mechanistic modelling techniques, the underpinning understanding for which are presented in Sections 4.3 and 4.4 respectively. The developed models were capable of making predictions of specific mass change, K_P values, elemental distribution changes and oxide layer thicknesses.

Based on results presented in Table 7.1, the deployment of both modelling techniques was successful, with predictions being made that agreed with experimental results obtained within this research. This good agreement is shown in Table 7.3, which outlines the percentage differences between experimental and predicted results of specific mass change, K_P and oxide layer thickness.

Table 7.3 – Summary of percentage differences between experimental and predicted values of specific mass change, K_P and oxide layer thickness over the 200-hour time duration, showing good agreement between the data sets.

Calculation Method	Specific Mass Change (%)	K_P (%)	Total Oxide Layer Thickness (%)
Experimental	**Baseline**	**Baseline**	**Baseline**
Empirical Model	5.76	11.4	12.8
Mechanistic Model	8.54	16.9	5.62

The two modelling methodologies take different approaches to predict the oxidation behaviour of Hastelloy C276 in a dry air environment, with the empirical model relying on the input of experimental data from literature to predict Cr_2O_3 formation of Hastelloy C276. In contrast, the mechanistic model predicts changes in the elemental distribution by the use of element diffusion coefficients and the coupon geometry. Subsequently, concentration changes at the substrate – air interface are used to predict oxide growth for individual oxides.

Due to the ability of the mechanistic model to capture the movement of alloying elements through the substrate and the growth of multiple metallic oxides, it provides a more representative insight of the high temperature oxidation mechanism of Hastelloy C276 in a dry air environment when compared with the empirical model. Despite this, both models make a number of assumptions in order

to simplify the modelling methodologies. These assumptions can impact the outputs from each model. Hence, changes to these assumptions, and their impact on the results from each model need to be understood.

7.3.1 Impact of modelling assumptions on high temperature oxidation predictions

To obtain numerical predictions using the two modelling methods previously discussed, assumptions were made which may limit the predictive capabilities of the numerical models. Analysis of these assumptions was conducted using a systematic approach, allowing for the most sensitive assumptions to be identified. These assumptions and their impact will be discussed in the following sections.

7.3.1.1 Empirical Model – Review of modelling assumptions

When considering the empirical model, two main assumptions were made. The first being that only Cr_2O_3 was being formed. This allowed for data relating to Cr_2O_3 forming alloys to be used, when in reality, a larger variety of oxides can be produced during the oxidation of a Ni-based alloy depending on the alloy composition and the experimental conditions. Therefore, the values of K_P utilised within this study to predict oxide formation may not be fully representative of the oxidation process taking place as they do not include the formation of additional metallic oxides from the reaction of alloying elements with oxygen. As a result of this assumption, the empirical model significantly overpredicts the growth of Cr_2O_3.

Another assumption is made regarding the calculation of the value of U for each alloy input into the model. It was assumed that the value of U could be calculated using the composition of the alloy and without measuring the concentrations of alloying elements present within the Cr_2O_3 layer. This assumption was made as mathematical analysis showed that the concentrations of alloying elements present within the oxide layer in the original study by Bensch et al. [88] were the same as the composition of the alloy. Utilising this calculation method for U resulted in a 1.83% difference between the value of U using the method in literature compared to the method used within this study which was deemed acceptable for the purposes of this model.

Assessing the sensitivity of the empirical model to changes in K_P and U showed that the empirical model was insensitive to changes in K_P, with the output values varying by the same amount as the input value. However, much larger changes in the output values were observed when the same changes were applied to values of U. In this case, output values varied much more than the change to the input

value. The sensitivity was quantified using a correlation coefficient, denoted as CC, which is defined as shown in equation 7.5:

$$CC = \frac{\%\ Change\ in\ output}{\%\ Change\ in\ input} \qquad \textbf{7.5}$$

Based on the results of this sensitivity study, the assumption regarding K_P values was deemed acceptable as the model was relatively insensitive to changes in these values. However, since the output values were highly sensitive to changes in the values of U for each of the input alloys, the method by which U was calculated may introduce error into the model, resulting in inaccurate oxidation predictions.

7.3.1.2 Mechanistic Model – Review of modelling assumptions

The same sensitivity study was applied to the assumptions of the mechanistic model to identify how the outputs from the model varied with changes to the input parameters. The main assumption made within the mechanistic model is the constant nature of the diffusion coefficients for each of the alloying elements. The diffusion coefficients directly impact the concentration changes for each element, from which oxide formation is predicted. Therefore, understanding the sensitivity of changes to the diffusion coefficients on the concentration changes for each element is critically important. A sensitivity study conducted using the same method as that of the empirical model was deployed, showing that the mechanistic model was highly insensitive to changes in the diffusion coefficients. Therefore, assuming that the diffusion coefficients were constant was deemed to be acceptable. The full sensitivity study undertaken for the empirical and mechanistic models is included as Appendix A.

7.3.2 Empirical and mechanistic model validation

High temperature oxidation of Hastelloy C276 was shown experimentally to follow parabolic oxidation kinetics, occurring as a result of the diffusion behaviour of anions and cations through the oxide scale. The numerical models follow the same kinetics, with numerical results matching those determined experimentally, with the values predicted falling with the range of experimental errors as illustrated in Table 7.1. However, the empirical model massively overpredicts Cr_2O_3 formation as it assumes that only Cr_2O_3 forms during the oxidation process. The mechanistic model therefore provides better agreement of the oxidation mechanism with experimental characterisation of the high temperature oxidation of Hastelloy C276 corroborating the predictions of Cr_2O_3 and NiO growth by the mechanistic model.

7.4 Corrosion behaviour of Hastelloy C276 in FLiNaK molten salt

The high temperature corrosion behaviour of Hastelloy C276 has been assessed using experimental techniques, as well as predicted by the development of a new numerical model building upon the mechanistic model also developed in this work for the oxidation of Hastelloy C276 in high temperature oxidising environments. The corrosion behaviour has been quantified experimentally at a temperature of 700 °C after durations of 50, 100 and 200 hours in an air atmosphere using a thermogravimetric method. In each experiment, approximately 184 grams of FLiNaK salt was added to achieve the desired surface area to volume ratio.

During static immersion experiments, higher mass losses were observed when compared with the mass gains observed during oxidation experiments. This difference would indicate that in a molten FLiNaK salt environment containing air, the corrosive effects of the salt outweigh the oxidation kinetics of Hastelloy C276, resulting in degradation of the substrate material. The calculated corrosion rates from the coupon mass changes at time intervals of 50, 100 and 200 hours are summarised in Table 7.4.

Table 7.4 – Summary of experimentally determined mass losses and their corresponding calculated corrosion rates of Hastelloy C276 coupons immersed in molten FLiNaK salt at 700 °C for experiment durations of 50, 100 and 200 hours.

Time Interval (hours)	Corrosion Product Specific Mass Change (mg/cm^2)	Corrosion Damage Specific Mass Change(mg/cm^2)	Corrosion Rate (mmpy)
50	0.216	-1.573	0.308
100	5.353	-3.278	0.321
200	24.307	-5.184	0.254

The experimental results shown in Table 7.4 show that the corrosion rate of Hastelloy C276 remains roughly constant over the full 200-hour duration, with their being a maximum variation of 23.4% between corrosion rate measurements, taken at time intervals of 100 and 200 hours. The consistency of the corrosion rate indicates that the corrosion product layer formed is not sufficient to prevent corrosion of the substrate material in a molten salt environment. This was observed to be the case when examining micrographs presented in Chapter 6 which showed regions of corrosion product and regions of exposed substrate material which had undergone corrosive attack. This section aims to discuss the reasoning behind the observed corrosion behaviour of Hastelloy C276.

7.4.1 Proposed mechanism of Hastelloy C276 in molten FLiNaK salt

Within this research, the corrosion of Hastelloy C276 in a high temperature environment containing molten FLiNaK salt and air was investigated using a static immersion technique. During corrosion assessments the formation of a corrosion product was observed along with aggressive corrosive attack to the underlying substrate material in the form of dealloying. This is highlighted in Figure 7.12 which shows regions of exposed substrate material co-existing alongside regions of corrosion product.

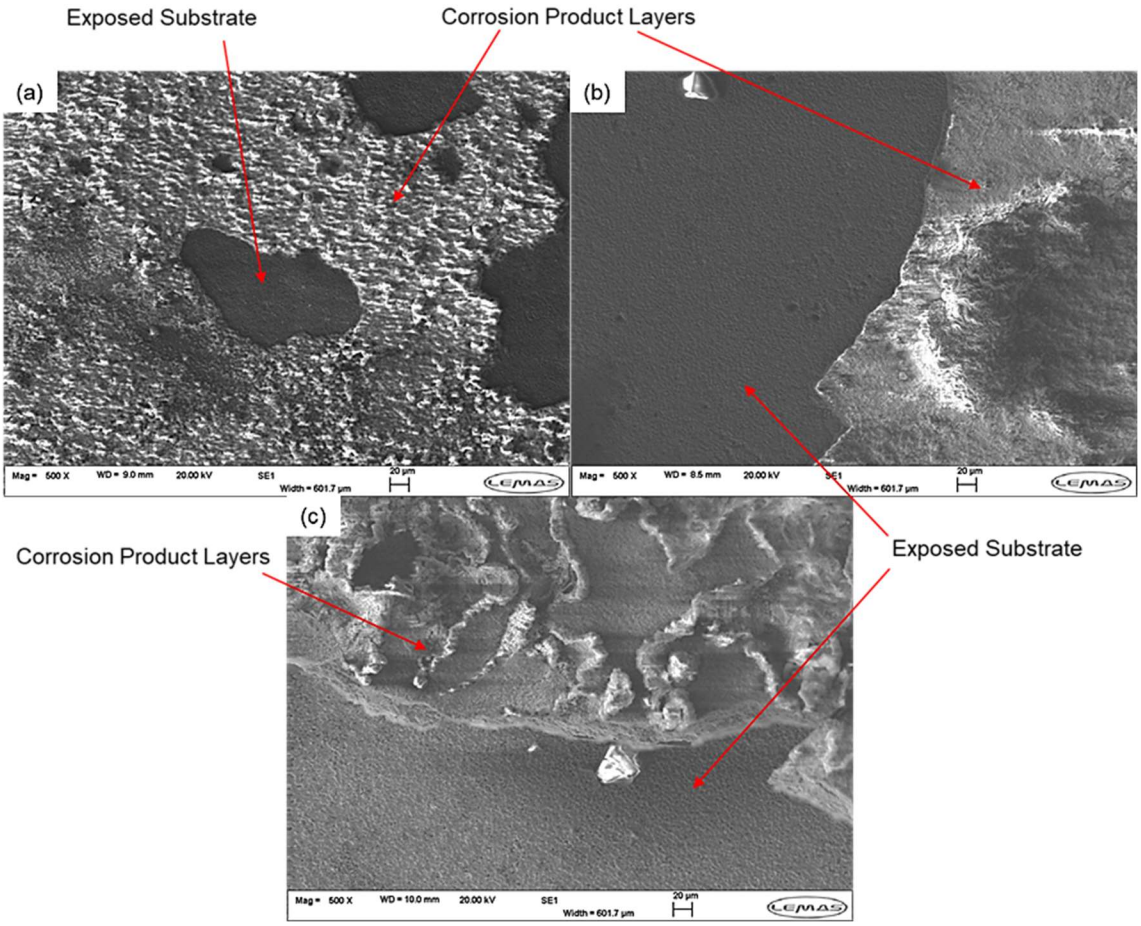


Figure 7.12 – Images highlighting regions of exposed substrate material to the molten salt environment as well as defects within the corrosion product layer which may lead to its removal.

The results presented as Figure 7.12 would indicate that corrosion product formation and corrosive attack are occurring simultaneously within the molten salt system. The corrosion behaviour, characterised by corrosion rate measurements, showed that the corrosion rate was constant as a function of time. This finding therefore leads to the conclusion that the corrosion product layer is non-protective to the underlying substrate material within the molten salt environment. This has also been shown to be the case by SEM imaging of cross-sections of corroded

coupons of Hastelloy C276, in which voids are observed within the substrate material, caused by corrosive attack to the substrate below the corrosion product layer. An example of this result is shown in Figure 7.13.

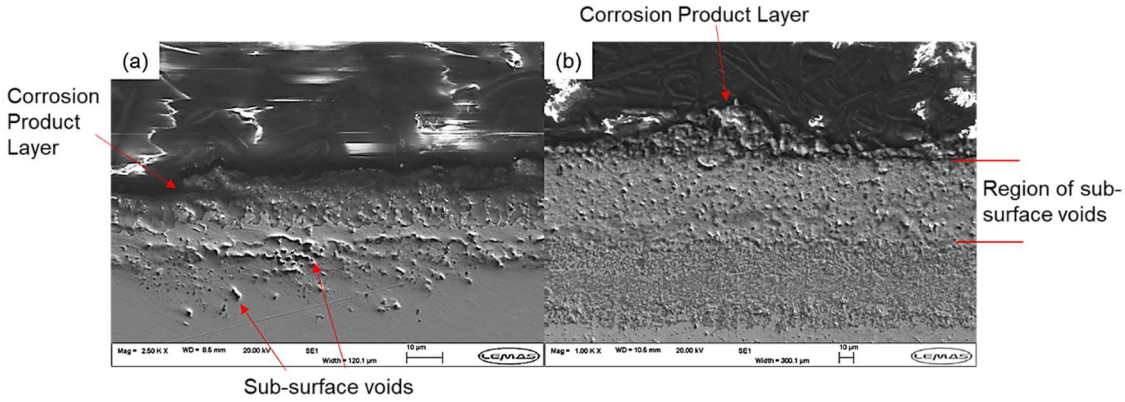


Figure 7.13 – Micrographs of cross-sections of Hastelloy C276 coupons immersed in molten FLiNaK salt at 700 °C for a) 100 and b) 200 hours, showing voids present within the substrate material.

As discussed in Chapter 6, the main corrosion product that was identified by XRD analysis was $LiCrO_2$, whilst corrosive attack of the substrate material appeared to be as a result of a dealloying corrosion mechanism. In the case of $LiCrO_2$ formation, this can be achieved by either the conversion of Cr_2O_3 to $LiCrO_2$, defined in equations 7.6 and 7.7, or by the direct reaction between species at the corrosion product – molten salt interface, defined in equation 7.8:

$$2Cr + \frac{3}{2}O_2 \rightarrow Cr_2O_3 \qquad \textbf{7.6}$$

$$Cr_2O_3 + O^{2-} + 2Li^+ \rightarrow 2LiCrO_2 \qquad \textbf{7.7}$$

$$Cr^{3+} + Li^+ + 2O^{2-} \rightarrow LiCrO_2 \qquad \textbf{7.8}$$

Despite the conversion of $LiCrO_2$ from Cr_2O_3 being commonly observed, Cr_2O_3 was not identified by XRD analysis presented in Chapter 6. Hence, $LiCrO_2$ is likely to form by the reaction between ions present at the substrate – molten salt interface, where Cr will initially be available at the interface by its diffusion from the bulk of the material to the interface through the Ni – matrix [133, 183]. This has been illustrated in Section 5.3.5 which shows predictions, from the mechanistic model developed within this work, of Cr diffusion from the bulk material to the substrate – molten salt interface in high temperature environments.

However, the continued growth of the $LiCrO_2$ layer may be aided by the dissolution of Cr from the substrate material, which has been shown to occur due to the interactions between the substrate material and the molten salt.

Examples of these interactions include the interactions between metallic fluorides and Cr as described in equations 7.9 - 7.11:

$$NiF_2 + Cr \rightarrow CrF_2 + Ni \quad \textbf{7.9}$$

$$FeF_2 + Cr \rightarrow CrF_2 + Fe \quad \textbf{7.10}$$

$$2CrF_3 + Cr \rightarrow 3CrF_2 \quad \textbf{7.11}$$

The formation of metallic fluorides which contribute to the dissolution of Cr from the substrate material have been shown previously to form due to the formation of the impurity HF within the salt melt and its subsequent reaction with alloying elements of Hastelloy C276, defined by the general equation, included as equation 7.12:

$$Me + xHF \rightarrow MeF_x + \frac{x}{2}H_2 \quad \textbf{7.12}$$

The dissolution of Cr from the Hastelloy C276 substrate by a dealloying mechanism was observed experimentally, with EDX line scans and elemental maps highlighting regions of Cr – depletion in the near surface regions of Hastelloy C276 coupons after 100 and 200 hours of immersion in molten FLiNaK salt. Examples of Cr-depleted regions within the substrate material are highlighted in Figure 7.14.

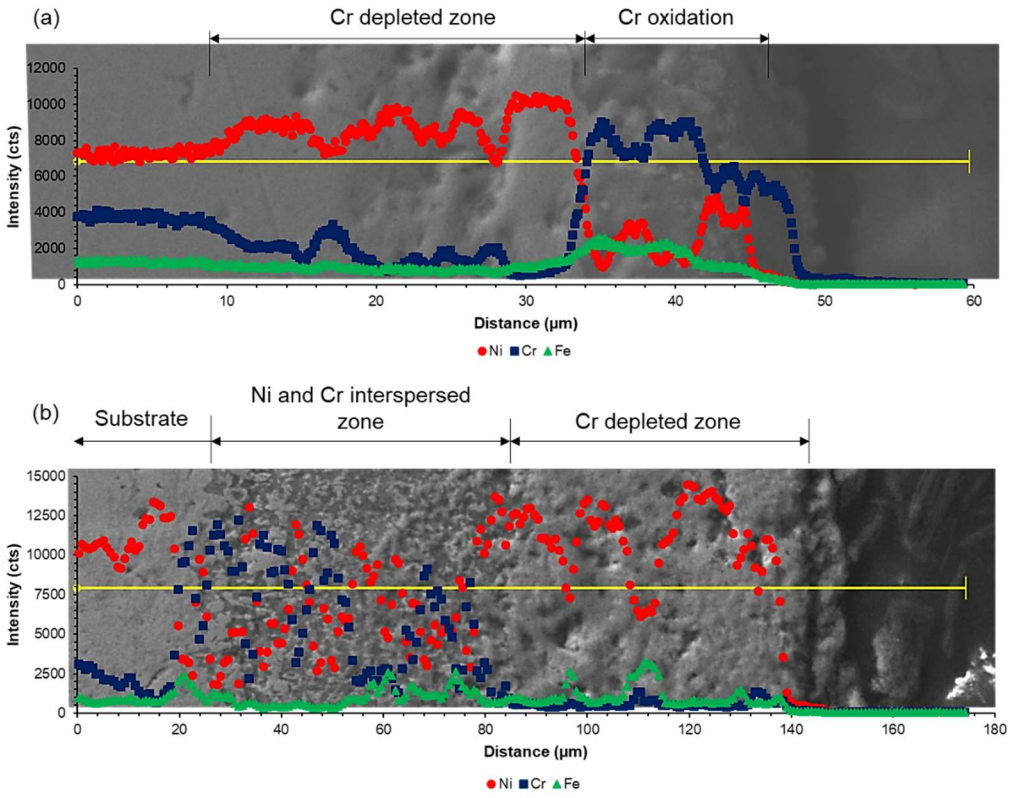


Figure 7.14 – Cross-sectional image of Hastelloy C276 coupon, exposed to FLiNaK molten salt at 700 °C for a) 100 hours and b) 200 hours illustrating Cr depletion from the substrate material in the near surface region, with depletion zones labelled.

Additional analysis conducted using EDX maps on cross-sections of Hastelloy C276, corroded for 200 hours in FLiNaK molten salt show regions complete devoid of Cr, as well as regions of Ni, Fe and O enrichment and depletion, highlighting the movement of alloying elements within the substrate during the corrosion process. This result is presented in Figure 7.15.

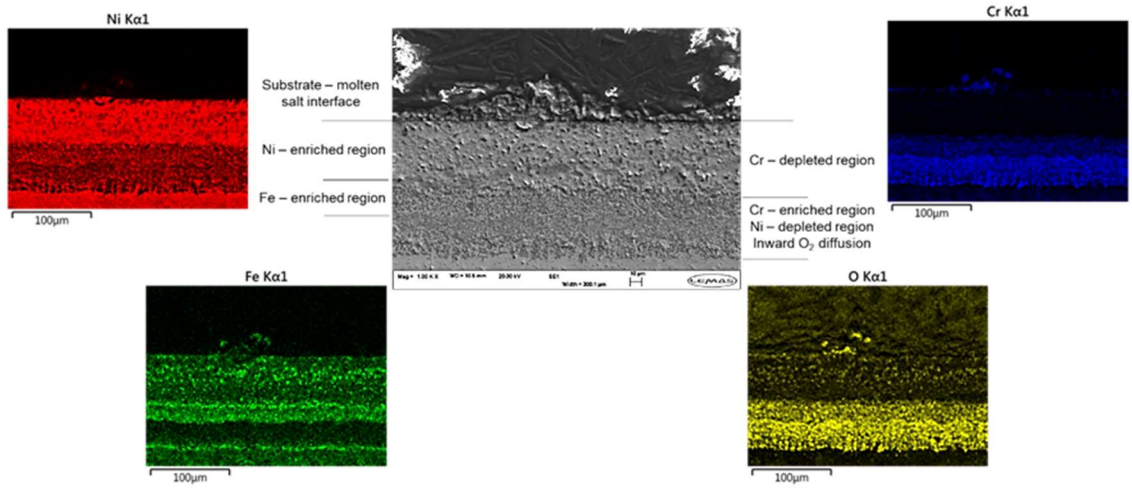


Figure 7.15 - Schematic highlighting regions of alloying element enrichment and depletion on Hastelloy C276 cross-sections after 200 hours of exposure to molten FLiNaK salt.

EDX analysis presented in Figure 7.14 and Figure 7.15 highlight the continued dissolution of Cr from the substrate material as a function of time, with the depth of Cr depletion increasing with each time interval. This is illustrated in Figure 7.14 which shows an increase in Cr depletion from approximately 26 µm to 60 µm when the immersion duration is increased from 100 to 200 hours. The dissolution of Cr observed in Figure 7.14 and Figure 7.15 is consistent with the corrosion mechanism proposed for Hastelloy C276 in a molten FLiNaK salt environment.

7.4.2 Correlation of corrosion product formation and corrosive attack

As shown previously the corrosion of Hastelloy C276 in a molten FLiNaK salt environment proceeds by two mechanisms, the formation of a corrosion product layer and dealloying, resulting in the heavy depletion of Cr as a function of time. Experimental result of specific mass change with respect to time also reflect these two mechanisms of material degradation. This is shown in Figure 7.16, which shows the overall specific mass change, specific mass change due to corrosion damage and specific mass change due to corrosion product formation.

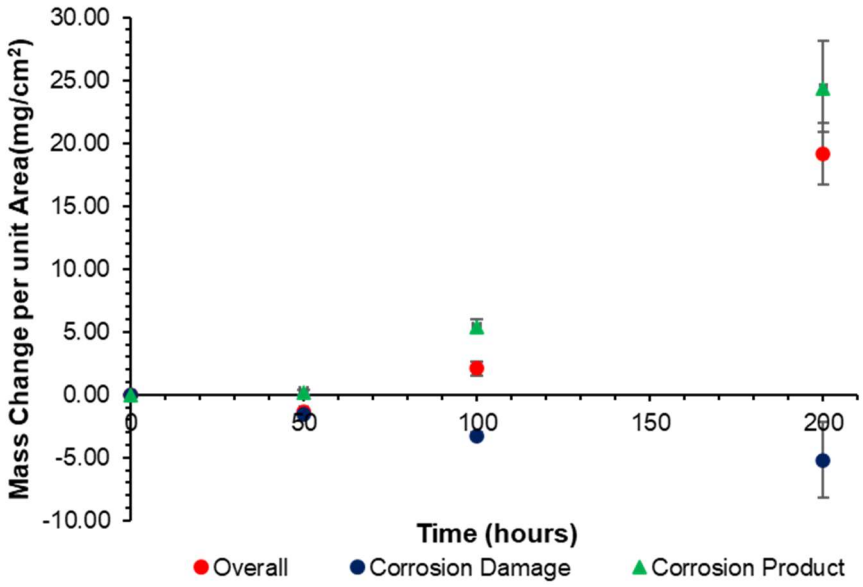


Figure 7.16 – Comparison of corrosion and oxidation rates of Hastelloy C276 in a molten FLiNaK salt at 700 °C for durations up to 200 hours, showing that the corrosion product formation outweighs corrosion mechanism.

Figure 7.16 shows a linear trend for the specific mass loss due to corrosion of Hastelloy C276 coupons in a molten salt environment which has been shown by experimental measurements to be due to a constant corrosion rate. As mentioned previously, the proposed corrosion mechanism is predicated on a two-part corrosion mechanism which involves both oxidation of the substrate material and the dissolution of Cr from the substrate. The result presented in Figure 7.16 shows clearly that the increase in specific mass loss of the substrate due to corrosion may contribute to the increase in the oxidation of the substrate by increasing the concentration of Cr available at the substrate – molten salt interface. This is a result that is expected due to the change in the combination of elements as the addition of Li and O to Cr to form $LiCrO_2$ will result in a greater mass increase than the amount of Cr removed from the substrate material.

The contribution of Cr dissolution to the growth of the corrosion product layer is highlighted in Figure 7.17 which compares the corrosion product formation kinetics in molten salt with the oxidation behaviour of Hastelloy C276 in a dry air environment.

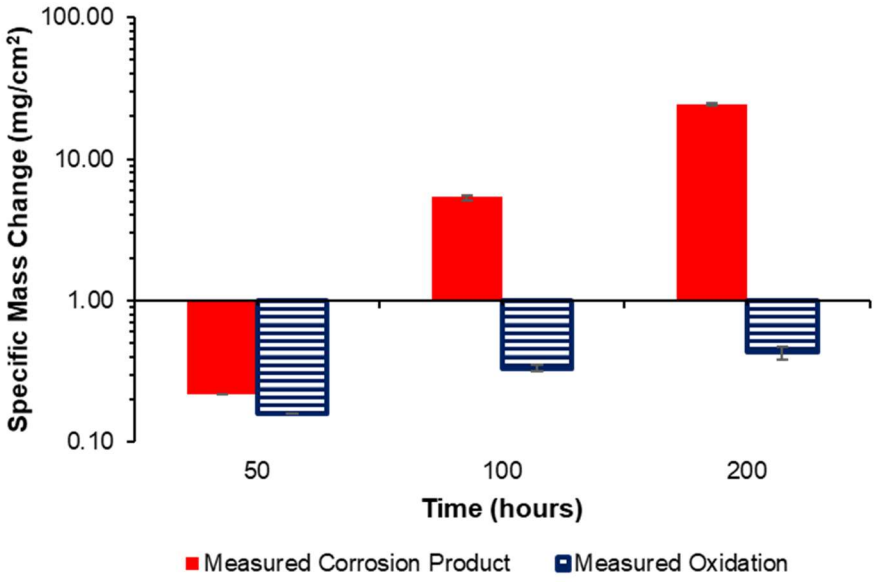


Figure 7.17 – Comparison of specific mass changes due to corrosion product formation in a molten salt environment and high temperature in a dry air environment. Corrosion product formation in a molten salt environment is much greater than the dry oxidation behaviour of Hastelloy C276 in a dry air environment, indicating that substrate oxidation and hence corrosion product formation is enhanced by Cr dissolution from the substrate by a corrosive medium.

Although the result presented in Figure 7.17 indicates that the specific mass lost due to corrosion damage may result in the specific mass gain due to the mass of the corrosion product, the specific mass change due to corrosion product formation is not proportional to the specific mass loss due to Cr dissolution from this Hastelloy C276 coupons. This is shown in both Figure 7.16 and Figure 7.17, particularly in Figure 7.16 which shows a positive overall specific mass change after 100 and 200 hours of immersion of Hastelloy C276 in a molten FLiNaK salt environment. The positive nature of the specific mass change is a result that is expected due to the change in the combination of elements as the addition of Li and O to Cr to form $LiCrO_2$ will result in a greater mass increase than the amount of Cr removed from the substrate material. However, the discrepancy lies in the lack of proportionality between the specific mass changes, with the specific mass gain due to corrosion product growth being greater much greater than the quantity of Cr being removed from the substrate due to corrosion damage.

When investigating the relationship between the corrosion damage and corrosion product formation, the specific mass loss due to corrosion was converted into a theoretical specific mass gain due to corrosion product formation. To do this, the specific mass loss from the substrate material was assumed to be due to the dissolution of Cr. It was also assumed that $LiCrO_2$ would be the corrosion product

formed. Using this method provided an overestimate of the specific mass change due to the formation of the $LiCrO_2$ corrosion product. A comparison between the predicted and actual specific mass changes due to corrosion product formation are presented in Figure 7.18.

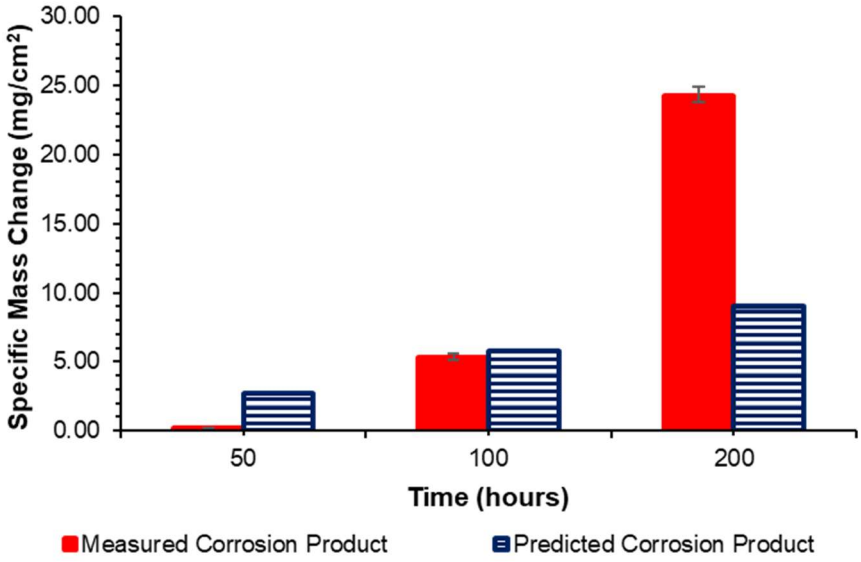


Figure 7.18 – Comparison between measured and predicted specific mass changes due to corrosion product formation, showing a large discrepancy between data points at 50 and 200 hours. Good agreement is observed between data points generated at 100 hours.

Comparison between the measured and predicted specific mass changes attributed to the formation of corrosion products shows good agreement at a time interval of 100 hours, with a difference of 6.88% being observed. However, at 50 and 200 hours, much larger differences were observed, with the values at 50 hours differing by a factor of 100, and the values at 200 hours differing by 91.3%.

The discrepancy at 50 hours may be explained by considering the corrosion kinetics at the substrate – molten salt interface. Initially, Cr dissolution from the substrate into the molten salt will be the main mechanism taking place. This will occur readily until O_2 has been able to diffuse to the substrate – molten salt interface, at which time the formation of corrosion products can begin. The negative overall specific mass change and small corrosion product mass changes observed in Figure 7.16 may therefore be indicators of faster corrosion kinetics in the time period of 0 – 50 hours when compared with the kinetics of corrosion product formation. This is shown in Figure 7.19 which shows dissolution of Cr from the substrate material in the initial stages, followed by the presence of O_2 at the substate – molten salt interface and subsequent corrosion product formation,

resulting in much greater mass loss due to corrosion than mass gain due to corrosion product formation.

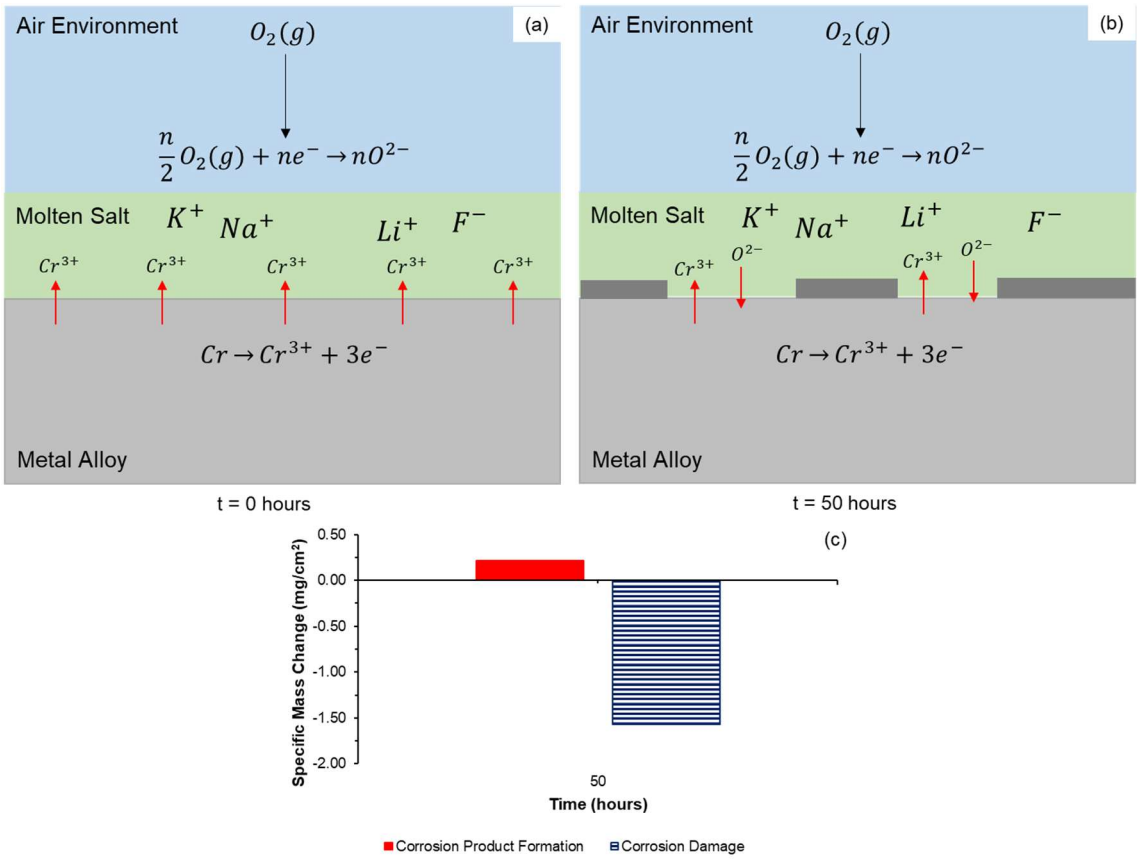


Figure 7.19 – Schematic showing a) initial Cr dissolution from the substrate material, followed by b) indicating the presence of O_2 at the substrate – molten salt interface resulting in corrosion product formation. The mass change result is shown in c) which shows much greater mass loss due to corrosion than mass gain due to corrosion product formation.

The discrepancy in the result presented at 200 hours is much larger than that observed at 50 hours and is also accompanied by large experimental errors as shown by the error bars presented in Figure 7.18. The reason for the observed discrepancy and the experimental errors may be due to a number of factors which will be discussed in the following section.

7.4.3 Assessment of corrosion product formation and corrosive attack correlation

The observed discrepancy between the kinetics of material loss and corrosion product formation could be due to many different factors. To fully evaluate the observed discrepancy, a study was undertaken. Initially, the kinetics of corrosion product formation will be considered by measuring the corrosion product layer thicknesses and calculating a specific mass change based on these. This will allow

for comparison between the measured specific mass changes and the actual specific mass change that would be expected.

Poor agreement between the measured and expected specific mass changes may have resulted due to irregularities within the methodologies used to clean coupons corroded in FLiNaK molten salt and measure specific mass changes. Ultimately, this would drastically impact the measured specific mass changes of corrosion product formation. Therefore, the following sections discuss the methodology deployed and the associated errors observed between measured and expected specific mass changes. A more robust method of cleaning coupons to ensure reliable and repeatable data is obtained will also be discussed.

7.4.3.1 Assessment of corrosion product formation

To assess the formation of the corrosion product, the thickness of the corrosion product layers was measured at each time interval to assess its formation kinetics. The taken measurements are presented in Figure 7.20.

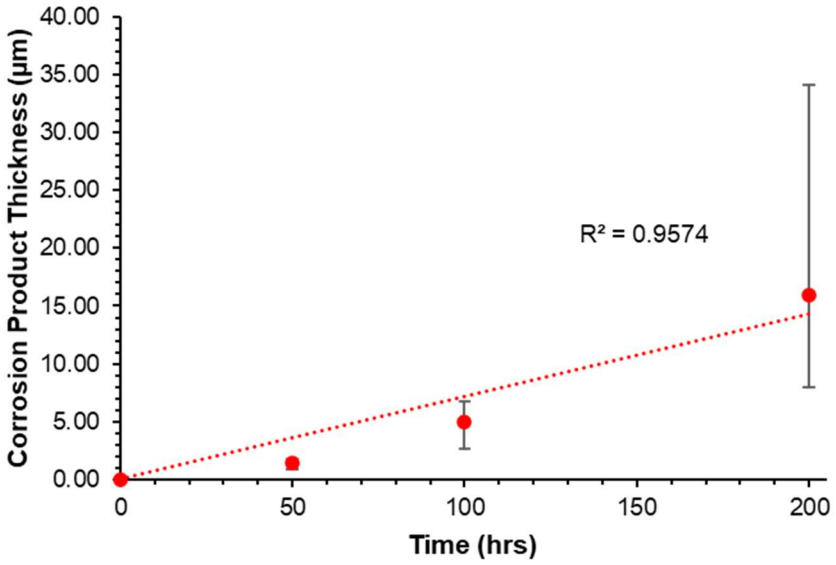


Figure 7.20 – Measured corrosion product layer thickness with respect to time, with measurements taken on Hastelloy C276 coupons immersed in molten FLiNaK salt for 50, 100 and 200 hour at 700 °C. Results shows corrosion product layer formation occurs linearly, matching the specific mass loss kinetics.

Figure 7.20 shows that the corrosion product layer thickness increases linearly with respect to time which follows the same trend as the specific mass loss observed for Hastelloy C276 in a molten salt environment presented previously. Assuming that the corrosion product layer was formed only of $LiCrO_2$ and was dense and non-porous, the thickness measurement was converted into a specific mass

change to allow for comparison with the experimental results and predicted results presented in Figure 7.18. This comparison is presented in Figure 7.21.

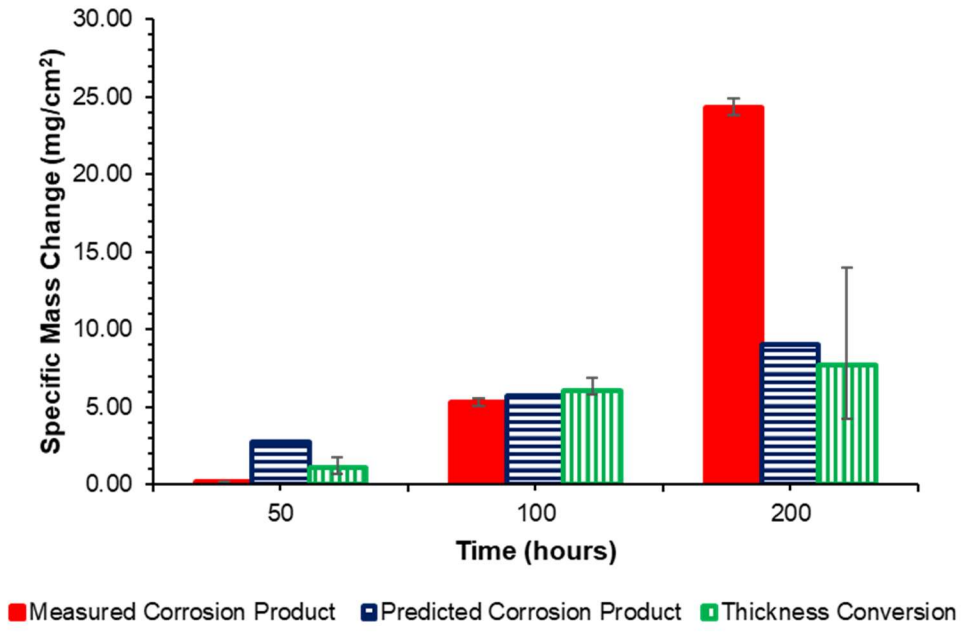


Figure 7.21 – Comparison of experimentally measured corrosion product specific mass change, predicted specific mass change from corrosion damage specific mass change and specific mass change predicted by conversion of corrosion product layer thickness after immersion periods of 50, 100 and 200 hours in FLiNaK molten salt.

Figure 7.21 shows better agreement between specific mass changes at 100 hours, with the specific mass changes from the measured corrosion product and the converted corrosion product thicknesses showing a difference of 12.8%. Predicted and measured values also show good agreement at 100 hours, with a small difference of 6.88% being calculated. However, large discrepancies are again observed between results obtained at 50 and 200 hours of immersion and the predicted values. These differences are summarised in Table 7.5.

Table 7.5 – Summary of discrepancies between experimental and predicted specific mass changes after 50 and 200 hours of immersion of Hastelloy C276 coupons in FLiNaK molten salt at 700 °C.

Time Interval	Percentage Difference – Experimental vs Predicted (%)	Percentage Difference – Experimental vs Converted (%)
50	170.9	134.8
200	91.3	103.5

Discrepancies between results obtained after 50 hours may be a result of the initially high corrosion rate due to the direct exposure of the Hastelloy C276 substrate to the highly corrosive FLiNaK molten salt. Hence, corrosion dominates the initial corrosion behaviour and greater specific mass losses are observed.

However, after this point, significant growth of corrosion product is observed. Since good agreement is observed after 100 hours of immersion, the discrepancy observed in results obtained after 200 hours could indicate an error in the specific mass change measurement of Hastelloy C276 coupons at this time interval.

7.4.3.2 Impact of measurement error on specific mass change results

Analysis presented in the previous section indicates an error in the measurement of the specific mass changes of coupons immersed in FLiNaK molten salt for 200 hours. This conclusion was drawn due to the non-proportional relationship between the measured corrosion product specific mass change and the specific mass change due to corrosion damage. The discrepancy is likely to be due to the incomplete removal of the corrosion product layer by its dissolution in a diluted HCl solution.

This mathematical analysis will focus on data collected after 200 hours of immersion as good agreement was observed between specific mass changes measured at 50 and 100 hours for corrosion product formation and corrosion damage. Therefore, the specific mass change of corrosion product formation was reduced by 1, 2.5, 5, 10 and 15 mg/cm^2, with the corresponding specific mass change due to corrosion damage being calculated. To complete the calculation, it was assumed that the corrosion product layer was $LiCrO_2$ and that Cr present within this layer had come solely from the substrate material. Hence the resulting specific mass change due to corrosion was due to Cr dissolution. This result is presented in Figure 7.22.

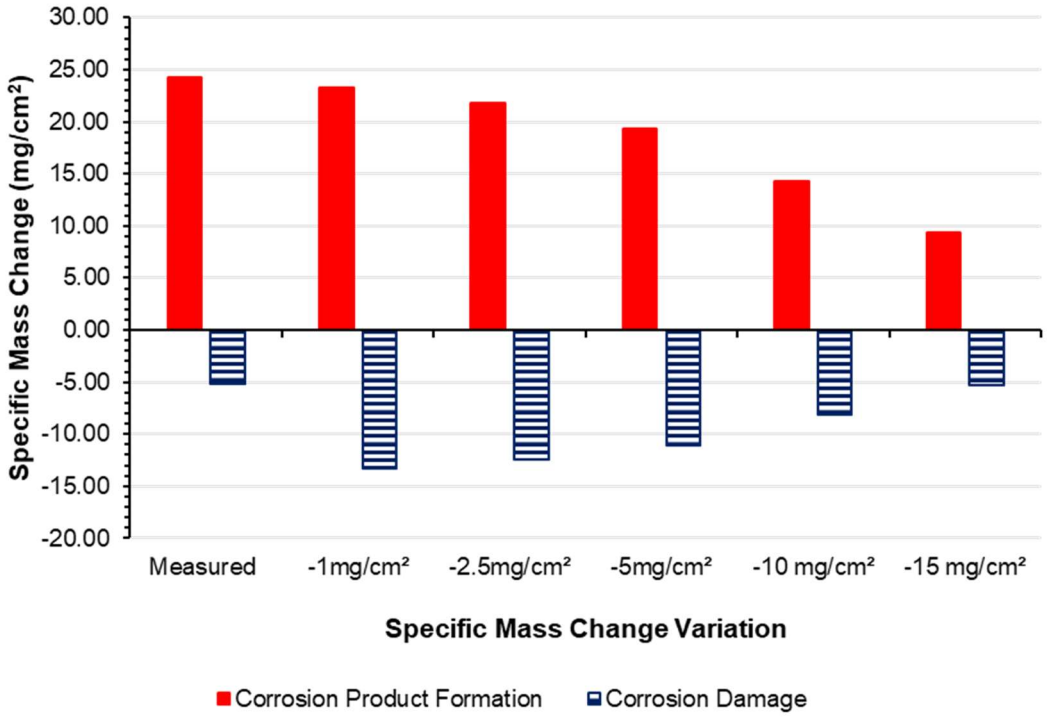


Figure 7.22 – Numerical study investigating the impact of reducing corrosion product formation specific mass change on the corrosion damage, with results showing that decreasing the corrosion product specific mass change decreases the corrosion damage which is as expected.

The study presented in Figure 7.22 show that reducing the specific mass change of corrosion product formed reduced the specific mass change due to corrosion which is as expected. However, to achieve the same specific mass change as that measured experimentally, -5.182 mg/cm^2, a reduction in the corrosion product specific mass change of approximately 15 mg/cm^2 is required, from approximately 24 mg/cm^2 down to 9 mg/cm^2. This result indicates that the main error influencing the result is the experimental measurement of the specific mass change of coupons after testing in molten FLiNaK salt and not the kinetics at the substrate – molten salt interface.

7.4.3.3 Deployed methodology and future considerations

When cleaning coupons of Hastelloy C276 after immersion in molten FLiNaK salt for 200 hours, two protocols were used. The first was to remove any solidified salt using distilled water before the first mass change measurement. This was to obtain a mass change measurement that included both corrosion damage and corrosion product formation. Following this, a distilled solution of HCl was used to remove any corrosion product layers as per ASTM G1-03 [158]. However, the mass change measurements obtained do not match those expected, hence, it was concluded

that the main source of error was within the method used to clean the coupons after testing.

To remove the corrosion product layers, coupons were immersed in the dilute HCl solution for 3 minutes as per ASTM G1-03 for this method of cleaning [158]. This resulted in a greater mass of corrosion product as not all corrosion product was removed successfully. To improve upon the deployed methodology, the corroded coupons would be immersed within the dilute HCl solution for a much longer time period to ensure full removal of the corrosion product. However, to prevent dissolution of the substrate within the HCl solution, the mass change would be monitored at distinct time intervals. This would allow for the mass change to be measured as a function of time and ensure that coupons were removed when the mass of the corroded coupons had reached a stable value as illustrated in Figure 7.23.

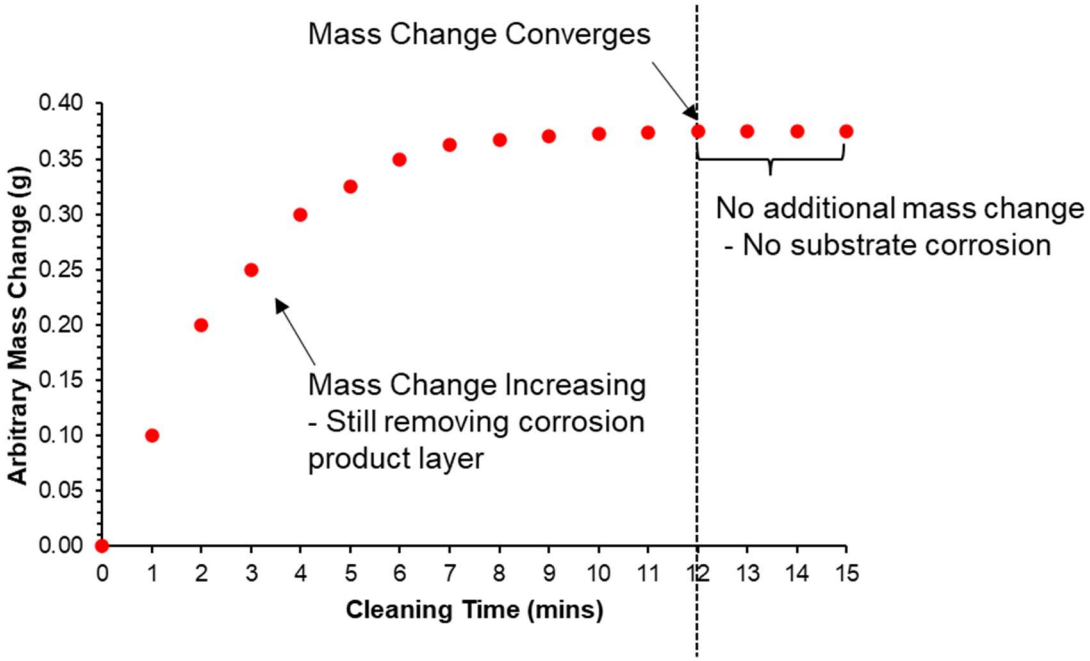


Figure 7.23 – Illustration of cleaning and mass measurement protocol, showing convergence of corroded coupon mass with increasing cleaning time [158].

7.5 Molten salt corrosion modelling using a mechanistic approach

To predict the corrosion behaviour of Hastelloy C276 in a molten FLiNaK salt environment, the mechanistic model for oxidation was expanded to include a four-step corrosion mechanism, deployed for molten nitrate salts by Li et al. [121]. The

original corrosion mechanism for 316L in Solar Salt containing a chloride impurity. However, the underpinning theory was changed from the original model to be representative of Cr dissolution from an alloy by a dealloying mechanism. The mathematics deployed therefore considered the interactions between metallic fluorides and impurities with the substrate material, which is consistent with the mechanism for Cr dissolution discussed in Section 7.4.1.

Key outputs from the mechanistic model included the specific mass change due to corrosion, corrosion rate of Hastelloy C276 and the corrosion depth. A comparison between the experimental and numerically predicted results at each time interval are presented in Figure 7.24 using the absolute percentage difference.

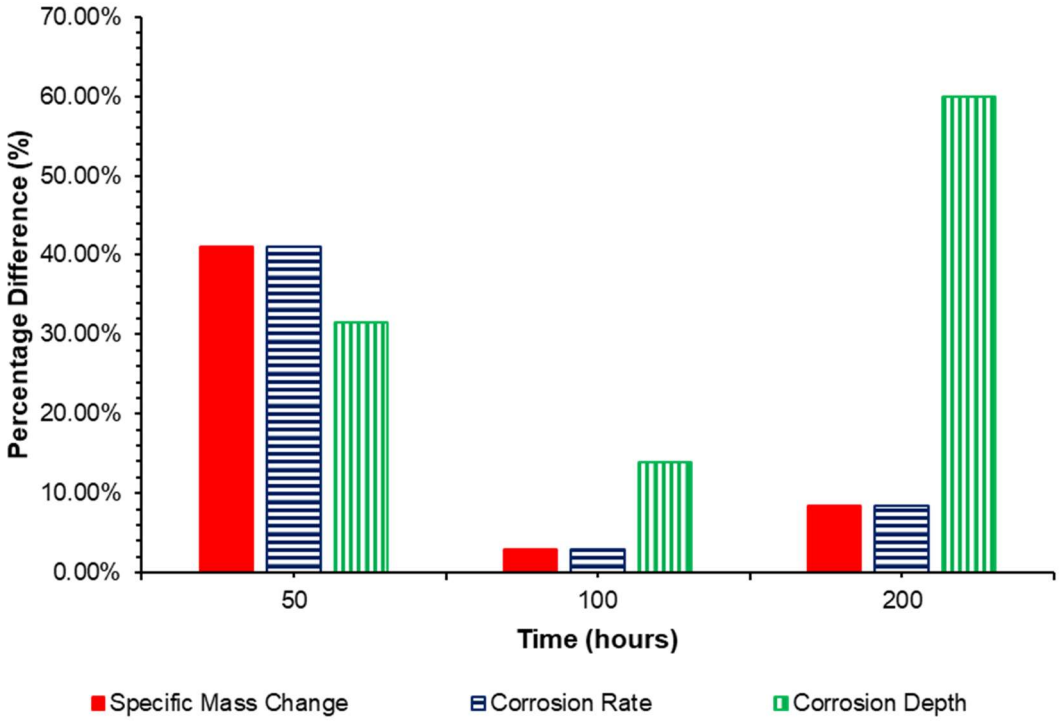


Figure 7.24 – Bar chart illustrating percentage differences between experimental and predicted specific mass changes, corrosion rates and corrosion depths at time intervals of 50, 100 and 200 hours of exposure of Hastelloy C276 coupons in molten FLiNaK salt at 700 °C, with the largest discrepancy being observed between experimentally observed corrosion depths, and those predicted mechanistically for durations of 200 hours.

Figure 7.24 shows large differences between experimental and predicted specific mass changes, corrosion rates and corrosion depths, particularly at 200 hours of exposure, despite the representative underpinning theory of the mechanistic model. Therefore, the mechanistic model may not be entirely representative of the molten salt corrosion process.

The key modelling output from the mechanistic model for corrosion is the corrosion depth, from which the specific mass change and corrosion rate are derived. Predictions of the corrosion depth are inherently linked to the predicted diffusion behaviour as concentration changes of CrF_2 are input directly into the equation for intrinsic corrosion, which is shown in equation 4.55. Hence, the predicted elemental change kinetics directly impact the molten salt corrosion predictions.

7.5.1 Impact of modelling assumptions on corrosion depth predictions

As presented in Figure 7.24, differences between experimental and predicted results for the corrosion depths at 50 and 100 hours are smaller than those observed at 200 hours. The largest difference between experimental and predicted results occurs for the corrosion depth of Hastelloy C276 at 200 hours of immersion, with a percentage difference of 60.0% being observed. This difference is 1.9 and 4.3 times greater than the differences in the experimental and predicted corrosion depths at time intervals of 50 and 100 hours, respectively.

To achieve the prediction of the corrosion depth, the mechanistic model relies upon concentration change predictions. These predictions have been shown throughout Chapter 5 to result in parabolic kinetics for oxidation. Similarly, the corrosion process was assumed to be controlled by the diffusion of species to and from the substrate – molten salt interface and hence would result in parabolic kinetics. This assumption is similar to that used in the model by Li et al. [121] described in Section 3.5.3 for corrosion of stainless steel 316L in Solar Salt. Parabolic kinetics were assumed in that model due to molten salt corrosion and oxidation mechanisms occurring simultaneously. Therefore, corrosion would be controlled by the diffusion of ions through a corrosion product layer. This is shown schematically in Figure 7.25.

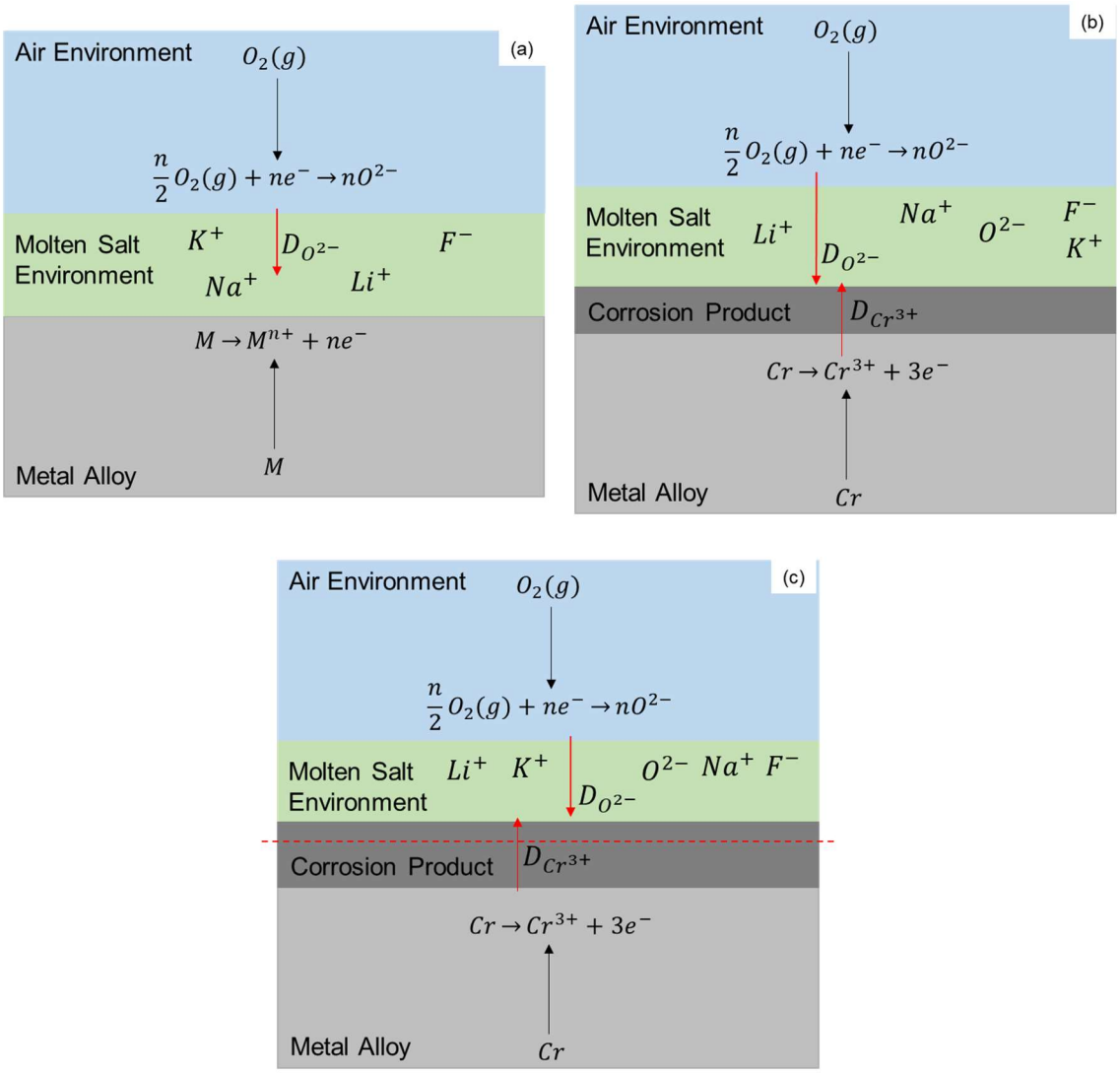


Figure 7.25 – Schematic showing the proposed corrosion mechanism with initial corrosion being shown in (a) where substrate is fully exposed to the molten salt. At time (b) the corrosion product has begun to form, with Cr and O_2 cations and anions needing to diffuse to the corrosion product – molten salt interface to continue corrosion product formation. Finally, in (c), the corrosion product thickness increases, increasing the diffusion barrier and hence reducing the rate of corrosion product formation.

However, the parabolic kinetics, input from the element change predictions, and assumed as part of the underpinning mathematics, were not observed experimentally. Experimentally, specific mass changes showed that mass was lost from the samples at a constant rate, which was corroborated by measurements of the corrosion depth which was shown to increase linearly over time. This indicates that Cr is being actively removed from the alloy whilst immersed in the molten salt environment. Therefore, the parabolic kinetics assumed and presented for the mechanistic model of molten salt corrosion is not wholly representative of the system that materials may be exposed to in a MSR environment.

Chapter 8 – Conclusions and Future Work

The high temperature molten salt corrosion in a FLiNaK and air containing environment has been investigated utilising Hastelloy C276 coupons at a temperature of 700 °C in the duration of 0 to 200 hours. The experimental analysis has included quantification of corrosion rates alongside the characterisation of corrosion products. Alongside this study, the high temperature oxidation of Hastelloy C276 has been investigated to obtain a baseline for the oxidation behaviour of Hastelloy C276 and understand the synergy between corrosion and oxidation in molten salt environments. Similarly, to the corrosion behaviour, oxidation behaviour was quantified using by measuring the oxidation kinetics, with characterisation of oxidation products taking place by SEM, EDX and XRD analysis. The measurements obtained experimentally were then used to validate predictive models, developing using MATLAB, for the prediction of the rates of corrosion and oxidation of Hastelloy C276. The main conclusions from this research are presented throughout this chapter.

8.1 Conclusions of Research

The oxidation research of Hastelloy C276 was presented in Chapter 5 and consisted of isothermal oxidation testing of Hastelloy C276 coupons, with quantification of the oxidation behaviour using a thermogravimetric technique. Alongside the experimental research, the development of computational models using empirical and mechanistic methods was undertaken.

The experimental and numerical methodologies deployed allowed for the quantification of rates of oxidation, whilst post-experimental analysis techniques allowed for the growth and structures of oxidation products to be fully characterised. In order to make the research as relevant as possible to MSR environments, experiments were conducted at a temperature of 700 °C, which is the typical inlet temperature of the MSR core. The conclusions from Chapter 5 after completing isothermal oxidation tests and developing numerical models are as follows:

- Isothermal oxidation tests conducted at 700 °C show an increase in the coupon mass with respect to time, with the coupon mass increasing in accordance with a parabolic rate law. Parabolic rate laws were also observed for the growth of the oxide layer thickness with respect to time.

- SEM analysis showed that increasing the exposure time led to both an increase in coverage of the oxide layer over the exposed surfaces and also an increase in the oxide crystal size.
- EDX analysis of the oxide layers showed that the outer most layer was predominantly a Ni-based oxide, with XRD showing that the layers of NiO, Cr_2O_3 and $NiCr_2O_4$ were present within the oxide layers.
- Cross-sectional analysis showed an increase in the oxide layer thickness with respect to time whilst also highlighting the external oxidation of Ni and the internal oxidation of Cr, determined by the diffusion properties of Ni, Cr and O respectively.
- Assessment of the rate of individual oxide layer growths indicated that both oxides followed a parabolic rate law and grew at roughly the same rate, both being controlled by the diffusion of species either through the oxide layer or to the substrate – oxide interface.

Isothermal oxidation tests were useful in understanding the baseline oxidation behaviour of Hastelloy C276 in a dry air environment, with the oxidation kinetics being quantified and the evolution of the oxide layers being understood.

In the case of the numerical models, both models predicted the oxidation kinetics with good agreement to the experimental results. However, the additional capability of the mechanistic model to predict elemental changes within the material during oxidation was a key factor in its subsequent use and further development in the corrosion study presented in Chapter 6. This was due to the chosen method of corrosion prediction and the requirement of this method to understand the microstructural evolution of the material.

Similarly, to the isothermal oxidation tests conducted in Chapter 5, isothermal corrosion tests were conducted in a molten FLiNaK salt environment, the results of which are presented in Chapter 6. The isothermal experiments were conducted using a static immersion technique, with the corrosion behaviour being quantified again using a thermogravimetric technique and any corrosion products being characterised using the same post-experimental methods described previously for the oxidation work presented in Chapter 5. The main conclusions to be drawn from the experimental research presented in Chapter 6 include:

- Specific mass changes obtained for the material loss of Hastelloy C276 under representative MSR operating conditions and in a molten FLiNaK salt environment follow linear kinetics, which is indicative of a constant corrosion rate.

- Experimentally determined specific mass changes indicated more mass was gained due to corrosion product formation when compared with material lost. This was shown through analysis of the experimental procedures to be due to a limitation in the process of corrosion product removal from the substrate before obtaining mass change measurements.
- Despite a significant error being observed in the specific mass change measurements after 200 hours, a constant corrosion rate was observed experimentally by conversion of the specific mass losses into a corrosion rate; hence, it was concluded that any corrosion product that had formed during immersion of Hastelloy C276 in FLiNaK salt was non-protective in nature.
- Identification of linear corrosion kinetics and elevated corrosion rates highlight the highly corrosive nature of the FLiNaK molten salt combination and the need for corrosion resistant alloys to be used in MSR applications. The high corrosion rates observed for the Hastelloy C276 alloy also indicate that it may not be suitable for use in environments containing FLiNaK molten salt.
- Corrosion to the underlying substrate combined with the formation of a corrosion product layer suggested a two-stage corrosion mechanism which involved oxidation of the substrate, to form the corrosion product layer, and the selective dissolution of less noble alloying elements from the substrate, in the case of Hastelloy C276, the dealloying of Cr.
- This was confirmed with post-experimental analysis which revealed the presence of a corrosion product layer that was rich in Cr and O and Cr depletion within the substrate material. The susceptibility of alloys to a dealloying corrosion mechanism, highlighted by the selective dissolution of Cr, may be a key consideration in the selection of alloys for MSR applications.
- XRD analysis of the corrosion product layer indicated the corrosion product was of the structure $LiCrO_2$, which has been shown to be non-protective to the substrate material in previous molten salt corrosion studies.

Alongside the experimental results obtained throughout this research, numerical models for the high temperature oxidation and molten salt corrosion processes were developed. Comparison with experimental results obtained in this study and in literature show good agreement for high temperature oxidation. However, some discrepancies were observed between the predicted and experimental molten salt corrosion results. Differences in the corrosion results were shown to be due to errors within the experimental methodologies, resulting in the larger than expected

specific mass changes being measured. The mechanistic model also under predicted the depth of corrosion due to the difference in kinetics observed experimentally and those assumed by the mechanistic model. The overall conclusions from the numerical modelling work deployed throughout this research are as follows:

- Empirical and mechanistic predictions of oxide growth, characterised by specific mass change and oxide layer thickness growth, showed good agreement with results for the oxidation of Hastelloy C276, obtained experimentally within this research and with results obtained in literature.
- The mechanistic model was capable of a deeper level of prediction due to the inclusion of the diffusion behaviour of all alloying elements and its capability in predicting their concentration changes of individual alloying elements and the growth of their corresponding oxides.
- Although the numerical quantification of the specific mass change from the empirical model was in good agreement with that observed experimentally, the value actually represented a large over prediction of the quantity of Cr_2O_3 that would form during oxidation, hence the result is not entirely representative of the oxidation mechanism taking place.
- Oxidation predictions from the mechanistic model showed good agreement with experimental results presented within this thesis. However, the modelled system may not have been fully representative of the whole oxidation mechanism, as diffusion through the formed oxide layers was not accounted for. Incorporation of this diffusion behaviour would increase model complexity and more accurately capture the oxidation process taking place.
- The mechanistic model was successfully expanded to include predictions of the corrosion behaviour of Hastelloy C276 in molten FLiNaK salt, with numerical results of the specific mass loss and corrosion rate showing good agreement to experimentally determined values.
- The simplicity of the model developed allows for good predictive capabilities with reduced computational demand and hence could be widely used for predicting alloy performance in simple test cases such as those presented in this work. However, to account for more complex test cases i.e. test cases including dynamic flowing conditions, additional modelling solutions would be required.
- Errors were observed between the experimentally measured and predicted corrosion depths due to the assumption of parabolic kinetics in the mechanistic model which may not accurately capture the actual corrosion

kinetics taking place. To predict the corrosion behaviour of Ni-based alloys more accurately in molten salt environments for MSR applications, consideration should be given to linear and linear – parabolic modelling methodologies.

8.2 Future Work

Based on the research conducted within this thesis, three key areas of research are suggested to improve the understanding of the corrosion of Ni-based alloys and other materials in molten fluoride salt environments containing air. The areas suggested in this section are aligned with the key research challenges also highlighted by the GIF for the future development of MSRs [20]. The areas and associated tasks are presented in Figure 8.1.

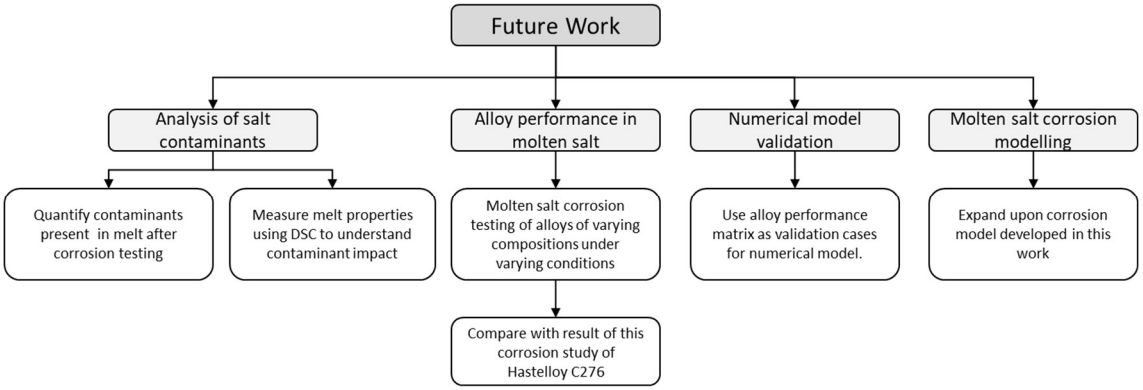


Figure 8.1 – Future work suggestions to compliment understanding of corrosion behaviour of Ni-based alloys in molten salt environments for MSR applications.

Much of the research presented herein aligns with many of the research goals presented in Figure 8.1, however, a future work program combining both experimental and numerical methods, using the research presented in this thesis as a basis, could aid in developing the understanding of Ni-based alloy corrosion in FLiNaK molten salt further. The additional work presented in Figure 8.1 aligns well with the following research and development objectives discussed by the GIF [20]:

1. Provide measurement of salt thermochemical and thermophysical properties.
2. Study materials issues associated with use of MSRs, including erosion, corrosion, radiation damage and creep-fatigue.

A major limiting factor in understanding the corrosive nature of molten salts is how the introduction of contaminants during the corrosion process influences the corrosion behaviour. To fully understand this, the identification and quantification of impurities present within the melt can be achieved utilising inductively coupled plasma optical emission spectroscopy (ICP-OES). Deploying this technique alongside techniques for quantifying the properties of the melt, such as differential scanning calorimetry (DSC) would allow for the impact of impurities on the properties of the melt to be identified. The monitoring of species within the melt from the result of ICP-OES will also give a good indication of the corrosion behaviour of the materials within the melt.

To achieve this, a robust corrosion testing program, covering a variety of materials which may have applications in an MSR and associated environment conditions, would need to be deployed to build meaningful understanding. This would allow for a material performance matrix to be developed which could then be used to further validate the numerical models developed and presented throughout this research. To improve on the experimental methods deployed during this research, time should also be taken to quantify the extent of oxidation and corrosion during heating up and cooling down processes to obtain a completely representative understanding of the kinetics associated with these processes. This would allow for a more robust understanding of oxidation and corrosion behaviour of Ni-based alloys under the desired test conditions.

Typically, existing corrosion models developed for predicting the corrosion of materials in molten salt environments are empirical in nature and based on existing data, with relationships being derived between data or by the training of a model using neural networks. However, the model developed in this work follows a more mechanistic approach in which the diffusion of elements and their subsequent reactions with other species are considered. Therefore, the models developed within this research can be developed further to offer unique insight into the oxidation and corrosion behaviour of a variety of varied materials, using the developed material performance matrix to validate against experimental data.

The results of the mechanistic model for oxidation of Hastelloy C276 shows that the developed model is capable of achieving a highly accurate predictions of oxidation kinetics. However, the model could be expanded to include the diffusion of species through the formed oxide layer. This would increase the complexity of the model but also make the mechanistic model more representative of the oxidation mechanism taking place and more robust in its predictive capabilities.

Despite the good agreement between experimental corrosion measurements and the results of the mechanistic model for the modelling of corrosion behaviour of Hastelloy C276, assumptions regarding the corrosion depth following parabolic kinetics were observed to be un-representative of the physical system. Hence, exploring linear or linear-parabolic kinetics may be an option in the development of future models to ensure the predictions are fully representative of the static test cases discussed throughout this thesis.

References

1. Van Ruijven, B.J., De Cian, E. and Sue Wing, I. Amplification of future energy demand growth due to climate change. *Nature communications.* 2019, **10**(1), p.2762.
2. Dincer, I. and Acar, C. A review on clean energy solutions for better sustainability. *International Journal of Energy Research.* 2015, **39**(5), pp.585-606.
3. Abram, T. and Ion, S. Generation-IV nuclear power: A review of the state of the science. *Energy policy.* 2008, **36**(12), pp.4323-4330.
4. Kelly, J.E. Generation IV International Forum: A decade of progress through international cooperation. *Progress in Nuclear Energy.* 2014, **77**, pp.240-246.
5. Doe, U. Nuclear Energy Research Advisory Committee and the Generation IV International Forum. *A technology roadmap for Generation IV nuclear energy systems.* 2002.
6. Serp, J., Allibert, M., Beneš, O., Delpech, S., Feynberg, O., Ghetta, V., Heuer, D., Holcomb, D., Ignatiev, V. and Kloosterman, J.L. The molten salt reactor (MSR) in generation IV: overview and perspectives. *Progress in Nuclear Energy.* 2014, **77**, pp.308-319.
7. Allen, T., Sridharan, K., Tan, L., Windes, W., Cole, J., Crawford, D. and Was, G.S. Materials challenges for generation IV nuclear energy systems. *Nuclear Technology.* 2008, **162**(3), pp.342-357.
8. Liu, M., Tay, N.S., Bell, S., Belusko, M., Jacob, R., Will, G., Saman, W. and Bruno, F. Review on concentrating solar power plants and new developments in high temperature thermal energy storage technologies. *Renewable and Sustainable Energy Reviews.* 2016, **53**, pp.1411-1432.
9. Williams, D.F., Toth, L.M. and Clarno, K.T. *Assessment of Candidate Molten Salt Coolants for the Advanced High Temperature Reactor (AHTR).* United States. Department of Energy, 2006.
10. Forum., G.I.I. *Generation IV International Forum Annual Report*. 2017.
11. Forsberg, C.W. Molten-salt-reactor technology gaps. In: *Proc. 2006 International Congress on Advances in Nuclear Power Plants (ICAPP'06)*: Citeseer, 2006, pp.4-8.
12. Sabharwall, P., Clark, D., Glazoff, M., Zheng, G., Sridharan, K. and Anderson, M. Advanced heat exchanger development for molten salts. *Nuclear Engineering and Design.* 2014, **280**, pp.42-56.
13. Roper, R., Harkema, M., Sabharwall, P., Riddle, C., Chisholm, B., Day, B. and Marotta, P. Molten salt for advanced energy applications: A review. *Annals of Nuclear Energy.* 2022, **169**, p.108924.
14. International, N. Corrosion Costs and Preventive Strategies in the United States. *Supplement to Materials Performance.* 2002.
15. Nishikata, A., Numata, H. and Tsuru, T. Electrochemistry of molten salt corrosion. *Materials Science and Engineering: A.* 1991, **146**(1-2), pp.15-31.
16. Guo, S., Zhang, J., Wu, W. and Zhou, W. Corrosion in the molten fluoride and chloride salts and materials development for nuclear applications. *Progress in Materials Science.* 2018, **97**, pp.448-487.
17. McCoy Jr, H. *Status of materials development for molten salt reactors.* Oak Ridge National Lab., 1978.

18. Orhan, M.F., Dincer, I., Rosen, M.A. and Kanoglu, M. Integrated hydrogen production options based on renewable and nuclear energy sources. *Renewable and Sustainable Energy Reviews.* 2012, **16**(8), pp.6059-6082.
19. Behar, C. Technology roadmap update for generation IV nuclear energy systems. In: *In OECD Nuclear Energy Agency for the Generation IV International Forum*, 2014, pp.2014-2003.
20. Forum., G.I.I. *Generation IV International Forum Annual Report*. 2021.
21. Rosenthal, M., Kasten, P. and Briggs, R. Molten-salt reactors—history, status, and potential. *Nuclear Applications and Technology.* 1970, **8**(2), pp.107-117.
22. Bettis, E., Schroeder, R., Cristy, G., Savage, H., Affel, R. and Hemphill, L. The aircraft reactor experiment—design and construction. *Nucl. Sci. Eng.* 1957, **2**(6), pp.804-825.
23. Heuer, D., Merle-Lucotte, E., Allibert, M., Brovchenko, M., Ghetta, V. and Rubiolo, P. Towards the thorium fuel cycle with molten salt fast reactors. *Annals of Nuclear Energy.* 2014, **64**, pp.421-429.
24. Judd, A.M. *An introduction to the engineering of fast nuclear reactors.* Cambridge University Press, 2014.
25. Haubenreich, P.N. and Engel, J. Experience with the molten-salt reactor experiment. *Nuclear Applications and Technology.* 1970, **8**(2), pp.118-136.
26. MacPherson, H. The molten salt reactor adventure. *Nuclear Science and engineering.* 1985, **90**(4), pp.374-380.
27. Koger, J. *Evaluation of Hastelloy N alloys after nine years exposure to both a molten fluoride salt and air at temperatures from 700 to 560 °C.* Oak Ridge National Lab., 1972.
28. Silverman, M., Huntley, W. and Robertson, H. *Heat transfer measurements in a forced convection loop with two molten-fluoride salts: LiF--BeF_2--ThF_2--UF_4 and eutectic $NaBF_4$--NaF.* Oak Ridge National Lab., 1976.
29. Sohal, M.S., Ebner, M.A., Sabharwall, P. and Sharpe, P. *Engineering database of liquid salt thermophysical and thermochemical properties.* Idaho National Lab.(INL), Idaho Falls, ID (United States), 2010.
30. Williams, D. *Assessment of candidate molten salt coolants for the NGNP/NHI heat-transfer loop.* Oak Ridge National Lab.(ORNL), Oak Ridge, TN (United States), 2006.
31. Forsberg, C.W., Renault, C., Le Brun, C. and Ignatiev, V. Liquid salt applications and molten salt reactors. *Revue Générale du Nucléaire.* 2007, **4**, p.63.
32. Lines, A., Bryan, S., Felmy, H. and Branch, S. On-line Monitoring for Molten Salt Reactor MC&A: Optical Spectroscopy-Based Approaches. *Pacific Northwest National Laboratory, PNNL-33367: Richland, WA.* 2022.
33. Sridharan, K., Allen, T., Anderson, M. and Simpson, M. *Thermal properties of LiCl-KCl molten salt for nuclear waste separation.* Univ. of Wisconsin, Madison, WI (United States); Idaho National Lab.(INL …, 2012.
34. Xu, T., Li, X., Wang, Y. and Tang, Z. Development of Deep Potentials of Molten $MgCl_2$–NaCl and $MgCl_2$–KCl Salts Driven by Machine Learning. *ACS Applied Materials & Interfaces.* 2023, **15**(11), pp.14184-14195.
35. Xu, X., Dehghani, G., Ning, J. and Li, P. Basic properties of eutectic chloride salts NaCl-KCl-$ZnCl_2$ and NaCl-KCl-$MgCl_2$ as HTFs and thermal storage media measured using simultaneous DSC-TGA. *Solar Energy.* 2018, **162**, pp.431-441.

36. Mathieu, L., Heuer, D., Merle-Lucotte, E., Brissot, R., Le Brun, C., Liatard, E., Loiseaux, J.-M., Méplan, O., Nuttin, A. and Lecarpentier, D. Possible configurations for the thorium molten salt reactor and advantages of the fast nonmoderated version. *Nuclear Science and engineering.* 2009, **161**(1), pp.78-89.
37. Forsberg, C.W., Peterson, P.F. and Pickard, P.S. Molten-salt-cooled advanced high-temperature reactor for production of hydrogen and electricity. *Nuclear Technology.* 2003, **144**(3), pp.289-302.
38. Allen, T., Busby, J., Meyer, M. and Petti, D. Materials challenges for nuclear systems. *Materials Today.* 2010, **13**(12), pp.14-23.
39. Zhang, D., Liu, L., Liu, M., Xu, R., Gong, C., Zhang, J., Wang, C., Qiu, S. and Su, G. Review of conceptual design and fundamental research of molten salt reactors in China. *International Journal of Energy Research.* 2018, **42**(5), pp.1834-1848.
40. Serrano-López, R., Fradera, J. and Cuesta-López, S. Molten salts database for energy applications. *Chemical Engineering and Processing: Process Intensification.* 2013, **73**, pp.87-102.
41. Kondo, M., Nagasaka, T., Xu, Q., Muroga, T., Sagara, A., Noda, N., Ninomiya, D., Nagura, M., Suzuki, A. and Terai, T. Corrosion characteristics of reduced activation ferritic steel, JLF-1 (8.92 Cr–2W) in molten salts Flibe and Flinak. *Fusion Engineering and Design.* 2009, **84**(7-11), pp.1081-1085.
42. Muránsky, O., Yang, C., Zhu, H., Karatchevtseva, I., Sláma, P., Nový, Z. and Edwards, L. Molten salt corrosion of Ni-Mo-Cr candidate structural materials for Molten Salt Reactor (MSR) systems. *Corrosion Science.* 2019, **159**, p.108087.
43. Ignatiev, V. and Surenkov, A. Alloys compatibility in molten salt fluorides: Kurchatov Institute related experience. *Journal of nuclear materials.* 2013, **441**(1-3), pp.592-603.
44. Ghaznavi, T., Persaud, S.Y. and Newman, R.C. The Effect of Temperature on Dealloying Mechanisms in Molten Salt Corrosion. *Journal of The Electrochemical Society.* 2022, **169**(11), p.111506.
45. Ghaznavi, T., Persaud, S.Y. and Newman, R.C. Electrochemical corrosion studies in molten chloride salts. *Journal of The Electrochemical Society.* 2022, **169**(6), p.061502.
46. Bell, S., Steinberg, T. and Will, G. Corrosion mechanisms in molten salt thermal energy storage for concentrating solar power. *Renewable and Sustainable Energy Reviews.* 2019, **114**, p.109328.
47. McCafferty, E. *Introduction to corrosion science.* Springer Science & Business Media, 2010.
48. Murty, K.L. *Materials Ageing and Degradation in Light Water Reactors: Mechanisms and Management.* Elsevier, 2013.
49. Ghali, E., Sastri, V.S. and Elboujdaini, M. *Corrosion prevention and protection: practical solutions.* John Wiley & Sons, 2007.
50. Qiu, J., Macdonald, D.D., Schoell, R., Han, J., Mastromarino, S., Scully, J.R., Kaoumi, D. and Hosemann, P. Electrochemical study of the dissolution of oxide films grown on type 316L stainless steel in molten fluoride salt. *Corrosion Science.* 2021, **186**, p.109457.
51. Patel, N.S., Pavlík, V. and Boča, M. High-temperature corrosion behavior of superalloys in molten salts–a review. *Critical Reviews in Solid State and Materials Sciences.* 2017, **42**(1), pp.83-97.

52. Olson, L., Sridharan, K., Anderson, M. and Allen, T. Nickel-plating for active metal dissolution resistance in molten fluoride salts. *Journal of nuclear materials.* 2011, **411**(1-3), pp.51-59.
53. Olson, L.C., Ambrosek, J.W., Sridharan, K., Anderson, M.H. and Allen, T.R. Materials corrosion in molten LiF–NaF–KF salt. *Journal of Fluorine Chemistry.* 2009, **130**(1), pp.67-73.
54. Pan, C.-q., Zhong, Q.-d., Yang, J., Cheng, Y.F. and Li, Y.-l. Investigating crevice corrosion behavior of 6061 Al alloy using wire beam electrode. *Journal of Materials Research and Technology.* 2021, **14**, pp.93-107.
55. Betts, A. and Boulton, L. Crevice corrosion: review of mechanisms, modelling, and mitigation. *British corrosion journal.* 1993, **28**(4), pp.279-296.
56. Rashidi, N., Alavi-Soltani, S.R. and Asmatulu, R. Crevice corrosion theory, mechanisms and prevention methods. 2007.
57. Rebak, R. Stress corrosion cracking (SCC) of nickel-based alloys. In: *Stress corrosion cracking*. Elsevier, 2011, pp.273-306.
58. Cattant, F., Crusset, D. and Féron, D. Corrosion issues in nuclear industry today. *Materials Today.* 2008, **11**(10), pp.32-37.
59. Delpech, S., Cabet, C., Slim, C. and Picard, G.S. Molten fluorides for nuclear applications. *Materials Today.* 2010, **13**(12), pp.34-41.
60. Odette, G. and Lucas, G. Embrittlement of nuclear reactor pressure vessels. *Jom.* 2001, **53**, pp.18-22.
61. Silvent, A. *Irradiation effects on the Ni alloys used in reactor core structures.* CEA Centre d'Etudes Nucleaires de Grenoble, 1975.
62. Nanstad, R.K., McClintock, D.A., Hoelzer, D.T., Tan, L. and Allen, T.R. High temperature irradiation effects in selected Generation IV structural alloys. *Journal of nuclear materials.* 2009, **392**(2), pp.331-340.
63. Standardization, I.O.f. *ISO 11463:2020 Corrosion of metal and alloys - Guidelines for the evaluation of pitting corrosion.* https://www.iso.org/standard/73318, 2020.
64. Burkle, D.P. *Understanding the Formation of Protective $FeCO_3$ on to Carbon Steel Pipelines during CO2 Corrosion*. thesis, University of Leeds, 2017.
65. De Motte, R.A. *A combined experimental and modelling approach to elucidate $FeCO_3$ scale formation kinetics*. thesis, University of Leeds, 2016.
66. Pessu, F.O. *Investigation of pitting corrosion of carbon steel in sweet and sour oilfield corrosion conditions: a parametric study*. thesis, University of Leeds, 2015.
67. Karfidov, E.A., Zaikov, Y.P., Nikitina, E.V., Seliverstov, K.E. and Dub, A.V. High-Temperature Passivation of the Surface of Candidate Materials for MSR by Adding Oxygen Ions to FLiNaK Salt. *Materials.* 2022, **15**(15), p.5174.
68. Sabharwall, P., Ebner, M., Sohal, M. and Sharpe, P. *Molten Salts for High Temperature Reactors: University of Wisconsin Molten Salt Corrosion and Flow Loop Experiments--Issues Identified and Path Forward.* Idaho National Lab.(INL), Idaho Falls, ID (United States), 2010.
69. Olson, L.C., Fuentes, R.E., Martinez-Rodriguez, M.J., Ambrosek, J.W., Sridharan, K., Anderson, M.H., Garcia-Diaz, B.L., Gray, J. and Allen, T.R. Impact of corrosion test container material in molten fluorides. *Journal of Solar Energy Engineering.* 2015, **137**(6), p.061007.

70. Olson, L., Sridharan, K., Anderson, M. and Allen, T. Intergranular corrosion of high temperature alloys in molten fluoride salts. *Materials at High Temperatures.* 2010, **27**(2), pp.145-149.
71. Kondo, M., Nagasaka, T., Muroga, T., Sagara, A., Noda, N., Xu, Q., Ninomiya, D., Masaru, N., Suzuki, A. and Terai, T. High performance corrosion resistance of nickel-based alloys in molten salt flibe. *Fusion Science and Technology.* 2009, **56**(1), pp.190-194.
72. Richardson, T.J. *Shreir's corrosion.* Elsevier, 2009.
73. Ghaznavi, T., Bryk, M.A., Persaud, S.Y. and Newman, R.C. Alloying effects in high temperature molten salt corrosion. *Corrosion Science.* 2022, **197**, p.110003.
74. Zheng, G. and Sridharan, K. Corrosion of structural alloys in high-temperature molten fluoride salts for applications in molten salt reactors. *Jom.* 2018, **70**, pp.1535-1541.
75. Wallwork, G. The oxidation of alloys. *Reports on Progress in Physics.* 1976, **39**(5), p.401.
76. Lawless, K.R. The oxidation of metals. *Reports on Progress in Physics.* 1974, **37**(2), p.231.
77. Young, D.J. *High temperature oxidation and corrosion of metals.* Elsevier, 2008.
78. Wood, G.C. High-temperature oxidation of alloys. *Oxidation of Metals.* 1970, **2**(1), pp.11-57.
79. Rhamdhani, M., Hayes, P. and Jak, E. Subsolidus phase equilibria of the Fe-Ni-O system. *Metallurgical and Materials Transactions B.* 2008, **39**, pp.690-701.
80. Shen, J., Guo, X. and Niu, Y. Thermodynamic Phase Diagrams of Ternary Alloys Exposed to a Single Oxidant. *Oxidation of Metals.* 2019, **92**, pp.195-225.
81. Rothman, S., Nowicki, L. and Murch, G. Self-diffusion in austenitic Fe-Cr-Ni alloys. *Journal of Physics F: Metal Physics.* 1980, **10**(3), p.383.
82. Murarka, S., Anand, M. and Agarwala, R. Diffusion of chromium in nickel. *Journal of Applied Physics.* 1964, **35**(4), pp.1339-1341.
83. Mrowec, S. On the mechanism of high temperature oxidation of metals and alloys. *Corrosion Science.* 1967, **7**(9), pp.563-578.
84. Berthod, P. Kinetics of high temperature oxidation and chromia volatilization for a binary Ni–Cr alloy. *Oxidation of Metals.* 2005, **64**(3-4), pp.235-252.
85. Haugsrud, R. On the high-temperature oxidation of nickel. *Corrosion Science.* 2003, **45**(1), pp.211-235.
86. Mortimer, D. and Post, M. The oxidation of Cr and an Fe-50% Cr alloy. *Corrosion Science.* 1968, **8**(7), pp.499-512.
87. Sato, A., Chiu, Y.-L. and Reed, R. Oxidation of nickel-based single-crystal superalloys for industrial gas turbine applications. *Acta Materialia.* 2011, **59**(1), pp.225-240.
88. Bensch, M., Sato, A., Warnken, N., Affeldt, E., Reed, R.C. and Glatzel, U. Modelling of high temperature oxidation of alumina-forming single-crystal nickel-base superalloys. *Acta Materialia.* 2012, **60**(15), pp.5468-5480.
89. Cottis, R. Modelling corrosion in nuclear power plant systems. In: *Nuclear Corrosion Science and Engineering*. Elsevier, 2012, pp.438-448.
90. Pint, B., Martin, J. and Hobbs, L. The oxidation mechanism of θ-Al_2O_3 scales. *Solid state ionics.* 1995, **78**(1-2), pp.99-107.

91. Kawagishi, K., Sato, A., Kobayashi, T. and Harada, H. Oxidation Properties for 2 super (nd)-5 super (th) Generation Ni-Base Single-Crystal Superalloys at 1023, 1173 and 1373 K. *Journal of the Japan Institute of Metals.* 2007, **71**(3), pp.313-319.
92. Michael, J.R. Phase identification using electron backscatter diffraction in the scanning electron microscope. *Electron backscatter diffraction in materials science.* 2000, pp.75-89.
93. Karunaratne, M., Ogden, S.L., Kenny, S.D. and Thomson, R.C. A multicomponent diffusion model for prediction of microstructural evolution in coated Ni based superalloy systems. *Materials science and technology.* 2009, **25**(2), pp.287-299.
94. Kim, H.-S., Park, S.-J., Seo, S.-M., Yoo, Y.-S., Jeong, H.-W. and Jang, H. Regression analysis of high-temperature oxidation of Ni-based superalloys using artificial neural network. *Corrosion Science.* 2021, **180**, p.109207.
95. Park, S.-J., Seo, S.-M., Yoo, Y.-S., Jeong, H.-W. and Jang, H. Statistical study of the effects of the composition on the oxidation resistance of Ni-based superalloys. *Journal of Nanomaterials.* 2015, **16**(1), pp.256-256.
96. Agarwal, D. Nickel and nickel alloys. *Handbook of Advanced Materials: Enabling New Designs.* 2004, pp.217-270.
97. Zong, G., Zhang, Z.-B., Sun, J.-H. and Xiao, J.-C. Preparation of high-purity molten FLiNaK salt by the hydrofluorination process. *Journal of Fluorine Chemistry.* 2017, **197**, pp.134-141.
98. Pint, B.A., Distefano, J.R. and Wright, I.G. Oxidation resistance: One barrier to moving beyond Ni-base superalloys. *Materials Science and Engineering: A.* 2006, **415**(1-2), pp.255-263.
99. Li, Y., Wang, S., Yang, J., Xu, D., Guo, Y., Qian, L. and Song, W. Corrosion characteristics of a nickel-base alloy C-276 in harsh environments. *International Journal of Hydrogen Energy.* 2017, **42**(31), pp.19829-19835.
100. Zhang, Q., Tang, R., Yin, K., Luo, X. and Zhang, L. Corrosion behavior of Hastelloy C-276 in supercritical water. *Corrosion Science.* 2009, **51**(9), pp.2092-2097.
101. Taylor, M., Evans, H., Stekovic, S. and Hardy, M. The oxidation characteristics of the nickel-based superalloy, RR1000, at temperatures of 700–900 °C. *Materials at High Temperatures.* 2012, **29**(2), pp.145-150.
102. Khanna, A.S. High temperature oxidation. In: *Handbook of environmental degradation of materials*. Elsevier, 2005, pp.105-152.
103. Bettis, E.S., Schroeder, R.W., Cristy, G.A., Savage, H.W., Affel, R.G. and Hemphill, L.F. The Aircraft Reactor Experiment—Design and Construction. *Nuclear Science and engineering.* 1957, **2**(6), pp.804-825.
104. Li, D.-S., Chen, G., Li, D., Zheng, Q., Gao, P. and Zhang, L.-L. Oxidation resistance of nickel-based superalloy Inconel 600 in air at different temperatures. *Rare Metals.* 2021, **40**, pp.3235-3240.
105. Xiao, J., Prud'Homme, N., Li, N. and Ji, V. Influence of humidity on high temperature oxidation of Inconel 600 alloy: Oxide layers and residual stress study. *Applied Surface Science.* 2013, **284**, pp.446-452.
106. Dudziak, T., Boroń, L., Deodeshmukh, V., Sobczak, J., Sobczak, N., Witkowska, M., Ratuszek, W. and Chruściel, K. Steam oxidation behavior of advanced steels and ni-based alloys at 800 C. *Journal of Materials Engineering and Performance.* 2017, **26**, pp.1044-1056.

107. Dudziak, T., Deodeshmukh, V., Backert, L., Sobczak, N., Witkowska, M., Ratuszek, W., Chruściel, K., Zieliński, A., Sobczak, J. and Bruzda, G. Phase investigations under steam oxidation process at 800 °C for 1000 h of advanced steels and Ni-based alloys. *Oxidation of Metals.* 2017, **87**, pp.139-158.
108. Dudziak, T., Jura, K., Polkowska, A., Deodeshmukh, V., Warmuzek, M., Witkowska, M., Ratuszek, W. and Chruściel, K. Steam oxidation resistance of advanced steels and Ni-based alloys at 700 °C for 1000 h. *Oxidation of Metals.* 2018, **89**, pp.755-779.
109. Boehlert, C. and Longanbach, S. A comparison of the microstructure and creep behavior of cold rolled HAYNES® 230 alloy™ and HAYNES® 282 alloy™. *Materials Science and Engineering: A.* 2011, **528**(15), pp.4888-4898.
110. Rashidi, S., Choi, J.-P., Stevenson, J.W., Pandey, A. and Gupta, R. High temperature oxidation behavior of aluminized Haynes 230. *Corrosion Science.* 2020, **174**, p.108835.
111. Archana, M., Rao, C.J., Ningshen, S. and Philip, J. High-temperature air and steam oxidation and oxide layer characteristics of Alloy 617. *Journal of Materials Engineering and Performance.* 2021, **30**, pp.931-943.
112. Ma, S., Ding, Q., Wei, X., Zhang, Z. and Bei, H. The Effects of Alloying Elements Cr, Al, and Si on Oxidation Behaviors of Ni-Based Superalloys. *Materials.* 2022, **15**(20), p.7352.
113. Wang, X. and Szpunar, J.A. Effects of grain sizes on the oxidation behavior of Ni-based alloy 230 and N. *Journal of Alloys and Compounds.* 2018, **752**, pp.40-52.
114. Gehlbach, R. and McCoy, H. Phase instability in Hastelloy N. In: *International Symposium on Structural Stability in Superalloys*: TMS Seven Springs, Pennsylvania, 1968, pp.346-366.
115. Chevalier, S. What did we learn on the reactive element effect in chromia scale since Pfeil's patent? *Materials and Corrosion.* 2014, **65**(2), pp.109-115.
116. Wagner, C. and Traud, W. Über die Deutung von Korrosionsvorgängen durch Überlagerung von elektrochemischen Teilvorgängen und über die Potentialbildung an Mischelektroden. *Zeitschrift für Elektrochemie und angewandte physikalische Chemie.* 1938, **44**(7), pp.391-402.
117. Forsberg, C.W. Reactors with molten salts: options and missions. *Frederick Joliot & Otto Hahn Summer School on Nuclear Reactors, Physics and Fuels Systems, Cadarache, France.* 2004.
118. Lee, M., Muránsky, O., Karatchevtseva, I., Huang, H. and Laws, K. Corrosion performance of Ni-based structural alloys for applications in molten-salt based energy systems: Experiment & numerical validation. *Corrosion Science.* 2021, **190**, p.109607.
119. Evans III, R., DeVan, J. and Watson, G. *Self-diffusion of chromium in nickel-base alloys.* Oak Ridge National Laboratory, 1961.
120. Mehrer, H., Peteline, S., Huang, M. and Chang, Y. Self-diffusion in nickel-manganese alloys. In: *Defect and Diffusion Forum*: Trans Tech Publ, 2005, pp.352-357.
121. Li, H., Yang, X., Yin, X., Wang, X., Tang, J. and Gong, J. Effect of chloride impurity on corrosion kinetics of stainless steels in molten solar salt for CSP

application: experiments and modeling. *Oxidation of Metals.* 2021, **95**, pp.311-332.
122. Sridharan, K. and Allen, T. Corrosion in molten salts. In: *Molten salts chemistry*. Elsevier, 2013, pp.241-267.
123. Pavlik, V., Kontrik, M. and Boča, M. Corrosion behavior of Incoloy 800H/HT in the fluoride molten salt FLiNaK+ MF_x (MF_x = CrF_3, FeF_2, FeF_3 and NiF_2). *New Journal of Chemistry.* 2015, **39**(12), pp.9841-9847.
124. Yin, H., Qiu, J., Liu, H., Liu, W., Wang, Y., Fei, Z., Zhao, S., An, X., Cheng, J. and Chen, T. Effect of CrF_3 on the corrosion behaviour of Hastelloy-N and 316L stainless steel alloys in FLiNaK molten salt. *Corrosion Science.* 2018, **131**, pp.355-364.
125. Pavlík, V., Boča, M. and Kityk, A. Accelerated corrosion testing in molten fluoride salts: Effect of additives and the crucible material. *Corrosion Science.* 2022, **195**, p.110011.
126. Misra, A.K. and Whittenberger, J.D. Fluoride salts and container materials for thermal energy storage applications in the temperature range 973–1400 K. In: *22nd Intersociety Energy Conversion Engineering Conference*: American Institute of Aeronautics and Astronautics, 1987, p.9226.
127. Ouyang, F.-Y., Chang, C.-H., You, B.-C., Yeh, T.-K. and Kai, J.-J. Effect of moisture on corrosion of Ni-based alloys in molten alkali fluoride FLiNaK salt environments. *Journal of nuclear materials.* 2013, **437**(1-3), pp.201-207.
128. Ouyang, F.-Y., Chang, C.-H. and Kai, J.-J. Long-term corrosion behaviors of Hastelloy-N and Hastelloy-B3 in moisture-containing molten FLiNaK salt environments. *Journal of nuclear materials.* 2014, **446**(1-3), pp.81-89.
129. Wang, Y., Liu, H., Yu, G., Hou, J. and Zeng, C. Electrochemical study of the corrosion of a Ni-based alloy GH3535 in molten (Li, Na, K) F at 700 °C. *Journal of Fluorine Chemistry.* 2015, **178**, pp.14-22.
130. Shaffer, J.H. *PREPARATION AND HANDLING OF SALT MIXTURES FOR THE MOLTEN SALT REACTOR EXPERIMENT.* Oak Ridge National Lab.(ORNL), Oak Ridge, TN (United States), 1971.
131. Qiu, J., Leng, B., Liu, H., Macdonald, D.D., Wu, A., Jia, Y., Xue, W., Yu, G. and Zhou, X. Effect of SO_4^{2-} on the corrosion of 316L stainless steel in molten FLiNaK salt. *Corrosion Science.* 2018, **144**, pp.224-229.
132. Zhu, Y., Qiu, J., Hou, J., Liu, W., Chen, H., Ai, H., Yu, G., Wang, J. and Zhou, X. Effects of SO_4^{2-} ions on the corrosion of GH3535 weld joint in FLiNaK molten salt. *Journal of nuclear materials.* 2017, **492**, pp.122-127.
133. Ai, H., Shen, M., Sun, H., Dolan, K.P., Wang, C., Ge, M., Yin, H., Li, X., Peng, H. and Li, N. Effects of O^{2-} additive on corrosion behavior of Fe–Cr–Ni alloy in molten fluoride salts. *Corrosion Science.* 2019, **150**, pp.175-182.
134. Sankar, K.M. and Singh, P.M. Effect of oxide impurities on the corrosion behavior of structural materials in molten LiF-NaF-KF. *Corrosion Science.* 2022, **206**, p.110473.
135. Ignatiev, V., Surenkov, A., Gnidoy, I., Kulakov, A., Uglov, V., Vasiliev, A. and Presniakov, M. Intergranular tellurium cracking of nickel-based alloys in molten Li, Be, Th, U/F salt mixture. *Journal of nuclear materials.* 2013, **440**(1-3), pp.243-249.
136. Ignatiev, V., Surenkov, A., Gnidoi, I., Fedulov, V., Uglov, V., Afonichkin, V., Bovet, A., Subbotin, V., Panov, A. and Toropov, A. Compatibility of selected Ni-based alloys in molten Li, Na, Be/F salts with PuF_3 and tellurium additions. *Nuclear Technology.* 2008, **164**(1), pp.130-142.

137. Qiu, J., Zou, Y., Yu, G., Liu, H., Jia, Y., Li, Z., Huai, P., Zhou, X. and Xu, H. Compatibility of container materials with Cr in molten FLiNaK salt. *Journal of Fluorine Chemistry.* 2014, **168**, pp.69-74.
138. Zheng, G., Kelleher, B., He, L., Cao, G., Anderson, M., Allen, T. and Sridharan, K. High-temperature corrosion of UNS N10003 in molten Li2BeF4 (FLiBe) salt. *Corrosion.* 2015, **71**(10), pp.1257-1266.
139. Wang, Y., Zeng, C. and Li, W. The influence of temperature gradient on the corrosion of materials in molten fluorides. *Corrosion Science.* 2018, **136**, pp.180-187.
140. Kondo, M., Nagasaka, T., Tsisar, V., Sagara, A., Muroga, T., Watanabe, T., Oshima, T., Yokoyama, Y., Miyamoto, H. and Nakamura, E. Corrosion of reduced activation ferritic martensitic steel JLF-1 in purified Flinak at static and flowing conditions. *Fusion Engineering and Design.* 2010, **85**(7-9), pp.1430-1436.
141. Kondo, M., Nagasaka, T., Sagara, A., Noda, N., Muroga, T., Xu, Q., Nagura, M., Suzuki, A. and Terai, T. Metallurgical study on corrosion of austenitic steels in molten salt LiF–BeF2 (Flibe). *Journal of nuclear materials.* 2009, **386**, pp.685-688.
142. Ma, L., Zhang, C., Wu, Y., Lu, Y. and Ma, C. Dynamic corrosion behavior of 316L stainless steel in quaternary nitrate-nitrite salts under different flow rates. *Solar Energy Materials and Solar Cells.* 2020, **218**, p.110821.
143. Zhang, X., Zhang, C., Wu, Y. and Lu, Y. Experimental research of high temperature dynamic corrosion characteristic of stainless steels in nitrate eutectic molten salt. *Solar Energy.* 2020, **209**, pp.618-627.
144. Caraballo, A., Galán-Casado, S., Caballero, Á. and Serena, S. Molten salts for sensible thermal energy storage: a review and an energy performance analysis. *Energies.* 2021, **14**(4), p.1197.
145. Wang, Y.L., Wang, Q., Liu, H.J. and Zeng, C.L. Effect of grain refinement on the corrosion of Ni-Cr alloys in molten (Li, Na, K) F. *Corrosion Science.* 2016, **109**, pp.43-49.
146. Maric, M., Muránsky, O., Karatchevtseva, I., Ungár, T., Hester, J., Studer, A., Scales, N., Ribárik, G., Primig, S. and Hill, M. The effect of cold-rolling on the microstructure and corrosion behaviour of 316L alloy in FLiNaK molten salt. *Corrosion Science.* 2018, **142**, pp.133-144.
147. Was, G., Jiao, Z., Getto, E., Sun, K., Monterrosa, A., Maloy, S., Anderoglu, O., Sencer, B. and Hackett, M. Emulation of reactor irradiation damage using ion beams. *Scripta Materialia.* 2014, **88**, pp.33-36.
148. Konings, R., Allen, T.R. and Stoller, R.E. Basic aspects of radiation effects in solids/basic aspects of multi-scale modeling. *(No Title).* 2012.
149. Zhu, H., Holmes, R., Hanley, T., Davis, J., Short, K. and Edwards, L. High-temperature corrosion of helium ion-irradiated Ni-based alloy in fluoride molten salt. *Corrosion Science.* 2015, **91**, pp.1-6.
150. Jiao, Z., Ham, N. and Was, G. Microstructure of helium-implanted and proton-irradiated T91 ferritic/martensitic steel. *Journal of nuclear materials.* 2007, **367**, pp.440-445.
151. Zhu, Z., Huang, H., Lei, G., Wu, Y., Ren, C., Liu, A. and Zhu, Z. Synergistic effect of irradiation and molten salt corrosion: Acceleration or deceleration? *Corrosion Science.* 2021, **185**, p.109434.

152. Zhou, W., Yang, Y., Zheng, G., Woller, K.B., Stahle, P.W., Minor, A.M. and Short, M.P. Proton irradiation-decelerated intergranular corrosion of Ni-Cr alloys in molten salt. *Nature communications.* 2020, **11**(1), p.3430.
153. *MATLAB Version: 9.10.0.1710957 (R2021a) Update 4.* The MathWorks Inc., 2021.
154. Liu, M., Zheng, J., Lu, Y., Li, Z., Zou, Y., Yu, X. and Zhou, X. Investigation on corrosion behavior of Ni-based alloys in molten fluoride salt using synchrotron radiation techniques. *Journal of nuclear materials.* 2013, **440**(1-3), pp.124-128.
155. Liu, Q., Qian, J., Barker, R., Wang, C., Neville, A. and Pessu, F. Application of double loop electrochemical potentio-kinetic reactivation for characterizing the intergranular corrosion susceptibility of stainless steels and Ni-based alloys in solar nitrate salts used in CSP systems. *Engineering Failure Analysis.* 2021, **129**, p.105717.
156. Standardisation, I.O.f. *ISO 17245:2015 Corrosion of metals and alloys — Test method for high temperature corrosion testing of metallic materials by immersing in molten salt or other liquids under static conditions.* https://www.iso.org/standard/59473.html, 2015.
157. Standardisation, I.O.f. *ISO 21608:2012 Corrosion of metals and alloys — Test method for isothermal-exposure oxidation testing under high-temperature corrosion conditions for metallic materials.* https://www.iso.org/standard/53990.html, 2012.
158. Standard, A. G1-03, 2017.". *Standard Practice for Preparing, Cleaning, and Evaluating Corrosion Test Specimens," ASTM International, West Conshohocken, PA. Doi.* 2017, **10**.
159. Institute, H.R. *VARIABLE PRESSURE SCANNING ELECTRON MICROSCOPE (VP-SEM).* [Online]. 2023. [Accessed 22/06/2023]. Available from: https://www.royce.ac.uk/equipment-and-facilities/variable-pressure-scanning-electron-microscope-vp-sem/
160. Bell, D.C. and Garratt-Reed, A.J. *Energy dispersive X-ray analysis in the electron microscope.* Garland Science, 2003.
161. Park, J.-H., Chen, L., Goretta, K., Koritala, R. and Balachandran, U. Oxidation of hastelloy C276. In: *AIP Conference Proceedings*: American Institute of Physics, 2002, pp.495-502.
162. Ziemniak, S.E., Anovitz, L.M., Castelli, R.A. and Porter, W.D. Thermodynamics of Cr_2O_3, $FeCr_2O_4$, $ZnCr_2O_4$, and $CoCr_2O_4$. *The Journal of Chemical Thermodynamics.* 2007, **39**(11), pp.1474-1492.
163. Kassim, S.A., Thor, J.A., Seman, A.A. and Abdullah, T.K. High temperature corrosion of Hastelloy C22 in molten alkali salts: The effect of pre-oxidation treatment. *Corrosion Science.* 2020, **173**, p.108761.
164. Cao, J., Zhang, J., Chen, R., Ye, Y. and Hua, Y. High temperature oxidation behavior of Ni-based superalloy GH202. *Materials Characterization.* 2016, **118**, pp.122-128.
165. Wang, J., Xue, H. and Wang, Y. Oxidation behavior of Ni-based superalloy GH738 in static air between 800 and 1000 °C. *Rare Metals.* 2021, **40**, pp.616-625.
166. Hua, Y., Rong, Z., Ye, Y., Chen, K., Chen, R., Xue, Q. and Liu, H. Laser shock processing effects on isothermal oxidation resistance of GH586 superalloy. *Applied Surface Science.* 2015, **330**, pp.439-444.

167. Tao, L., Jiasheng, D., Hui, L., Zhijun, L., Xingtai, Z. and Langhong, L. Oxidation Behavior of GH3535 Superalloy at 700 °C and 900 °C. *Chinese Journal of Materials Research.* 2015, **28**(12), pp.895-900.
168. Chen, J., Rogers, P. and Little, J. Oxidation behavior of several chromia-forming commercial nickel-base superalloys. *Oxidation of Metals.* 1997, **47**, pp.381-410.
169. Greene, G. and Finfrock, C. Oxidation of Inconel 718 in air at high temperatures. *Oxidation of Metals.* 2001, **55**, pp.505-521.
170. Kumar, L., Venkataramani, R., Sundararaman, M., Mukhopadhyay, P. and Garg, S. Studies on the oxidation behavior of Inconel 625 between 873 and 1523 K. *Oxidation of Metals.* 1996, **45**, pp.221-244.
171. Pérez-González, F., Garza-Montes-de Oca, N. and Colás, R. High temperature oxidation of the Haynes 282© nickel-based superalloy. *Oxidation of Metals.* 2014, **82**, pp.145-161.
172. Maier, K., Mehrer, H., Lessmann, E. and Schüle, W. Self-diffusion in nickel at low temperatures. *Physica status solidi (b).* 1976, **78**(2), pp.689-698.
173. Murarka, S., Anand, M. and Agarwala, R. Diffusion of vanadium in aluminium and nickel. *Acta Metallurgica.* 1968, **16**(1), pp.69-72.
174. Wu, Q., Li, S.-S., Ma, Y. and Gong, S.-K. First principles calculations of alloying element diffusion coefficients in Ni using the five-frequency model. *Chinese Physics B.* 2012, **21**(10), p.109102.
175. Swalin, R., Martin, A. and Olson, R. Diffusion of magnesium, silicon, and molybdenum in nickel. *Jom.* 1957, **9**, pp.936-939.
176. Askill, J. *Tracer diffusion data for metals, alloys, and simple oxides.* Springer Science & Business Media, 2012.
177. Campbell, C.E., Boettinger, W.J. and Kattner, U.R. Development of a diffusion mobility database for Ni-base superalloys. *Acta Materialia.* 2002, **50**(4), pp.775-792.
178. Allison, H.W. and Samelson, H. Diffusion of aluminum, magnesium, silicon, and zirconium in nickel. *Journal of Applied Physics.* 1959, **30**(9), pp.1419-1424.
179. Kearney, D., Herrmann, U., Nava, P., Kelly, B., Mahoney, R., Pacheco, J., Cable, R., Potrovitza, N., Blake, D. and Price, H. Assessment of a molten salt heat transfer fluid in a parabolic trough solar field. *J. Sol. Energy Eng.* 2003, **125**(2), pp.170-176.
180. Wang, Y. and Zhang, J. Electrochemical properties of CrF_2 in FLiNaK molten salt and the new analytical methods for their determination. *Journal of The Electrochemical Society.* 2020, **167**(8), p.086503.
181. Yang, Q., Ge, J. and Zhang, J. Electrochemical study on the kinetic properties of Fe^{2+}/Fe, Ni^{2+}/Ni, Cr^{2+}/Cr and Cr^{3+}/Cr^{2+} in molten $MgCl_2$-KCl-NaCl salts. *Journal of The Electrochemical Society.* 2021, **168**(1), p.012504.
182. Li, X., Xu, T., Liu, M. and Zuo, Y. Diffusion behaviors of HF in molten LiF-BeF_2 and LiF-NaF-KF eutectics studied by FPMD simulations and electrochemical techniques. *Journal of nuclear materials.* 2022, **572**, p.154031.
183. Liu, Q., Liu, X., Hao, G. and Xu, H. Effect of O^{2-} additive on the corrosion behavior of Hastelloy N alloy in molten FLiNaK. *Corrosion Science.* 2023, **213**, p.111001.

184. Massot, L., Cassayre, L., Chamelot, P. and Taxil, P. On the use of electrochemical techniques to monitor free oxide content in molten fluoride media. *Journal of Electroanalytical Chemistry.* 2007, **606**(1), pp.17-23.
185. Whittle, D., Shida, Y., Wood, G., Stott, F. and Bastow, B. Enhanced diffusion of oxygen during internal oxidation of nickel-base alloys. *Philosophical Magazine A.* 1982, **46**(6), pp.931-949.
186. Lu, J., Choi, E. and Zhou, H. Physical properties of Hastelloy® C-276™ at cryogenic temperatures. *Journal of Applied Physics.* 2008, **103**(6).
187. Burgess, S., Li, X. and Holland, J. High spatial resolution energy dispersive X-ray spectrometry in the SEM and the detection of light elements including lithium. *Microscopy and Analysis.* 2013, **6**, pp.S8-S13.
188. Atkinson, A. and Taylor, R. The self-diffusion of Ni in NiO and its relevance to the oxidation of Ni. *Journal of Materials Science.* 1978, **13**, pp.427-432.
189. Greskovich, C. Kinetics of $NiCr_2O_4$ formation and diffusion of Cr^{3+} ions in NiO. *Journal of the American Ceramic Society.* 1970, **53**(9), pp.498-502.
190. Chen, K., Zhang, L. and Shen, Z. Understanding the surface oxide evolution of T91 ferritic-martensitic steel in supercritical water through advanced characterization. *Acta Materialia.* 2020, **194**, pp.156-167.
191. Atkinson, H. A review of the role of short-circuit diffusion in the oxidation of nickel, chromium, and nickel-chromium alloys. *Oxidation of Metals.* 1985, **24**, pp.177-197.

Appendix A

Sensitivity of empirical and mechanistic models to input parameters

This appendix includes the sensitivity study of empirical and mechanistic model outputs to key input parameters used to model the high temperature oxidation and molten salt corrosion of Hastelloy C276. In this sensitivity study. Within this study, input parameters were varied by ±1%, ±5% and ±10%, with the percentage change in the output in each instance being calculated. This allowed for the most influential parameters to be identified allowing potential sources of error in the predictive model outputs to be discussed.

A.1 Introduction

To discuss potential reasons for differences between the results of predictive models and experimental research, a study was conducted to determine the sensitivity of the empirical and mechanistic models to their input parameters. A summary of the input parameters to the empirical and mechanistic models is presented in Table A.1.

Table A.1 - Summary of input parameters to empirical and mechanistic models for predicting the high temperature oxidation and molten salt corrosion behaviour of Hastelloy C276.

Modelling Methodology	Key Input Parameters
Empirical Method	Material Compositions
	Material K_P Values
	Test Conditions
Mechanistic Method	Element Diffusion Coefficients
	Material Composition
	Coupon Geometry
	Test Conditions

In both models, the material compositions are input into the model, however, they are utilised differently. Within the empirical model, the material compositions are used to calculate values of U which were then used in developing predictions of K_P. This differs from the mechanistic model, in which the material composition is used to provide initial concentrations of each alloying element, allowing for

elemental distributions and concentrations changes at the substrate – air interface to be calculated. Therefore, since the material composition directly impacts the result obtained from the empirical model, the impact of changes to the composition on predicted K_P values needs to be understood.

In the case of the mechanistic model, the key input parameters are the element diffusion coefficients, which differ depending on sources of literature. To combat these differences, diffusion coefficients were utilised from different sources of literature to provide minimum and maximum specific mass change predictions. However, the diffusion coefficients impact the elemental distribution predictions and consequentially the specific mass change. Therefore, this sensitivity study will investigate how changes in the diffusion coefficients impact the elemental distribution predictions and hence how the minimum and maximum specific mass change predictions vary.

A.2 Empirical model sensitivity to input parameters

In the case of the empirical model, many of the calculations stemmed from the material compositions input into the model. For each material utilised within the model, the material compositions were used to calculate values of U which are subsequently used in the prediction of the K_P value for Hastelloy C276, Therefore, values of U for the alloys used within the empirical model were varied by ±1%, ±5% and ±10%. A summary of the test cases utilised within this sensitivity study are presented in Table A.2.

Table A.2 – Summary of input parameters to empirical and mechanistic models for predicting the high temperature oxidation and molten salt corrosion behaviour of Hastelloy C276.

Material	Baseline U Input (kJ/mol)	Baseline U ± 1% (kJ/mol)	Baseline U ± 5% (kJ/mol)	Baseline U ± 10% (kJ/mol)
Hastelloy C276	181.35	183.16 179.54	190.42 172.28	199.48 163.21
Udimet	318.39	321.58 315.21	334.31 302.47	350.23 286.56
Waspaloy	342.12	345.54 338.70	359.26 325.01	376.33 307.91
Astroloy	323.64	326.87 320.40	339.82 307.46	356.00 291.27
GH586	253.40	255.93 250.86	266.07 240.73	278.74 228.06
GH202	298.57	301.55 295.58	313.50 283.64	328.43 268.71

Based on the output K_P value calculated, the correlation coefficient, CC, expressed as equation A.1, was calculated to express how the percentage change in the input influenced the percentage change in the result:

$$CC = \frac{\%\ Change\ in\ output}{\%\ Change\ in\ input} \qquad \textbf{A.1}$$

The resulting values of CC for each change in the input values of U are presented in Figure A.1.

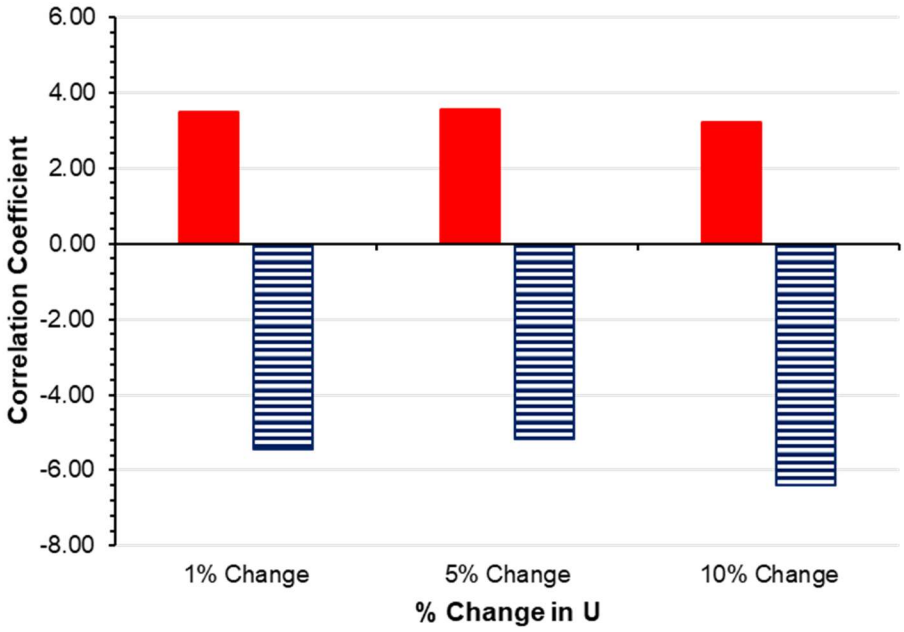


Figure A.1 - Correlation coefficients for parabolic rate constants of Hastelloy C276 in dry air at 700 °C up to 200 hours showing correlation coefficients ranging from 3.2 to 6.4 indicating that results obtained from the empirical model are extremely sensitive to the input values of U.

As shown in Figure A.1, 1%, 5% and 10% changes in the values of U result in changes in K_P between 3.2 times and 6.4 the change in the input value. Therefore, small errors within the input values of U can have a significant impact on the oxidation prediction. As an extension of this, the values of U are dependent on the input material composition and hence, changes in the material composition can have an impact on the K_P values.

A.3 Mechanistic model sensitivity to input parameters

The same sensitivity analysis was conducted within the mechanistic model, with elemental diffusion coefficients varied by 1%, 5% and 10% to obtain CC values for changes in the oxidation prediction, particularly the predicted specific mass changes due to oxide formation and the associated parabolic rate constant for Hastelloy C276 in a dry air environment. The resulting CC values for both the specific mass changes and corresponding parabolic rate constants are presented in Figure 8.2.

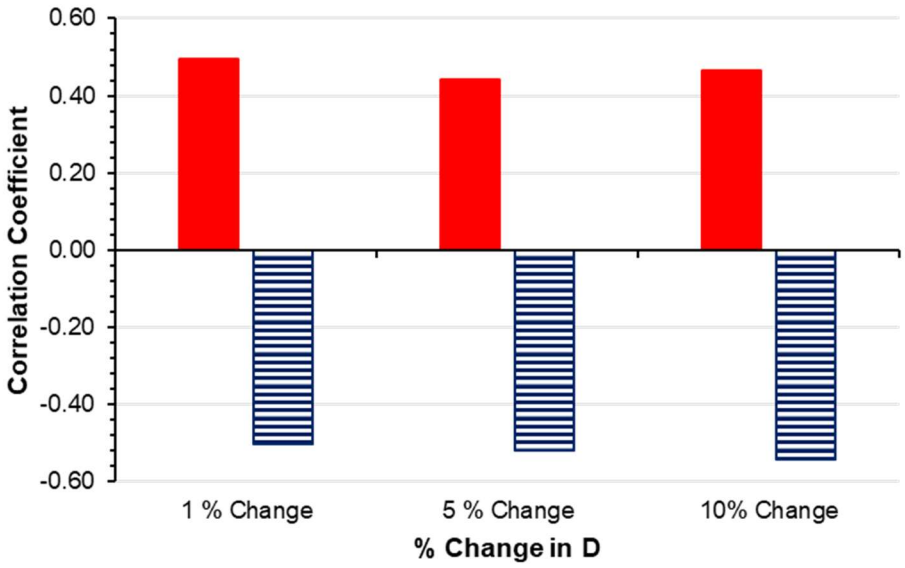


Figure 8.2 – Correlation coefficients for specific mass changes and parabolic rate constants of Hastelloy C276 in dry air at 700 °C up to 200 hours showing values are less than unity. Hence, the mechanistic model is not very sensitive to changes in the input diffusion coefficients of each alloying element.

The CC values presented in Figure 8.2 are all than unity, indicating that the percentage change in the output is half of the change of the input. Therefore, it can be said that the specific mass change result, and hence the parabolic rate constants output by the mechanistic model, are insensitive to errors within the diffusion coefficient values and results obtained by the mechanistic model are reliable.

However, the input diffusion coefficients have a direct impact on the predicted concentration changes for each element. Since concentration changes of the different alloying elements, particularly Cr, are utilised in the corrosion model, it is important that understand the sensitivity of these results to changes in the input data. Therefore, CC values were calculated for each element for which the concentration change is predicted. To maintain consistency across all sensitivity studies, the input diffusion coefficients were varied by ± 1%, ± 5% and ± 10%. The CC values for each element across all six sensitivity test cases are presented in Figure 8.3.

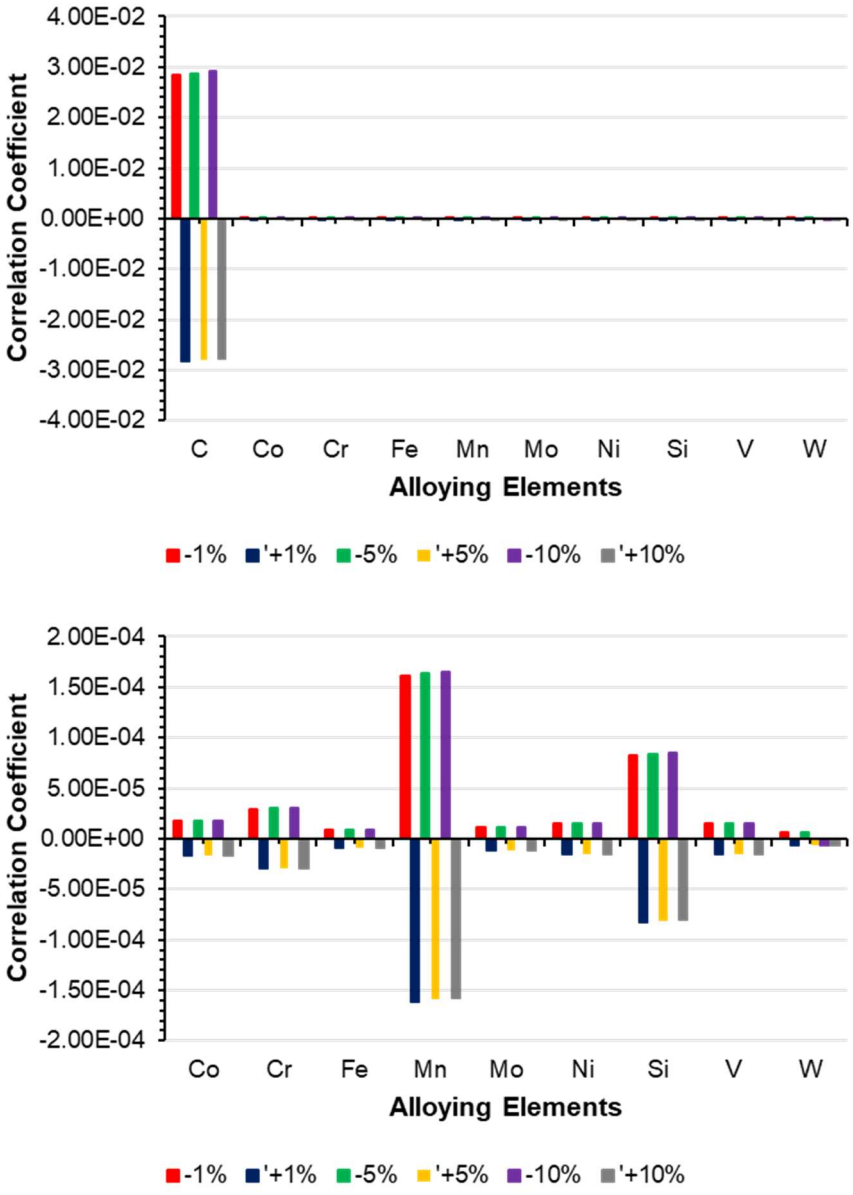


Figure 8.3 – CC values for the concentration changes each alloying element present in Hastelloy C276 when diffusion coefficients were varied by 1%, 5% and 10% in both the positive and negative directions. Results show very little change in the element concentrations; hence, concentration values are insensitive to the input diffusion coefficients.

The result presented in Figure 8.3 shows that over relatively small variations in the diffusion coefficients used, elemental concentration changes and the predicted specific mass changes are stable and insensitive to changes in the input diffusion coefficients. The largest variation is observed for C, whose diffusion coefficient is largest by a factor of a minimum of $1x10^2$. Larger changes were also observed for Mn and Si which have the second and third largest diffusion coefficients respectively. It therefore makes sense that larger variations are observed for the concentration changes of C, Mn, and Si as 1, 5 and 10% variations in these

diffusion coefficients are greater than the same percentage changes in the diffusion coefficients of all other alloying elements. Despite these changes, all CC values are far less than one, hence the concentration changes of all elements are insensitive to small changes in the diffusion coefficients.

However, when studying examining the differences in the diffusion coefficients used within this study, large variations can be observed depending on the sources of literature. A summary of the differences in diffusion coefficients used for elements where more than one diffusion coefficients are used are presented in Table A.3.

Table A.3 – Summary of diffusion coefficients utilised in this research, as originally defined in Table 4.10, with the difference between the diffusion coefficients for each element expressed as a percentage difference.

Element	Input Diffusion Coefficients (cm^2/s)	Percentage Difference (%)
Co	6.70×10^{-16} 2.12×10^{-15}	103.94
Cr	4.24×10^{-15} 3.51×10^{-15}	18.84
Fe	4.77×10^{-16} 2.36×10^{-16}	67.60
Mn	3.58×10^{-13} 6.40×10^{-15}	192.98
Mo	2.77×10^{-16} 9.16×10^{-16}	107.13
Ni	1.17×10^{-15} 8.65×10^{-16}	29.98
W	1.22×10^{-16} 2.01×10^{-16}	48.92

In this research, the discrepancies observed in the diffusion coefficients presented in Table A.3 were large with a maximum difference of 192.98% being observed between the quoted diffusion coefficients for Mn. However, the use of multiple diffusion coefficients allowed for a minimum and maximum prediction of the specific mass change to be made. The minimum and maximum values were presented as error bars in Figure 5.11, as shown again in Figure 8.4.

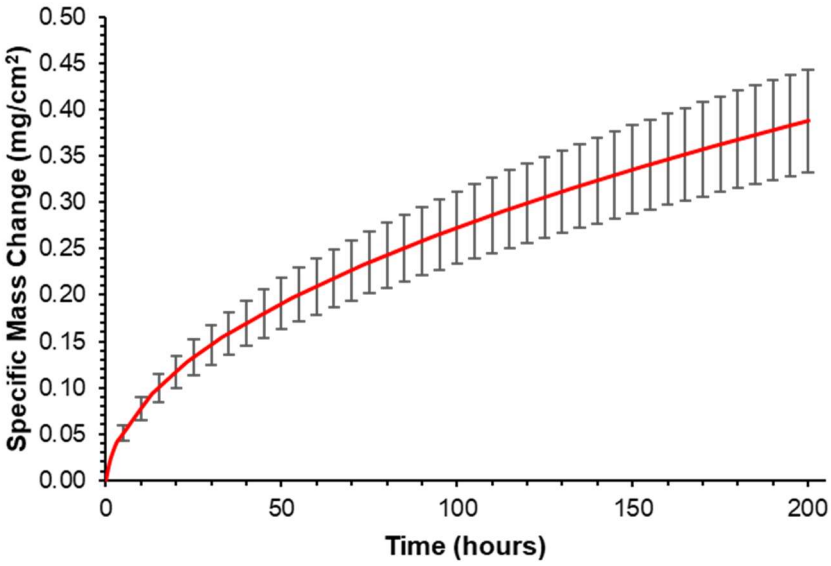


Figure 8.4 – Repeat image of diffusion based prediction for the high temperature oxidation of Hastelloy C276 in a dry air environment at 700 °C, with error bars showing the minimum and maximum specific mass change predictions based on the different diffusion coefficients.

Despite the large differences observed in the diffusion coefficients presented in Table A.3, much smaller differences in specific mass change due to oxide formation presented in Figure 8.4 are observed. CC values calculated at these higher percentage discrepancies were still had a value around 0.5, as shown in Figure 8.5, further illustrates the mechanistic model's insensitivity to errors within the input parameters.

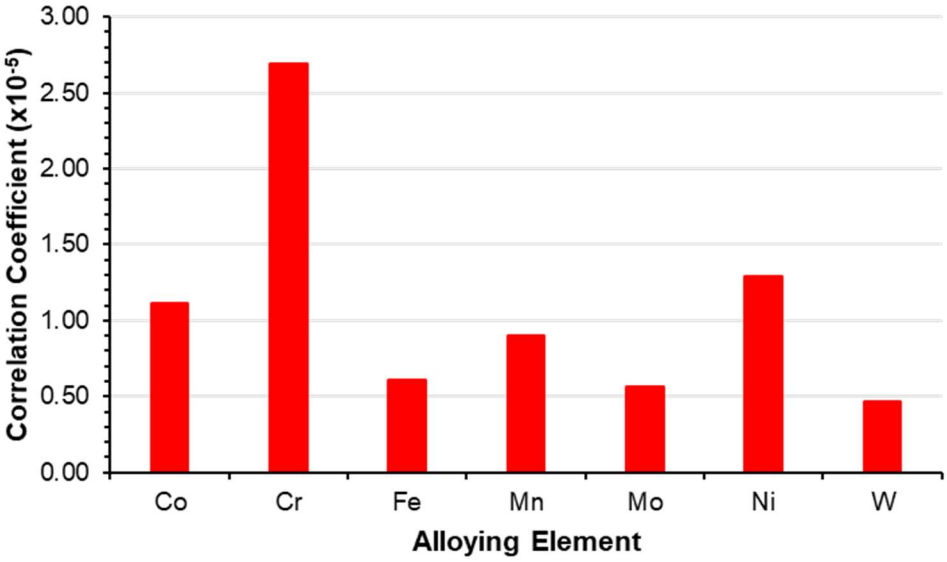


Figure 8.5 – CC values comparing differences in the diffusion coefficients presented in Table A.3 to the predicted minimum and maximum concentration changes for each element, showing CC values less than unity, confirming that the mechanistic model is insensitive to significantly large changes in the input parameters.